UNIVERSIDAD COMPLUTENSE DE MADRID
FACULTAD DE CIENCIAS QUÍMICAS

TESIS DOCTORAL

Self-assembly of electroactive supramolecular architectures: a bio-inspired approach

Auto-ensamblaje de estructuras supramoleculares electroactivas: estrategias bio-inspiradas

MEMORIA PARA OPTAR AL GRADO DE DOCTORA

PRESENTADA POR

Alicia López Andarias

DIRECTORES

Nazario Martín León
Carmen María Atienza Castellanos

Madrid

UNIVERSIDAD COMPLUTENSE DE MADRID
FACULTAD DE CIENCIAS QUÍMICAS
Departamento de Química Orgánica

Self-assembly of electroactive supramolecular architectures: a bio-inspired approach

Auto-ensamblaje de estructuras supramoleculares electroactivas: estrategias bio-inspiradas

TESIS DOCTORAL

Alicia López Andarias

Madrid, 2019

Self-assembly of electroactive supramolecular architectures: a bio-inspired approach

Auto-ensamblaje de estructuras supramoleculares electroactivas: estrategias bio-inspiradas

Directores:

Dr. Nazario Martín León

Dra. Carmen Mª Atienza Castellanos

Memoria para optar al grado de

DOCTORA EN CIENCIAS QUÍMICAS

que presenta

Alicia López Andarias

Madrid, 2019

UNIVERSIDAD COMPLUTENSE
MADRID

DECLARACIÓN DE AUTORÍA Y ORIGINALIDAD DE LA TESIS PRESENTADA PARA OBTENER EL TÍTULO DE DOCTOR

D./Dña. Alicia López Andarias, estudiante en el Programa de Doctorado en Química Orgánica, de la Facultad de Ciencias Químicas de la Universidad Complutense de Madrid, como autora de la tesis presentada para la obtención del título de Doctor y titulada: *Self-assembly of electroactive supramolecular architectures: a bio-inspired approach; Auto-ensamblaje de estructuras supramoleculares electroactivas: estrategias bio-inspiradas* y dirigida por: D. Nazario Martín León y Dña. Carmen Mª Atienza Castellanos,

DECLARO QUE:

La tesis es una obra original que no infringe los derechos de propiedad intelectual ni los derechos de propiedad industrial u otros, de acuerdo con el ordenamiento jurídico vigente, en particular, la Ley de Propiedad Intelectual (R.D. legislativo 1/1996, de 12 de abril, por el que se aprueba el texto refundido de la Ley de Propiedad Intelectual, modificado por la Ley 2/2019, de 1 de marzo, regularizando, aclarando y armonizando las disposiciones legales vigentes sobre la materia), en particular, las disposiciones referidas al derecho de cita. Del mismo modo, asumo frente a la Universidad cualquier responsabilidad que pudiera derivarse de la autoría o falta de originalidad del contenido de la tesis presentada de conformidad con el ordenamiento jurídico vigente.

En Madrid, a 12 de Septiembre de 2019

D. Nazario Martín León, Catedrático de Universidad del Departamento de Química Orgánica de la Universidad Complutense de Madrid y **Dª. Carmen Mª Atienza Castellanos**, Profesora Titular del Departamento de Química Orgánica de la Universidad Complutense de Madrid,

CERTIFICAN:

Que la presente Memoria titulada: *Self-assembly of electroactive supramolecular architectures: a bio-inspired approach; Auto-ensamblaje de estructuras supramoleculares electroactivas: estrategias bio-inspiradas,* se ha realizado bajo su dirección en el Departamento de Química Orgánica de la Facultad de Ciencias Químicas de la Universidad Complutense de Madrid por la Licenciada en Química Dª. Alicia López Andarias y autorizan su presentación para ser calificada como Tesis Doctoral.

Y para que conste firman el presente certificado en Madrid, a 12 de Septiembre de 2019.

Fdo. Dra. Carmen Mª Atienza Castellanos Fdo. Dr. Nazario Martín León

A mis padres y mi hermano,

Agradecimientos

Esta Tesis Doctoral se ha llevado a cabo en el Departamento de Química Orgánica de la Universidad Complutense de Madrid bajo la dirección de los Profesores Carmen Mª Atienza y Nazario Martín, a los que agradezco enormemente la orientación, sugerencias y estímulo durante estos años. También Nazario, muchas gracias por la confianza depositada desde el primer momento.

La realización del presente trabajo es también fruto de la colaboración con otros grupos de investigación, a los que quiero agradecer su contribución:

Al grupo del Prof. José L. Carrascosa (CNB-CSIC), por los estudios de Crio-microscopía electrónica expuestos en el primer capítulo. En especial a Javi Chichón, por su contribución y ayuda también en la preparación de las muestras.

Al grupo de la Prof. Silvia Osuna (Universidad de Girona), por su contribución en la modelización computacional del capítulo 2.

Al grupo del Prof. Shu Seki (Kyoto University) por la realización de las medidas de fotocorriente.

Especialmente quiero dar las gracias al grupo de la Prof. Aitziber L. Cortajarena (CIC biomaGUNE), no solo por su gran contribución al desarrollo del capítulo dos, sino también por darme la oportunidad de realizar una estancia en su grupo. Gracias también a Antonio, Aline, Edu, Leire, Aldo, Dani y Elena por el buen recibimiento en el grupo. En especial gracias también a Mantas, por todo lo que aprendí durante la estancia y por su ayuda.

También quiero dar las gracias a las personas que conforman los diferentes CAI y centros que han sido indispensables para la realización de muchos de los experimentos recogidos en esta Tesis. A Ángel Sánchez, a la Dra. Dolores Molero y a la Dra. Elena Sáez, del CAI de RMN por su gran dedicación y ayuda en los experimentos de RMN. A los CAI de Espectrometría de Masas de la Facultad de Ciencias Químicas de la UCM y del SIdI de la UAM. Al Centro de Microscopía Electrónica, especialmente a Ana Soubrié (AFM) y Javier García y Adrián Gómez (TEM) por la realización de las imágenes de microscopía. Por último, agradecer a los técnicos de laboratorio, Laura García y Javier Cornejo su ayuda y disposición y, también, a Francisco Javier García la realización de los espectros de FTIR.

Muchísimas gracias también a todos mis compañeros y amigos del departamento, por todo lo que hemos disfrutado juntos. Me llevo muy buenos recuerdos, repletos de risas, con todos vosotros: Alberto, Paula, Elena, Mayka, Dani, Yago, Canario, Sergio, Matías, Paloma. Muy en especial, gracias Jorge, por los cafés (sin que faltase el horóscopo), cervecitas en el Paraninfo (que se complicaban de vez en cuando), sesiones de "cine" y todos los momentos divertidos que he vivido contigo estos años.

Gracias también al grupo de Luís Sánchez, Julia, Yeray, Elisa, Cris y Manu, por su ayuda y los buenos ratitos que echamos durante las comidas.

Mª Ángeles, Beti, Ángel, Andreas, David y Luis, gracias por vuestra ayuda. Agradecer también a Salvo sus bromas y el buen humor que siempre transmite. Gracias Virginia por tu simpatía. Por último, muchas gracias Ana por estar siempre pendiente y ayudarnos tanto.

Por supuesto, agradecer a todos mis compañeros del grupo: Alfon, Rosa, Miki, Javi, Laura, Chus, Paul, Sonia, Marina, muchas gracias por hacer el día a día ameno, repleto de risas y tonterías que hacen que a cualquiera se le olvide un mal día. Gracias también a Valentina, Marta y Sarita, con las que lo he pasado tan bien y a las que he echado mucho de menos este último tiempo. A mis compañeros de IMDEA: Agus, Jose, Javi, Eider, Inés y Rafa, gracias por su ayuda y compañía.

Quiero agradecer ahora a todos los amigos que me han acompañado no solo estos años, sino toda una vida, y lo seguirán haciendo. Al team Swim Happy, con los que he vivido tantísimos buenos momentos y que siempre están ahí. Además, aún sin saber mucho de Química, siempre os habéis preocupado de cómo iban las cosas y saber "de qué va la Tesis". También quiero dar las gracias a mis gemelillos, Sergio y Raúl, por tantos años tan buenos a vuestro lado. También a las *pajarillas*, con las que tan buenos momentos he pasado en la Universidad.

También agradecer a toda mi familia por su apoyo incondicional.

Por último, dar las gracias a las personas que más quiero:

A Andrés, el gran regalo de esta etapa. En los momentos difíciles siempre me has escuchado y apoyado, y me has ayudado a superarlos. Gracias por ser tan positivo, por tantos buenos momentos juntos y porque siempre me motivas para conseguir lo que me proponga.

A mi hermano, por acompañarme siempre, hasta en mis primeros meses de esta Tesis tuve la suerte de estar contigo. Me has enseñado muchísimo, y no hablo sólo de Química, eres la mejor guía que podría tener y un ejemplo a seguir.

Por supuesto, mil gracias a mis padres, por los que soy como soy y he conseguido todo lo que tengo. Porque siempre nos habéis dado todo lo que habéis podido y habéis confiado plenamente en nosotros. Gracias por vuestro cariño, paciencia, entusiasmo y darnos siempre vuestra ayuda con la mejor sonrisa. Os quiero.

Abbreviations and acronyms

1D	One dimensional
2D	Two dimensional
3D	Three dimensional
a. u.	Arbitrary units
AFM	Atomic force microscopy
APCI	Atmospheric-pressure chemical ionization
CD	Circular dichroism
CNT	Carbon nanotube
CT	Charge transfer
CTPR	Consensus tricopeptide repeat
CV	Cyclic voltammetry
DBU	1,8-Diazabicyclo[5.4.0]undec-7-ene
DMF	*N*,*N*-Dimethylformamide
DMSO	Dimethylsulfoxyde
DNA	Deoxyribonucleic acid
DTT	DL-Dithiotreitol
ESI	Electrospray ionization
exTTF	π-Extended tetrathiafulvalene
FTIR	Fourier transform infrared
Fmoc	Fluorenylmethyloxycarbonyl
FP-TRMC	Flash-photolysis time-resolved microwave conductivity
FPLC	Fast protein liquid chromatography
HBTU	*o*-(Benzotriazole-1-yl)-*N,N,N',N'*-tetramethyluronium hexafluorophosphate
HBC	Hexabenzocoronene
HIVP	Human immunodeficiency virus protease
HOMO	Highest occupied molecular orbital
HR	High resolution
LUMO	Lowest unoccupied molecular orbital
MALDI	Matrix-assisted laser desorption/ionization
MS	Mass spectrometry
MW	Molecular weight
NMR	Nuclear magnetic resonance
PBI	Perylenebisimide
PBS	Phosphate buffered saline
PCBM	1-(3-Methoxycarbonylpropyl)-1-phenyl[6,6]methanofullerene
PCC	Pyridinium chlorochromate
PDB	Protein data bank
PDTD	Proteins from the drug target database
PTLC	Preparative thin-layer chromatography
RET	Resonant energy transfer
r.p.m.	Revolution per minute
rt	Room temperature
SEM	Scanning electron microscopy

SAM	Self-assembled monolayer
STM	Scanning tunneling microscope
SWCNT	Single wall carbon nanotube
TEA	Triethylamine
TEM	Transmission electron microscopy
TFA	Trifluoroacetic acid
TLC	Thin-layer chromatography
UV	Ultraviolet
XPS	X-ray photoelectron spectroscopy
XRD	X-ray diffraction

Table of Contents

Summary

"Self-assembly of electroactive supramolecular architectures: a bio-inspired approach"

Introduction

Accomplishing the great level of complexity and sophistication of natural systems is presented as a major challenge to scientists. A multidisciplinary approach is intended to design and create the next generation of advanced materials and, in this regard, supramolecular chemistry can play a key role. In particular, the combination of organic molecules and biomolecules has appeared as a fascinating approach to take advantage of the self-assembling properties and great specificity of the biological systems to obtain materials with enhanced photophysical features. Peptides and proteins are crucial components in living beings and have demonstrated their versatility to construct artificial systems. Although great progress has been made in terms of control and diversity of structure, translating structure into functionality still remains as a major challenge.

Objectives

Chapter 1. Constructing electroactive supramolecular architectures from very simple molecular building blocks which include a small peptide to guide the self-assembly process.

Chapter 2. Designing CTPR proteins as scaffolds for the self-assembly of electroactive organic molecules.

Results and discussion

Chapter 1: Peptide-based electroactive assemblies with enhanced electronic properties.

In the first section of this chapter, we have explored the self-assembling properties in aqueous media of an exTTF derivative endowed with the peptide sequence AGAGA. Derivatives containing small changes in the peptide sequence, such as glycine- or alanine-enriched derivatives, have also been investigated. Temperature-dependent UV/Vis and CD spectroscopy allowed us detecting two different aggregates which are in competition, namely a kinetic state and its thermodynamically stable counterpart. A careful selection of the experimental conditions enabled us obtaining one over the other and characterizing them. Finally, we have studied the redox properties of these

molecules and their respective aggregates and confirmed the different behavior arising from the molecular arrangement in the aggregates.

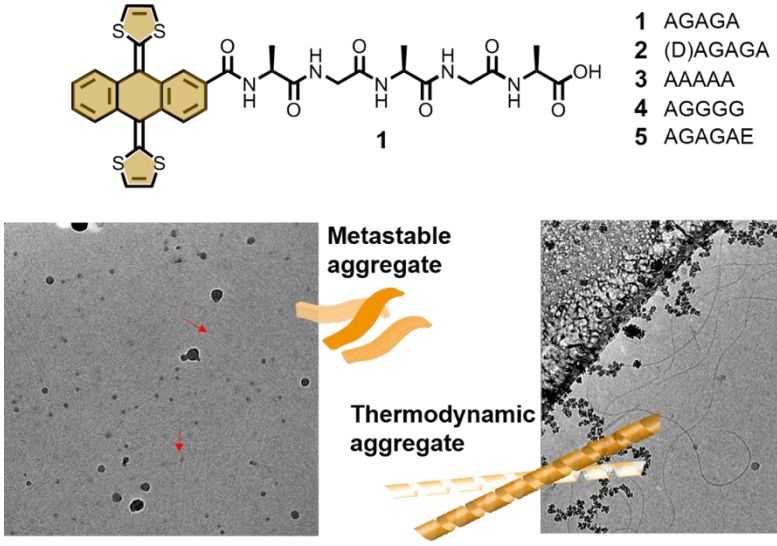

The second section comprises the study of the self-assembly process of a peptide-π-peptide triblock based on quaterthiophene and the pentapeptide AGAGA. As in the previous section, we have been able to obtain different supramolecular polymers by controlling the experimental conditions in solution, such as temperature, concentration and pH. Additionally, we designed two electron-acceptor derivatives based on [60]fullerene and PBI for their ionic co-assembly with the latter quarterthiophene-based electron-donor materials. For that purpose, the molecular design included guanidinium groups, which have a strong affinity for the carboxylate moiety in the peptide chain. The resulting donor-acceptor materials have been fully characterized and the charge carrier mobility along the *n*/*p*-channels has been evaluated by photoconductivity (FP-TRMC) measurements.

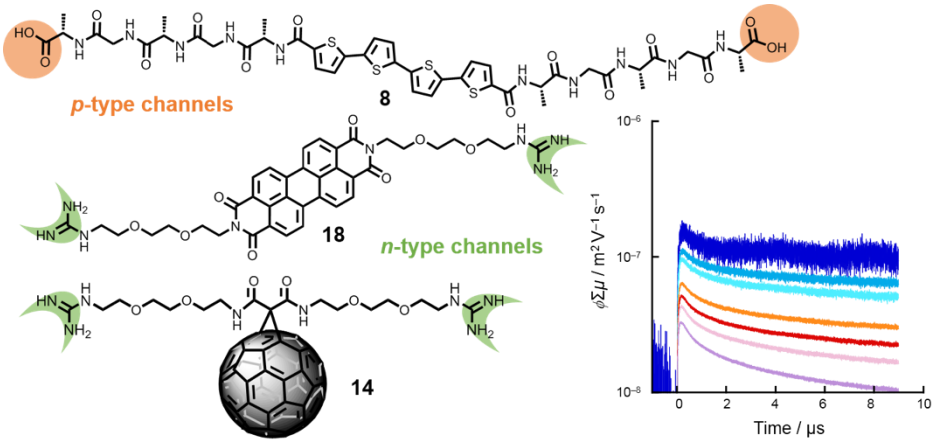

In the last section, we have designed and synthesized a very simple Zn metalloporphyrin mono-substituted in the *meso*-position with the pentapeptide AGAGA. Investigations on the self-assembly properties in aqueous media of the latter system revealed an unusual temperature response. While loosely packed H-type aggregates are found at room temperature, high temperatures led to much ordered fiber-like J-aggregates. The free-base counterpart, as well as their tetra-substituted analogues were also synthesized to shed light on this scarcely reported phenomenon.

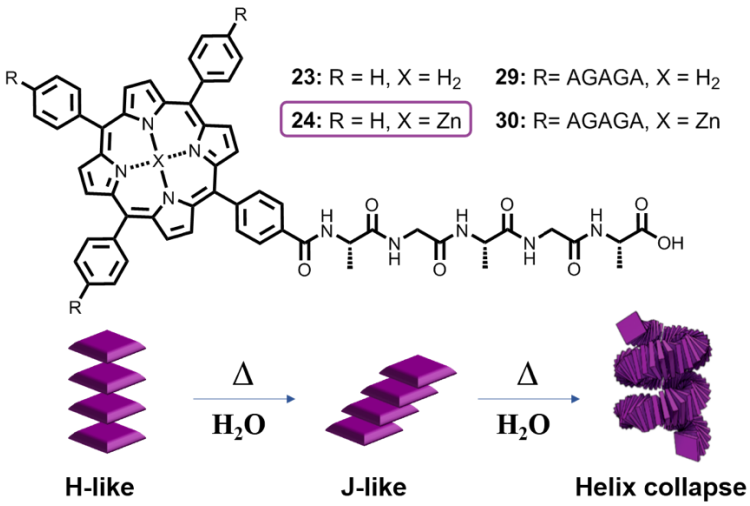

Chapter 2: CTPR proteins as model scaffold for the arrangement of electroactive molecules.

In the first section of this chapter, we envisioned the CTPR proteins as good candidates to bind [60]fullerene. In this sense, van der Waals interactions with the π-surface of this organic molecule and shape complementarity of the C_{60} with the concave surface of the protein, would play a major role. Although C_{60}-conjugates could be obtained, a more water-soluble derivative, C_{60} pyrrolidine tris-acid, was also tested and showed a higher binding affinity. Moreover, by introducing two additional tyrosine mutations, we created new specific binding sites to host the fullerene cage, thus achieving a higher degree and yield of conjugation. The conjugates showed an increased thermal stability due to the new protein-C_{60} interactions. Theoretical calculations supported the experimental findings, confirming that the fullerene interactions occurs in tyrosine-rich binding sites, along with cation-π interactions sites. Finally, photoconductivity (FP-TRMC) measurements showed an enhancement in the charge carrier mobility of the material.

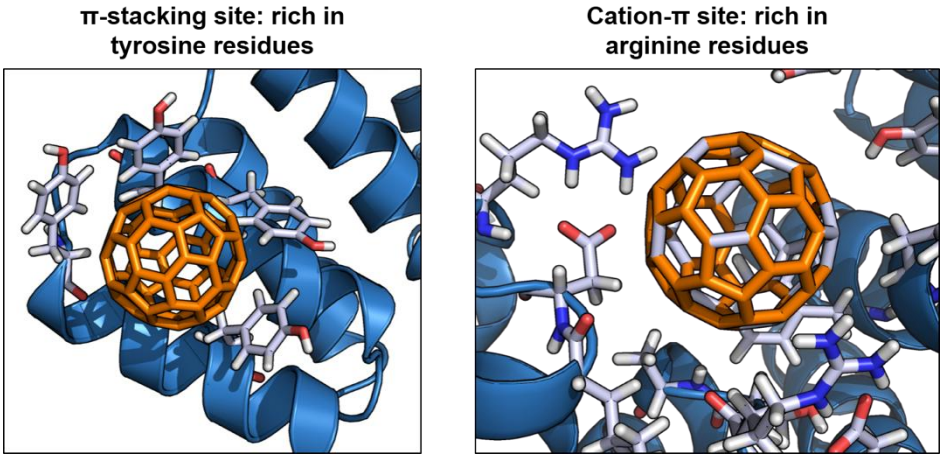

The second section is focused on constructing donor-acceptor materials using the CTPR as template. We took advantage of a previously designed mutated TPR with two different kind of binding sites. On one hand, cysteine mutations were introduced in the turns and Zn-porphyrins, suitably functionalized with maleimide groups, were introduced through thiol Michael addition. On the other hand, two histidine residues per repeat were mutated in the concave surface of the protein. Thus, a [60]fullerene derivative containing a

NTA-chelate ligand was designed to coordinate the imidazole side chains. Preliminary investigations using a rhodamine-based label containing the NTA group, revealed that this chelate ligand was able to bind the mutated histidines of the protein, both in the absence or presence of the Zn-porphyrin.

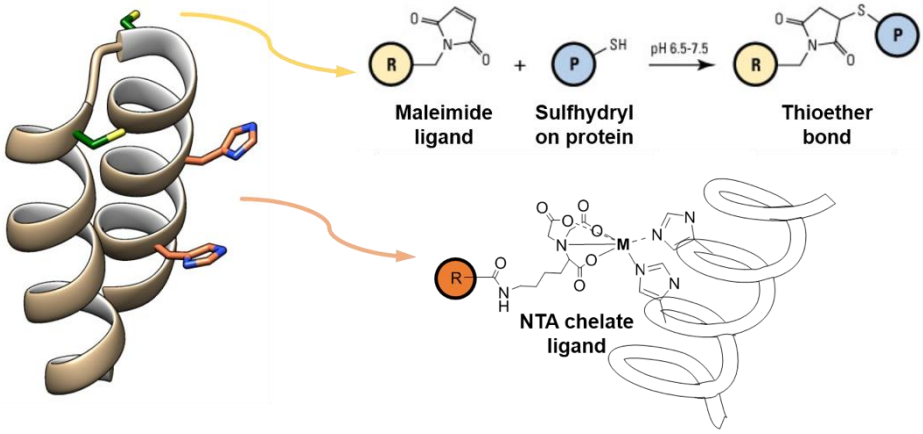

Conclusions

Chapter 1. Amphiphilic structures containing an electroactive π-core and the pentapeptide AGAGA have been designed to investigate their self-assembling properties in aqueous media. The synergy between H-bonding by this minimalistic peptide moiety and π-π interactions has afforded different aggregates by controlling the conditions of the solution (temperature, pH, solvent mixture). In all cases, we have shown through different techniques an important enhancement of the electronic properties in the supramolecular assemblies.

Chapter 2. CTPR proteins have been presented as a versatile scaffold for the organization of [60]fullerene. The high knowledge on the stability and structure of this protein has allowed introduce mutations at specific positions to create new binding sites for this electroactive organic molecule. New properties, such as increased thermal stability or enhanced charge carrier mobility, have been observed in these hybrid materials.

Resumen

"Auto-ensamblaje de estructuras supramoleculares electroactivas: estrategias bio-inspiradas"

Introducción

Conseguir el gran nivel de complejidad y sofisticación que presentan los sistemas naturales constituye un gran reto científico. Para el diseño y desarrollo de una nueva generación de materiales avanzados es necesario un enfoque multidisciplinar, donde la química supramolecular puede jugar un papel clave. En concreto, la combinación de moléculas orgánicas y biomoléculas se figura como una estrategia fascinante con la que beneficiarse de la capacidad de auto-ensamblaje y la gran especificidad de los sistemas biológicos y, así, obtener materiales con mejores propiedades fotofísicas. Los péptidos y las proteínas son componentes esenciales en los seres vivos y han demostrado su gran versatilidad a la hora de crear sistemas artificiales. Sin embargo, pese al gran progreso conseguido en términos de control y diversidad estructural, su aplicación práctica continúa presentándose como un gran reto.

Objetivos

Capítulo 1. Construcción de arquitecturas supramoleculares electroactivas basadas en bloques moleculares simples que incluyen una secuencia peptídica corta para guiar el proceso de auto-ensamblaje.

Capítulo 2. Diseño de proteínas tipo CTPR para actuar como plantilla en el auto-ensamblaje de moléculas orgánicas electroactivas.

Discusión de resultados

Capítulo 1: Ensamblajes electroactivos basados en péptidos con propiedades electrónicas reforzadas.

En la primera sección de este capítulo, exploramos las propiedades de auto-ensamblaje en medio acuoso de un derivado de exTTF provisto de la secuencia peptídica AGAGA. También se investigan una serie de derivados que contienen pequeñas modificaciones en la secuencia peptídica, como derivados enriquecidos en glicina o alanina. Experimentos de espectroscopía UV/Vis y de dicroísmo circular a temperatura variable han permitido detectar dos agregados diferentes en competición, en concreto, un estado cinético y el correspondiente termodinámicamente estable. Un meticuloso escrutinio de las condiciones experimentales nos permitió obtener y aislar cada uno de ellos y caracterizarlos.

Por último, estudiamos las propiedades redox de estos derivados y sus respectivos agregados, confirmando que aparece un nuevo comportamiento fruto de la organización intermolecular que existe en los ensamblajes supramoleculares.

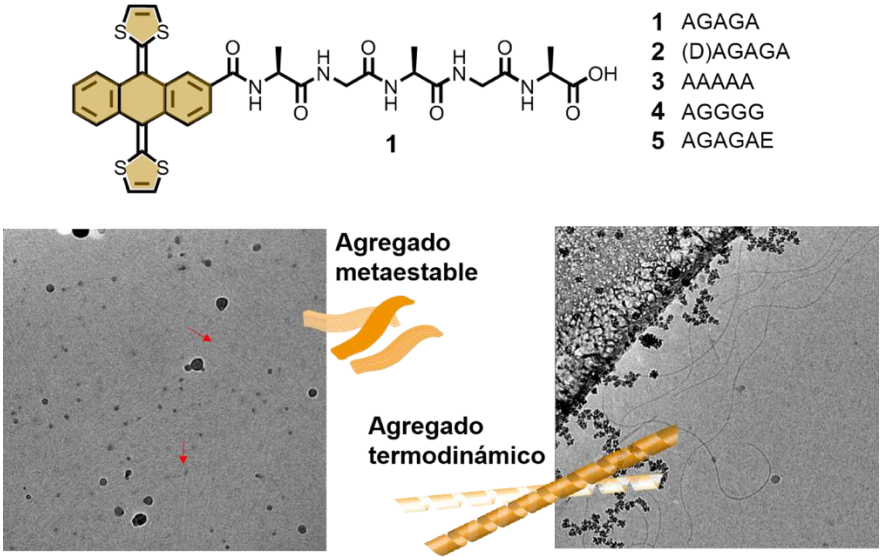

La segunda sección abarca el estudio del proceso de auto-ensamblaje de un sistema tipo péptido-π-péptido basado en cuatertiofeno y el pentapéptido AGAGA. De forma análoga a la sección anterior, hemos sido capaces de obtener diferentes polímeros supramoleculares controlando las condiciones experimentales de la disolución, como la temperatura, la concentración o el pH. De forma adicional, se diseñaron dos derivados de tipo aceptor basados en [60]fullereno y PBI para su co-ensamblaje iónico con los anteriores materiales dadores basados en cuatertiofeno. Para ello, se incluyeron en el diseño molecular grupos guanidinio, que tienen una gran afinidad por los carboxilatos presentes en la cadena peptídica. Los materiales dador-aceptor resultantes fueron completamente caracterizados y se evaluó su capacidad de movilidad de carga a lo largo de los canales tipo *n*/*p* mediante medidas de fotocorriente (FP-TRMC).

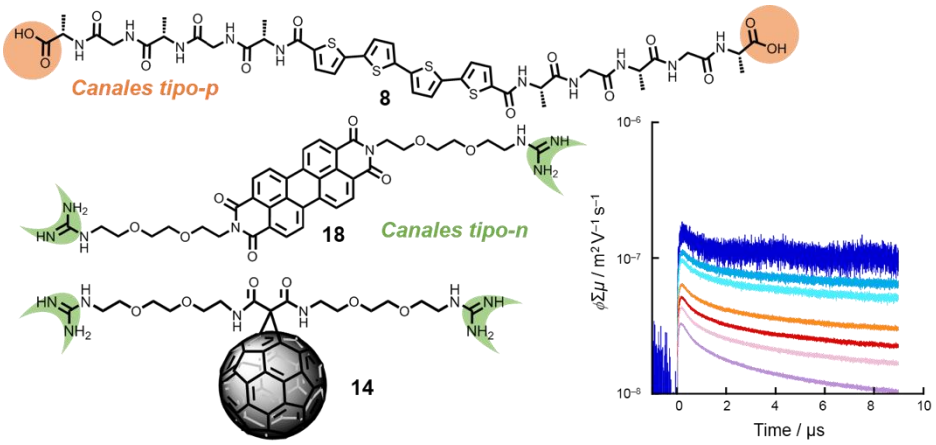

En la última sección de este capítulo, diseñamos y sintetizamos una metaloporfirina de Zn mono-sustituida en la posición *meso* con el pentapéptido AGAGA. Sus propiedades de auto-ensamblaje fueron investigadas en medio acuoso y pusieron de manifiesto una inusual respuesta a la temperatura. Mientras que a temperatura ambiente se encontraron agregados de tipo-H débilmente empaquetados, el aplicar altas temperaturas llevó a la formación de agregados-J en forma de fibras. También se sintetizaron el derivado equivalente de base libre y los análogos tetra-sustituidos para intentar arrojar luz sobre este fenómeno, que ha sido escasamente descrito en la bibliografía.

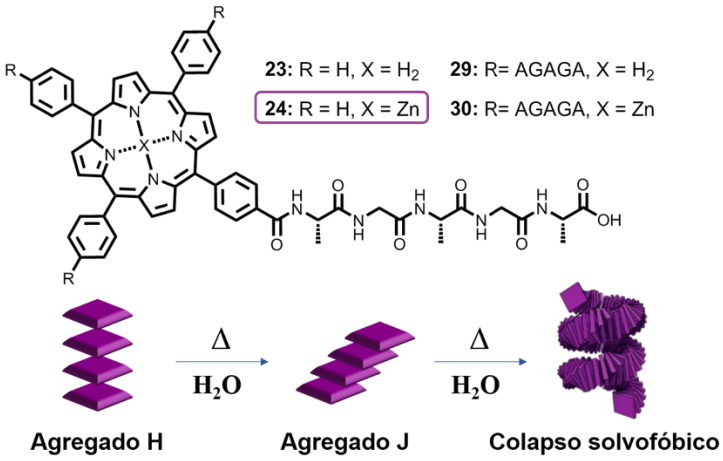

Capítulo 2: Proteínas CTPR como modelo para la organización de moléculas electroactivas.

En la primera sección de este capítulo, postulamos que las proteínas tipo CTPR podrían ser buenas candidatas para la auto-organización de [60]fullereno. En concreto, serán claves las interacciones tipo van der Waals con la superficie π de la molécula orgánica, así como la complementariedad de forma del C_{60} con la superficie cóncava de la proteína. Pese a que se observó la formación de conjugados C_{60}-proteína, decidimos examinar también el derivado C_{60} pirrolidina tris-ácido, más soluble en agua y que mostró mayor afinidad por la proteína. Además, se introdujeron dos tirosinas adicionales para crear nuevos sitios de unión específica para albergar al [60]fullereno, consiguiendo así un grado y un rendimiento de conjugación mayores. Los conjugados mostraron una mayor estabilidad térmica como consecuencia de las nuevas interacciones proteína-C_{60}. Además se han realizado cálculos teóricos, que respaldan que las interacciones con el fullereno ocurren en los sitios de unión ricos en residuos tirosina, así como sitios de interacción catión-π. Por último, medidas de fotocorriente (FP-TRMC) mostraron un incremento en la movilidad de carga en el material.

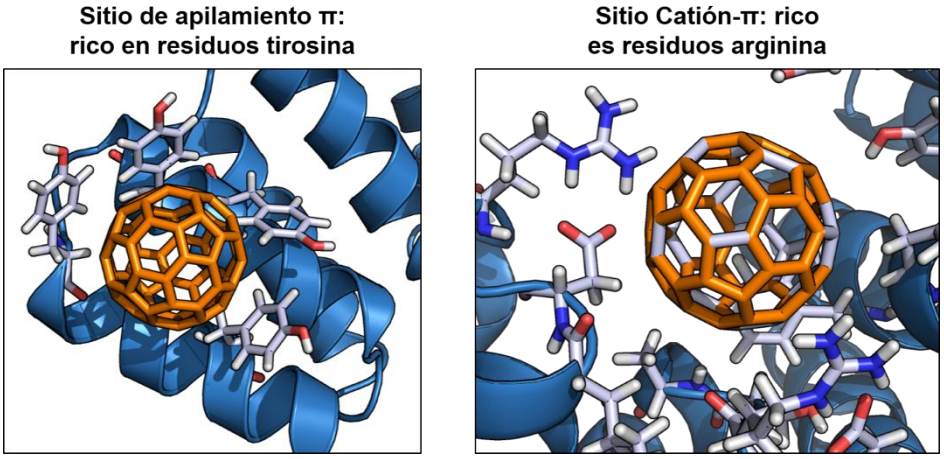

La segunda sección tiene como objetivo la construcción de materiales dador-aceptor usando la proteína CTPR como plantilla. Para ello, nos hemos beneficiado de una TPR mutada diseñada anteriormente y que contiene dos tipos de sitios de unión. Por un lado, dos mutaciones cisteína fueron introducidas en los giros para anclar porfirinas de Zn sustituidas con un grupo maleimida

mediante adicción de Michael al grupo tiol. Por otro lado, dos residuos histidina fueron mutados en la superficie cóncava de la proteína. Por ello, se diseñó un derivado de [60]fullereno con un ligando quelato NTA para coordinar los grupos imidazol presentes en las cadenas laterales de las histidinas. Los resultados preliminares llevados a cabo con un marcador basado en rodamina, revelaron que este ligando quelato es capaz de unirse a las histidinas, incluso en presencia de las porfirinas de Zn.

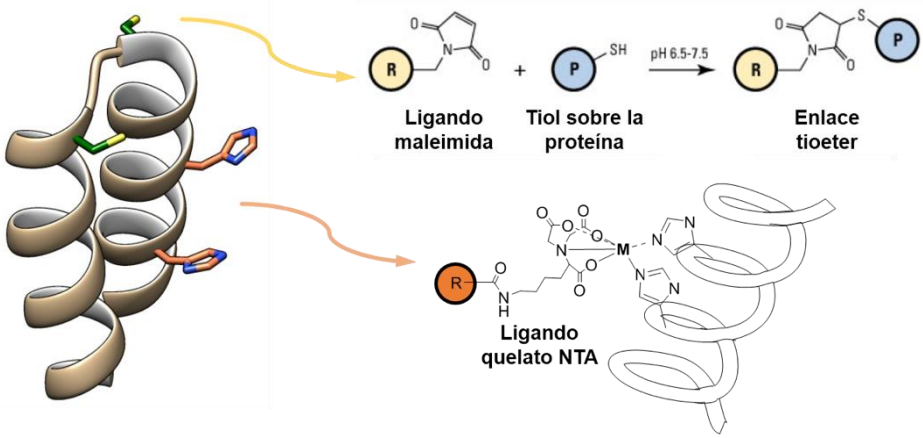

Conclusiones

Capítulo 1. Se han diseñado estructuras anfifílicas que contienen un centro π electroactivo y el pentapéptido AGAGA para investigar sus propiedades de autoensamblaje en medio acuoso. La sinergia entre los enlaces de hidrógeno del péptido y las interacciones π-π, han proporcionado distintos agregados mediante el control de las condiciones de la disolución (temperatura, pH, mezcla de disolventes). En todos los casos, hemos demostrado mediante diferentes técnicas una mejora importante de las propiedades electrónicas en el ensamblaje supramolecular.

Capítulo 2. Se ha mostrado la gran versatilidad de las proteínas CTPR como estructuras para la organización de [60]fullereno. El gran conocimiento sobre la estabilidad y la estructura de esta proteína ha permitido introducir mutaciones en posiciones específicas y así crear nuevos sitios de unión para esta molécula orgánica. Han surgido nuevas propiedades en estos materiales híbridos, como un incremento en la estabilidad térmica y mayor movilidad de carga.

Introduction

Humans have looked at nature for answers to problems throughout their existence. We have always sought to improve our way of life, trying to take advantage of natural resources and transforming them to obtain better products aimed at satisfying specific needs. Nature has accomplished materials of great diversity, complexity and functionality, exhibiting properties such as self-healing abilities and harnessing solar energy. A new world opened up with the possibility of studying these materials at the nanoscale, the scale at which much biology occurs. The ideas and concepts behind nanoscience and nanotechnology were first presented by physicist Richard Feynman in 1959. In a lecture entitled "There's Plenty of Room at the Bottom: An Invitation to Enter a New Field of Physics", he unveiled the possibilities available in the molecular world long before the term nanotechnology was first used. Professor Norio Taniguchi coined the term nanotechnology over a decade later, but it can be said that modern nanotechnology began in 1981, with the development of the scanning tunneling microscope and the atomic force microscope a few years later. Other milestones in the early stage of nanotechnology, such as the publication of *Engines of creation: the coming era of nanotechnology* (K. Eric Drexler, 1986) or the discovery of buckyballs and nanotubes are depicted in Figure I. 1.

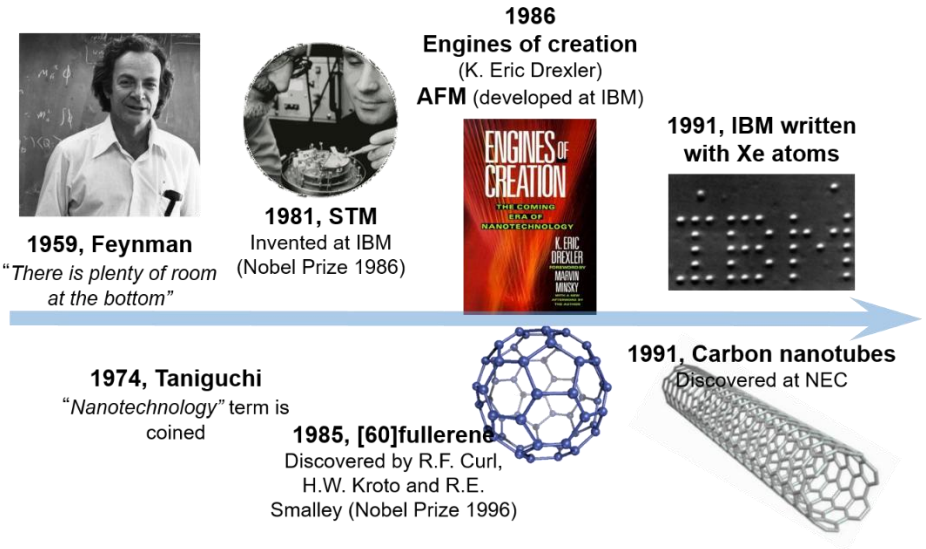

Figure I. 1. Timeline of some milestones in the first decades of the emerging field of nanotechnology.

Most of the bottom-up approaches to nanotechnology are based on

supramolecular chemistry, as large structures can be readily accessed from the self-assembly of small and simple molecules, thus requiring less synthetic effort. Molecular self-assembly can be defined as the spontaneous association of molecules under equilibrium conditions into stable, structurally well-defined aggregates joined by non-covalent interactions. This process is ubiquitous in nature and in the last decades has gained much attention and represented a source of innovation in nanotechnology and materials science. In 1987, the Nobel Prize in Chemistry was awarded to Donald J. Cram, Jean-Marie Lehn, and Charles J. Pedersen *"for their development and use of molecules with structure-specific interactions of high selectivity"* (Figure I. 2). They pioneered the field of supramolecular chemistry discovering and determining host-guest interactions in crown-ethers and cryptands.[1]

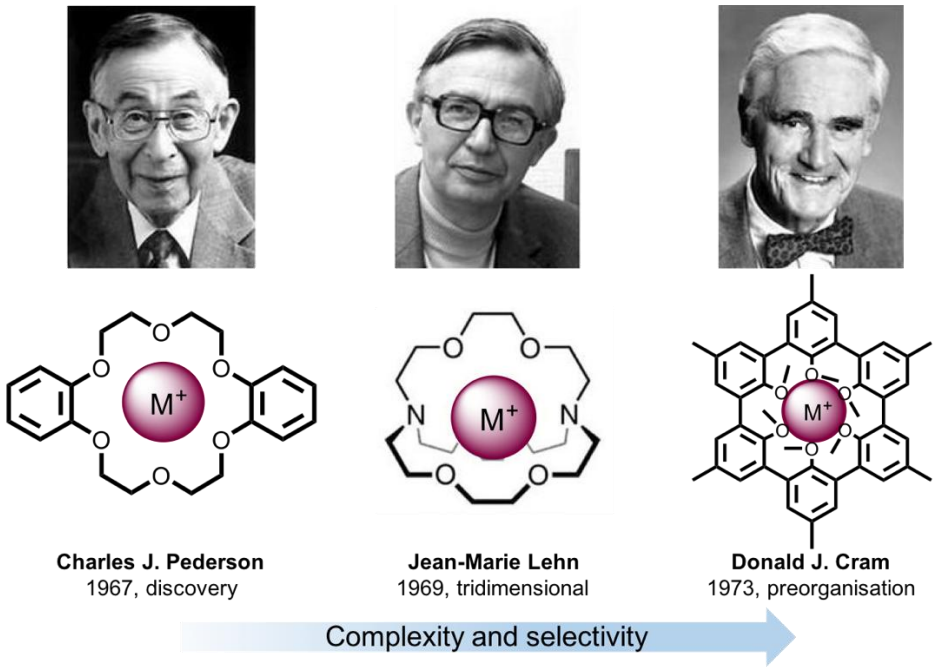

Figure I. 2. The 1987 Nobel Prize in Chemistry awarded for Charles J. Pedersen, Jean-Marie Lehn, and Donald J. Cram for their contributions to the field of supramolecular chemistry related to host-guest interactions in crown-ethers and cryptands.

[1] a) C. J.Pedersen, *J. Am. Chem. Soc.* **1967**, *89*, 7017–7036; b) B. Dietrich, J.-M. Lehn, J. P. Sauvage, *Tetrahedron Lett.* **1969**, *34*, 2885-2888; c) G. W. Gokel, D. J. Cram, *J. Chem. Soc. Chem. Commun.* **1973**, *76*, 481-482.

Despite being a young discipline, supramolecular chemistry has been widely explored in various areas and it is considered as a cross discipline of organic and physical chemistry, polymers science, materials science, biology, and so on.[2] Advantages of supramolecular materials include easy processing, facile material fabrication and recycling, as well as stimuli-responsive and self-healing properties.[3] The advancements in synthetic chemistry has allowed chemists producing practically any molecule, thus making possible to engineer a monomer to generate ordered nanostructures with diverse shapes, dimensionalities and physicochemical properties.

Supramolecular chemistry is particularly intriguing in aqueous solution, not only because water is the solvent of nature, indispensable for life and involved in most of the biochemical reactions, but also for its unique properties. Water offers many advantages as solvent for self-assembly processes, as strong interactions between amphiphilic π-systems may occurred in water, even at very high dilution, thanks to the so-called hydrophobic effect. Molecules of water build infinite, branched networks through hydrogen bonds,[4] and this especial molecular construction is responsible of its anomalous and fascinating physical properties. This network will be disrupted if a hydrophobe is dropped in the aqueous medium and new hydrogen bonds will form around. This orientation makes the system more structured with a decreased of the total entropy of the system (Figure I. 3).

[2] a) J.-M. Lehn, *Supramolecular Chemistry. Concepts and Perspectives*, Wiley-VCH, Weinheim, **1995**; b) J.-M. Lehn, J. L. Atwood, J. E. D. Davies, D. D. Macnicol, F. Vögtle, *Comprehensive Supramolecular Chemistry*, Vol. 1-11, Pergamon/Elsevier, Oxford, **1996**; c) P. D. Beer, P. A. Gale, D. K. Smith, *Supramolecular Chemistry*, Oxford University Press, Oxford, **1999**; d) J. W. Steed, J. L. Atwood, Supramolecular Chemistry, 2nd ed., John Wiley & Sons, Wiltshire, **2009**; J. W. Steed, P. A. Gale, *Supramolecular Chemistry: From Molecules to Nanomaterials*, John Wiley & Sons, **2012**.

[3] a) D. B. Amabilino, D. K. Smith, J. W. Steed, *Chem. Soc. Rev.* **2017**, *46*, 2404-2420; b) A. Jain, S. J. George, *Materials Today* **2015**, *18*, 206-214.

[4] Y. Zubavicus, M. Grunze, *Science* **2004**, *304*, 974-976.

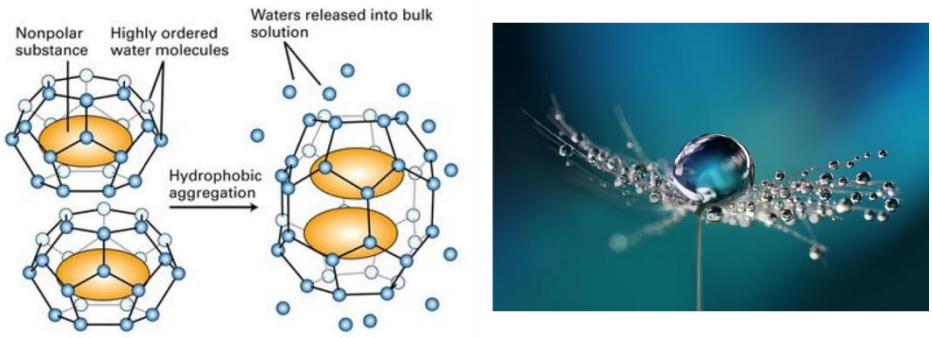

Figure I. 3. Hydrophobic effect. On the left, schematic representation of the aggregation of a non-polar entity in aqueous media and consequently restructuration of the molecules of water. On the right, droplets of water forming spherical shapes to minimize contact with a hydrophobic surface.

The hydrophobic effect is key in biological self-assembly as evidenced in the folding of proteins or the formation of cellular membranes.[5] Hydrophobic interactions can be very strong, thus providing robustness, but they lack the high directionality of other non-covalent interactions, such as hydrogen-bonding. Thus, a convenient approach to create highly ordered materials involves the combination of several well-defined interaction patterns (hydrogen bonding, sequences of donor and acceptor or hydrophilic and hydrophobic groups, ion coordination sites, etc.) in a designed molecule.

An additional great advantage of working in aqueous media is the possibility of combining organic materials with biomolecules. The unique properties of biological molecules make them appealing to be used as molecular templates or supramolecular scaffolds. The self-assembling properties of proteins, peptides, nucleic acids, lipids and other biomacromolecules is so fascinating that they are able to build the basic biological unit, the cell. Among all biomolecules, peptides and proteins are the most abundant in living bodies. Enzymes, hormones or antibodies are made up of proteins, and thanks to their dynamic behavior and assembling properties, they enable the proper functioning of a living organism. The exponential growth of the number of yearly publications on peptide and protein-based materials over the last two decades

[5] a) J. Kyte, *Biophys. Chem.* **2003**, *100*, 193-203; b) C. Tanford in *The Hydrophobic Effect: Formation of Micelles and Biological Membranes*, Wiley, New York, **1980**.

confirms they are some of the most promising building-blocks to create the next generation of advanced materials.[6]

Nowadays, peptides and proteins can be produced on large scales and our knowledge on how to manipulate them to create artificial functional systems has remarkably grown.[7] This kind of biomolecules are specially versatile. On one hand, proteins have inspired approaches to design functional materials mimicking the properties of well-know families of bioactive proteins.[8] Some examples include robust materials based on silk (Figure I. 4),[9] dynamic materials based on actin,[10] or bioactive materials based on collagen.[11]

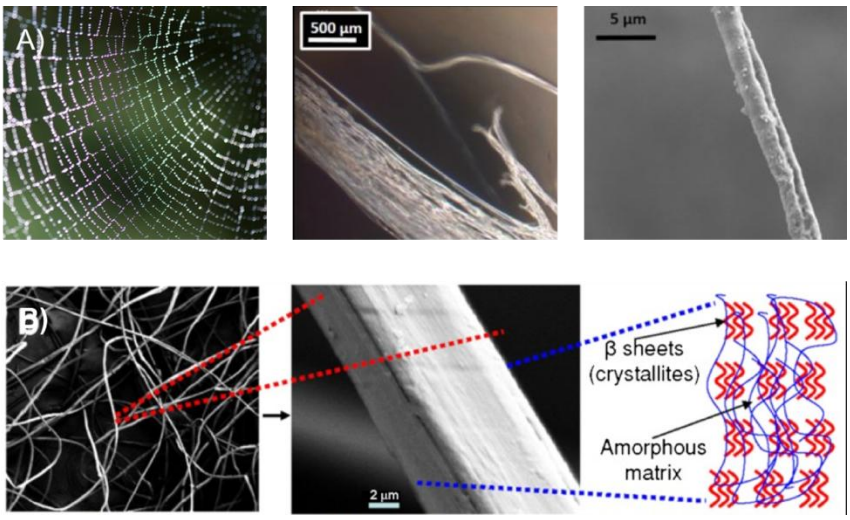

Figure I. 4. A) Spider silk at different magnifications. B) SEM image showing an artificial silk-fiber morphology and possible arrangements.

[6] R. V. Ulijn, R. Jerala, *Chem. Soc. Rev.* **2018**, *47*, 3391-3394.
[7] J. Clarke, L. Regan, *Curr. Opin. Struct. Biol.* **2010**, *20*, 480-481.
[8] a) N. P. King, J. B. Bale, W. Sheffler, D. E. McNamara, S. Gonen, T. Gonen, T. O. Yeates, D. Baker, *Nature* **2014**, *510*, 103-108; (b) N. P. King, W. Sheffler, M. R. Sawaya, B. S. Vollmar, J. P. Sumida, I. André, T. Gonen, T. O. Yeates, D. Baker, *Science* **2012**, *336*, 1171-1174; (c) H. Garcia-Seisdedos, C. Empereur-Mot, N. Elad, E. D. Levy, *Nature* **2017**, *548*, 244-247.
[9] B. B. Mandal, A. Grinberg, E. Seok Gil, B. Panilaitis, D. L. Kaplan, *Proc. Natl. Acad. Sci. U. S. A.* **2012**, *109*, 7699-7704.
[10] R. Galland, P. Leduc, C. Guérin, D. Peyrade, L. Blanchoin, M. Théry, *Nat. Mater.* **2013**, *12*, 416-421.
[11] L. A. Micol, M. Ananta, E.-M. Engelhardt, V. C. Mudera, R. A. Brown, J. A. Hubbell, P. Frey, *Biomaterials* **2011**, *32*, 1543-1548.

On the other hand, peptides are structurally simpler which is reflected in a higher degree of control and predictable assembly. Peptide amphiphiles, π-peptide conjugates, or self-assembling peptides have been developed for a wide variety of applications, such as cell growth and adhesion,[12] medicine[13] and materials science.[14]

A rational design of the amino acid sequence is crucial to understand the fundamental principles that underlie structure, stability and function. Certain modes of folding or assembly of natural proteins are well related with conserved amino acid sequence patterns. For example, a binary pattern containing non-polar and polar amino acids in proteins is related with the formation of β-sheet domains. This fact inspired the design of a number of oligopeptides with alternating non-polar/polar amino acids that self-assemble into β-sheet-like nanostructures.[15] However, while a great progress has been made in terms of control and diversity of structure, translating structure into functionality with practical applications continues to be a major challenge in this emerging area.

[12] a) B. P. Lee, P. B. Messersmith, J. N. Israelachvili, J. H. Waite, *Annu. Rev. Mater. Res.* **2011**, *41*, 99-132; b) M. J. Webber, J. Tongers, C. J. Newcomb, K.-T. Marquardt, J. Bauersachs, D. W. Losordo, S. I. Stupp, *Proc. Natl. Acad. Sci. U. S. A.* **2011**, *108*, 13438.

[13] H. Hosseinkhani, P. Hong, D. Yu, *Chem. Rev.* **2013**, *113*, 4837-4861.

[14] J. D. Tovar, *Acc. Chem. Res.* **2013**, *46*, 1527-1537.

[15] a) S. Zhang, T. Holmes, C. Lockshin, A. Rich, *Proc. Natl. Acad. Sci. U. S. A.* **1993**, *90*, 3334-3338; b) H. Xiong, B. L. Buckwalter, H.-M. Shieh, M. H. Hecht, *Proc. Natl. Acad. Sci. U. S. A.* **1995**, *92*, 6349-6353; c) J. P. Schneider, D. J. Pochan, B. Ozbas, K. Rajagopal, L. Pakstis, J. Kretsinger, *J. Am. Chem. Soc.* **2002**, *124*, 15030-15037; d) J. Gao, C. Tang, M. A. Elsawy, A. M. Smith, A. F. Miller, A. Saiani, *Biomacromolecules* **2017**, *18*, 826-834.

Chapter 1

Peptide-based electroactive assemblies with enhanced electronic properties.

1.1. Background

1.1. Background

1.1.1. Supramolecular polymerization

Molecular self-assembly is essential for living systems, where complex and dynamic assemblies are responsible of very sophisticated functions such as replication, signaling or cellular transport. A self-assembly process can be defined as the association or arrangement of molecules without guidance or management from an outside source. When this association results in linear polymers due to reversible non-covalent interactions, the self-assembly is referred as a supramolecular polymerization. Supramolecular polymers share characteristics with their covalent counterparts, but also fascinating new properties emerge from their dynamic nature. With the introduction of this new kind of polymers, the field of polymers science broadened and was no longer limited to macromolecular species. In the past decades, supramolecular chemists have developed a vast amount of artificial assembling systems able to build well-defined supramolecular architectures.

The concept to make materials out of small molecules was introduced in the late eighties by Stadler.[16] In 1990, Lehn reported the first supramolecular polymer based on the self-assembly of ditopic monomers with complementary hydrogen-bonding groups.[17] However, this first example lacked a high degree of polymerization due to the low association constant of the system. Later on, Meijer and his group introduced a new strong, self-complementary unit which resulted in a supramolecular polymer with unprecedented properties.[18] Their design was based on ureidopyrimidone quadruple hydrogen-bonded and it is considered a landmark achievement in supramolecular chemistry. Since then, the field of supramolecular polymerization has exploded.

As aforementioned, the key feature in supramolecular chemistry is reversibility. The extent of the process is then directly related to thermodynamic forces derived from parameters such as solvent nature, concentration or

[16] R. Stadler, L. de Lucca Freitas, *Colloid Polym. Sci.* **1986**, *264*, 773-779.
[17] C. Fouquey, J.-M. Lehn, A.-M. Levelut, *Adv. Mater.* **1990**, *2*, 254-257.
[18] a) R. P. Sijbesma, F. H. Beijer, L. Brunsveld, B. J. B. Folmer, Hirschberg, J. H. K. K., R. F. M. Lange, J. K. L. Lowe, E. W. Meijer, *Science* **1997**, *278*, 1601-1606; b) F. H. Beijer, R. P. Sijbesma, H. Kooijman, A. L. Spek, E. W. Meijer, *J. Am. Chem. Soc.* **1998**, *120*, 6761-6769.

temperature.[19] Depending on the kinetic parameters governing the process, we can distinguish between three main polymerization mechanisms:

- *Isodesmic mechanism:* this mechanism is characterized by a single binding constant (*K*) to define each reversible step in the assembly pathway. A general scheme describing an isodesmic polymerization process is depicted in Figure 1. 1. A. The affinity of a monomer for the growing chain is independent of the length of the polymer and the successive addition of monomers leads to a constant decrease in the free energy. For this reason, the obtained polymers tend to have a great polydispersity.
- *Cooperative mechanism:* in this case two well-defined stages with distinct binding constants can be identified (Figure 1. 1. A). The first step consists of a linear isodesmic growth of a nucleus with an appropriate size and an association constant K_n for the addition of each monomer. The polymerization process continues with the so-called elongation process, with an association constant K_e higher than K_n. As a result, it can be defined a critical concentration or temperature at which the elongation of the chain occurs. This kind of polymerization is characterized by a bimodal mass distribution identified with non-activated monomers or nuclei and activated supramolecular elongated polymers, with relatively low polydispersity.
- *Anti-cooperative mechanism:* in contraposition, the anticooperative mechanism occurs with a higher association constant for the initial formation of the nucleus than the subsequent elongation step. Although anticooperative growth in supramolecular polymerization has received much less attention than cooperative growth in the past, it is very convenient for the formation of discrete structures with a high degree of monodispersity.

A straightforward approach to identify a polymerization mechanism is measuring the dependence of an intrinsic property (absorbance, emission, circular dichroism signal, etc.) with temperature or concentration. A sigmoidal curve is characteristic of an isodesmic mechanism (red line in Figure 1. 1. B), while an initial linear isodesmic polymerization (close to zero slope) followed by and hyperbolic loop is attributed to a cooperative mechanism (blue line in Figure 1. 1. B)

[19] De Greef, Tom F. A., M. M. J. Smulders, M. Wolffs, Schenning, Albert P. H. J., R. P. Sijbesma, E. W. Meijer, *Chem. Rev.* **2009**, *109*, 5687-5754.

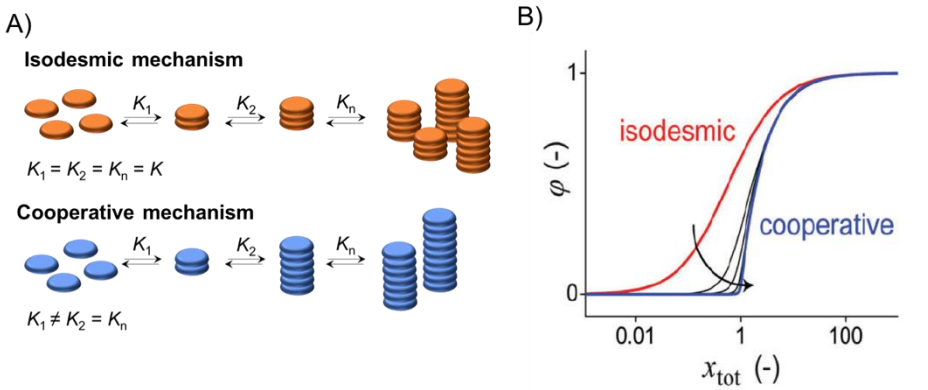

Figure 1. 1. A) Schematic representation of a polymerization growth following an isodesmic or a cooperative mechanism. B) Variation of an intrinsic property (φ) *versus* concentration or temperature (χ) in isodesmic and cooperative mechanisms.

Supramolecular chemistry has been traditionally centered on thermodynamically stable species, which are accomplished no matter the pathway followed to reach the equilibrium. However, in the last years an increasing interest on investigating out-of-equilibrium supramolecular polymerization has grown. The level of sophistication and complexity shown in natural systems is precisely due to self-organization processes implying non-equilibrium states. To achieve this pathway complexity, a deep investigation on the experimental procedures and preparation protocols of the polymer is crucial.[20] In a comprehensive review, Hermans and col. provided the proper information to identify and characterize the self-assembled states that have been explored so far,[21] as it is shown in Figure 1. 2. They classified the systems into *dissipative*, when the systems constantly require energy or matter, or *non-dissipative*. If the fuel supply stops, a dissipative system will spontaneously relax to a non-dissipative thermodynamic or non-equilibrium state.

[20] F. Tantakitti, J. Boekhoven, X Wang, R. V. Kazantsev, T. Yu, J. Li, E. Zhuang, R. Zandi, J. H. Ortony, C. J. Newcomb, L. C. Palmer, G. S. Shekhawat, l. C. de, G. C. Schatz, S. I. Stupp, *Nat. Mater.* **2016**, *15*, 469-476.
[21] A. Sorrenti, J. Leira-Iglesias, A. J. Markvoort, T. F. A de Greef, T. M. Hermans, *Chem. Soc. Rev.* **2017**, *46*, 5476-5490.

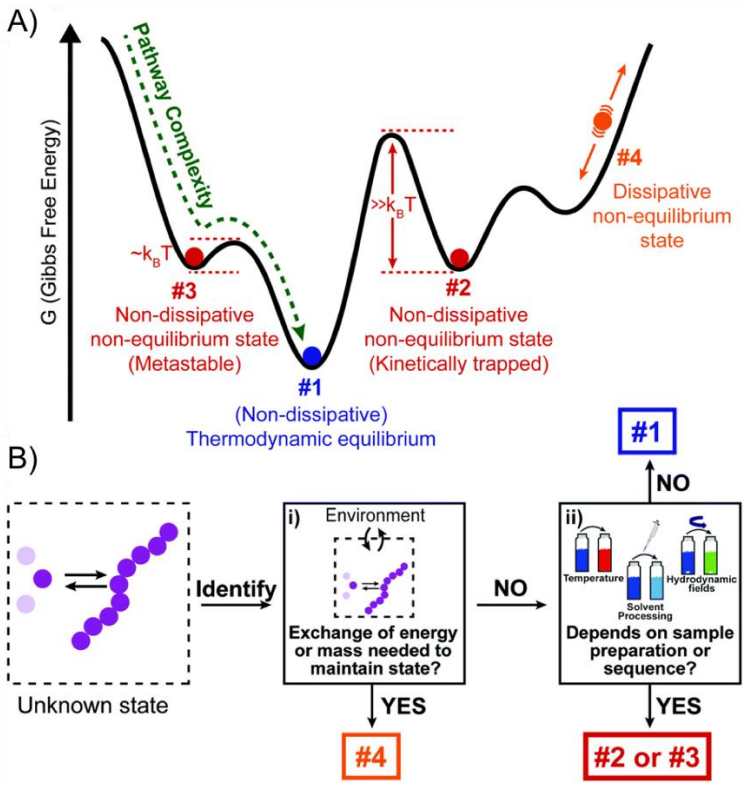

Figure 1. 2. Identifying the different states in supramolecular self-assembly. A) Schematic Gibbs free energy landscape. B) Decision tree to identify the different states shown in A.

As aforementioned, a thermodynamic state is accomplished no matter the preparation protocol. As indicated in Figure 1. 2. A, it resides in the global minimum of energy (#1 in Figure 1. 2. A) and is comprised of equilibrium structures. The aggregation from the monomers to the assembly does dissipate energy (normally as heat release), but once the structure is under equilibrium no-further dissipation takes place. Nonetheless, along the pathway to the global minimum, the monomers may encounter several local minima (#2 or #3 in Figure 1. 2. A) and the evolution time to the thermodynamic state will depend on the energy barriers. Typically, if the barrier is relatively low, the state is called *metastable* (#3 in Figure 1. 2. A). Higher energy barriers lead to *kinetically trapped* (#2 in Figure 1. 2. A) systems which remain captured in the local

minimum for a period much longer than the experimental observation. Here, suitable experiments may let the system "scape" from its trap.

Controlling the kinetics and pathway complexity can trigger the formation of aggregates with unexpected morphology, molecular organization and, ultimately, function.

1.1.2. Functional supramolecular polymers

Whitesides and his group developed the concept of self-assembly to create functional materials from rationally-designed building blocks. In just a few decades, supramolecular polymers have demonstrated their great potential.[22] Some of their inherent strengths for industrialization comprise: easy synthesis, compatibility with existing polymeric systems, and their intrinsic reversibility, that makes the materials easily removable. Currently, a great number of patents have been issued or applied using supramolecular architectures in the fields of adhesives, printing, coatings and cosmetics and personal care.

Three main functions have been investigated and exploited in the area of functional supramolecular polymers. Firstly, and probably very unexpected, their excellent mechanical properties and unique ease of processing. Hence, when the association constant of the monomers is high enough, the supramolecular polymer possesses similar properties to classical covalent polymers. Elastomers, organogels and hydrogels or self-healing materials have been developed in this area.[23] Secondly, supramolecular polymers constitute an emerging field in biomedicine and regenerative medicine as they can exhibit biological activity. Seminal work from the research group of Stupp demonstrates the unique and outstanding properties of supramolecular biomaterials based on

[22] a) T. Aida, E. W. Meijer, S. I. Stupp, *Science* **2012**, *335*, 813-817; b) X. Yan, F. Wang, B. Zheng, F. Huang, *Chem. Soc. Rev.* **2012**, *41*, 6042-6065; c) E. A. Appel, J. Del Barrio, X. J. Loh, O. A. Scherman, *Chem. Soc. Rev.* **2012**, *41*, 6195-6214; d) G. R. Whittell, M. D. Hager, U. S. Schubert, I. Manners, *Nat. Mater.* **2011**, *10*, 176-188; e) L. Yang, X. Tan, Z. Wang, X. Zhang, *Chem. Rev.* **2015**, *115*, 7196-7239.

[23] a) L. Voorhaar, R. Hoogenboom, *Chem. Soc. Rev.* **2016**, *45*, 4013-4031; b) M. Suzuki, K. Hanabusa, *Chem. Soc. Rev.* **2010**, *39*, 455-463; c) X. Du, J. Zhou, J. Shi, B. Xu, *Chem. Rev.* **2015**, *115*, 13165-13307; d) E. A. Appel, J. del Barrio, X. J. Loh, O. A. Scherman, *Chem. Soc. Rev.* **2012**, *41*, 6195-6214.

peptide amphiphiles.[24] Lastly, the electronic functions of π-conjugated self-assembling materials have led to great advances in the field of supramolecular electronics. The first two issues are out of the scope of this thesis, and we have focused our attention on supramolecular assemblies based on π-systems.

As a consequence of supramolecular polymerization, π-systems confined within assemblies exhibit optoelectronic properties that differ from the molecularly dissolved species. The electronic coupling between the dipole moments of the π-conjugated aggregates can give rise to exciton effects as described by the exciton model of Kasha.[25] The exciton splitting of excited states is the reason to the appearance of spectral shifts of the absorption bands in an aggregate. Simplifying Kasha's model, we can consider the monomer and dimers depicted in Figure 1. 3, where two monomers can be sandwich-type or head-to-tail arranged. The first case is known as H-aggregation (H denotes hypsochromic), and lead to absorption bands shifted to shorter wavelength (hypsochromically shifted) with respect to the monomer band and exhibit, in most cases, low or no fluorescence.[26] The second case is known as J-aggregate (J for Jelly, one of the first workers who investigated these kind of shifts) and the absorption bands are shifted to longer wavelengths (bathochromically shifted) with respect to the monomer absorption band. In contrast to H-aggregates, J-aggregates are characterized by small Stoke shifts and it is possible to observe fluorescence with high quantum yields.[27]

[24] a) M. P. Hendricks, K. Sato, L. C. Palmer, S. I. Stupp, *Acc. Chem. Res.* **2017**, *50*, 2440-2448; b) J. D. Hartgerink, E. Beniash, S. I. Stupp, *Science* **2001**, *294*, 1684-1689; c) G. A. Silva, C. Czeisler, K. L. Niece, E. Beniash, D. A. Harrington, J. A. Kessler, S. I. Stupp, *Science* **2004**, *303*, 1352-1355; d) Jiang, H.; Guler, M. O.; Stupp, S. I. Soft Matter 2007, 3, 454; e) C. H. Chen, L. C. Palmer, S. I. Stupp, *Nano Lett.* **2018**, *18*, 6832-6841; f) R. Freeman, M. Han, Z. Álvarez, J. A. Lewis, J. R. Wester, N. Stephanopoulos, M. T. McClendon, C. Lynsky, J. M. Godbe, H. Sangji, E. Luijten, S. I. Stupp, *Science* **2018**, *362*, 808-813.
[25] M. Kasha, H. R. Rawls, M. A. E. Bayoumi, *Pure Appl. Chem.* **1965**, *11*, 371-392.
[26] A. H. Herz, *Adv. Colloid Interface Sci.* **1977**, *8*, 237-298.
[27] F. Würthner, T. E. Kaiser, C. R. Saha-Möller, *Angew. Chem. Int. Ed.* **2011**, *50*, 3376-3410.

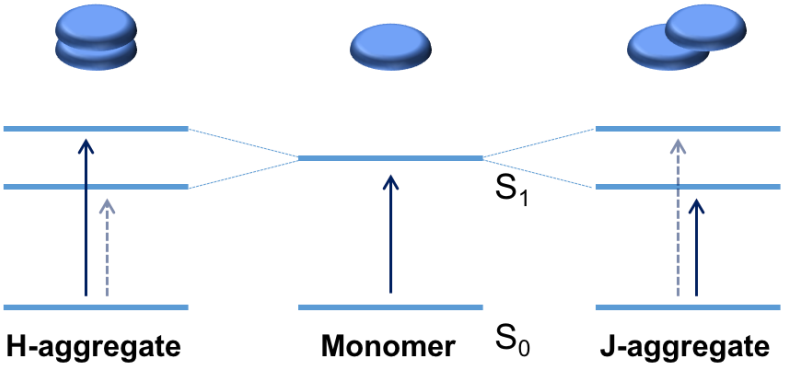

Figure 1. 3. Schematic illustration of exciton splitting of the energy levels derived from the exciton coupling in the dimeric form. Solid arrows represent allowed transitions and dashed arrows represent forbidden transitions.

The group of Würthner has beautifully illustrated the strong impact of self-assembling in the optoelectronic properties of peryelene bisimide (PBI) dyes. They have presented a wide variety of PBIs with different substitution patterns to have a fine control on their high propensity to π-π stack. Highly interesting optical and electronic properties, which are not inherent to the respective individual molecules, emerge through their supramolecular polymerization. Both, H- and J-aggregates have been prepared out of suitable PBIs monomers.[28] J-aggregates, due to the appearance of aggregation-induced emission phenomenon, are specially interesting. They were able to accomplish such self-assembled J-aggregates by an engineered design of tetra bay-substituted PBIs bearing free NH groups at the imide positions.[29] The synergistic formation of hydrogen bonds between the imide groups and π-π interactions between the central organic core was triggered in different mixtures of polar/non-polar organic solvents. The J-aggregates exhibited about 100 nm bathochromically shifted absorption bands and high fluorescence quantum yields. Later on, the formation of hydrogen-bonded columnar liquid-crystalline J-aggregates with this molecular structure was reported. The latter novel material

[28] F. Würthner, C. R. Saha-Möller, B. Fimmel, S. Ogi, P. Leowanawat, D. Schmidt, *Chem. Rev.* **2016**, *116*, 962-1052.
[29] T. E. Kaiser, H. Wang, V. Stepanenko, F. Würthner, *Angew. Chem., Int. Ed.* **2007**, *46*, 5541-5544; b) T. E. Kaiser, V. Stepanenko, F. Würthner, *J. Am. Chem. Soc.* **2009**, *131*, 6719-6732; c) S. Herbst, B. Soberats, P. Leowanawat, M. Lehmann, F. Würthner, *Angew. Chem., Int. Ed.* **2017**, *56*, 2162-2165.

found application as photonic materials in inorganic[30] and organic[31] microcavities. More recently, they reported a bay-substituted PBI bearing four dendrons decorated with methoxy-triethyleneglycol chains able to aggregate in aqueous media and give hydrogels and lyotropic liquid crystalline states (Figure 1. 4. A).[32] Performing temperature-dependent absorption and photoluminescence studies in diluted conditions, they observed no significant emission at room temperature, while upon heating the formation of J-aggregates procured the fluorescence turn-on in the far-red region of the spectrum (Figure 1. 4. C). The hydrogel is particularly interesting as an adaptive biocompatible material exhibiting temperature-responsive reversible color changes (red in hydrogel **1** to blue in hydrogel **2**, Figure 1. 4. B).

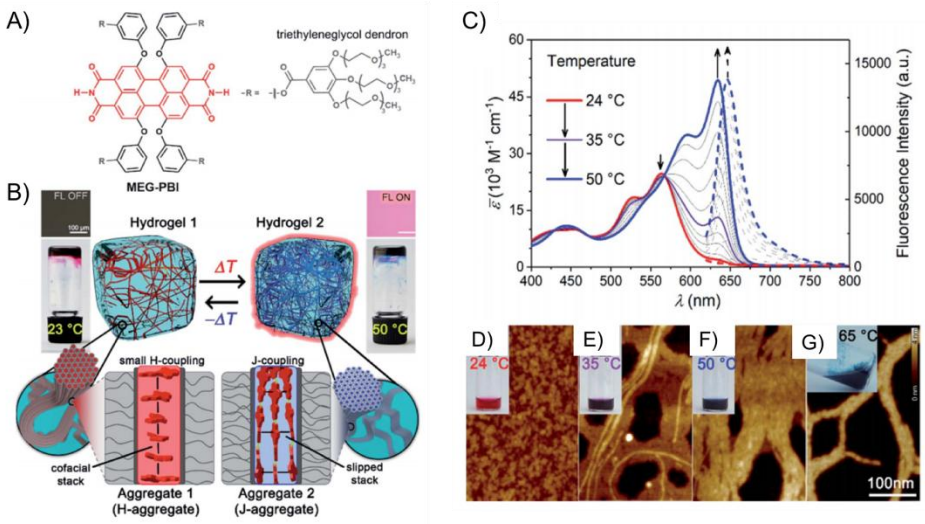

Figure 1. 4. A) Chemical structure of the PBI derivative. B) Schematic illustration of the reversible temperature response of the H- and J-aggregate hydrogels. C) UV/Vis (solid lines) and fluorescence spectra (dashed lines) upon increasing the temperature from 24 ºC (red, monomer) to 50 ºC (blue, J-aggregate). D)-G) AFM images and photographs of vials with aqueous solutions at different temperatures.

[30] L. Tropf, C. P. Dietrich, S. Herbst, A. L. Kanibolotsky, P. J. Skabara, F. Würthner, I. D. W. Samuel, M. C. Gather, S. Höing, *Appl. Phys. Lett.* **2017**, *110*, 153302.
[31] P. Lova, V. Grande, G. Manfredi, M. Patrini, S. Herbst, F. Würthner, D. Comoretto, *Adv. Opt. Mater.*, **2017**, *5*, 1700523.
[32] V. Grande, B. Soberats, S. Herbst, V. Stepanenko, F. Würthner, *Chem. Sci.* **2018**, *9*, 6904-6911.

This example highlights the great dynamic nature of soft matter, thanks to the easy rearrangement of the chromophores from cofacial (H-aggregate) to slipped (J-aggregate) packing. Hence, this dynamism is the key to achieve stimuli-responsive materials.

Bio-inspired systems that respond to a multitude of stimuli have been developed by introducing electroactive organic species. George and *col*. reported a redox responsive amphiphilic foldamer that operates under the effect of a chemical fuel which mimics the behavior of the redox responsive conformational change in coenzyme Q-cytochrome c reductase (Figure 1. 5).[33]

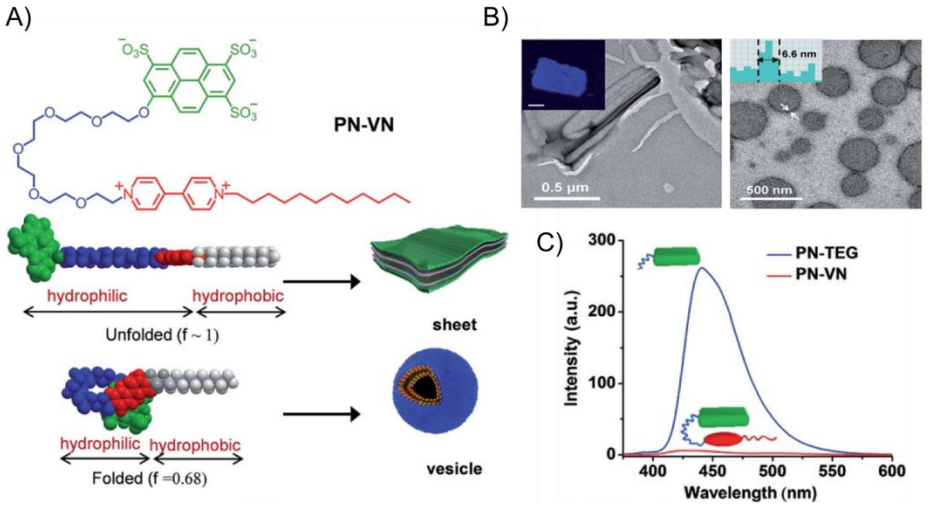

Figure 1. 5. A) Molecular structure of the foldamer designed by George and col. and schematic representation for the transient conformational response of the foldamer mediated via charge transfer interactions between the pyrene and viologene moieties. B) TEM images of the different morphologies of the self-assembled materials. C) Quenching of the emissive properties in the folded state.

Modulating charge transfer interactions between the pyrene and the viologen moieties conforming the foldamer through an enzymatic pathway, it was possible to bring morphological changes from vesicles to sheets. Glucose oxidase in the presence of glucose and oxygen produces hydrogen peroxide which can oxidize viologen radical cation, $VN^{\cdot+}$, to the viologen dication VN^{2+}. The latter

[33] K. Jalani, S. Dhiman, A. Jain, S. J. George, *Chem. Sci.* **2017**, *8*, 6030-6036.

results in a decreased acceptor strength of viologen, and thus a weakening of the charge transfer interaction and the subsequent unfolding of the foldamer to give the sheet-like nanostructures. The folded and unfolded states not only led to ensembles with different morphologies, but also totally different electronic and spectroscopic properties.

It is worthy to highlight that the latter examples share a similar molecular design, that is, an amphiphilic structure which combines strong π-π interactions, coming from a hydrophobic organic core, endowed with solubilizing chains, alkyl- or polyethyleneglycol-based chains. Additionally, hydrogen-bonding groups are also normally introduced due to their inherent high selectivity and directionality. Recent advancements in the area of hydrogen-bonded assemblies of π-conjugated systems involve, however, their combination with biological molecules. These moieties not only ensure water solubility to create new biomaterials, but afford a great propensity to self-associate. One particularly versatile class of biomaterials are those based on oligopeptides. The ease of synthesis and established procedures for their functionalization, make them the material of choice for the construction of a great variety of artificial self-assembling materials. Biological applications and unique optoelectronic and physical properties have emerged from this class of hybrid materials.

1.1.3. Peptide-π conjugates

Adding electronic functionality to biologically macromolecules such as nucleotides,[34] carbohydrates,[35,36] steroids,[37] and amino acids,[14,38] offers the potential to develop functional biomaterials. As aforementioned, oligopeptides are especially convenient due to their easy synthesis and their propensity to self-

[34] a) L. M. Cassidy, B. T. Burcar, W. Stevens, E. M. Moriarty, L. B. McGown, *Astrobiology* **2014**, *14*, 876-886; b) P. Zhou, R. Shi, J. Yao, C. Sheng, H. Li, *Coord. Chem. Rev.* **2015**, *292*, 107-143; c) C. Aimé, R. Nishiyabu, R. Gondo, K. Kaneko, N. Kimizuka, *Chem. Commun.* **2008**, 6534-6536; d) G. M. Peters, J. T. Davis, *Chem. Soc. Rev.* **2016**, *45*, 3188-3206.

[35] M. Delbianco, P. Bharate, S. Varela-Aramburu, P. H. Seeberger, *Chem. Rev.* **2016**, *116*, 1693-1752.

[36] a) H. Klok, J. J. Hwang, J. D. Hartgerink, S. I. Stupp, *Macromolecules* **2002**, *35*, 6101-6111; b) S. Abraham, R. K. Vijayaraghavan, S. Das, *Langmuir* **2009**, *25*, 8507-8513.

[37] a) S. Schmid, E. Mena-Osteritz, A. Kopyshev, P. Bäuerle, *Org. Lett.* **2009**, *11*, 5098-5101; b) S. Schmid, E. Marion Schneider, E. Brier, P. Bäuerle, *J. Mater. Chem. B* **2014**, *2*, 7861-7865.

[38] D. González-Rodríguez, Schenning, Albertus P. H. J., *Chem. Mater.* **2011**, *23*, 310-325.

associate to adopt a variety of secondary motifs in completely aqueous environments. These biological species are presented as ideal moieties for the construction of synthetic supramolecular systems, affording high selectivity and directionality through hydrogen-bonding.[39] It is very well-known how amide groups provide good alignment within supramolecular fiber systems.[40] The molecular design of self-assembling π-systems units requires a careful consideration of the enthalpic stabilization derived from π-electron-centered quadrupolar interactions and peptide-centered intermolecular hydrogen bonds balanced with entropic/solvation factors.

The dihedral angles between the adjacent peptide planes defines different geometries, being α-helices and β-sheets (Figure 1. 6) the most common secondary structures in nature. For that reason, they also constitute the most predominant conformations for the construction of artificial peptide-based materials.[41] The amino acid sequence or primary structure establishes the formation of the latter motifs and thus provides a route to functional self-assembly. The derived macroscale properties in the final material will be, therefore, a direct consequence of the designed peptide sequence.[42]

Interactions among β-sheets occur in natural proteins or oligopeptides and have attracted much attention due to their involvement in the formation of amyloid and amyloid-like fibrillar aggregates. This conformation is directly associated with medical pathologies such as Alzheimer's or Parkinson's diseases, and yet it is also very advantageous for nano- and biotechnological applications. β-sheets consist of β-strands connected laterally through a network of hydrogen bonds, forming a pleated sheet as shown in Figure 1. 6.[43] Here, the amide groups in the backbone of one strand creates hydrogen bonds with the carbonyl groups of the adjacent strands. Adjacent β strands can form hydrogen bonds in antiparallel, parallel, or mixed arrangements. In the anti-parallel arrangement, N-terminus of one strand is adjacent to the C-terminus of the next

[39] A. Jatsch, E. Schillinger, S. Schmid, P. Bäuerle, *J. Mater. Chem.* **2010**, *20*, 3563-3578.
[40] S. S. Babu, V. K. Praveen, A. Ajayaghosh, *Chem. Rev.* **2014**, *114*, 1973-2129.
[41] a) Y. Wu, J. H. Collier, *WIREs Nanomed Nanobiotechnol* **2017**, *9*, 1424-1430; b) B. Pepe-Mooney, R. Fairman, *Curr. Opin. Struct. Biol.* **2009**, *19*, 483-494; c) S. Kim, J. H. Kim, J. S. Lee, C. B. Park, *Small* **2015**, *11*, 3623-3640.

[42] H. Ardoña Ann M., K. Besar, M. Togninalli, H. E. Katz, J. D. Tovar, *J. Mater. Chem. C* **2015**, *3*, 6505-6514.
[43] a) P.-N. Cheng, J. D. Pham and J. S. Nowick, *J. Am. Chem. Soc.* **2013**, *135*, 5477-5492; b) J. D. Pham, R. K. Spencer, K. H. Chen and J. S. Nowick, *J. Am. Chem. Soc.* **2014**, *136*, 12682-12690.

strand while in a parallel arrangement, the N-terminus of both strands are oriented in the same direction. The lateral groups (R) are oriented to both, inside and outside of the sheet.

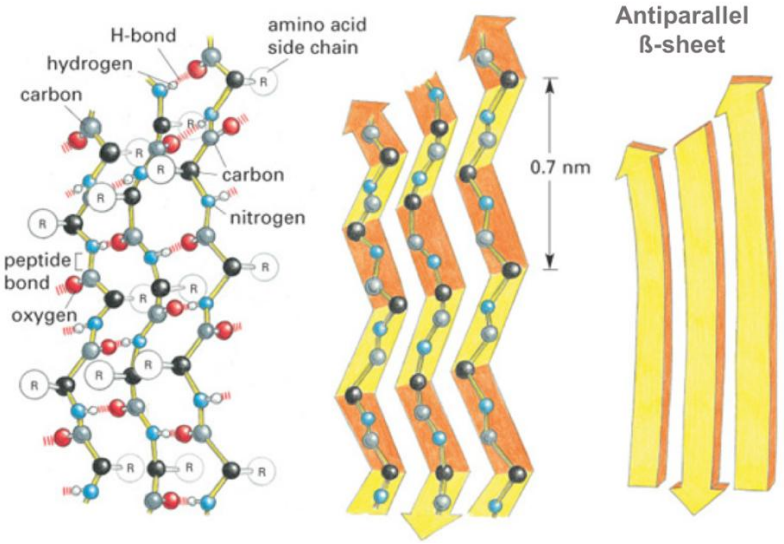

Figure 1. 6. Different schematic representations for a β-sheet-like conformation, in this case, with an antiparallel arrangement.

The attachment of functional molecules to peptide sequences is a partnership that has opened up opportunities for the design of smart materials at the nanoscale. Peptide-π-conjugates allow bringing together the semiconducting, optical, or electroluminescent properties of π-systems with the self-assembling, specific binding, and stimuli responsive behavior of these biological moieties.[44] Moreover, the conjugation of peptides and organic molecules not only ensures solubility of the building blocks in aqueous media, but also allows directing long-range spatial organization. For these reasons, this approach has been widely applied and reported in the literature in the area of organic electronics.

The research group of Tovar has studied a wide variety of promising π-electron systems in the area of bioelectronics[38,42] and explored the photophysics,

[44] S. S. Panda, H. E. Katz, J. D. Tovar, *Chem. Soc. Rev.* **2018**, *47*, 3640-3658.

self-assembly behavior and hydrogel properties from a sequence-dependence point of view. It is very interesting to note how small changes in the peptide sequence can dramatically impact the morphological and electronic properties of the supramolecular array. They designed a petide-π-peptide triblock molecule (in this case quaterthiophene as π-core) and varied the hydrophobicity and the size of peptides, changing from glycine (G), alanine (A), valine (V), isoleucine (I) to phenylalanine (F), while keeping a terminal charged residue, aspartic acid (D), constant (Figure 1. 7).[42]

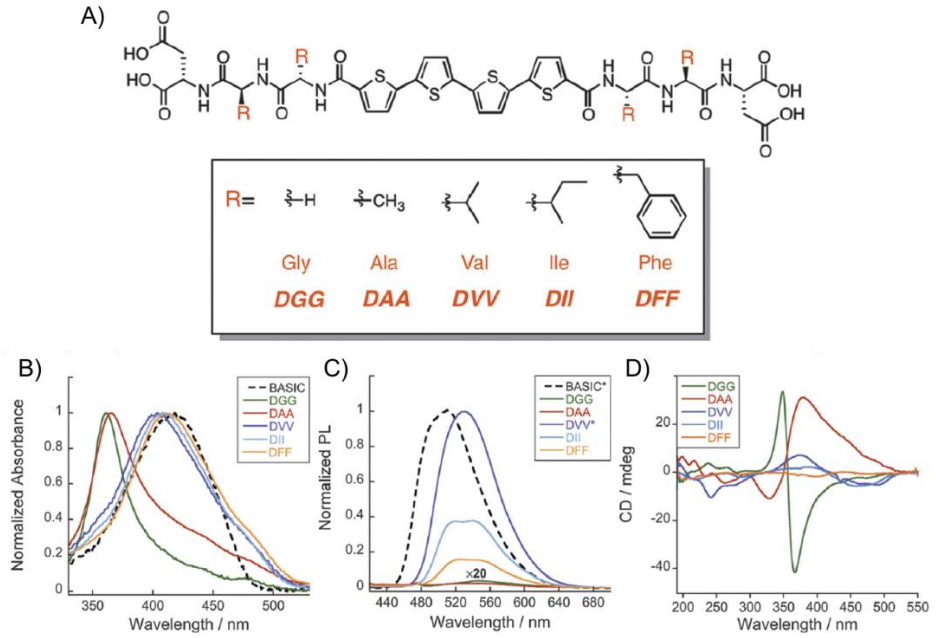

Figure 1. 7. A) Molecular structures of the quaterthiophene-based hydrogelators studied by Tovar and col. B) UV/Vis, C) photoluminiscence and D) circular dichroism of the different species.

In general, two different trends in the photophysical response were found, distinguishing the smaller DGG and DAA peptides and the bulky DVV, DII, DFF peptides. In all cases, a H-like aggregation was observed, been much more pronounced in the case of the smaller peptides, with a dramatic blue-shift in the absorption maxima in comparison with the molecularly dissolved species in basic aqueous conditions. Similarly, the emission properties were substantially quenched in the case of the smaller peptides. The circular dichroism intensity of the larger DVV, DII and DFF peptides was also lower than the DGG

and DAA peptides, indicative of a different extent of exciton coupling of quaterthiophene units within each chiral peptide environment. Moreover, regarding the electrical properties of these materials, it was found that only the DGG peptide film exhibited considerable photoconductive response.

Not only modifications on the peptide sequence can lead to dramatic changes in the self-assembly process. Indeed, it is very striking how the incorporation of different functionalities in the terminal position of the peptide allows a fine control on the nanostructures formed. In this regard, Lee and co-workers reported the synthesis and self-assembly behavior of three tripeptides based on lysine, where the middle lysine was functionalized with pyrene and the N-termini was either leave as a free amine or functionalize with acetyl or Fmoc (fluorenylmethyloxycarbonyl) groups (derivatives **3**, **2** and **1** respectively in Figure 1. 8).[45]

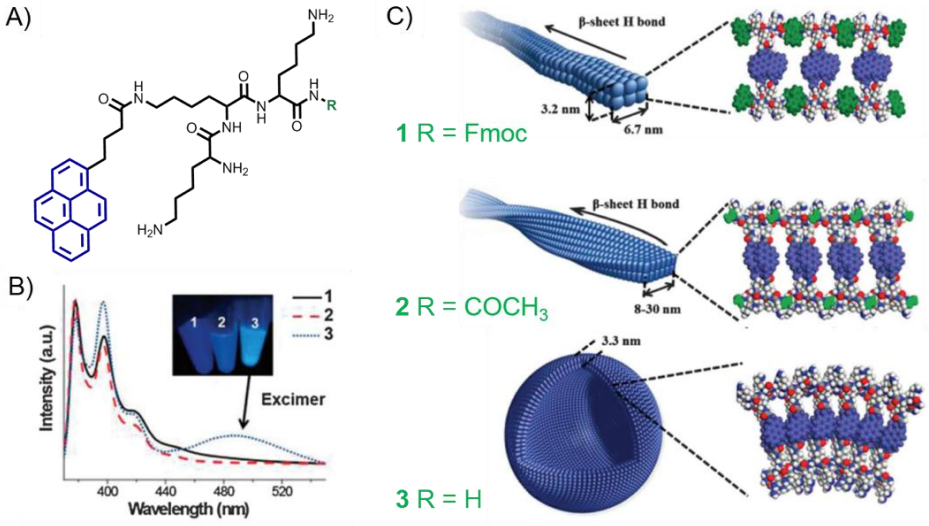

Figure 1. 8. A) Molecular structure of the lysine-based tripeptide containing a pyrene moiety, in blue, and different N-termini substituents, in green. B) Absorption spectra of the different self-assembled nanostructures **1**-**3**. C) Schematic representation of the morphologies and molecular arrangement observed for the three ensembles.

The morphological outcomes ranged from flat and twisted nanoribbons

[45] I. Choi, I. Park, J. Ryu, M. Lee, *Chem. Commun.* **2012**, *48*, 8481-8483.

to spherical hollow capsules. This latter array showed closely packed pyrene units, as demonstrated in the fluorescence spectra with the presence of the characteristic excimer peak.

As briefly introduced in section 1.1.2, an emerging area of great importance for peptide-based supramolecular materials is their use for biomedical applications and it has been extensively investigated by Stupp's research group.[24,46] They have worked on designing and using peptide amphiphiles consisting of a peptide sequence covalently linked to an aliphatic tail that can also include other functionalities such as fluorescent dyes for super-resolution microscopy techniques[47] or recognizing elements for binding proteins.[48] They have widely contributed as well in the area of fundamental supramolecular chemistry and materials science to develop novel rationalized molecular designs to assemble into functional materials.[20, 49]

1.1.4. Segregated donor-acceptor stacks.

Self-assembly is known to be a powerful strategy to organize functional molecules into supramolecular architectures, however, self-assembly of donor-acceptor organic semiconductors still remains as a challenging task. To improve the charge-carrier generation and transport properties in organic devices, segregating the donor and the acceptor moieties as coaxially aligned heterojunctions is desirable to get an optimal phase separation. However, mixing donor and acceptor species generally results in the formation of mixed stacks and hence, many research efforts have been focused in creating segregated ordered *n*/*p*-coassemblies. Different strategies have been developed on this regard. Probably the most extended methodology consists in the synthesis of a covalent donor-acceptor dyad suitably designed to self-assembly in ordered

[46] a) K. Sato, M. P. Hendricks, L. C. Palmer, S. I. Stupp, *Chem. Soc. Rev.* **2018**, *47*, 7539-7551; b) M. P. Hendricks, K. Sato, L. C. Palmer, S. I. Stupp, *Acc. Chem. Res.* **2017**, *50*, 2440-2448.

[47] S. Khan, S. Sur, P. Y. W. Dankers, da Silva, Ricardo M. P., J. Boekhoven, T. A. Poor, S. I. Stupp, *Bioconjugate Chem.* **2014**, *25*, 707-717.

[48] S. S. Lee, T. Fyrner, F. Chen, Z. Álvarez, E. Sleep, D. S. Chun, J. A. Weiner, R. W. Cook, R. D. Freshman, M. S. Schallmo, K. M. Katchko, A. D. Schneider, J. T. Smith, C. Yun, G. Singh, S. Z. Hashmi, M. T. McClendon, Z. Yu, S. R. Stock, W. K. Hsu, E. L. Hsu, S. I. Stupp, *Nat. Nanotech.* **2017**, *12*, 821.

[49] a) Z. Yu, F. Tantakitti, T. Yu, L. C. Palmer, G. C. Schatz, S. I. Stupp, *Science* **2016**, *351*, 497; b) R. Helen Zha, Y. S. Velichko, R. Bitton, S. I. Stupp, *Soft Matter* **2016**, *12*, 1401-1410.

supramolecular materials.

A remarkable example was reported by Aida and *col.* in which photoconductive nanotubes with coaxial *p*/*n*-heterojunction based on trinitrofluorene (TNF)-appended hexabenzocoronene (HBC) amphiphiles were obtained.[50] In the latter configuration, a molecular layer of electron-accepting TNF laminates and an electrondonating graphitic layer of π-stacked HBC ensure the spatial separation of the charge carriers which prevents a rapid recombination, thereby enabling the photoconduction along the nanotubes. Latter on, they reported a similar dyad, in this case based on [60]fullerene and HBC.[51] In the resultant highly carbon-rich nanotubes, a hole-transporting graphite-like layer was covered on both sides by an electron-transporting molecular layer of C_{60} (Figure 1. 9).

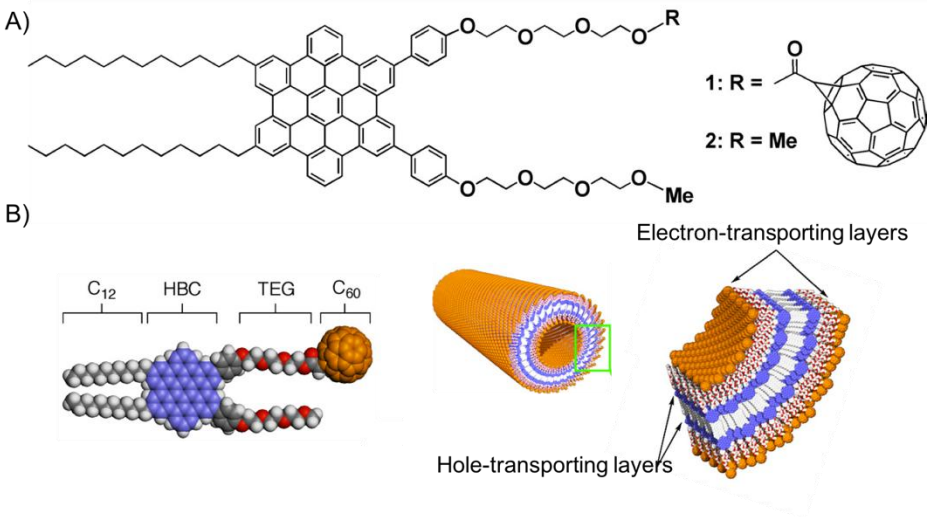

Figure 1. 9. Molecular structure of the covalent HBC-C_{60} dyad (A) and schematic representation of the coassembled nanotubes (B) reported by Aida and col.

The material showed an intratubular charge-mobility as large as the intersheet mobility in graphite, in addition to photovoltaic response. Conductivity measurements showed a decrement of the conductivity at low

[50] Y. Yamamoto, T. Fukushima, Y. Suna, N. Ishii, A. Saeki, S. Seki, S. Tagawa, M. Taniguchi, T. Kawai, T. Aida, *Science*, **2006**, *314*, 1761-1764.
[51] Y. Yamamoto, G. Zhang, W. Jin, T. Fukushima, N. Ishii, A. Saeki, S. Seki, S. Tagawa, T. Minari, K. Tsukagoshi, T. Aida, *Proc. Natl. Acad. Sci. USA* **2009**, *106*, 21051-21056.

temperatures, indicating the semiconductive nature of the system. From the I-V profile, the resistivity at 285 K was determined to be 2.5 megohms, which is remarkably high for an organic semiconductor (comparable to that of an inorganic semiconductor nanotube composed of gallium nitride, resistivity of ca. 10 megohms).

Rencently, Giussepone and col. reported triarylamine-fullerene covalent dyad which self-assembled upon light exposure (Figure 1. 10.).[52] This process involved excitation of triarylamine units which, by oxidation, stacked with their neutral counterparts to form charge transfer complexes in the form of *p*-type conducting channels. Fullerenes were consequently enforced in coaxial *n*-conducting columnar arrangements. Interestingly, the morphology of the resulting nanostructures can be modulated by the variation of the light source (Figure 1. 10. B-C) or intensity which is highly attractive to develop tunable or responsive supramolecular heterojunctions. Electrochemical and theoretical studies demonstrated the potential of this system for ambipolar charge transport as both, the donor and the acceptor moieties, acted as isolated redox sites.

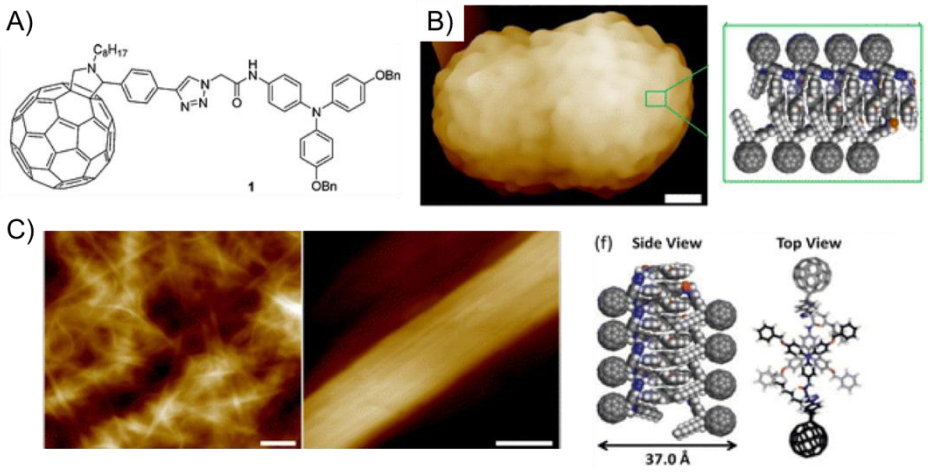

Figure 1. 10. A) Molecular structure of the C_{60}-triarylamine dyad. B) AFM images of the self-assembled structures obtained from a UV-light irradiated solution of **1** (scale bar: 1 μm) and molecular modeling of the triarylamine stacks made of **1**. C) Self-assembled structures obtained from a solution of **1** irradiated with white-light for 15 min (scale bars: 2 μm and 20 nm) and molecular modeling of the triarylamine stacks.

[52] E. Busseron, J. Cid, A. Wolf, G. Du, E. Moulin, G. Fuks, M. Maaloum, P. Polavarapu, A. Ruff, A. Saur, S. Ludwigs, N. Giuseppone, *ACS Nano* **2015**, *9*, 2760-2772.

In these previous examples, the key point was the synthesis of a covalent D-A dyad. However, a stepwise supramolecular coassembly of the donor- and acceptor-layers has gained a great attention when compared to those covalent methodologies. Higher versatility and easier ensembles preparation are the main benefits for these non-covalent approaches.

On this regard, Aida and co-workers further extended their strategy for the formation of HBC-based nanostructures with two different homotropic domains non-covalently connected.[53] The nanotubular segments were electronically communicable with one another over the heterojunction interface and displayed characteristic excitation energy transfer and charge transport properties.

Other convenient approaches in stepwise coassembly implicate the use of *p*-type and *n*-type building blocks containing complementary units to ensure their further coassembly. Meijer and *col*. reported one of the first examples involving D-A arrays, namely oligo(*p*-phenylene vinylene)s and perylene bisimides, connected through complementary hydrogen bonding between diaminotriazine and imide groups (Figure 1. 11).[54] Comparative studies on H-bonded versus covalently linked building blocks demonstrate that both systems form well-ordered J-type aggregates in methylcyclohexane, but only hydrogen-bonded arrays afford hierarchically assembled chiral superstructures. The latter well-defined coaggregated materials exhibit photoinduced electron transfer with a lifetime of the charge separated states in the range of picoseconds.

[53] W. Zhang, W. Jin, T. Fukushima, A. Saeki, S. Seki, T. Aida, *Science* **2011**, *334*, 340-343.
[54] Schenning, Albertus P. H. J., J. v. Herrikhuyzen, P. Jonkheijm, Z. Chen, F. Würthner, E. W. Meijer, *J. Am. Chem. Soc.* **2002**, *124*, 10252-10253.

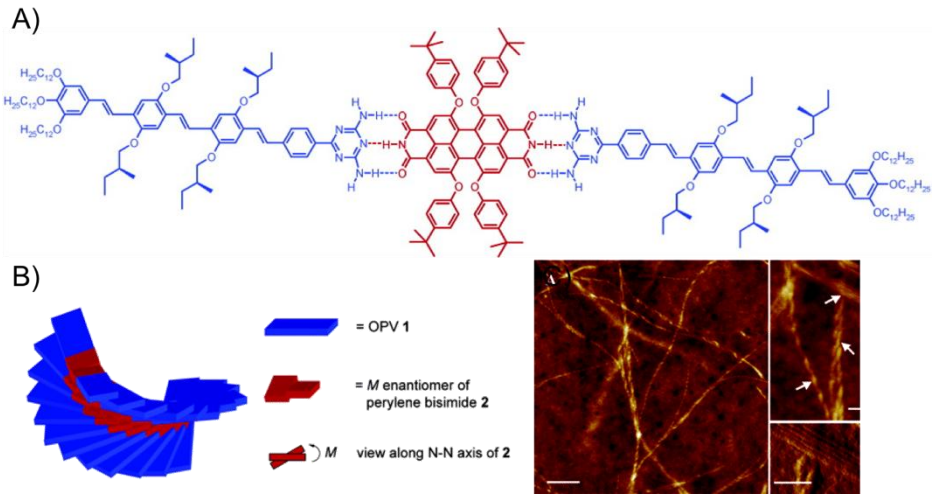

Figure 1. 11. A) Chemical structure of the coassembled building blocks based on oligo(p-phenylene vinylene) and perylene bisimide. B) Left-handed helical stacking model for the coassembled complex. C) AFM images of the coassembled material showing well-defined chiral superstructures.

Our research group developed a novel approach based on complementary ionic coassembly. From small and simple building blocks based on π-extended tetrathiafulvalene, as electron donor, and perylene bisimide, as electron acceptor, highly ordered donor-acceptor functional materials were obtained.[55] The key point for the electrostatic coassembly was to endow the molecular species with ionic groups with opposite charges on their surfaces, specifically, carboxylate and ammonium or guanidinium groups, as depicted in Figure 1. 12. This methodology procured alignments between nanofibers resulting in a material with alternately segregated D-A domains. Photoconductivity measurements showed values as high as 0.8 $cm^2\ V^{-1}\ s^{-1}$, confirming the effectiveness in the design of these heterojunction structures.

[55] J. López-Andarias, M. J. Rodriguez, C. Atienza, J. L. López, T. Mikie, S. Casado, S. Seki, J. L. Carrascosa, N. Martín, *J. Am. Chem. Soc.* **2015**, *137*, 893-897.

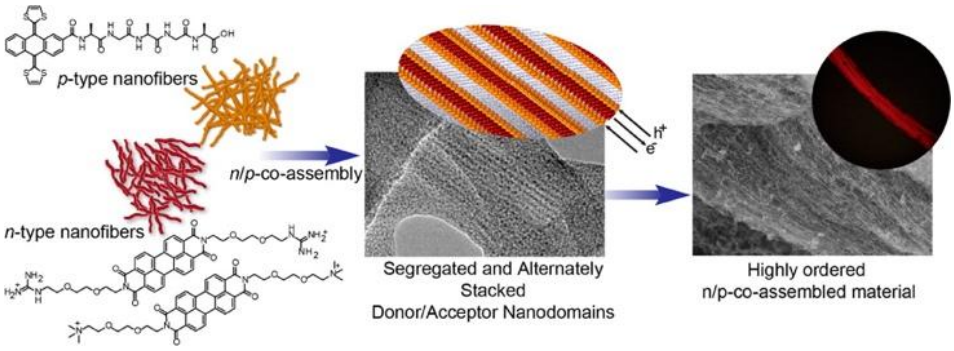

Figure 1. 12. (Left) Molecular structures of the building blocks and (right) schematic representation and electronic microscopy images of the *n*/*p*-material obtained by the coassembly of previously self-assembled molecules.

Finally, there are very few examples in the literature combining the supramolecular polymerization under kinetically control of the semiconducting molecules and their further coassembly. Very recently Tovar and col. reported a remarkable work where the coassembly of three distinct π-systems [oligo(*p*-phenylenevinylene) quaterthiophene and naphthalenediimide], covalently connected to peptide units, is controlled by utilizing different acidification triggers (Figure 1. 13).[56] Addition of glucono-δ –lactone (GdL) provided a slow drop of the pH in the solution, thus, allowing the formation of self-sorted assemblies. However, addition of HCl favored kinetically controlled random mixing of the components, which can reorganize upon aging. Both coassembled nanostructures formed chiral, self-supported hydrogels which showed evidence for energy and electron transfer processes. Controlling the spatial ordering of the chromophores allowed obtaining segregated D-A nanostructures, which is useful for establishing *p*/*n*-heterojunctions, or randomly mixed stacks, which is useful for creating photosynthetic mimics that require high energy transfer efficiency.

[56] H. Ardoña Ann M., E. R. Draper, F. Citossi, M. Wallace, L. C. Serpell, D. J. Adams, J. D. Tovar, *J. Am. Chem. Soc.* **2017**, *139*, 8685-8692.

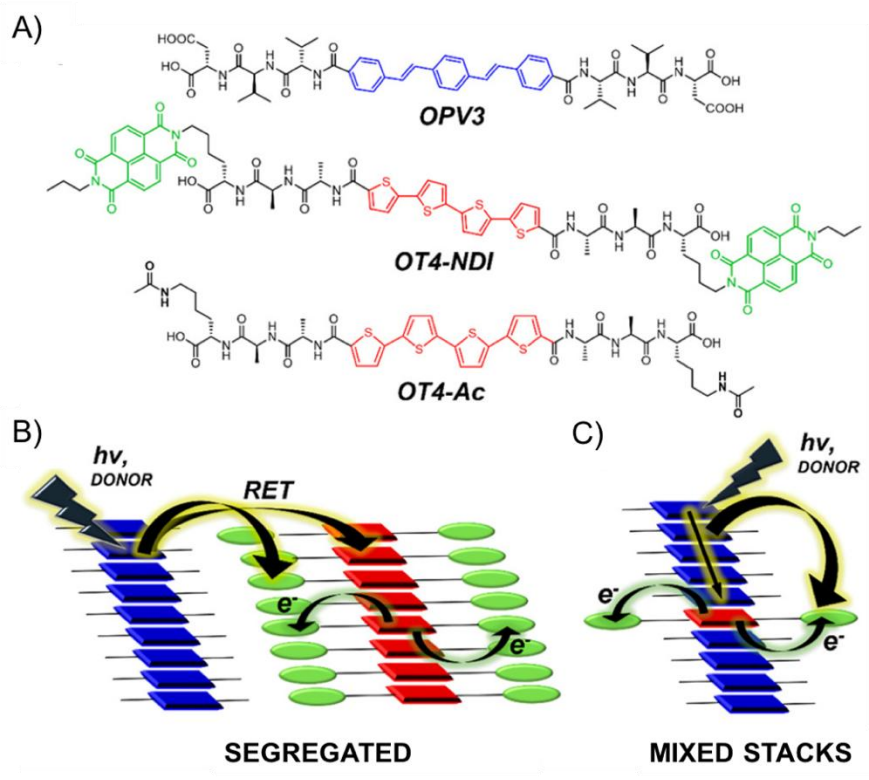

Figure 1. 13. A) Molecular structures of the peptide-based building blocks. B) Segregated coassemblies with a diagram of resonance-energy transfer (RET) and electron-transfer process. C) Randomly coassembled systems and electron-transfer events.

1.2. Objectives

1.2. Objectives

The aim of this chapter is the construction of functional supramolecular architectures by the combination of peptides and π-electroactive systems. The remarkable ability of peptides to self-organize through highly directional hydrogen bonding, is presented to us as a powerful strategy to modulate the properties of organic molecules. Hence, the ultimate goal is to obtain ordered nanostructures to impact the optoelectronic properties of the final materials.

The general strategy is to decorate different π-scaffolds with a simple peptide sequence consisting of alternated alanine and glycine residues, namely AlaGlyAlaGlyAla. This minimalistic pentapeptide has been conjugated to well-known functional π-systems, affording simple building blocks able to build much sophisticated materials with enhanced properties.

This chapter is divided in three sections, each one targeting different molecules of interest. In all cases, we have investigated the supramolecular polymerization in aqueous media of the designed molecules as the key step. Playing with equilibrium and out-of-equilibrium conditions, has allowed obtaining assemblies with different electronic properties out of a single building block.

- *Different electronic properties arising form kinetically vs. thermodynamically controlled polymerization.*

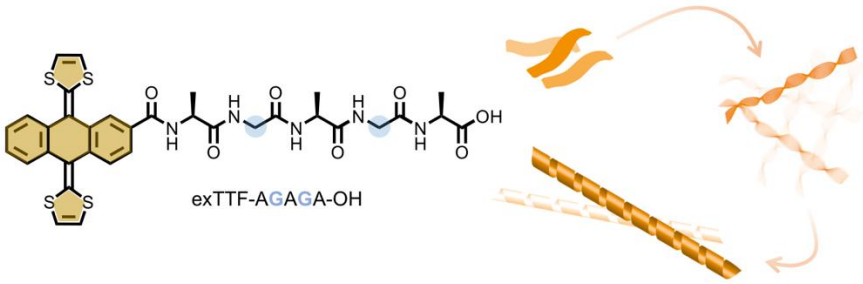

In the first section, we have carried out a comprehensive study on the self-assembly process of a peptide-based amphiphile containing an extended tetrathiafulvelene as electroactive moiety. We aim to control the polymerization pathway through fine modifying parameters such as concentration and ionic

strength of the media and heating/cooling processing of the solutions. The outcomes will allow us to give fundamental insights on the structure-properties-function relationships and to shed light on the relevance of trapping out-of-equilibrium species as final goals.

- *Supramolecular donor-acceptor coassemblies.*

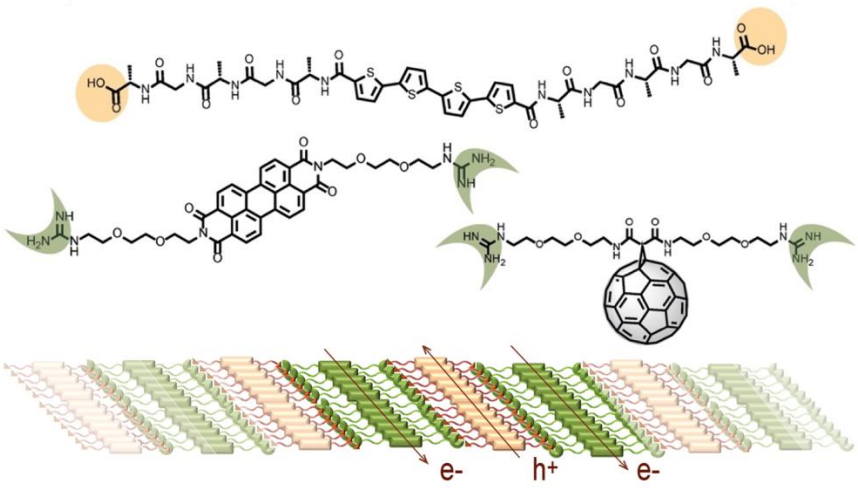

Inspired by the results obtained in the previous section, we will expand this strategy to quaterthiophene, a promising molecule in the field of photovoltaics due its outstanding electronic properties. Similarly to the previous section, the supramolecular organization of this derivative should allow tuning the electronic coupling between the π-systems embedded in the organized peptide network. We propose going a step further and create *n*/*p*-coassemblies by the mixing the pre-assembled *p*-type aggregates with *n*-type counterparts in order to relate the conductive properties of the final materials with their processing. For this purpose, suitably functionalized perylene bisimide and C_{60} species have been designed. Finally, we will elucidate the impact of the pre-assemble step, guided by the peptide-based donor material, on the photoconductivity properties of the *n*/*p* hybrid materials.

- *Porphyrin-based aqueous-soluble nanostructures with outstanding temperature-responsiveness.*

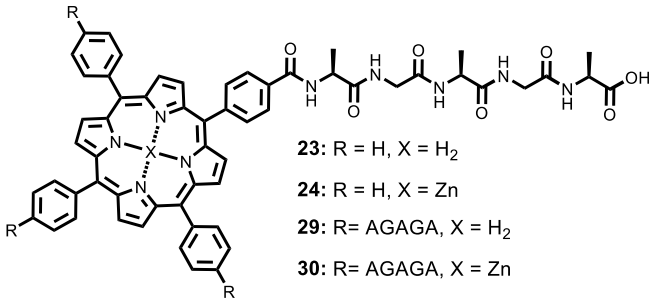

The last section is focused on porphyrin scaffolds directly functionalized in the *meso* position with the pentapeptide sequence, AlaGlyAlaGlyAla. Unexpected results have been obtained in the supramolecular polymerization of these derivatives in aqueous media. A pronounced excitonic coupling of the chromophores is observed upon heating the solution. This effect is directly related with entropically-driven self-assembly in aqueous media, and only a few examples in the field of π-amphiphiles are reported in the literature. Thus, investigating the supramolecular polymerization of these derivatives, we aim to shed light on the mechanisms governing such processes.

1.3. Results and discussion

1.3. Results and discussion

1.3.1. Electronic properties arising from kinetically vs thermodynamically controlled polymerization

An increased interest in understanding the pathway complexity in artificial assembling systems has emerged in the field of supramolecular chemistry. Investigations about the supramolecular polymerization of π-peptide conjugates on the basis of thermodynamic equilibria were previously carried out in our research group. In the present work, we aim to consider out-of-equilibrium conditions to achieve different nanostructures and, consequently, functionalities.

In first place, we performed a comprehensive investigation of the self-assembly process of the π-peptide building block, **1** (Figure 1. 14). The molecular design, previously described in our group,[57] included a π-extended tetrathiafulvalene (exTTF) as electroactive unit, covalently connected to the N-terminus of a short peptide sequence. The peptide sequence is comprised of alternated alanyl- and glycyl- residues and was included in the design due to its well-known ability to yield *β*-sheet domains in both, natural and artificial systems.[58] Moreover, the terminal carboxylic acid functionality enables the formation of supramolecular assemblies by tuning the conditions of the aqueous media, such as pH and ionic strength (*I*).

In a second part, we extended our studies by introducing small changes in the peptide sequence. Four new molecules, **2**-**5** (Figure 1. 14), have been synthesized using the same synthetic route to that for derivative **1**, in order to investigate their self-assembly properties from a sequence-dependence point of view.

[57] J. López-Andarias, J. L. López, C. Atienza, F. G. Brunetti, C. Romero-Nieto, D. M. Guldi, N. Martín, *Nat. Commun.* **2014**, *5*, 3763-3774.
[58] a) A. Jatsch, E. K. Schillinger, S. Schmid and P. Bauerle, *J. Mater. Chem.* **2010**, *20*, 3563-3578; b) Q. Wang, Y. Chen, P. Ma, J. Lu, X. Zhang and J. Jiang, *J. Mater. Chem.* **2011**, *21*, 8057-8065; c) G. W. M. Vandermeulen, K. T. Kim, Z. Wang and I. Manners, *Biomacromolecules* **2006**, *7*, 1005-1010.

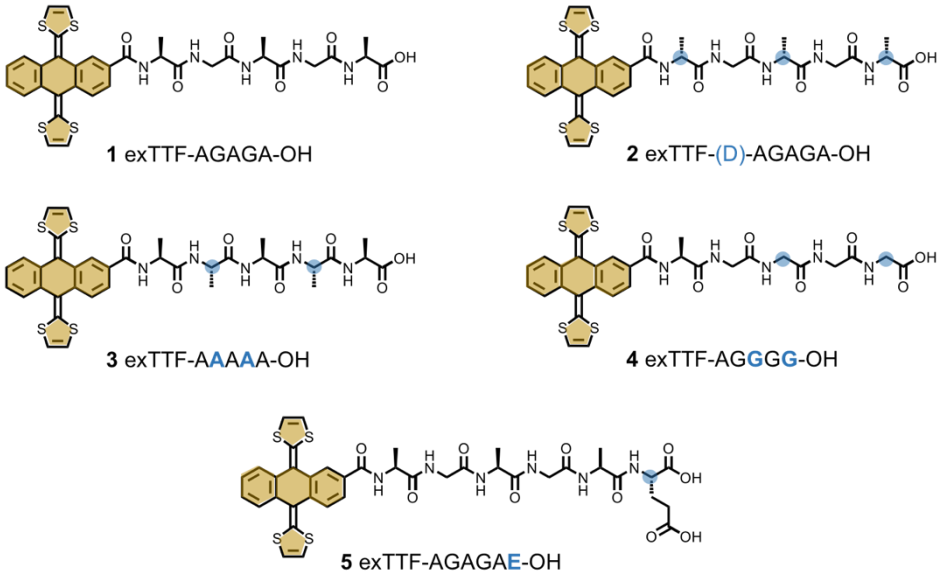

Figure 1. 14. Chemical structure of the exTTF-based building blocks highlighting in blue the structural differences when compared with **1**.

A brief introduction of the structural and electronic properties of the exTTF system is provided below for clarity:

1.3.1.1. π-extended TTF

Tetrathiafulvalene (TTF) is a well-known non-aromatic heterocyclic molecule with outstanding conducting properties which has highly contributed to the field of organic electronics.[59] The great interest in TTFs has triggered the development of new derivatives with a wide range of chemical modifications to enhance its features. One of these alterations is the separation of the 1,3-dithiole rings through a *p*-quinoid π-conjugated system conferring a strong donor character to the molecule, namely π-extended TTF or exTTF.[60]

As shown in Figure 1. 15, the minimum-energy conformation for this molecule corresponds to a butterfly-shaped non-planar structure. The planar

[59] J. Yamada, T. Sugimoto, *TTF Chemistry: Fundamentals and Applications of Tetrathiafulvalene;* Kodansha, **2004**.
[60] F. G. Brunetti, J. L. Lopez, C. Atienza, N. Martín, *J. Mater. Chem.* **2012**, *22*, 4188-4205

conformation of the molecule is strongly hindered by the very short contacts between the sulfur and the hydrogen atoms in the *peri* positions. Contrary to other TTF-based analogues, that show two well-separated one-electron oxidation processes at relatively low oxidation potential values (E_{ox}^1 = 0.37 V and E_{ox}^2 = 0.67 V), exTTF exhibits a two-electron oxidation process to form the dication species (E_{ox}^1 = 0.44 V).[61] The latter dication is fully aromatic and constituted by a planar anthracene unit with the two charged dithiole rings lying orthogonal to the anthracene plane.

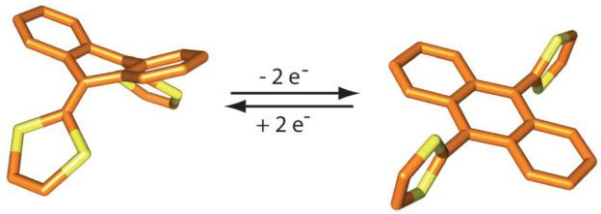

Figure 1. 15. Geometrical change of exTTF molecule upon oxidation process.

The lack of planarity has been traditionally considered as a disadvantageous property for the construction of ordered materials. However, our research group reported for the first time the formation of exTTF-based nanostructures in solution. Moreover, it was demonstrated that the π-π interactions between exTTF units played a key role for the stabilization and the growing of such assemblies.[62] Photophysical studies confirmed that the self-assembly of this derivative enables tuning its electronic properties with a remarkable stabilization of the photogenerated radical ion (3 μs lifetime of the radical-ion-pair state). In a most recent study, we reported the construction of well-ordered nanofibers based on exTTF containing a tripeptide or pentapeptide sequence based on alternating alanine and glycine residues.[57] The combination of these aggregates with single-wall carbon nanotubes (SWCNT) resulted in stable supramolecular gels with long-range order (Figure 1. 16).

[61] N. Martín, L. Sánchez, C. Seoane, E. Ortí, P. M. Viruela, R. Viruela, *J. Org. Chem.* **1998**, *63*, 1268-1279.
[62] J. L. Lopez, C. Atienza, W. Seitz, D. M. Guldi, N. Martin, *Angew. Chem. Int. Ed.* **2010**, *49*, 9876-9880.

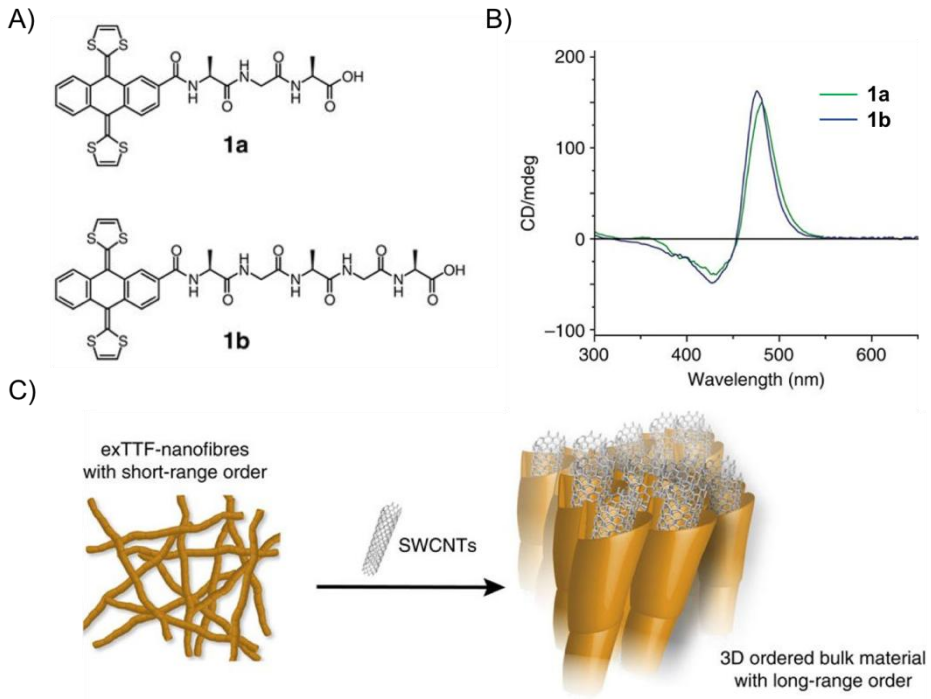

Figure 1. 16. A) Molecular structure of the exTTF derivatives previously described in our group. B) Circular dichroism of their corresponding aggregates. C) Schematic representation of the conjugation of the exTTF nanofibers with SWCNTs.

*1.3.1.2. Synthesis of exTTF-derivative **1***

Synthesis of **1** was carried out by an optimized synthetic route using the succinimidyl ester of the exTTF as the key intermediate. The synthetic procedure is described below:

In first place, a well-stablished procedure was reproduced to synthesize the dimethyl 1,3-dithiol-2-ylphosphonate precursor. This protocol involved the S-methylation, reduction, treatment with HBF_4 and phosphonylation with trimethylphosphite of the commercially available vinylene trithiocarbonate starting material (Scheme 1. 1).

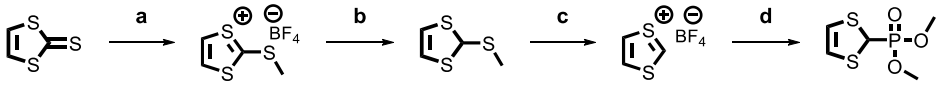

Scheme 1. 1. Synthesis of 1,3-dithiol-2-ylphosphonate precursor. (a) 1) Me_2SO_4, 100 ºC; 2) AcOH, 0 ºC, 3) $HBF_4 \cdot Et_2O$, 0 ºC, 95 %, (3 steps); (b) $NaBH_4$, EtOH, rt, 95%; (c) $HBF_4 \cdot Et_2O$, Ac_2O, 0 ºC, 90%; (d) $P(OMe)_3$, NaI, MeCN, rt, 95%.

Double carbonyl olefination of anthraquinone-2-carboxylic acid with 1,3-dithiol-2-ylphosphonate, followed by esterification reaction with N-hydroxy succinimide yielded the activated ester **6**. Finally, amidation reaction with the desired penpapeptide rendered the final product, **1** (Scheme 1. 2)

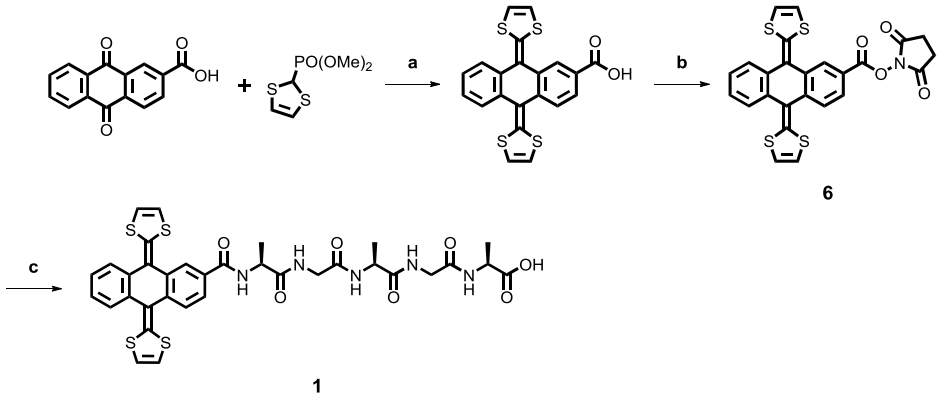

Scheme 1. 2. Synthesis of the succimidyl ester precursor **6** and final product **1**. (a) *n*-BuLi, THF, -78 ºC, 49%; (b) N-hydroxy succinimide, DCC, THF, rt, 88%; (c) L-Alanyl-glycyl-L-alanyl-glycyl-L-alanine trifluoroacetate, $NaHCO_3$, DMSO, 60 ºC, 86%.

Derivatives **2**-**5** were synthesized using the same methodology, but reacting the corresponding peptide sequence with succinimidyl ester **6** in the amidation step.

1.3.1.3. Supramolecular polymerization studies

As previously reported, this molecule self-organizes to yield twisted nanofibers in soft basic aqueous solution.[57] However, previous studies were

focus on aggregates under thermodynamic equilibrium. Carefully investigating the spectral changes of this supramolecular polymer with temperature, revealed a strong hysteresis of the signals. Thus, to have a better understanding on this process, temperature-dependent UV/Vis and circular dichroism (CD) experiments were carried out. A freshly prepared aqueous solution of **1** (c = 0.1 mM, I = 20 mM) showed hypochromic and red-shifted bands which are characteristic of π-π coupled exTTFs within a supramolecular array. Upon heating this solution to 90 ºC or the addition of a good solvent such as methanol, the recovery of the typical bands at 374 and 432 nm corresponding to the molecularly dissolved species was observed. Upon slowly cooling the solution from 90 to 10 ºC (1 ºC/min) the appearance of multiple isosbestic points suggested the transition between two states with monomer-like and J-aggregate-like spectral properties (Figure 1. 17. A). Interestingly, a pseudo nucleation-elongation profile with an anomalous amplification of the polymerization at around 60 ºC was found. To clarify this atypical behavior, we decided performing the same experiment by using circular dichroism spectroscopy.

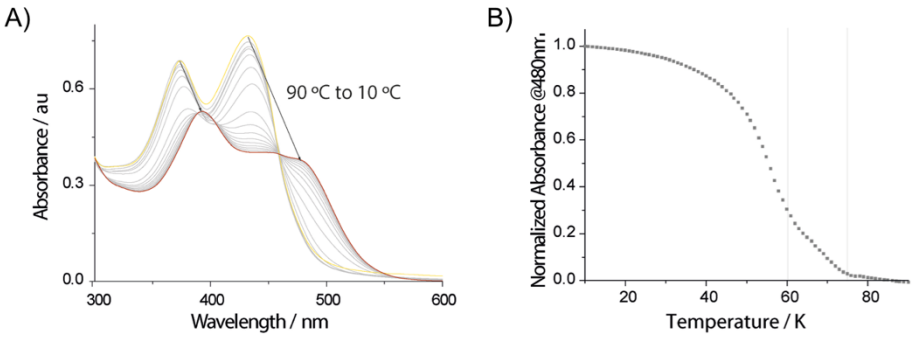

Figure 1. 17. A) Temperature-dependent UV/Vis spectra of **1** (c = 0.1 mM, I = 20 mM $NaHCO_3$) from 90 to 10 ºC. B) Evolution of the absorption at 480 nm with temperature extracted from the cooling experiment, A).

The CD signal of an aged solution of **1** in aqueous media was formerly characterized in a previous work[57] as an intense positive Cotton effect with a maximum at 475 nm and two minima at 426 and 385 nm (Figure 1. 18. A). When performing a cooling study, from 90 to 10 ºC, this reported CD profile started to emerge at 60 ºC. However, above this temperature it drastically changed and evolved to a completely different weak negative Cotton effect with two minima at 498 and 447 nm and one maximum at 400 nm (red line, Figure 1. 18. B).

Subsequent heating back to 90 ºC resulted in an enigmatically broad hysteresis of the CD value. The former positive Cotton effect with even a higher optical signal, was recovered between 40-65 ºC which further disappears with increasing temperature due to the complete denaturation of the aggregate (Figure 1. 18. C-D).

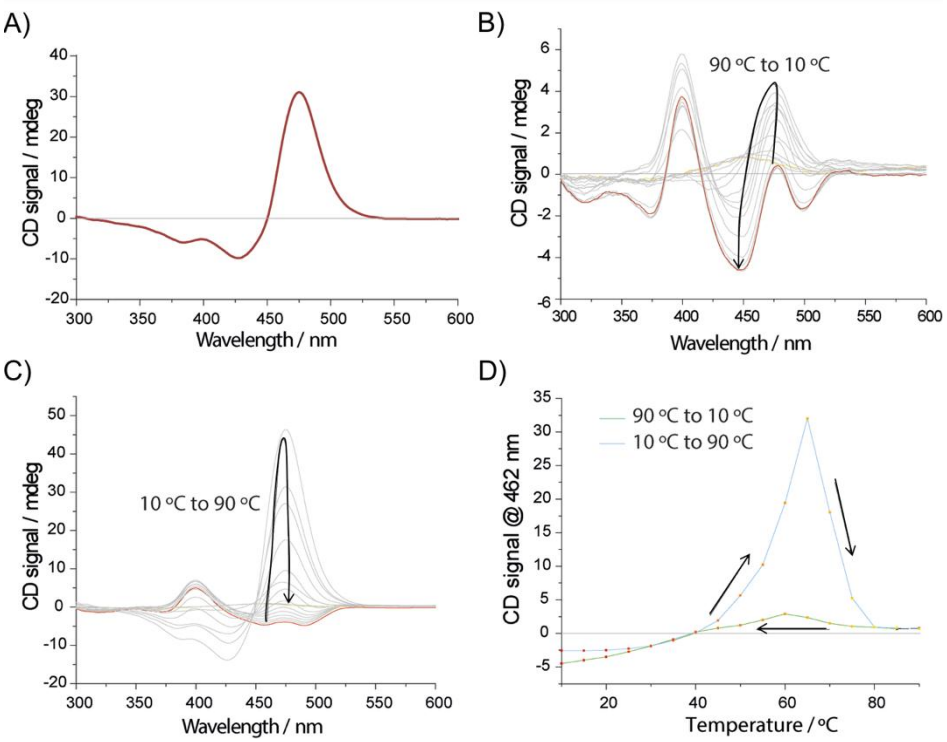

Figure 1. 18. A) CD spectra of an aged solution of **1** (*c* = 0.1 mM). B) Temperature-dependent CD spectra of **1** (*c* = 0.1 mM, *I* = 20 mM) from 90 to 10 ºC. C) Same as (B) from 10 to 90 ºC. D) CD signal at 462 nm extracted from temperature-dependent CD studies during the cooling (green line) and heating (blue line).

All these results pointed to the existence of two different aggregation pathways during the self-assembly process of monomer **1**. We identified the aggregate with the strong positive Cotton effect as a thermodynamically stable system, namely **1-T**, as aged solutions always possessed the latter CD profile fingerprint. Then, we presumed the existence of a metastable aggregate, namely

1-M, in competition. To achieve a precise control, we decided to perform these CD experiments varying both, the concentration of **1** and the ionic strength of the solution. This screening evidenced the great predominance of **1-T** at higher concentrations, while a mixture of both polymers, **1-T** and **1-M**, was discerned at concentrations below 0.2 mM from the complicated CD profiles (Figure 1. 19. A). Similarly, when keeping concentration constant at 0.1 mM, higher ionic strengths reinforced the formation of thermodynamically stable aggregates, **1-T** (Figure 1. 19. B).

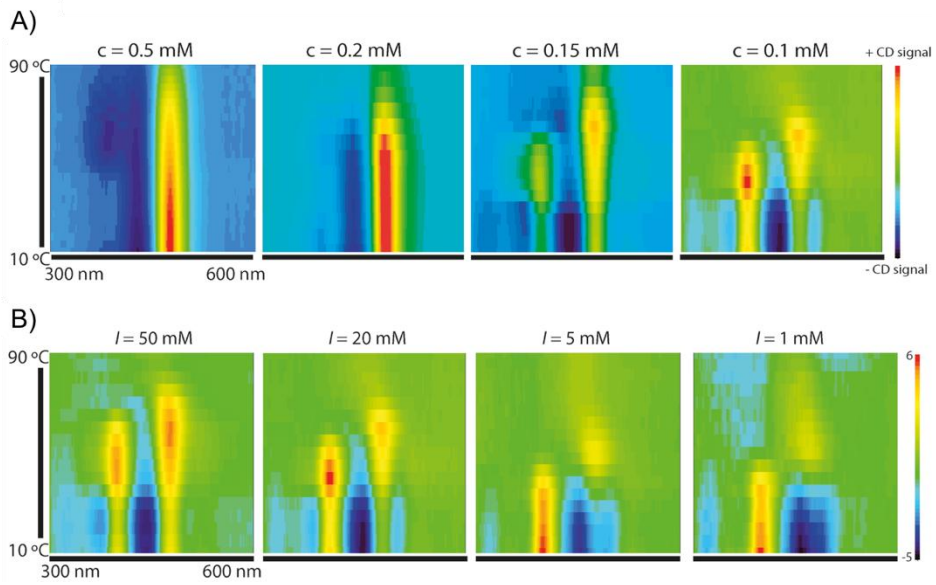

Figure 1. 19. A) Temperature-dependent CD signal of **1** at different concentrations (I = 20 mM). B) Temperature-dependent CD signal at different ionic strengths (from 50 mM to 1 mM $NaHCO_3$) keeping concentration constant (c = 0.1 mM).

Thus, we were able to prevent the formation of the thermodynamic polymer during the cooling experiment at low concentrations of both, monomer and inorganic salt (c = 0.1 mM, I = 1 mM). Using these conditions, we determined the growth of **1-M** via a pure nucleation-elongation process with a temperature of elongation of 46 ºC (Figure 1. 20. A). In such a case, the temperature of activation of **1-T** was lower than that of **1-M**, explaining this result. We also investigated the possibility to obtain the polymerization curve belonging to the formation of the pure thermodynamic aggregate with a much

lower cooling rate (0.1 ºC/min) (Figure 1. 20. B). However, the formation of these so-called metastable entities could not be avoided, suggesting that **1-M** is a non-equilibrium intermediate of **1-T**.[21]

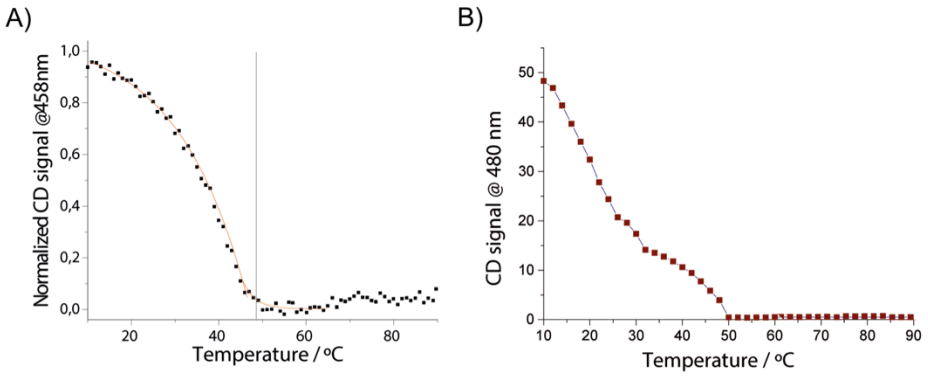

Figure 1. 20. A) Normalized CD signal at 458 nm of **1-M** (c = 0.1 mM, I = 1 mM) from 10 to 90 ºC at 1 ºC/min showing a cooperative polymerization process. B) Evolution of the CD signal at 480 nm from the monomeric **1** (c = 0.1 mM, I = 1 mM) to the formation of **1-T** at 10 ºC at 0.1 ºC/min

At this point, we aimed finding the appropriate parameters to isolate each polymer under the same concentration (c = 0.2 mM, I = 10 mM). Having the temperature of elongation of **1-M** settled at around 50 ºC, a solution of molecularly dissolved **1** was cooled down from 90 ºC to 50 ºC in the shortest period of time possible (around 1 min), thus, avoiding the formation of seeds of **1-T** in this range of temperature. The solution was then kept at this temperature for 15 min and further cooled down to 10 ºC (10 ºC/min) in order to first, favor the formation of **1-M**, and second, trap it at lower temperatures (or reduce the rate of transformation toward the most stable thermodynamic polymer **1-T**) (Figure 1. 21. A). With this treatment, the metastable polymer **1-M** could be obtained under relatively high concentrations of both the monomer and the inorganic salt. It is worthy to highlight the possibility of obtaining two states of aggregation under identical conditions by simply changing the processing sequence.

This precise control over the polymerization process allowed us to well-characterize the spectroscopic features of both species. Regarding their absorption properties, these two pure states presented some characteristic

differences, with a broader red-shifted and hypochromic absorbance compared to the molecularly dissolved monomer **1** (Figure 1. 21. B). These effects were more pronounced in the case of **1-M**, suggesting a modestly stronger coupling between the aggregated exTTF cores in the case of the metastable polymer. Additionally, the differences between both states are particularly outstanding in terms of circular dichroism. An aged solution of **1-T** possessed an intense positive Cotton effect, while we observed a much weaker dichroic signal with opposite negative Cotton effect for **1-M** (Figure 1. 21. C).

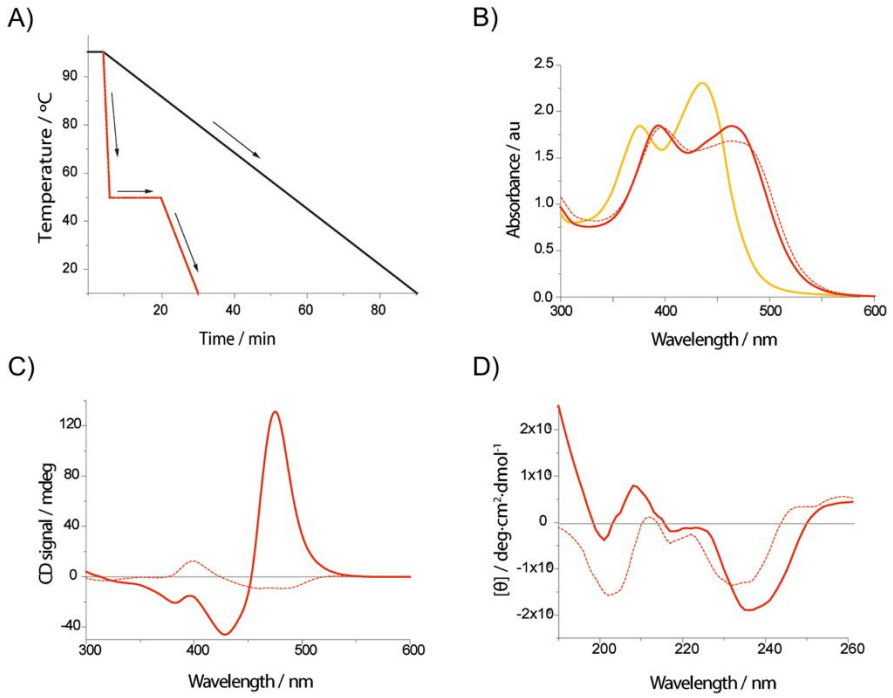

Figure 1. 21. A) Processing sequence for the formation of pure **1-M** starting from disaggregated **1** (c = 0.2 mM, I = 10 mM) (red line) in contrast to a traditional cooling sequence with a homogeneous cooling rate (black line). B) UV/Vis spectra of disaggregated **1** (yellow line), **1-T** (red solid line) and **1-M** (red dashed line) under the same conditions (c = 0.2 mM, I = 10 mM). C) CD spectra of pure **1-T** (solid line) and **1-M** (dashed line) under the same conditions (c = 0.2 mM, I = 10 mM). D) CD spectra of the peptide region of pure **1-T** (solid line) and **1-M** (dashed line) under the same conditions (c = 0.2 mM, I = 10 mM).

Furthermore, the CD signal in the peptide absorption range of both aggregates was also investigated (Figure 1. 21. D). Nonetheless, it is important to remark that the exTTF chromophore also presents absorbance in this region, thus, hindering the assignment of the secondary structure of the peptide backbone. The CD spectrum of **1-M** showed two negative peaks at 202 nm and 232 nm which, considering the improbable possibility of this peptide sequence to form a α-helix conformation, we assigned this profile to a mixture of non-defined intermolecular interactions between the peptide fragments in the metastable aggregate. Thus, we believe the π-π intermolecular interaction plays the major role in the formation of this metastable array. This hypothesis is in agreement with the stronger coupling between exTTF chromophores observed in the UV/Vis spectrum and the weaker CD signal in the chromophore absorption range of **1-M**. In contrast, the CD spectrum of **1-T** in the peptide region showed a more defined profile with a negative peak at 236 nm and a positive peak at 208 nm. This profile can be assigned to a twisted or aggregated β-sheet conformation, indicated by the red-shift in the signature band of a typical β-sheet, as previously demonstrated.[63] In good agreement with this higher ordered peptide arrangement in **1-T**, is the stronger CD-effect in the chromophore range, suggesting a major ordering of π-π interacting exTTFs in the form of chiral arrays.

To further demonstrate that **1-T** is a thermodynamic state and for that reason, it is preferred under any condition, we studied the dependency of the interconversion rate from **1-M** to **1-T** against the concentration of monomer. These studies were performed at 50 ºC to accelerate the process, avoiding data collection over extremely long periods of time; and at low ionic strength (I = 1 mM) to prevent the formation of gel-type precipitates, which would decrease the sample concentration, and consequently, alter the dichroic signal. For these experiments, three samples (c = 0.1, 0.2 and 0.5 mM; I = 1 mM) were heated up to 90 ºC for 15 min to isolate the molecularly dissolved species and subjected to the same cooling treatment described before to stabilized the metastable aggregates. For the highest concentration (c = 0.5 mM), a thermodynamic-like profile of the CD signal was predominantly observed and we were unable to monitor the interconversion. Pure **1-M** dichroic signals were obtained for c = 0.1 and 0.2 mM after the heating-cooling treatment and, surprisingly, the latter showed higher stabilization of the metastable aggregate, which remained stable

[63] H. C. Fry, J. M. Garcia, M. J. Medina, U. M. Ricoy, D. J. Gosztola, M. P. Nikiforov, L. C. Palmer, S. I. Stupp, *J. Am. Chem. Soc.* **2012**, *134*, 14646-14649.

for more than 5 hours at 50 ºC (Figure 1. 22. A). In comparison, the 0.1 mM **1-M** solution rapidly converted in the thermodynamic self-assembled product (< 1 hour). Nevertheless, formation of **1-T** is preferred under virtually any concentration and/or ionic strength, even at lower temperatures, as observed for all the samples aged during several days or weeks at room temperature (15 – 25 ºC).

Finally, we tested the addition of **1-T** seeds in a solution of pure **1-M** polymer, a well-known experiment to ensure that **1-T** is a thermodynamic product. After the addition of a 5% (v:v) of thermodynamic seeds in the stabilized solution of **1-M** at 10 ºC, the evolution of the CD signal at 480 nm at 50 ºC was followed (Figure 1. 22. B). We found that after the addition, the **1-M** to **1-T** interconversion immediately took place, confirming that **1-T** is a thermodynamic product.

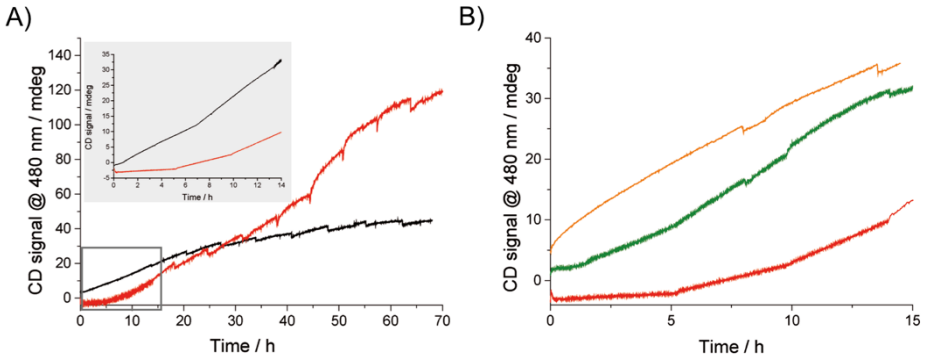

Figure 1. 22. A) Kinetics from **1-M** at different concentrations (c = 0.1 (black) and 0.2 mM (red), I = 1 mM) to the formation of **1-T** by heating the solution at 50 ºC up to 3 days. Inset: amplification from 0 to 14 hours. B) Kinetics at the same dilution conditions (c = 0.2 mM, I = 1 mM, $NaHCO_3$), from molecularly dissolved **1** (orange), from **1-M** (red, same as Figure A) and after stabilization of **1-M** and further addition of 100 µL (5%) of thermodynamic seeds (green).

1.3.1.4. Time-lapse morphological characterization

Once having a fine control on the formation of the two different aggregation states, we investigated the morphological differences between both polymers and even, the transformation during the interconversion process. Cryogenic transmission electron microscopy (cryo-TEM), in particular time-

lapse cryo-TEM, was selected as the best technique to study our system, since any other kind of microscopic technique would lead to surface and concentration-dependent conformational changes non-related to the native state in solution.[64] To achieve a high stability of **1**-**M**, we decided to perform all experiments with a sample concentration of 0.2 mM. Initially, we freshly prepared a solution of **1**-**M** supramolecular polymer and took an aliquot for imaging the kinetically trapped aggregate. This solution was subsequently incubated in a thermoblock at 50 ºC and several aliquots were taken to sweep different incubation times. In Figure 1. 23, representative images at t = 15 min, t =10 h and t = 48 h are shown. Initially, flat and short tapes with a diameter of about 6 nm and lengths between 100 and 200 nm were observed, corresponding to the metastable state. Conversely, with much longer incubation times twisted tapes started to appear (Figure 1. 23. B). The latter, with diameters of about 9 nm in the widest site and and 4.3 nm in the twisted areas and a full turn of 53 nm which was uniform all along the supramolecular structures. The final thermodynamic state (Figure 1. 23. C) appears as well-defined coiled ribbons with a 4 nm width and up to several μm length scales

[64] J. P. Patterson, Y. Xu, M. Moradi, N. Sommerdijk, H. Friedrich, *Acc. Chem. Res.* **2017**, *50*, 1495-1501.

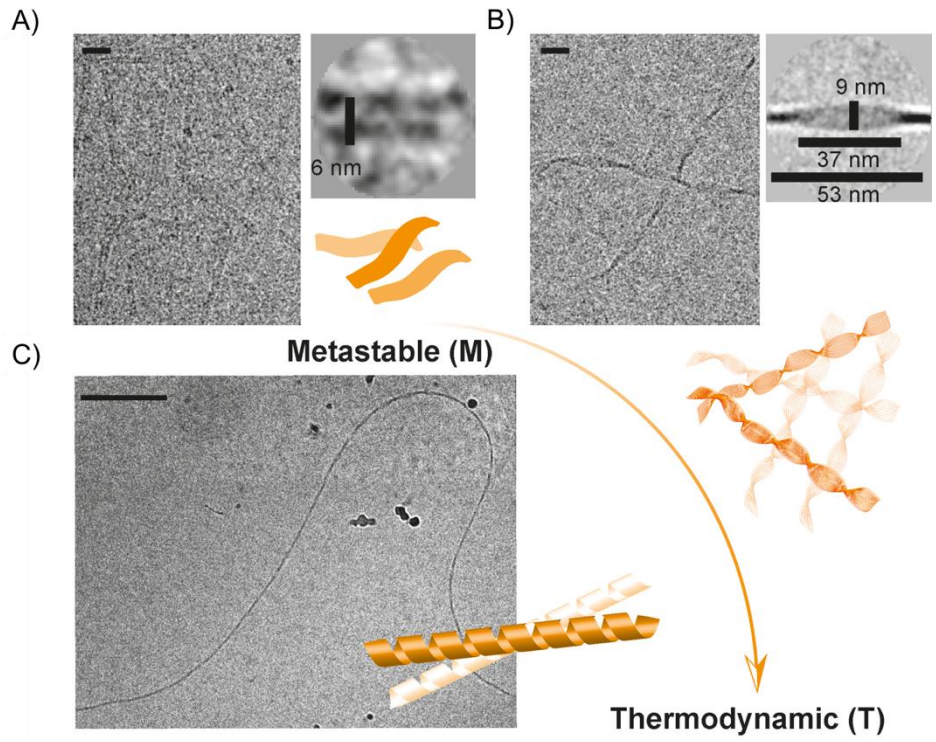

Figure 1. 23. Cryo-TEM images showing the evolution from **1-M** to **1-T** (*c* = 0.2 mM, *I* = 1 mM) under different heating times at 50 ºC; t = 15 min (A); t = 10 h (B); 48 h (C). Scale bars: 100 nm.

1.3.1.5. Insights on the structure-properties relationship

To establish the dependency of the aggregation behavior of these exTTF-based monomers with their chemical structure, we proposed to modify their peptide sequence introducing small changes which, in turn, would allow us to extract some conclusions on the polymerization pathways of these kind of building blocks. For this propose, molecules **2**-**5** were synthesized and their self-assembling properties were studied.

Having a well-stablished procedure to obtain **1-M** or **1-T** at will, we decided to apply the same aforementioned heating-cooling procedure to these new species. We started with derivative **2**, the enantiomer of **1**, bearing the non-natural counterpart of the three alanine residues, that is, D-alanine. Both, **2-M**

and **2-T** were obtained under the same conditions to those for **1-M** and **1-T**, respectively. As expected, the CD spectra of the pair of enantiomers appeared as mirror images (Figure 1. 24. A-B). These findings further confirmed that the helical sense of both the metastable and the thermodynamic polymers are ruled by the chirality of the peptide backbone. Cryo-TEM images showed the same trend, with morphologies of flat and short tapes for the corresponding metastable aggregate and well-defined coiled ribbons for the thermodynamic state (Figure 1. 24. C-D).

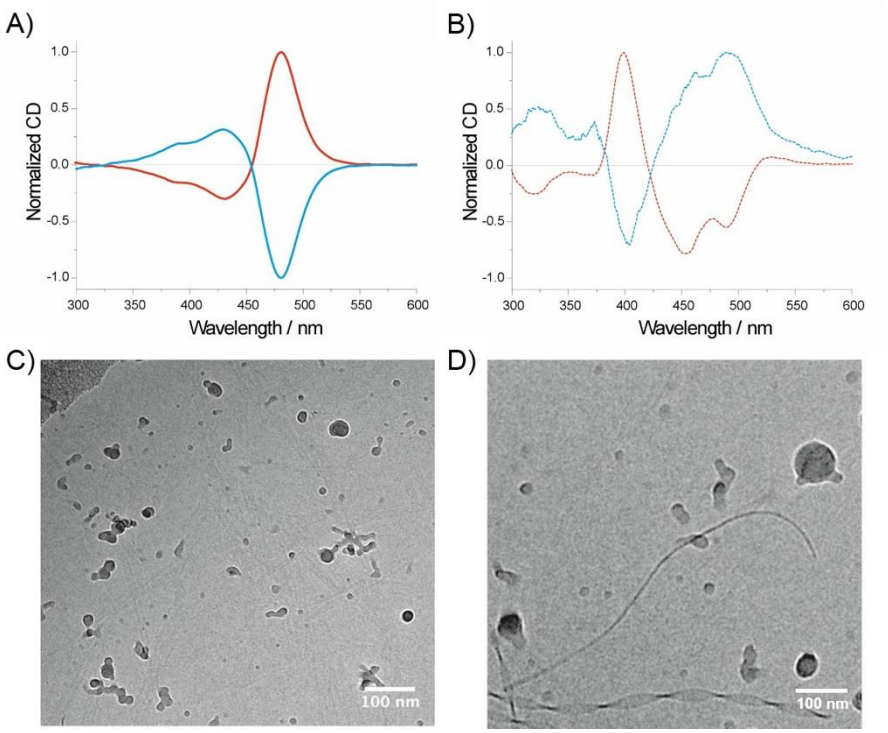

Figure 1. 24. A) CD signal of **1-T** (red line) and **2-T** (blue line). B) CD signal of **1-M** (red line) and **2-M** (blue line). C) Cryo-TEM image of **2-M**. D) Cryo-TEM image of **2-T**. In all cases c = 0.2 mM, I = 1 mM.

Afterwards, we analyzed the alanine-rich derivative, **3** (AAAAA), and, in contrast, exTTF **4**, a glycine-rich species (AGGGG), with only one alanine directly connected to the exTTF scaffold and four glycine residues. Analogously, pure thermodynamic or metastable products could be isolated by applying

similar procedures and the same spectroscopic features previously observed for **1** were found (Figure 1. 25).

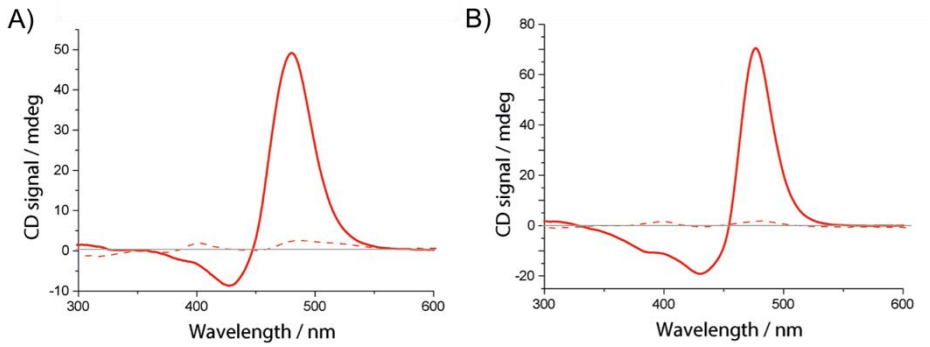

Figure 1. 25. A) CD spectra of **3M** (dashed line) and **3T** (solid line). B) CD spectra of **4M** (dashed line) and **4T** (solid line). In all cases c = 0.1 mM, I = 10 mM.

Temperature-dependent CD studies gave rise to a broad thermal hysteresis (Figure 1.26). The most appreciable difference, if we compare with derivative **1**, concerned the activation temperature of the corresponding metastable aggregates which was found similar in the case of **3-M** (ca. 50 ºC), but lower in the case of the glycine rich derivative, **4-M** (ca. 35 ºC). Additionally, we observed an enhancement of the dichroic signal of the thermodynamic product **4-T**. We attribute this behavior to the higher conformational flexibility of glycine when compared to alanine, resulting in more pronounced ellipticity of the generated thermodynamic fibers.[65] These facts did not affect the morphological characteristics of the obtained aggregates (Figure 1.26 C-D). Thus, short flat tapes were observed for the metastable aggregates **3-M** and **4-M**, while **3-T** and **4-T** appeared as long twisted nanofibers.

[65] F. Huang, W. M. Nau, *Angew. Chem. Int. Ed*. **2003**, *42*, 2269-2272.

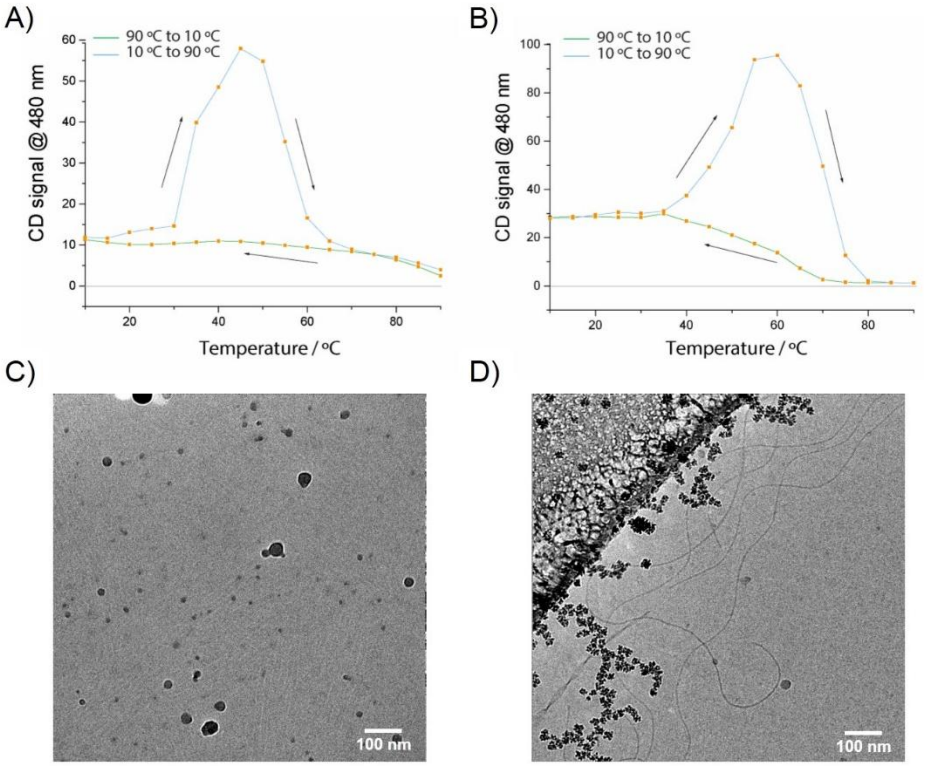

Figure 1. 26. CD signal evolution of **3** (A) and **4** (B) at 480 nm extracted from temperature-dependent CD studies during the cooling (green line) and heating (blue line) processes (rate 1 ºC/min). C) Cryo-TEM image of **3-M**. D) Cryo-TEM image of **3-T**. In all cases c = 0.2 mM, I = 1 mM.

A very different tendency was observed in the case of derivative **5**. ExTTF **5** contains one extra amino acid, glutamic acid (AGAGAE), in the C-terminal position, which affords a second carboxylic acid group in the building block. Probably due to the strong repulsion derived from the presence of these two carboxylic acids in the molecule, no sign of aggregation in soft basic nor neutral conditions was observed. Thus, the UV/Vis spectrum of this compound remained unaltered compared to that of the monomer, presenting at the same time a null dichroic signal. We decided to use a soft acid aqueous environment (pH 3.6) which gave rise to the appearance of an intense dichroic signal with the same profile than the previously observed thermodynamic aggregates of derivatives **1**-**4** (Figure 1. 27). However, the presence of metastable products was never observed during these experiments. Similarly, only long coiled fibers were

found during cryo-TEM studies, that is the same morphology as the rest of the thermodynamic-like aggregates.

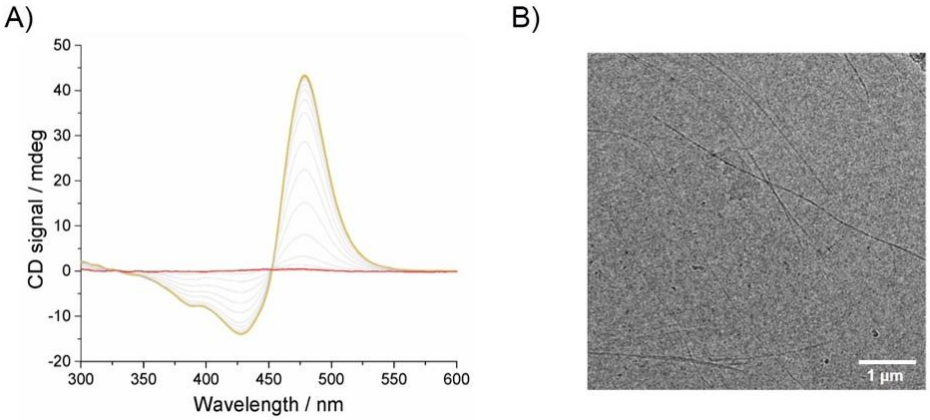

Figure 1. 27. A) CD dependency of **5** (*c* = 0.05 mM, *I* = 10 mM, citric acid/sodium citrate buffer, pH 3.6) with temperature (from 90 ºC to 10 ºC). B) Cryo-TEM image of **5-T**.

1.3.1.6. Electrochemical characterization

To get insights about the structure-function relationship of the two different kind of aggregates, we performed their electrochemical characterization, which is a property pretty much unexplored in supramolecular polymers. In order to determine the electrochemical properties of both aggregates (**M** and **T**), cyclic voltammetry (CV) and differential pulse voltammetry (DPV) were performed. Molecularly dissolved **1** (rt, *c* = 0.2 mM, *I* = 10 mM of KCl) was obtained by adding a 30 % (v/v) of DMSO, yielding an oxidation potential of 155 mV. Being aware of the possible influence of the DMSO in the obtained values, we decided to compare the oxidation behavior of **1-T** at different heatling times to have a comparative between freshly prepared and aged solutions. A freshly prepared solution of **1-T** (rt, *c* = 0.2 mM, *I* = 10 mM of KCl) gave an oxidation potential at 133 mV. This value decreased to more cathodic values as the heatling time increased, reaching 59 mV in the equilibrium (heatling time ≥ 72 h, rt). We attributed this behavior to a better stabilization of the dicationic exTTF species with a higher degree of polymerization. On the other hand, a freshly prepared solution of metastable aggregate showed an oxidation wave at 86 mV. We let this solution evolve,

resulting in a wide signal with clearly two components that resembled a mixture of metastable and early thermodynamic assemblies (Figure 1. 28).

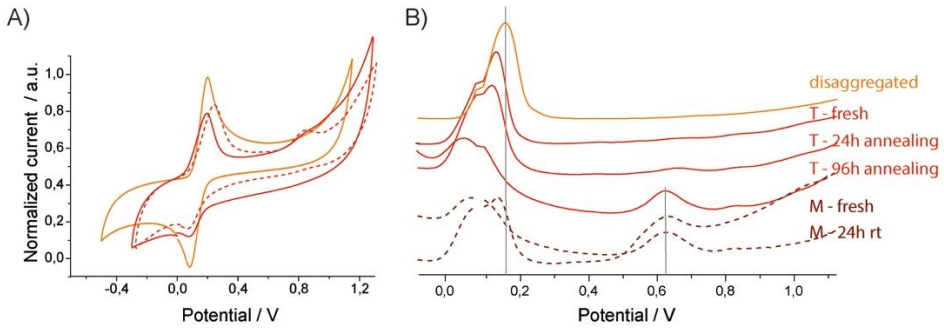

Figure 1. 28. A) Cyclic voltammograms of molecularly dissolved **1** (orange), **1-T** (solid red line) and **1-M** (dashed red line). B) Differential pulse voltammograms of disaggregate **1** (orange) and both aggregates, **1-T** (solid red lines) and **1-M** (dashed red lines) under different heating times.

The same electrochemical behavior was observed for the rest of derivatives (**2**-**4**). In this case, just the freshly prepared **M**-aggregates and the aged **T**-aggregates were investigated (Figure 1. 29).

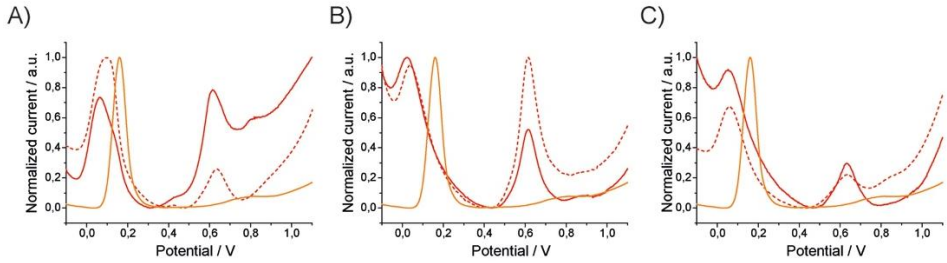

Figure 1. 29. Differential pulse voltammograms of **2**, **2-T** and **2-M** (A); **3**, **3-T** and **3-M** (B); **4**, **4-T** and **4-M** (C). Disaggregate species in orange, **T**-species in solid red lines and **M**-species in dashed red lines.

The measurements confirmed the trend previously observed for **1-M** and **1-T**, obtaining the best values of oxidation for the aged solutions of thermodynamic-like aggregates as compiled in Table 1. 1.

Table 1. 1. First oxidation potentials extracted from differential pulse voltammetry for derivatives **1**-**4**

	1st E_{ox} / mV			
Derivative	**1**	**2**	**3**	**4**
Disaggregated	155	151	149	152
Thermodynamic	59	61	51	22
Metastable	86	92	62	40

Furthermore, both, thermodynamic and metastable aggregates, showed a much stronger oxidation behavior than their former molecularly dissolved building blocks. It is worthy to mention that the best values corresponded to the assemblies from the glycine-rich derivative, **4**, in the same way that these aggregates showed a greater ellipticity due the higher degree of conformational flexibility supplied by the glycine residues.

1.3.2. Supramolecular donor-acceptor coassemblies.

This section was encouraged by the results obtained with compounds **1-5**, where a fine control on the supramolecular polymerization process through pathway selection allowed us to enhance the electrochemical properties of the donor-nature building block. Directing the molecular organization of self-assembled structures is possible to tune the electronic properties, shape and morphology or chirality in the material. Here, we employ an easy and straightforward strategy previously described in our research group which allowed us obtaining ordered *n*/*p*-coassembled materials with appealing optoelectronic properties. Now we go a step further and propose demonstrating that a precise pre-organization of the main building blocks can impact the conductivity properties of the mixed donor-acceptor coassembly.

For this purpose we have designed a well-known *p*-type semiconducting molecule, quaterthiophene (**8**, Scheme 1. 3), directly embedded in the pentapeptide sequence AGAGA which, as mentioned before, tends to self-organize in a β-sheet-like motif.

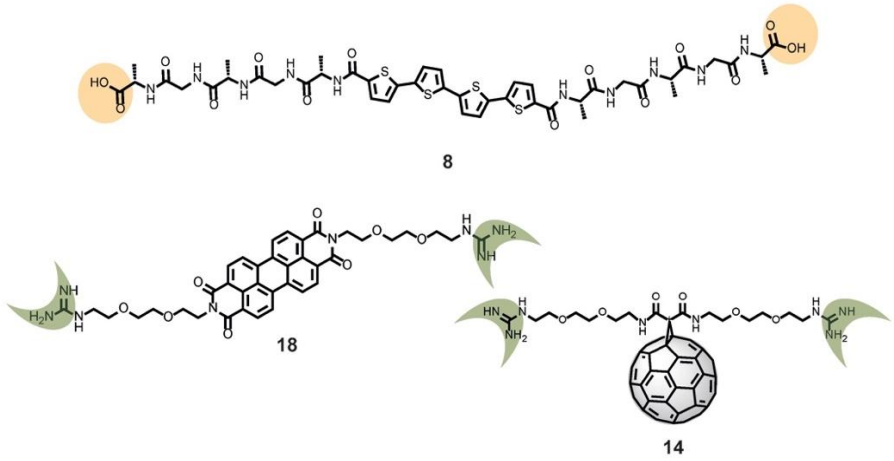

Scheme 1. 3. Chemical structure of the designed building blocks **8**, **14** and **18** highlighting the complementary ionic groups.

As *n*-type complementary semiconductors, we have designed the [60]fullerene derivative **14** and perylene bisimide derivative **18** previously prepared in our research group,[55] which are symmetrically functionalized with polar tails to ensure the solubility in aqueous medium (Scheme 1. 3).

As in the previous section, a brief introduction to basic structural and spectroscopic properties of these building blocks is given below:

1.3.2.1. Quaterthiophene-based supramolecular architectures

Oligothiophenes constitute an important family of organic electronic materials. Due to their properties, it is particularly interesting their use as active components in devices and molecular electronics where they have found numerous applications in OLEDs, OFETs, chemosensors and biosensors.[66] These systems are viewed as ideal because the electron rich oligothiophene backbone is not only able to provide positive charges, but to transport them through self-assembled monolayers or thin films.[67] The synthesis of functional oligothiophenes is very well stablished, generally by either oxidative homocoupling (lithiation followed by addition of $CuCl_2$ or $Fe(acac)_3$) or metal-catalyzed C-C coupling reactions.[66a]

The assembling properties of oligothiophenes were originally reported by Liedberg *et al.* using thiol- and disulfide-functionalized terthiophenes assembled between gold electrodes via sulfur-gold bonds.[68] More recently, many other approaches for the supramolecular organization of oligothiophene derivatives working by non-covalent bonds have been reported. In a recent work, Yagai and col. reported the use of a barbituric acid-substituted oligothiophene leading to hierarchically organized helical nanofibers (Figure 1. 30). This organization was maintained in the presence of a $PC_{71}BM$, used as *n*-channel, affording bulk heterojunction nanostructures with an outstanding performance among those systems based on hydrogen-bonding small molecular materials.[69]

[66] a) A. Mishra, C. Ma, P. Bäuerle, *Chem. Rev.* **2009**, *109*, 1141-1276; b) L. Zhang, N. S. Colella, B. P. Cherniawski, S. C. B. Mannsfeld, A. L. Briseno, *ACS Appl. Mater. Interfaces*, **2014**, *6*, 5327-5343.
[67] F. Jäckel, M. D. Watson, K. Müllen, J. P. Rabe, *Phys. Rev. Lett.* **2004**, *92*, 188303; b) E. Mena-Osteritz, P. Bäuerle, *Adv. Mater.* **2006**, *18*, 447-451.
[68] B. Liedberg, Z. Yang, I. Engquist, M. Wirde, U. Gelius, G. Götz, P. Bäuerle, R. M. Rummel, C. Ziegler, W. Gopel, *J. Phys. Chem. B*, **1997**, *101*, 5951–5962.
[69] H. Ouchi, T. Kizaki, M. Yamato, X. Lin, N. Hoshi, F. Silly, T. Kajitani, T. Fukushima, K. Nakayama, S. Yagai, *Chem. Sci.* **2018**, *9*, 3638-3643.

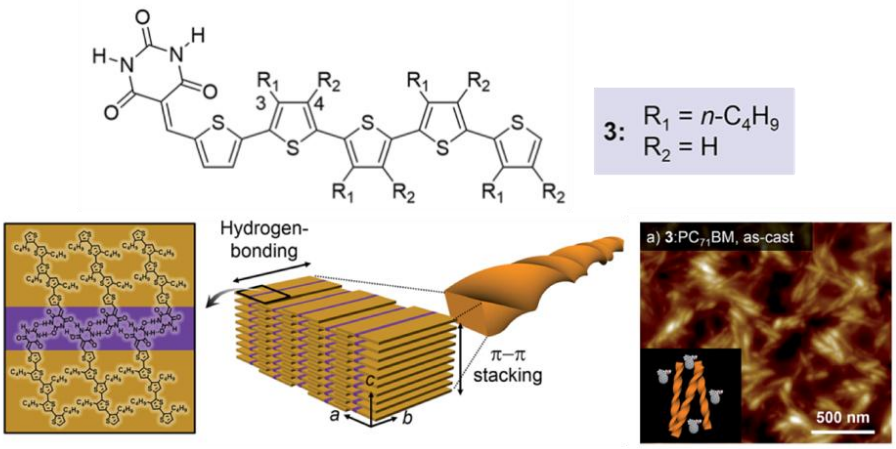

Figure 1. 30. Molecular structure and supramolecular organization of the barbiturate quaterthiophene derivative described by Yagai and col.

As presented in the backfround section, Bäuerle,[70] Tovar,[38,¡Error! Marcador no definido.,¡Error! Marcador no definido.,56] Stupp[12b,46,71] and co-workers, among others, have widely contributed to the field. Some of their research have stablished fundamental aspects of the self-assembling behavior of quaterthiophene and other semiconducting molecules from a bioinspired approach using peptides to guide the supramolecular polymerization.

1.3.2.2. Supramolecular chemistry of perylene bisimide

Perylene bisimide (PBI) is an organic molecule that belongs to the family of rylene-like dyes. PBI derivatives were initially developed as industrial dyes and they are used for textile and industrial paint applications.[72] Nowadays, there is a very active field of research pursuing new applications for PBI in the

[70] a) E.-K. Schillinger, M. Kümin, A. Digennaro, E. Mena-Osteritz, S. Schmid, H. Wennemers, P. Bäuerle, *Chem. Mater.*, **2013**, *25*, 4511-4521; b) A. K. Shaytan; E.-K. Schillinger, P. G. Khalatur, E. Mena-Osteriz, J. Hentschel, H. G. Böner, P. Bäuerle, A. R. Khokhlov, *ACS Nano*, **2011**, *5*, 6894-6909.
[71] a) D. A. Stone, L. Hsu, S. I. Stupp, *Soft Matter*, **2009**, *5*, 1990-1993; b) J. A. Lehrman, H. Cui, W. Tsai, T. J. Moyer, S. I. Stupp, *Chem. Commun.* **2012**, *48*, 9711-9713.
[72] a) H. Zollinger, *Color Chemistry*, 3rd edn., VCH, Weinheim, **2003**; b) W. Herbst and K. Hunger, *Industrial Organic Pigments: Production, Properties, Applications*, 2nd edn., WILEY-VCH, Weinheim, **1997**.

area of organic electronics[73] due to its outstanding photophysical properties. It is worthy to highlight their strong visible-light absorption, high chemical and photo- stability and electron accepting ability (Figure 1. 31). More importantly, the HOMO/LUMO levels of perylene bisimide derivatives can be easily tuned via substitution.

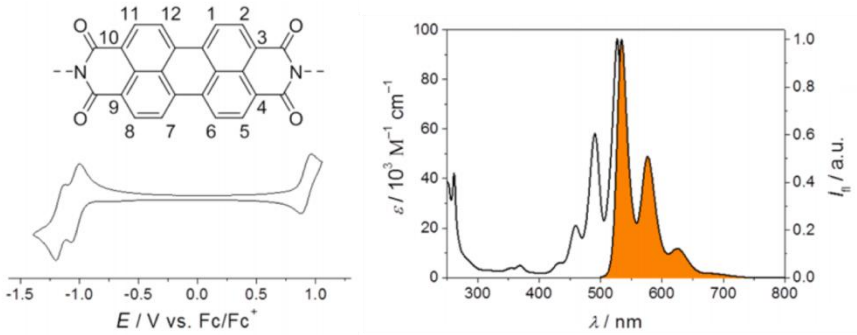

Figure 1. 31 Molecular structure of the parent perylene-3,4:9,10-tetracarboxylic acid bisimide scaffold, typical cyclic voltammogram and UV/Vis and fluorescence spectra.

PBI possesses a high tendency to interact by π-π stacking generating very insoluble materials. In this regard, well-stablished approaches have been developed in order to gain better solubility. Langhals and col. were the pioneers by introducing solubilizing substituents at the imide nitrogen.[74] Another approach, although more elaborated, involves introducing substituents at the carbocyclic scaffold, in the so-called bay-area.[75] The aggregation of these molecules in solution is an area of research that is constantly expanding and developing. Würthner and co-workers have widely explored the self-assembly behavior of PBIs and studied the fascinating photophysical properties emerging from their supramolecular architectures.[28]

[73] a) A. Nowak-Król, K. Shoyama, M. Stolte, F. Würthner, *Chem. Commun.* **2018**, *54*, 13763-13772; b) F. Würthner, *Angew. Chem. Int. Ed*. **2001**, *40*, 1037-1039; c) L. Schmidt-Mende, A. Fechtenkötter, K. Müllen, E. Moons, R. H. Friend and J. D. MacKenzie, *Science*, **2001**, *293*, 1119–1122; d) K.-Y. Law, *Chem. Rev*. **1993**, *93*, 449-486.
[74] H. Langhals, *Heterocycles*, **1995**, *40*, 477-500.
[75] F. Würthner, *Chem. Commun.* **2004**, 1564-1579.

In a recent study, they reported an slightly core-twisted PBI with substituents in the bay position that self-assembled preferentially as kinetically trapped non-fluorescence H-aggregates which eventually evolved into thermodynamically favored fluorescence J-aggregates (Figure 1. 32). [76]

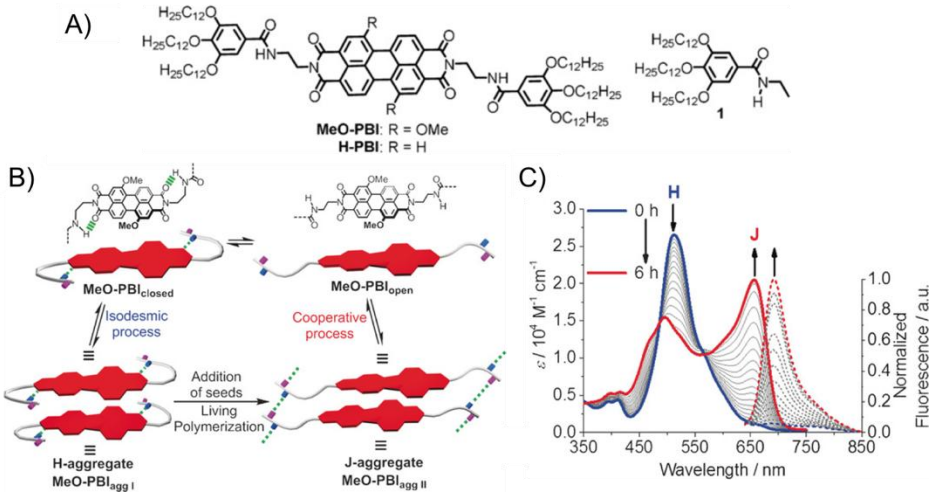

Figure 1. 32. A) Molecular structure of the core-twisted PBI amphiphile. B) Schematic representation of the H- to J-aggregate transition. C) Spectroscopic changes in the transformation of the H-specie to the thermodynamically favored J-aggregate.

As it can be seen in Figure 1. 32. C, the transition between the H- and the J-aggregates was accompanied by great changes in the spectroscopic features.

1.3.2.3. Supramolecular organization of [60]fullerene

[60]Fullerene has become one of the most studied carbon nanomaterials since its discovery in 1985 by Kroto, Curl and Smalley,[77] due to their excellent redox and optoelectronic properties. C_{60}, with a diameter of 7.1 Å, possesses the symmetry of a truncated icosahedron (I_h) with 20 hexagons and 12 pentagons in which all carbon atoms are sp^2-hybridized (Figure 1. 33. A). Fullerene C_{60} is able

[76] W. Wagner, M. Wehner, V. Stepanenko, S. Ogi, F. Würthner, *Angew. Chem. Int. Ed.* **2017**, *56*, 16008-16012.
[77] H. W. Kroto, J. R. Heath, S. C. O'Brien, R. F. Curl, R. E. Smalley, *Nature*, **1985**, *318*, 162-163.

to accept up to 6 electrons (Figure 1. 33. C), with a first reduction potential (E^0_{red}) comparable to those of benzoquinones, due to a triply degenerated LUMO orbital.[78]

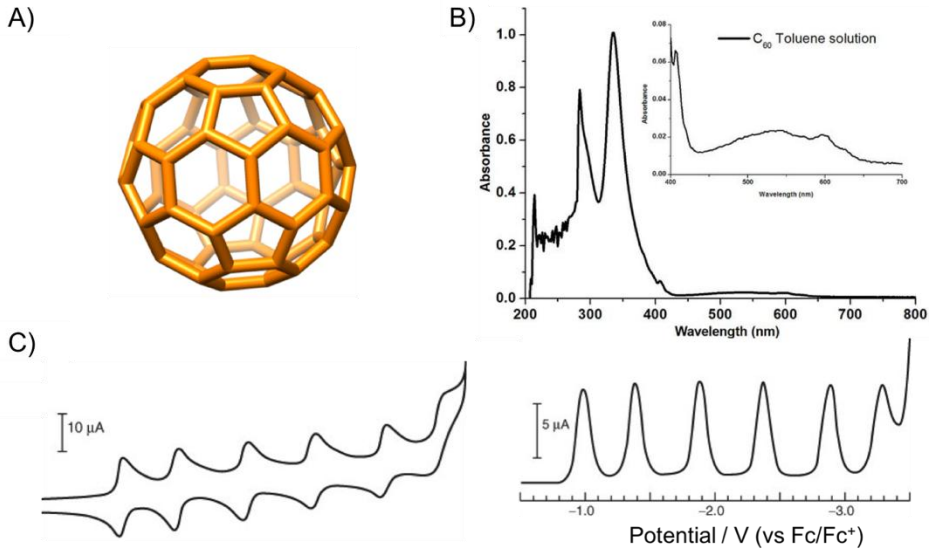

Figure 1. 33. A) Chemical structure of C_{60} fullerene. B) Absorption bands of pristine C_{60} in toluene. C) Electrochemical analysis of [60]fullerene. Reduction of C_{60} in CH_3CN/toluene at -10 ºC by cyclic voltammetry (left) and differential pulse voltammetry (right).

The spectroscopic features of C_{60} derivatives, shown in Figure 1. 33. B, are dominated by allowed $^1T_{1u}$-^1A_g transitions (absorption bands between 190 and 410 nm) and weak singlet-singlet forbidden transitions due to the high symmetry of C_{60} (bands between 410 and 620 nm).[79]

Moreover, it is a very attractive system as electroactive material for organic electronic devices such as OFETs and solar cells due to its low reorganization energy in electron transfer processes. This use of fullerenes was initiated by the work of Heeger and co-workers, who in 1996 produced a two-

[78] Q. Xie, E. Pérez-Cordero, L. Echegoyen, *J. Am. Chem. Soc.* **1992**, **114**, 3978-3980.
[79] H. Ajie, M. M. Alvarez, S. J. Anz, R. D. Beck, F. Diederich, K. Fostiropoulos, D. R. Huffman, W. Kraetschmer, Y. Rubin, K. E. Schriver, D. Sensharma, R. L. Whetten, *J. Phys. Chem.* **1990**, *94*, 8630-8633.

component composite material of conducting polymers and fullerenes to fabricate the first so-called bulk heterojunction solar cell. [80]

The importance of ordering fullerenes at the nano- and the macroscopic scale has been proved as critical for the device performance. For fullerenes, an ordered packing is beneficial for intermolecular charge transport and energy transfer processes. However, especially for functionalized cages, due to the often extensive solvation and steric effects of functional groups, it is a tricky task to achieve. Here, many research efforts are focused on the development of new strategies for designing donor-acceptor arrays. In this sense, Imahori and co-workers, reported a Pd-mediated stepwise coassembly of porphyrin-C_{60} hybrids for photocurrent generation.[81] The modification of a SnO_2 electrode with Zn-porphyrin followed by the assembly of pyridylfullerene moieties through coordination to the zinc atoms together with π-π interactions (Figure 1. 34), rendered composites with high photon-to-current efficiencies.

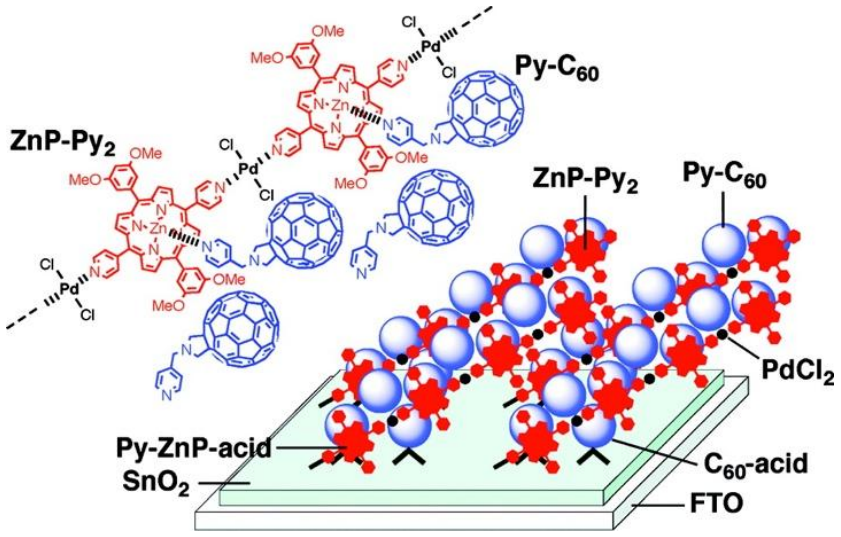

Figure 1. 34. Schematic representation of the porphyrin−fullerene arrays on a SnO_2 electrode.

[80] G. Yu, J. Gao, J. C. Hummelen, F. Wudl, A. J. Heeger, *Science*, **1996**, *270*, 1789-1791.

[81] A. Kira, T. Umeyama, Y. Matano, K. Yoshida, S. Isoda, J. K. Park, D. Kim, H. Imahori, *J. Am. Chem. Soc.* **2009**, *131*, 3198-3200.

1.3.2.4. Synthesis of the target building blocks

As aforementioned, we aimed to synthesize three different building blocks: a donor-character derivative bearing a quarterthiophene core as electroactive moiety, **8**; and two acceptor species based on [60]fullerene, **14**, and PBI, **18**.

Synthesis of **8** was carried out relying on well-stablished procedures.[82] As depicted in Scheme 1.4, precursor **7** was obtained by Stille coupling reaction between 5,5′-bis(tributylstannyl)-2,2′-bithiophene and 5-bromo-2-tert-butoxycarbonyl-thiophene. Finally, amidation reaction with the corresponding penpapeptide in the presence of HATU as coupling agent, rendered the final product.

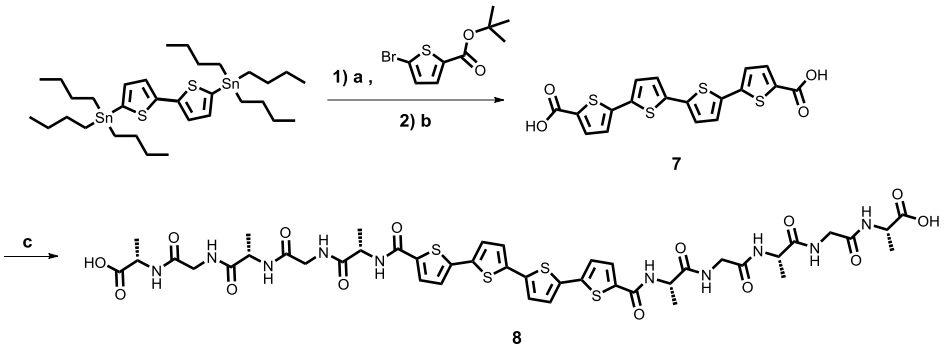

Scheme 1. 4. Synthesis of derivative **8**. (a) $Pd(PPh_3)_4$, DMF, 80 ºC; (b) CH_2Cl_2/TFA (3:2), rt, 70% (2 steps); (c) i) HATU, TEA, DMF, rt; ii) AGAGA, Na_2CO_3, THF/1,4-Dioxane/H_2O (1:1:1), rt, 84%.

For the synthesis of both *n*-type building blocks, the ethyleneglycol-based chain, **9**, was synthesized in order to: i) enhance the water-solubility in the final structures and; ii) include suitable complementary groups for the coassembly with the *p*-type quartethiophene-based nanostructures.

Adapting described prodedures,[83] the first step was the monoprotection of 2,2′-(ethylenedioxy)bis(ethylamine) with di-tert-butyl dicarbonate to yield the

[82] a) S. Kawano, N. Fujita, S. Shinkai, *Chem. Eur. J.*, **2005**, *11*, 4735-4742; b) J. Areephong, E. Orentas, N. Sakai, S. Matile, *Chem. Commun*. **2012**, *48*, 10618-10620.
[83] M. Braun, U. Hartnagel, E. Ravanelli, B. Schade, C. Böttcher, O. Vostrowsky, A. Hirsch, *Eur. J. Org. Chem.* **2004**, *2004*, 1983-2001.

corresponding tert-butyl 2-[2-(2-aminoethoxy)ethoxy]ethyl)carbamate (**9**), suitable to react with malonyl chloride and render the desired malonate **10** (Scheme 1. 5).

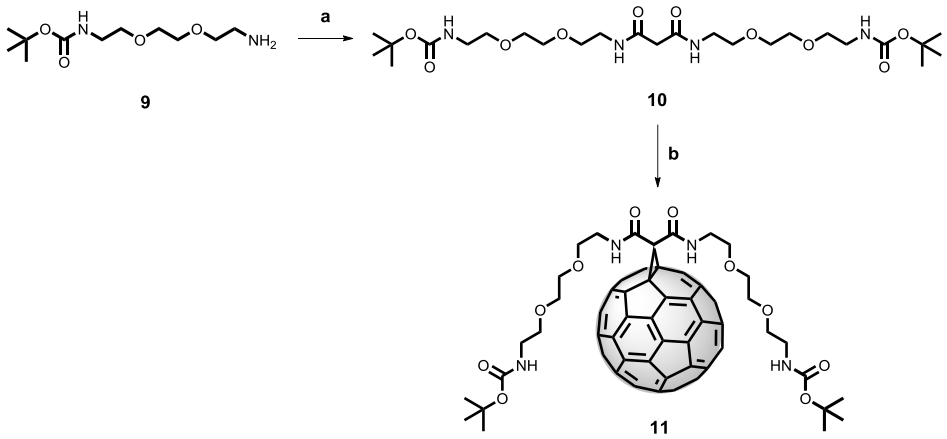

Scheme 1. 5. Synthesis of methanofullerene **11**. a) Malonyl dichloride, TEA, CH_2Cl_2, 0 ºC-rt, 43 %; b) C_{60}, I_2, DBU, toluene, 0 ºC-rt, 25%.

Compound **10** gave the corresponding cyclopropanation reaction with C_{60} in the presence of I_2 and DBU, obtaining the methanofullerene monoadduct **11**. Deprotection of the amino groups was carried out in the presence of TFA to obtain **12** which was transformed in derivative **13** using bis(tert-butoxycarbonyl)-2-methyl-2-thiopseudourea as guanylation agent. Finally, removal of the Boc-protecting groups in acidic media yielded the desired product **14** as a hydrochloride salt.

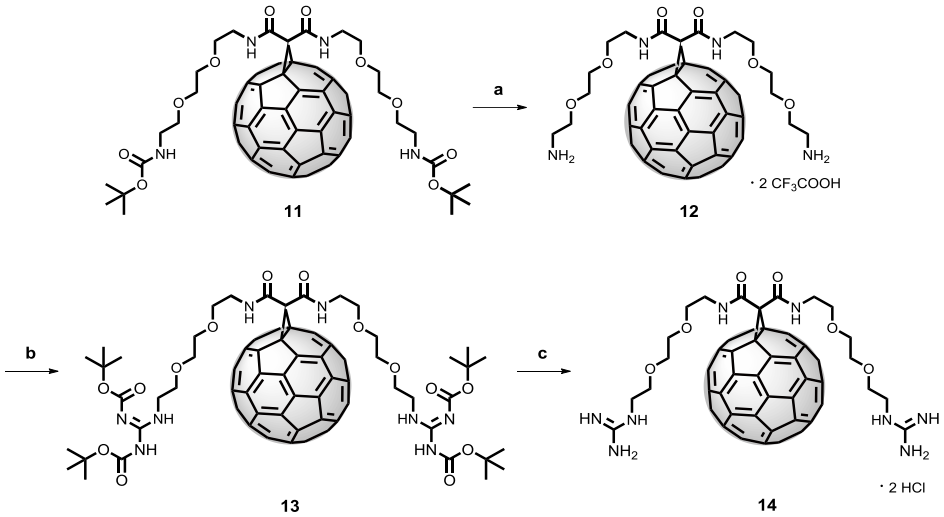

Scheme 1. 6. Synthesis of methanofullerene **14**. (a) TFA, $CHCl_3$, rt, quant.; (b) 1,3-bis(tert-butoxycarbonyl)-2-methyl-2-thiopseudourea, TEA, DMF, 40 ºC, 52%; (c) HCl (37%), CH_3OH, rt, 88%.

In the case of the PBI derivative, tert-butyl 2-[2-(2-aminoethoxy) ethoxy]ethylcarbamate was reacted with perylene-3,4,9,10-tetracarboxylic acid bisimide in the presence of zinc acetate and imidazole to render compound **15**. Afterwards, we proceeded as aforementioned to transform primary amines in **16** into guanidine functional groups to obtain the final product **18** after deprotection of **17** in acid media (Scheme 1.7)

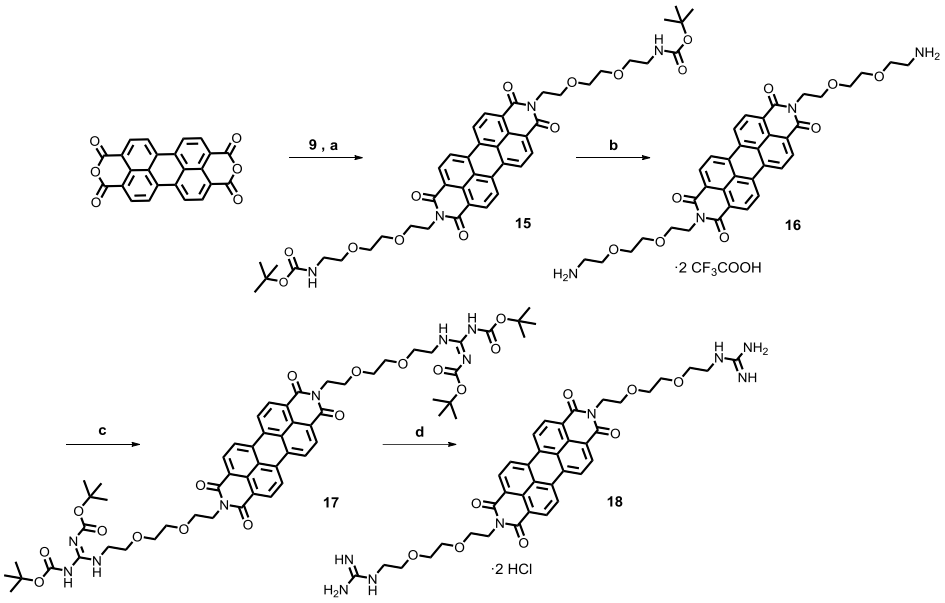

Scheme 1. 7. Synthetic scheme for the synthesis of PBI **18**. (a) tert-butyl 2-[2-(2- aminoethoxy)ethoxy]ethylcarbamate, $Zn(OAc)_2$, imidazole, 150 ºC, 80%; (b) TFA, $CHCl_3$, rt, 92%; (c) 1,3-Bis(tert-butoxycarbonyl)-2-methyl-2-thiopseudourea, TEA, DMF, 40 ºC, 46%; (d) HCl (aq), CH_3OH, rt, quant.

*1.3.2.5. Self-assembly behavior of quarterthiophene **8**.*

For derivative **8**, bearing two peptides moieties, H-bonding and π-π stacking are the intermolecular forces expected to govern the self-assembly process.

UV/Vis spectroscopy showed the first evidences of self-organization in aqueous media. First, we recorded the absorption spectra of **8** in a good solvent for this molecule, as it is methanol, obtaining the expected sharp absorption band at λ_{max} = 415 nm. To increase the ionic strength of the media under controlled pH, we decided to use PBS buffer solution (pH = 7.2). In this neutral pH aqueous media, namely **8-PBS** (c = 0.1 mM, PBS buffer pH = 7.2, I = 10 mM), a slightly hypsochromic effect in the absorption band, with λ_{max} = 405 nm and a shoulder between 470 and 500 nm, appeared. Heating the solution to 95 ºC allowed the gradual recovery of the spectroscopic features of the molecularly dissolved

species, previously observed in methanol, while slowly cooling back to room temperature provided the formation of the previously observed spectroscopic features (Figure 1. 35. A). The latter process was reversible upon heating and cooling back.

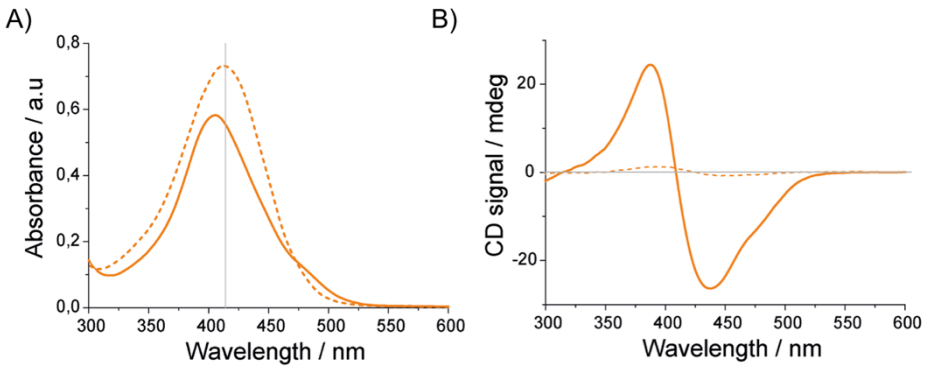

Figure 1. 35. UV/Vis (A) and CD (B) spectra of **8** (*c* = 0.2 mM, *I* = 50 mM PBS) as molecularly dissolved species at 95 ºC (dashed lines) and aggregated as **8-PBS** at room temperature (solid lines).

The presence of chiral centers in the peptide backbone allowed us following these spectroscopic changes by circular dichroism, where a negative Cotton effect was observed (Figure 1. 35. B). Increasing both, the ionic strength (10, 50 and 100 mM) (Figure 1. 36) or the sample concentration (0.2 and 0.5 mM), just led to an amplification of the dichroic signal.

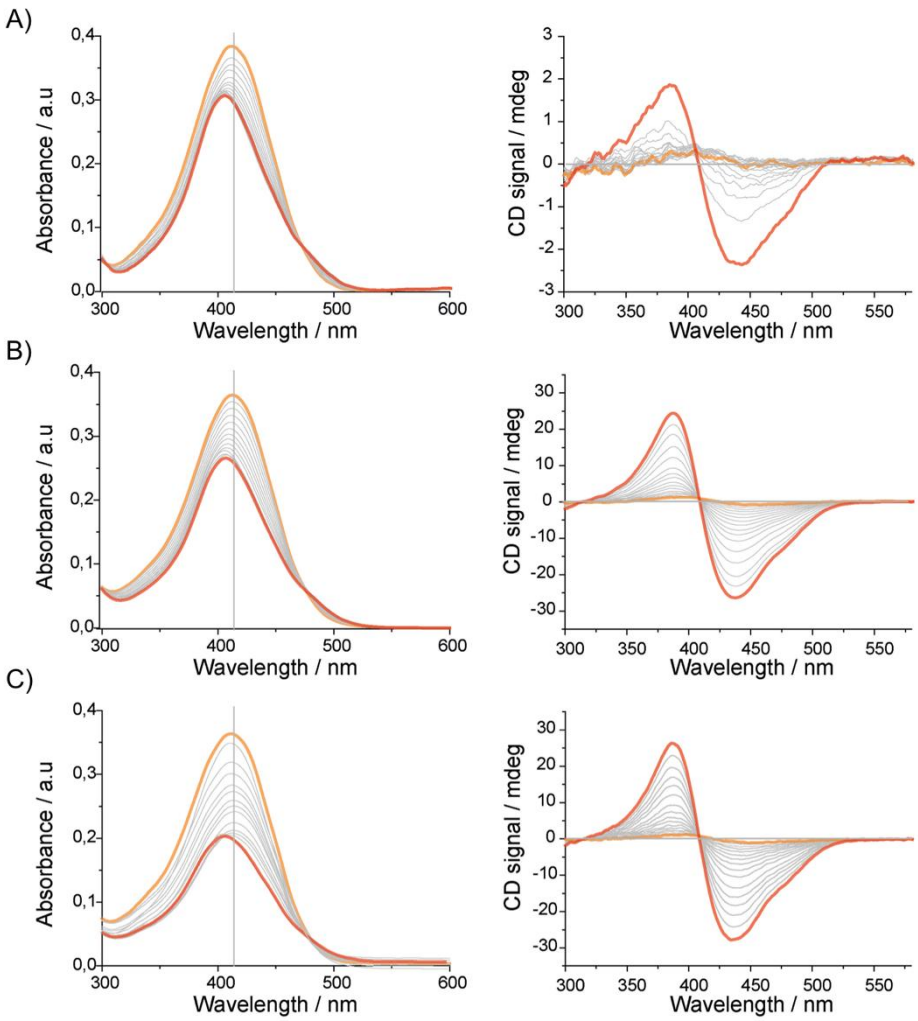

Figure 1. 36. Temperature-dependent UV/Vis (left) and CD (right) experiments at different ionic strengths (in PBS). A) c = 0.1 mM; I = 10 mM. B) c = 0.1 mM; I = 50 mM. C) c = 0.1 mM; I = 100 mM.

To further investigate the self-assembly behavior of this molecule, we decided to explore acid conditions. Addition of a drop of HCl (1 M) into a water solution of **8** (c = 0.1 mM) led to the sudden precipitation of the sample. Hence, we decided to use a softer acidic media (citric acid/sodium citrate buffer solution), setting the pH in 3.6, that is, slightly above the alanine pK_a value (~

2.4) to avoid precipitation. Working at this pH, we could observe the presence of an initial ensemble with strongly hypsochromic and hypochromic absorption features (λ_{max} = 378 nm, weak shoulder around 450 nm). Moreover, the absorption spectrum was quickly evolving at room temperature until thermodynamic equilibration to give a more pronounced blue-shifted profile. Upon heating the latter solution up to 50 ºC these changes in the absorption instantaneously took place, with the absorption maximum at 366 nm and a weak shoulder around 450 nm (Figure 1. 37. A). This aggregate could not be denatured by heating the solution up to 95 ºC, but remained stable once equilibrated.

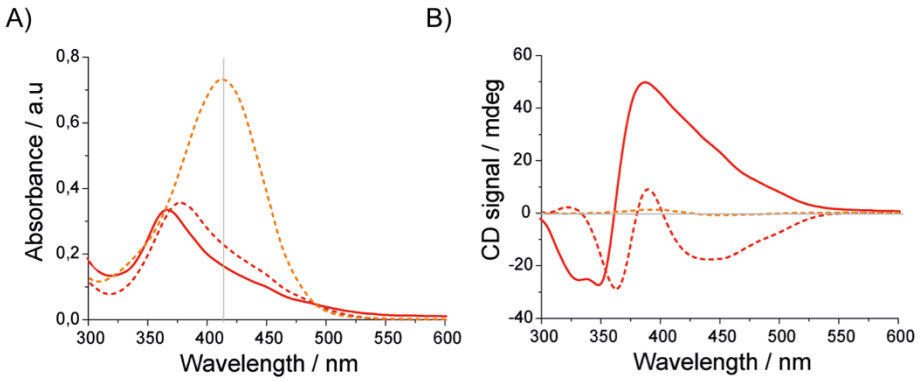

Figure 1. 37. UV/Vis (A) and CD (B) spectra of molecularly dissolved **8** (methanol, dashed orange lines) and citric acid/sodium citrate buffered solutions freshly prepared (**8-M**, dashed red lines) and aged (**8-T**, solid red lines). In all cases *c* = 0.2 mM and *I* = 10 mM in buffered solutions.

Here, upon acidification, a strong H-like aggregation was favored wherein the peptide hydrogen-bonding networks supports near cofacial interactions between the quaterthiophene units. This fact only happened upon removal of the repulsive forces due to a partial protonation of the carboxylate moieties. Surprisingly, we obtained two different CD profiles for **8** in citric acid/sodium citrate buffer solution freshly prepared and after equilibration (Figure 1. 37. B). An initial trisignate signal (-/+/-) assigned to a metastable entity, so called **8-M**, provided a different CD signal with an intense positive Cotton effect after one hour at room temperature (a maximum at 387 nm, a zero-crossing point at 361 nm and two minima at 348 and 330 nm). Nonetheless, it was possible to trap this metastable state by decreasing the temperature around 4 ºC (fridge storage) for at least a week (no control after that time). We monitored

the evolution of the dichroic signal at 370 nm at room temperature, which reached the thermodynamic equilibrium, so-called **8-T**, in less than 30 minutes (Figure 1. 38).

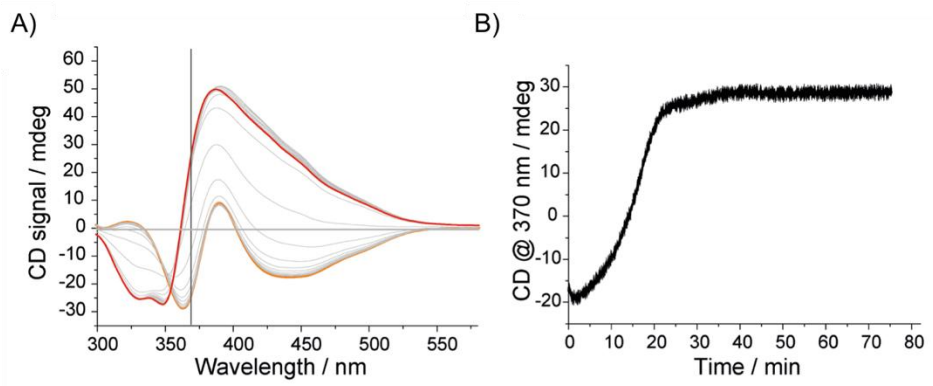

Figure 1. 38. A) CD signal over time at room temperature of a fresh solution of **8** (c = 0.1 mM; I = 10 mM) in citric acid/sodium citrate buffer solution, **8-M** (orange line) to **8-T** (red line); B) CD signal evolution at 370 nm derived from previous experiment.

CD experiments on the peptide region revealed a strong molecular coupling with the features of a twisted β-sheet in the case of **8-T**, while a more random arrangement, similar to the molecularly dissolved species, were observed for **8-M** and **8-PBS** (Figure 1. 39).

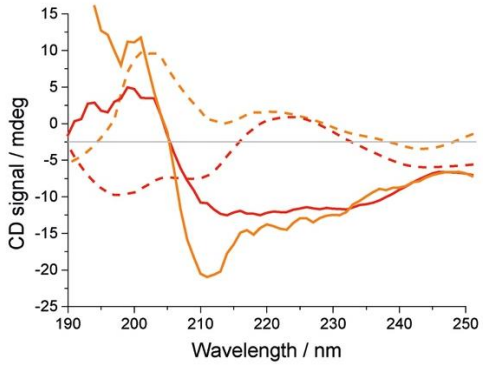

Figure 1. 39. CD signal in the peptide region for **8** (*c* = 0.1 mM) in PBS buffered solution (*I* = 50 mM) at 95 ºC (molecularly dissolved species, dashed orange line) and 20 ºC (solid orange line) and in citric acid/sodium citrate buffer solution (*I* = 10 mM) for **8-M** (dashed red line) and **8-T** (solid red line).

Once these different aggregates were characterized in solution, we proceeded to visualized their morphology. TEM of **8-PBS** rendered fibers with lengths of several microns and usually appearing with loops, thus, showing certain flexibility (Figure 1. 40. A). In acid media we followed the evolution of the supramolecular polymerization by TEM by taking samples with three different equilibration times. A freshly prepared sample yielded small nanoparticles without well-defined shapes that after 15 min of equilibration at room temperature evolved into short and straight fibers, in this case, well-aligned in some regions. Finally, the sample was aged to thermodynamic equilibrium and showed particles featuring a nucleation center made of bundles of needle-like fibers.

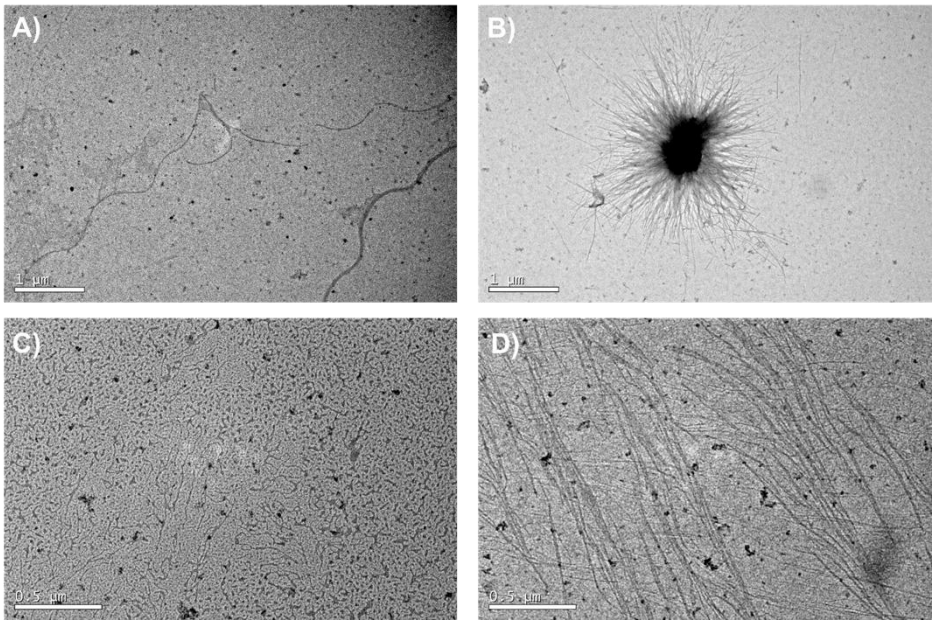

Figure 1. 40. TEM images of **8** (0.1 mM) under different assembling conditions. A) **8-PBS** (*I* = 10mM); B) **8-T** (*I* = 10 mM); C) **8-M** freshly prepared (*I* = 10 mM); and (D) after 15 min at room temperature. In acid conditions, all samples belong to the same batch.

Atomic force microscopy showed similar morphologies as aforementioned, and in all cases with heights of ca. 1.5 nm for the most individualized fibers, according to an unimolecular height.

*1.3.2.6. n-Type nanostructures based on derivatives **14** and **18***

Once we characterized the self-assembly process of the *p*-type building block under different conditions, we proceeded to study the ability of compounds **14** and **18** to form self-assembled architectures by UV/Vis spectroscopy and microscopic techniques.

The absorption spectra of the [60]fullerene derivative (**14**) in a good solvent as DMSO showed the characteristic C_{60} bands at 330 and 430 nm, the

latter associated to the saturation of a C-C double bond in C_{60} monoadducts.[84] However, with increasing amounts of water, a depletion of the band at 330 nm and the loss of feature band at 430 nm occurred due to aggregation (Figure 1. 41. A). TEM images of an aqueous solution (c = 0.1 mM) gave heterogeneous arrays of undefined morphology for the [60] fullerene derivative as shown in Figure 1. 41. B. These aggregates in PBS and citric acid/sodium citrate buffer solutions showed a similar arrangement (Figure 1. 41. C-D).

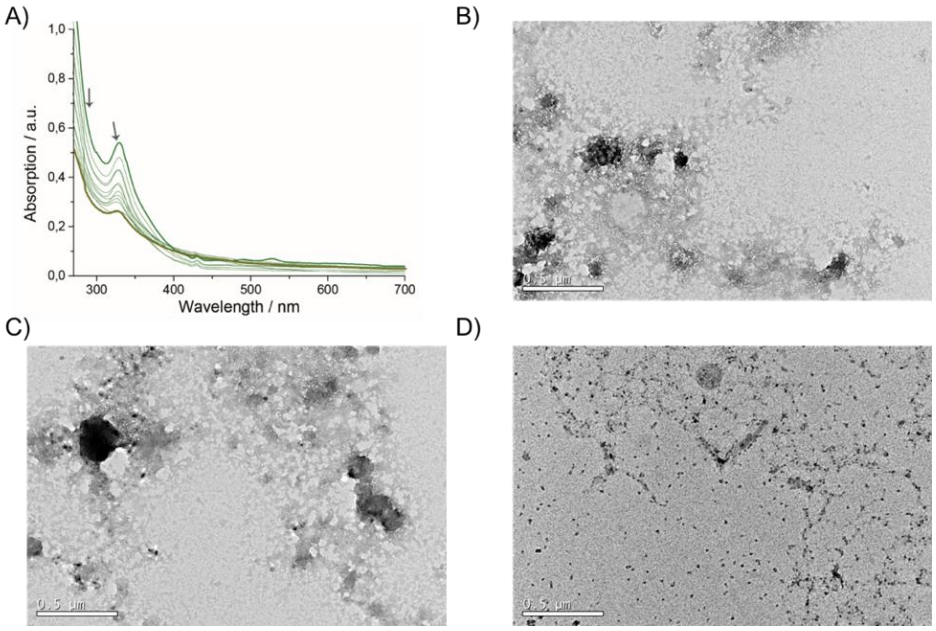

Figure 1. 41. UV/Vis spectra **14** (A) from DMSO to water **(***c* = 0.1 mM**)** and TEM images of each aggregate in Mili-Q water (B), PBS buffer (C) and citric acid/sodium citrate buffer (D). Arrows indicate the evolution of the absorption bands with increasing amounts of water.

The absorption spectra of the PBI derivative (**18**) in DMSO showed a well-resolved vibronic structure between 400 and 500 nm, which is characteristic for the S_0−S_1 transition of molecularly dissolved perylenebisimide derivatives. However, the absorption spectra of PBI with

[84] a) E. E. Maroto, S. Filippone, A. Martín-Domenech, M. Suarez, N. Martín, *J. Am. Chem. Soc.*, **2012**, *134*, 12936-12938; b) K. Sawai, Y. Takano, M. Izquierdo, S. Filippone, N. Martín, Z. Slanina, N. Mizorogi, M. Waelchli, T. Tsuchiya, T. Akasaka, S. Nagase, *J. Am. Chem. Soc.*, **2011**, *133***,** 17746-17752.

increasing amounts of water showed a much broader spectrum with lower intensity and red-shift of the absorption maximum (ca. 20 nm) (Figure 1. 42. A). These features suggested the formation of face-to-face π stacks (H-aggregate) of PBI chromophores.[27] The morphology of these PBI aggregates dried from aqueous solution (*c* = 0.1 mM) showed the formation of undefined nanostructures and molecular islands in water, as well as in both buffered solutions Figure 1. 42. B-D.

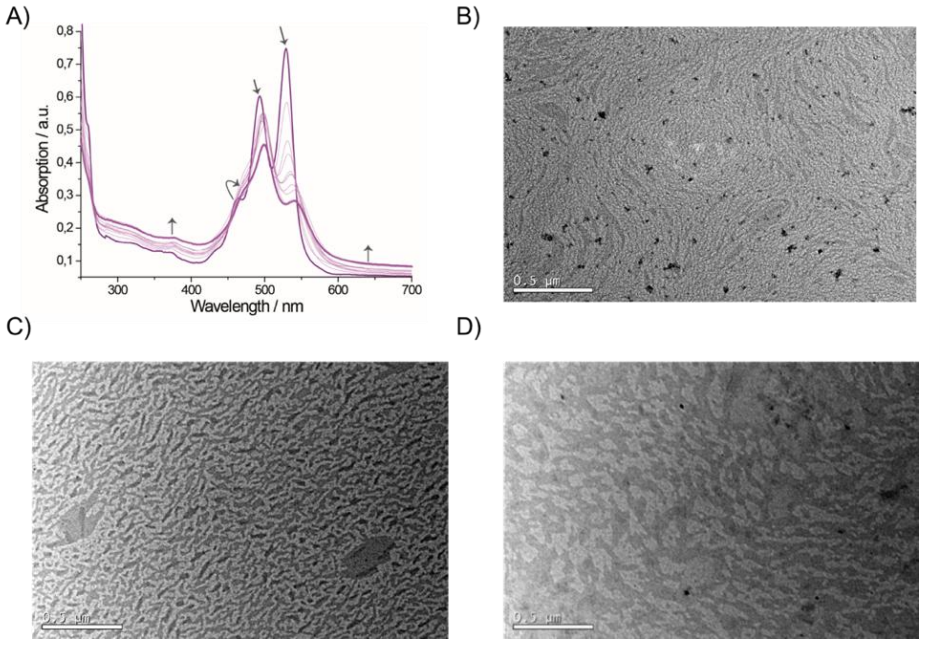

Figure 1. 42. UV/Vis spectra of **18** (A) from DMSO to water **(***c* = 0.1 mM**)** and TEM images of each aggregate in water (B), PBS buffer (C) and citric acid/sodium citrate buffer (D). Arrows indicate the evolution of the absorption bands with increasing amounts of water.

1.3.2.7. Coassembly and characterization of the n/p-materials

The *n*/*p*-hybrid materials were prepared by mixing each pre-assembled building blocks in its corresponding aqueous solution in a 1:1 ratio. After equilibration of the solutions, precipitation of the material was noticed and the obtained powders were washed to remove any traces of salts and free organic molecules. The materials were dispersed in water to provide their CD spectra,

which resembled the former ones from their parent quarterthiophene-based nanofibers (Figure 1. 43, left). Therefore, we assumed that the obtained coassemblies retained the chiroptical properties and the organization from the supramolecular arrays. In order to find out the composition and ratio of organic molecule in the hybrid materials, additionally, we mixed the building blocks in different ratios (2:1 and 1:2). After the equilibration and washing processes, the materials were dissolved, and consequently, denatured, using DMSO in order to record their UV/Vis spectrum (Figure 1. 43, right).

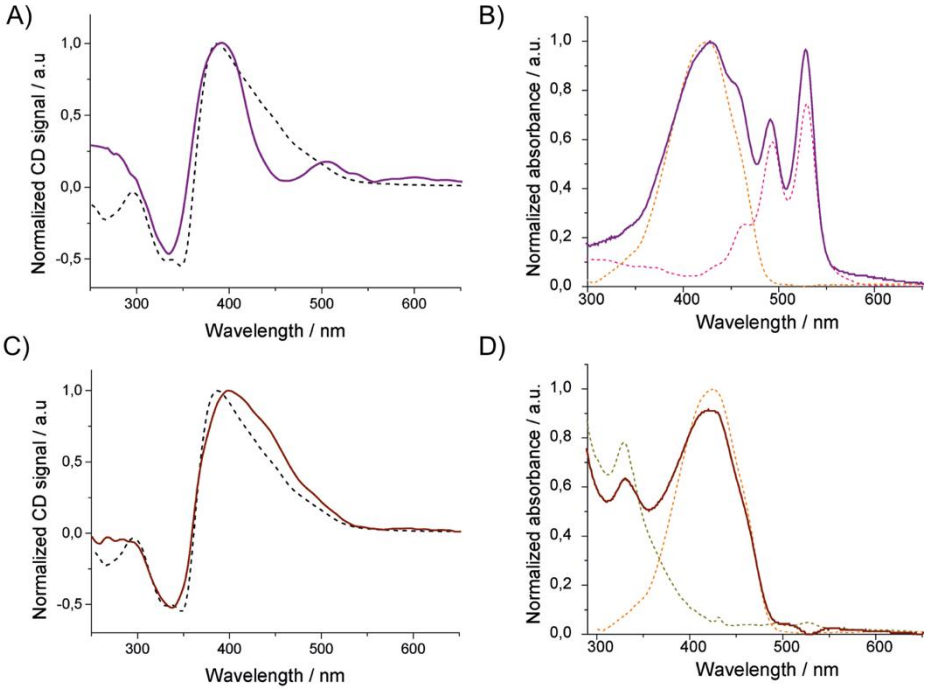

Figure 1. 43. Spectroscopic properties of the hybrid materials **8:18-T** (A-B) and **8:14-T** (C-D). A), C) Normalized CD signal of the *n*-/*p*-materials dispersed in water (solid line) compared to the former pre-assembled building block, **8-T** (dashed line). B), D) normalized UV/Vis spectra of the denatured *n*-/*p*-materials in DMSO (solid lines) compared to the absorption spectra of the former building blocks **8** (orange dashed line), **14** (pink dashed line) and **18** (green dashed line).

All absorption spectra, including the ones mixed in a 2:1/1:2 ratios, showed the sum of the absorption bands from the corresponding molecularly dissolved components. The relative intensity of these bands matches with a 1:1 ratio, as expected from the molecular design of the building blocks.

In addition, we confirmed the elemental composition of the *n*/*p*-hybrid materials by X-ray photoelectron spectroscopy (XPS). In the XPS survey spectra we observed the spectroscopic signature of the carbon (C-1s), oxygen (O-1s), nitrogen (N-1s) and sulfur (S-2s and S-2p) signals around 284, 533, 400, 227 and 162 eV, respectively (Figure 1. 44. A). It is important to remark that no detectable signals of sodium (Na-1s) as counter cation of **8** and chloride (Cl-2p) as counter anion of **14** and **18**-based nanofibers were observed in the 1072 eV, 198 eV and 620 eV regions, respectively. The lack of these ions is indicative of the interactions occurring between carboxylate and guanidinium groups.

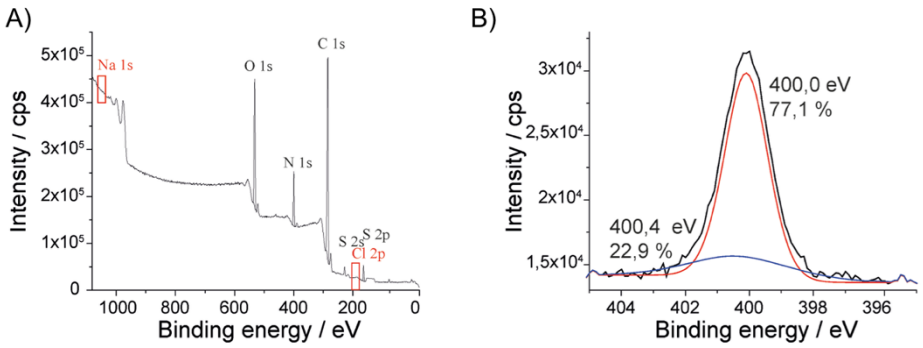

Figure 1. 44. A) XPS survey spectra of a solid sample of **8:14-T** highlighting in red the absence of signals corresponding to sodium or chloride ions. B) High-resolution spectra of the N-1s region and its Gaussian deconvolution to determine the populations of guanidinium-nature (blue line) and amine-like (red line) nitrogen atoms.

By analyzing in detail the high resolution spectra of the N-1s region it was possible to determine the populations of electronically distinct N atoms (Figure 1. 44. B and Table 1. 2).[85] Deconvolution of the N-1s energy level revealed the presence of two different Gaussians-Lorentzians curves, with approximately a 22 % (21.40 ± 2.4 %) of the oscillator strength derived from the guanidinium amines, with higher binding energy than the rest of the amines (78.6 ± 1.9 %). These values are in agreement with the calculated theoretical values for a 1:1 ratio coassembly, confirming the previous spectroscopic findings.

[85] J. H. Olivier, P. Deria, J. Park, A. Kumbhar, M. Andrian-Albescu, M. J. Therien, *Angew. Chem. Int. Ed.* **2013**, *52*, 13080-13085.

Table 1. 2. Experimental values extracted from the deconvolution of the high-resolution spectra of the N-1s region which allowed the determination of the population (expressed as %) of electronically distinct N atoms.

Sample	GUANIDINIUM AMINES		OTHER AMINES	
	Quantification	Position / eV	Quantification	Position / eV
8:14-PBS	22.8	400.1	77.2	399.8
8:18-PBS	21.2	399.4	78.8	399.0
8:14-T	21.8	399.8	78.2	399.6
8:18-T	22.9	400.4	77.1	400.0
8:14-M	19.5	399.8	80.5	399.5
8:18-M	20.2	400.0	79.8	399.7

Infrared spectroscopy also showed evidences of the coassembly between the donor and the acceptor species through the carboxylate moieties. The FT-IR spectra was closely examined in the carbonyl region. The guanidinium area around 3400 cm^{-1} was, however, too broad to be interpreted. The $\nu_{C=O}$ band of free carboxylic acids usually appears around 1700 cm^{-1}, although in the case of molecule **8**, which was isolated as chloride salt, we observed the corresponding band at 1660 cm^{-1}. A shift of ca. 30 cm^{-1} toward lower frequencies, which was reproducible in all cases, was obtained for the formed *n*/*p*-hybrid materials compared to molecular species **8** (Figure 1. 45). This band located around 1630-1650 cm^{-1} (depending on the extent of proton polarizability), has been previously assigned to carboxylate-guanidinium interactions through H-bonding.[86]

[86] A. Kamino, H. Koyano, K. Ariga, T. Kunitake, *Bull. Chem. Soc. Jpn.* **1998**, *69*, 3619−3631.

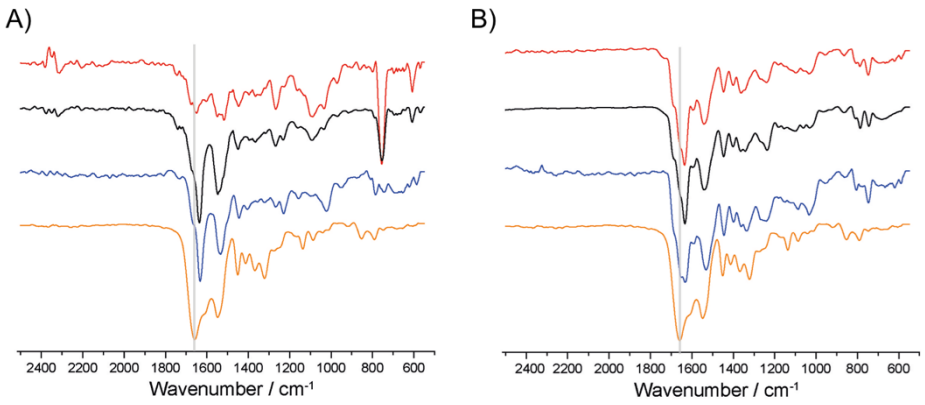

Figure 1. 45. FTIR spectra of **8** (orange) and the *n*/*p*-materials in the carbonyl-stretching area. **8:14** (A) and **8**:**18** (B) in PBS (red), and in citric acid/sodium citrate buffer under thermodynamic (black) and metastable (blue) conditions.

Thermogravimetric analysis (TGA) of the hybrid materials revealed a thermal stabilization due to the considerably stronger new ionic interactions generated through the coassembly process. For comparison, we recorded the analysis of the organic building blocks. The latter showed the typical sharp weight loss profile, attributed to organic molecules, between 300 and 350 ºC. However, the materials showed much broader profiles and an enhancement of the thermal stability was observed (Figure 1. 46).

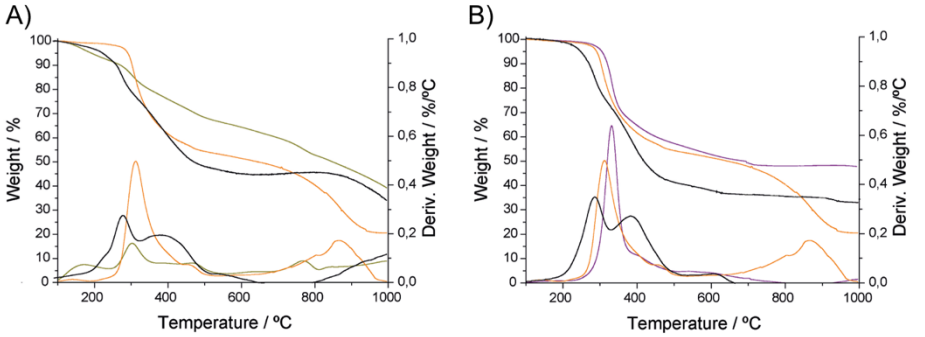

Figure 1. 46. Thermogravimetric analysis of the coassemblies and their corresponding former building blocks showing the weight loss and the first derivative of the TGA curve: **8:14-T** (A) and **8:18-T** (B). Black solid lines correspond to each coassembled material and orange, green and purple lines correspond to molecules **8**, **14** and **18**, respectively.

Finally, it is worthy to highlight the drastic change in morphology in the materials in comparison with the former building blocks. TEM images of the hybrid materials under the three previously described conditions showed, in general, the presence of bundles of fibers, which are especially well-aligned in the case of **8:18-T**. All **8:18**-based materials are comprised of intertwining bundles of fibers, while in the case of **8:14**-based materials clusters of organic material, presumably C_{60} clusters, all around the fibers were observed. As a representative example, TEM images of **8:14-T** and **8:18-T** are shown in Figure 1. 47. Moreover, AFM showed much higher height profiles than for the former building blocks due to the association of the *p*- and *n*-type nanostructures.

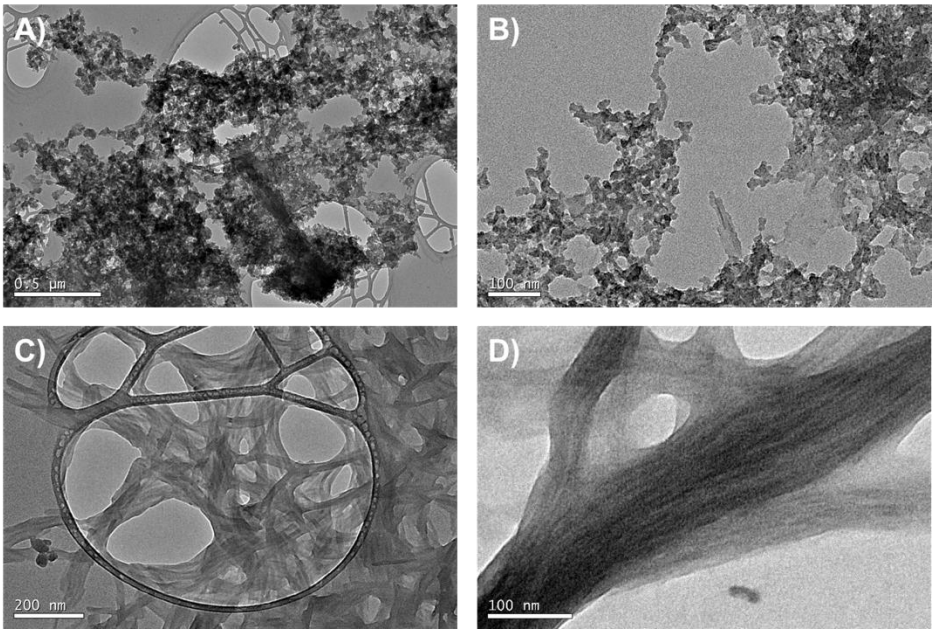

Figure 1. 47. TEM images of **8:14-T** (A, B) and **8:18-T** (C, D) at different magnifications.

1.3.2.8. Photoconductivity properties

We hypothesized that all the aforementioned spectroscopic and morphologic variations must be reflected in the intra-fibril charge transport properties in the segregated donor-acceptor stacks. To address the photoconductivity properties, flash-photolysis time-resolved microwave

conductivity (FP-TRMC) and transient absorption spectroscopy were carried out in the group of Prof. Shu Seki (Kyoto University).

Upon photoexcitation with a 355 nm laser pulse at room temperature, films of these composites on quartz substrates displayed fairly clear photoconductivity transients ($\phi\Sigma\mu$), where ϕ and $\Sigma\mu$ denotes the quantum yield of charge-carrier generation and the sum of the charge-carrier mobilities, respectively. Particularly, **8:14-T** and **8:18-T** structures exhibited the highest values of $\phi\Sigma\mu$ of 3.2×10^{-3} and 1.5×10^{-3} $cm^2V^{-1}s^{-1}$, respectively, suggesting the presence of pathways for highly mobile charge carriers. In contrast, the photoconductivity transients of the pristine solid films (respective components of the coassemblies, that is, **8-PBS**, **8-T**, **14** and **18**) decreased up to two orders of magnitude. Similar values were observed for the coassemblies derived from **8-PBS** arrays, while those arising from **8-M** had intermediate values in the range of 10^{-4} $cm^2V^{-1}s^{-1}$. To evidence the importance of a careful examination and control over the self-assembly process, and consequently, the impact of the pre-assembly step, we ensemble the building blocks skipping this step (Figure 1. 48. A-B, orange lines). For that experiment, the molecularly dissolved building blocks were mixed and let equilibrate prior to measurements, obtaining values of $\phi\Sigma\mu$ in the range of 10^{-5} $cm^2V^{-1}s^{-1}$. Thus, the observed photoconductivity transients in the hybrid materials suggested a strong dependence on the building block pre-assemble process (Table 1. 3).

Table 1. 3. Maximum values of the transients $(\phi\Sigma\mu)_{max}$ for the *n*/*p*-materials and the building blocks separately.

n-/p-material	$\phi\Sigma\mu$ / $cm^2V^{-1}s^{-1}$
8:14-PBS	3.3×10^{-5}
8:18-PBS	1.4×10^{-4}
8:14-T	1.5×10^{-3}
8:18-T	3.2×10^{-3}
8:14-M	3.4×10^{-4}
8:18-M	2.0×10^{-4}

Building blocks	$\phi\Sigma\mu$ / $cm^2V^{-1}s^{-1}$
8-PBS	3.8×10^{-5}
8-T	6.3×10^{-5}
18	1.4×10^{-5}
14	1.2×10^{-5}

The shapes of kinetic traces observed for **8:14** and **8:18** were almost overlapped, exhibiting neither 1st order nor 2nd order. Charge recombination

dynamics in the heterojunction systems were then confirmed by the kinetic traces under the modulation of excitation density, as shown in Figure 1. 48. C. With the attenuation of the excitation density from 10^{16} to 10^{13} cm^{-2} (approximately from 3×10^{18} to 3×10^{15} photons cm^{-3} in average calibrated by steady state absorbance of an **8:18** film), the decay profile was approaching to those of pseudo 1st order manner, suggesting the bulk recombination of photogenerated electrons and holes suppressed enough at the lowest excitation density limit.

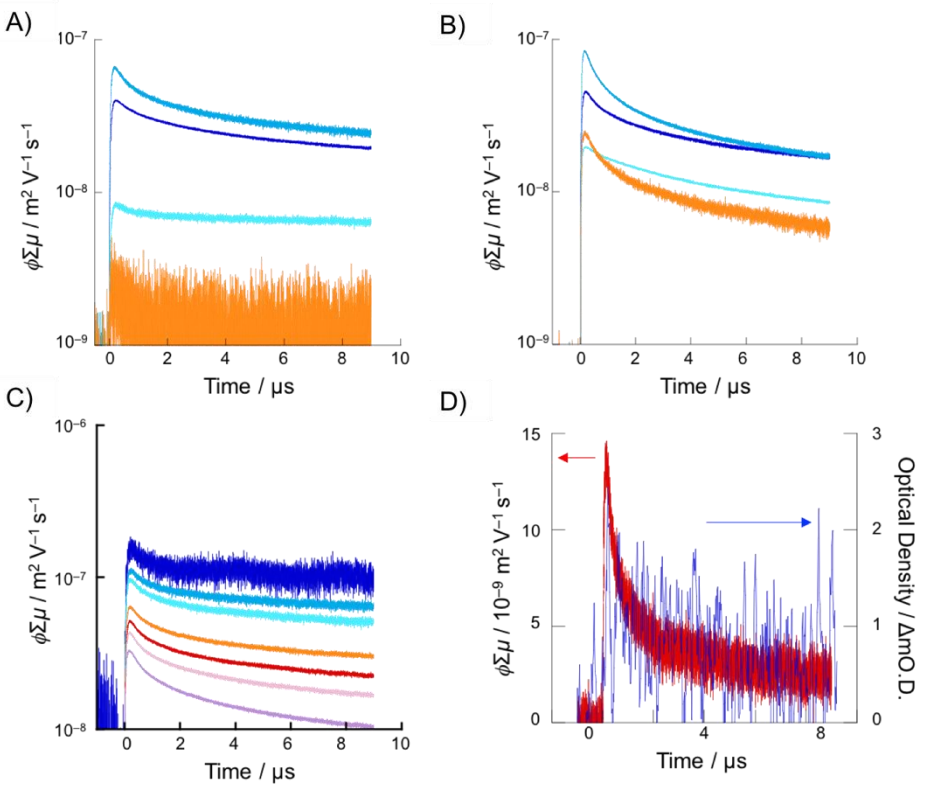

Figure 1. 48. Kinetic traces of photoconductivity transients observed for a film of **8:14** (A) and of **8:18** (B). Kinetic traces for the coassemblies in PBS (blue) , thermodynamic-form (skyblue), metastable-form (turquoise) and skipping the pre-assemble step (orange) were observed upon excitation of 355 nm laser pulses. C) Dependence of decay rate of the conductivity transients on excitation photon density varying from 0.15 (blue), 0.91 (skyblue), 1.8 (turquoise), 4.6 (orange), 6.4 (red), 9.1 (pink), and 18 (purple) × 10^{15} photons cm^{-2}. D) Kinetic traces overlapping between photoconductivity and transient absorption monitored at 710 nm upon excitation at 355 nm, 1.8×10^{16} photons cm^{-2}.

The yield of photogenerated charge carriers was also determined by combination of transient absorption spectroscopy and photoconductivity transients (Figure 1. 48. D). Because of the mismatch between the dynamic range of the spectroscopic techniques, the excitation was carried out at ~10^{16} photons cm^{-2}, where the initial decay kinetics were predominantly governed by the 2nd order bulk recombination of electron and holes. In spite of the initial kinetics, both transients were almost overlapped in the μs range, securing the experimental determination of ϕ with the molar extinction coefficient of PBI anion radicals.[87] The deduced value upon excitation at 1.8×10^{16} photons cm^{-2} was 0.06 % at 4 s after pulse exposure, which leads the intra-fibril mobility of charge carriers as 0.4 $cm^2V^{-1}s^{-1}$. This high value of $\Sigma\mu$ is in the interplaying regime of thermally activated hopping and phonon-scattering band conduction, suggesting relatively shallow trapping depth of the charge carriers in the order of thermal energy at room temperature. The photoconductivity transients were recorded in the dried solid films prepared from corresponding aqueous solutions. It is assumed that there is not residual water as the solvation effects would lead to a much higher stabilization of charge carriers, which is inconsistent with the value of μ eventually estimated. These obtained values are almost equivalent to the mobility values observed in lamellae stacking of oligothiophene chain, suggesting the high electric conductive nature of the present nanofibril systems.

The 2nd order bulk recombination regime also implied much higher yield of photo-generated charge carriers under the lower excitation density, such as an illumination by a steady light source/sun light. Based on the ϕ value, the free charge carrier yield under an excitation of 1.5×10^{14} photons cm^{-2} was given as 0.4 % at 0 s (an averaged value over time constant of the present conductivity measurement system of ~ 50 ns) without any external electrical potential applied.

It is important to remark that the different values of $\phi\Sigma\mu$ obtained are related with a more effective organization in these systems, being better for the thermodynamic aggregates, than metastable and PBS states. Moreover, high mobility values, in good agreement with the results previously reported in our research group, have been observed for both systems, **8:14** and **8:18**. Therefore the efficiency and versatility of this methodology for creating donor-acceptor heterojunction systems has been proved by successfully extending it to different systems with remarkable photoconductivity values.

[87] D. Gosztola, M. P. Niemczyk, W. Svec, A. S. Lukas, M. R. Wasielewski, *J. Phys. Chem. A*, **2000**, *104*, 6545-6551.

1.3.3. Porphyrin-based aqueous-soluble nanostructures with outstanding temperature-responsiveness

In the last section of this chapter, we will expand our previous design and methodology to porphyrins, a very well-known dye. We started our studies with derivative **24** (Figure 1. 49), which showed an anomalous behavior with temperature in aqueous media. Even though self-assembly is normally an entropically-disfavored process and, therefore, occurs upon cooling, in our case we observed the formation of J-aggregates upon increasing the temperature. To understand this behavior, we have additionally synthesized the free base counterpart, **23**, and the tetra-*meso*-substituted analogues, derivatives **29** and **30**, for comparison purposes. Only a few examples of this kind of entropically-driven assemblies are reported to date, the majority of them related to PBIs functionalized with polyethyleneglycol chains as hydrophilic tails.[88] Thus, we aim to explore the self-assembly in aqueous media of these amphiphilic π-systems to unravel the fascinating physicochemical principles that govern their formation.

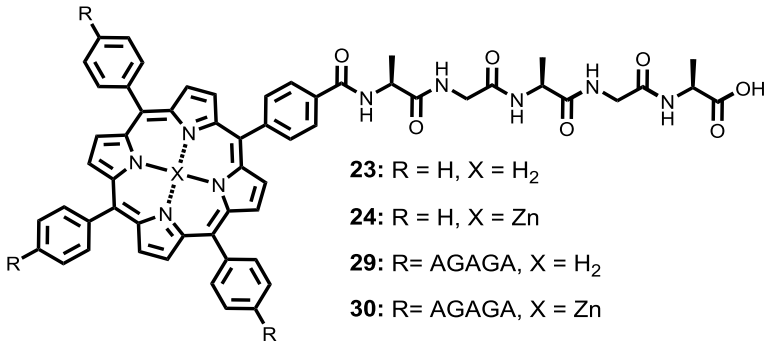

Figure 1. 49. Molecular structure of porphyrin derivatives **23**, **24**, **29** and **30**.

[88] a) V. Grande, B. Soberats, S. Herbst, V. Stepanenko, F. Würthner, *Chem. Sci.* **2018**, *9*, 6904-6911; b) D. Görl, F. Würthner, *Angew. Chem. Int. Ed.* **2016**, *55*, 12094-12098; c) D. Görl, B. Soberats, S. Herbst, V. Stepanenko, F. Würthner, *Chem. Sci.* **2016**, *7*, 6786-6790; d) D. Görl, X. Zhang, V. Stepanenko, F. Würthner, *Nat. Commun.* **2015**, *6*, 7009-7017; e) X. Zhang, D. Görl, V. Stepanenko, F. Würthner, *Angew. Chem. Int. Ed.* **2014**, *53*, 1270-1274.

1.3.3.1. Porphyrins: properties and supramolecular chemistry

Porphyrins are known as the pigments of life for their key roles in natural systems such as photosynthetic apparatus,[89] heme proteins,[90] and cytochrome family (Figure 1. 50).[91] The unique physicochemical and structural features of these systems grant them a great potential for many applications as sensing, catalysis and photovoltaics.[92,93]

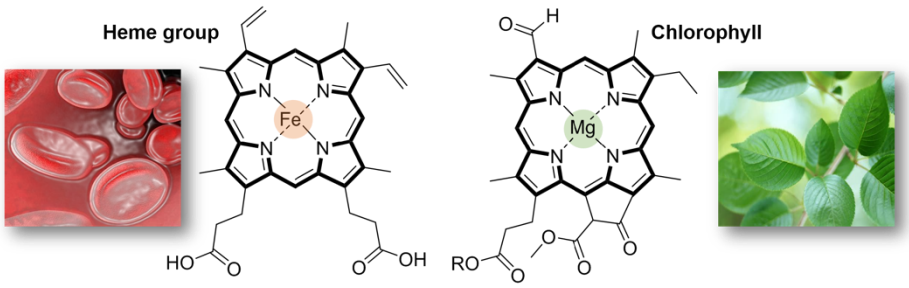

Figure 1. 50. Pigments of life: heme group, responsible of binding oxygen in hemoglobin (left), and chlorophyll, vital in the photosynthesis (right). The fully conjugated tetrapyrrolic macrocycle, that is, the porphyrin core, is highlighted in bold.

Porphyrin dyes are a family of organic macrocyclic compounds composed of four pyrrole subunits interconnected at their α carbon atoms via methine bridges. They are considered as really versatile building blocks due to the possibility of their straightforward skeleton functionalization and coordination in the core to a wide variety of ions. Moreover, synthesis and

[89] J. Deisenhofer, H. Michel, *Angew. Chem. Int. Ed.* **1989,** *28*, 829-847.
[90] a) J. C. Kendrew, G. Bodo, H. M. Dintzis, R. G. Parrish, H. W. Wychoff, D. C. Phillips, *Nature* **1958**, *181*, 662-666 ; b) M. F. Perut, M. G. Rossmann, A. F. Cullis, H. Muirhead, A. C. T. North, *Nature* **1960**, 185, 416-420.
[91] T. L. Poulos, B. C. Finzel, A. J. Howard, *Biochemistry* **1986**, *25*, 5314-5322.
[92] a) T. S. Balaban, *Acc. Chem. Res.* **2005**, *38*, 612-623; b) M. R. Wasielewski, *Acc. Chem. Res.* **2009**, *42*, 1910-1921; c) M. J. Mayoral Muñoz, G. Fernández, *Chem. Sci.* **2012**, *3*, 1395-1398.
[93] a) J. A. A. W. Elemans, R. van Hameren, R. J. M. Nolte, A. E. Rowan, *Adv. Mater.* **2006**, *18*, 1251-1266; b) C. M. Drain, A. Varotto, I. Radivojevic, *Chem. Rev.* **2009**, *109*, 1630-1658; c) C. J. Medforth, Z. Wang, K. E. Martin, Y. Song, J. L. Jacobsen, J. A. Shelnutt, *Chem. Commun.* **2009**, 7261-7277; d) A. Yella, H.-W. Lee, H. N. Tsao, C. Yi, A. K. Chandiran, M. Nazeeruddin, E. W.-G. Diau, C.-Y. Yeh, S. M. Zakeeruddin, M. Grätzel, *Science* **2011**, *334*, 629-634.

functionalization protocols are very well stablished in literature.[94]

These chromophores strongly absorb in the visible-light range, have accessible oxidation and reduction potentials and hold fast energy and/or electron-transfer donor abilities. For these properties, their use as photosensitizers to harvest light for the conversion of solar energy has been widely exploited for the construction of solar cells, mimicking chlorophyll in natural photosynthesis.[95]

The aforementioned outstanding properties of porphyrins make them fascinating π-systems for the construction of supramolecular materials, a fast evolving field that has led to a wide variety of multifunctional assemblies.[96] Aida and col. reported a set of tetra-*meso*-substituted porphyrins and related the molecular strcuture with the pathway complexity in the self-assembly. The assemblies consisted of different porphyrin stacking modes, J-, H- and short-slipping J-aggregates, with different dimensionalities, namely, 0D nanoparticle, 1D nanofibre and 2D nanosheet, respectively.[97] As it is shown in Figure 1. 51. A, subtle changes in the molecular structure, as changing a pentyl- for an hexyl-chain (compounds **5** and **6**, respectively), resulted in a drastic switch in the self-assembly pathway. As a result, the spectroscopic properties and the morphology of the ensembles were greatly influenced. Moreover, the obtained nanostructures showed different electronic properties, which evidences the pathway-dependent material properties.

[94] a) K. M. Smith, *Strategies for the synthesis of octaalkylporphyrin systems*. In: K. M. Smith, *The Porphyrin Handbook*. Vol. 1. Academic Press; Boston: **1999**. p. 1-43; b) N. Aratani, D. Kim, A. Osuka, *Acc. Chem. Res.* **2009**, *42*, 1922-1934; c) I. Beletskaya, V. S. Tyurin, A. Y. Tsivadze, R. Guilard, C. Stern, *Chem. Rev.* **2009**, *109*, 1659-1713; d) W.-S. Li, T. Aida, *Chem. Rev.* **2009**, *109*, 6047-6076; e) J. P. Lewtaka, D. T. Gryko, *Chem. Commun.* **2012**, *48*, 10069-10086; f) C. M. B. Carvalho, T. J. Brocksom, K. T. de Oliveira, *Chem. Soc. Rev.* **2013**, *42*, 3302-3317.

[95] a) T. Hasobe, *J. Phys. Chem. Lett.* **2013**, *4*, 1771-1780; b) M. R. Wasielewski, *Acc. Chem. Res.* **2009**, *42*, 1910-1921.

[96] a) S. S. Babu, D. Bonifazi, *ChemPlusChem* **2014**, *79*, 895-906; b) L. Li, E. W. Diau, *Chem. Soc. Rev.* **2013**, *42*, 291-304.

[97] T. Fukui, S. Kawai, S. Fujinuma, Y. Matsushita, T. Yasuda, T. Sakurai, S. Seki, M. Takeuchi, K. Sugiyasu, *Nat. Chem.* **2016**, *9*, 493-500.

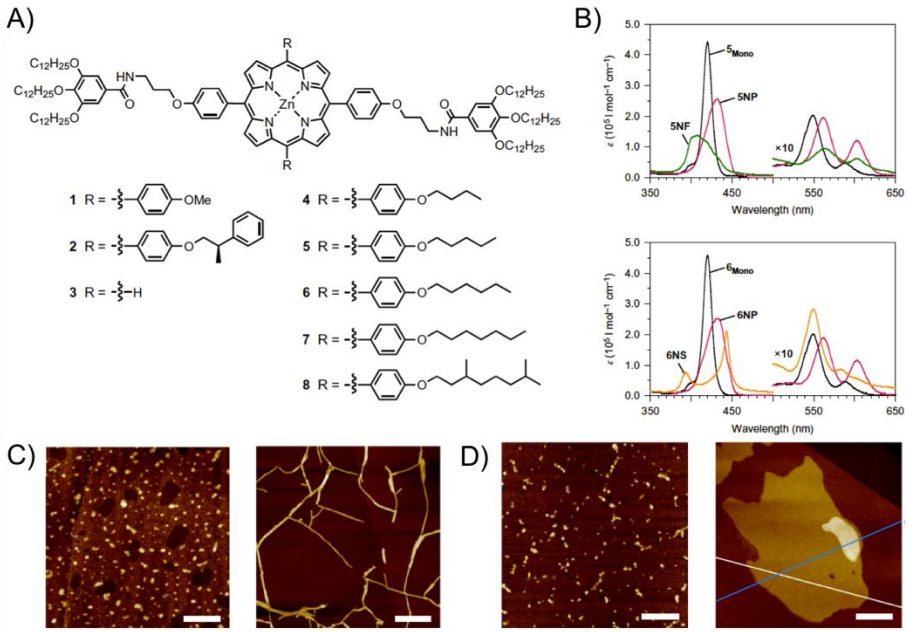

Figure 1. 51. A) Molecular building blocks. B) Absorption spectra of derivatives **5** and **6** as molecularly dissolved species, H-aggregates (**5NP** and **6NP**) and J-aggregates (**5NF** and **6NS**). C) Morphology of **5**-based assemblies (**5NP**, left; **5NF**, right). D) Morphology of **6**-based assemblies (**6NP**, left; **6NS**, right).

1.3.3.2. Synthesis of the porphyrin-based building blocks

For the synthesis of both, the mono- and the tetra-substituted derivatives, we employed the standard Rothemund-Lindsey protocol involving the condensation and oxidation of pyrrol and the desired aldehydes for the synthesis of the macrocyclic core.[98]

For the synthesis of derivatives **23** and **24**, we started creating the porphyrin core by reacting a mixture of methyl 4-formylbenzoate, benzaldehyde and pyrrol under acidic conditions and further oxidation by refluxing the mixture

[98] a) P. Rothemund, *J. Am. Chem. Soc.* **1935**, *57*, 2010-2011; b) J. S. Lindsey, I. C. Hsu, I. C. Schreiman, *Tetrahedron Lett.* **1986**, *27*, 4969-4970.

in the presence of tetrachloro-1,4-benzoquinone. After purification, free-base porphyrin **19** was obtained. Zn-metalloporphyrin **20** was easily obtained by reaction of **19** with zinc acetate. These species, **19** and **20**, were hydrolyzed to the corresponding carboxylic acid derivatives **21** and **22** by refluxing in the presence of KOH. Finally, the amidation step was carried out by activation of the carboxylic acid moieties with HATU and further coupling of the pentapeptide (Scheme 1. 8).

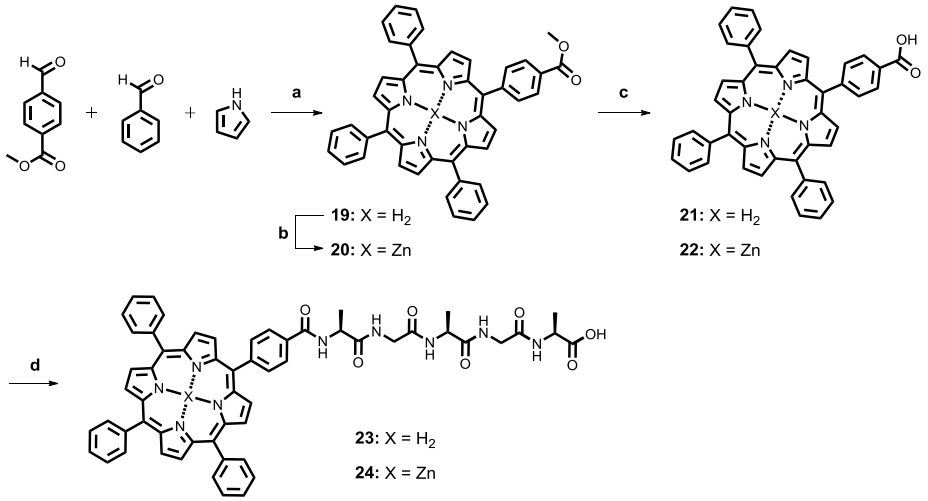

Scheme 1. 8. Synthetic route to yield the mono-substituted free base porphyrin ,**23**, and Zn metalloporphyrin, **24**. a) i) $BF_3 \bullet Et_2O$, rt; ii) tetrachloro-1,4-benzoquinone, reflux; $CHCl_3$, 16%; b) $Zn(OAc)_2$, $CHCl_3$/MeOH, rt, 74%; c) KOH, THF/H_2O, reflux, quant. (**21** and **22**); d) i) HATU, TEA, DMF, rt; ii) AGAGA, Na_2CO_3, THF/1,4-Dioxane/H_2O (1:1:1), rt, 63% (**23**), 86% (**24**).

Tetra-*meso*-substituted derivatives **29** and **30** were synthesized using a similar procedure. The first step in this case, consisted in the condensation of methyl 4-formylbenzoate and pyrrol under reflux in propionic acid. The following steps were carried out in the same conditions as described for their mono-substituted counterparts, just adjusting the number of equivalents. The final products **29** and **30** were obtained in moderate yields (Scheme 1. 9).

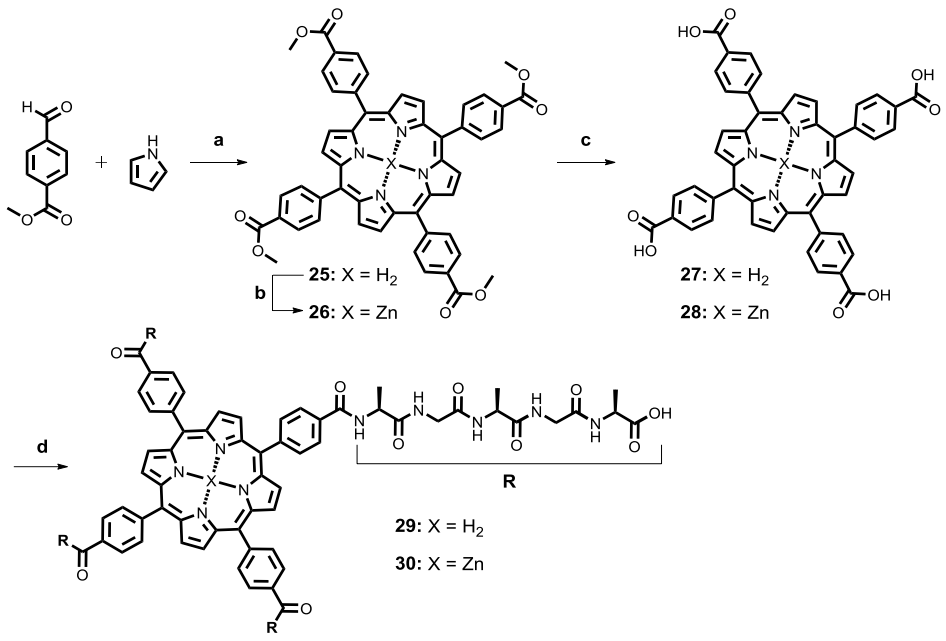

Scheme 1. 9. Synthetic route to yield the tetra-substituted free base porphyrin **29** and Zn metalloporphyrin **30**. a) CH_3CH_2COOH, 150 ºC, 23%; b) $Zn(OAc)_2$, $CHCl_3$/MeOH, rt, 83%; c) KOH, THF/H_2O, reflux, 97% (**27**), 96% (**28**); d) i) HATU, TEA, DMF, rt; ii) AGAGA, Na_2CO_3, THF/1,4-Dioxane/H_2O (1:1:1), rt, 75% (**29**), 78% (**30**).

*1.3.3.3. Self-assembly of derivative **24** in solution*

We started investigating the self-assembling properties of the Zn-metalloporphyrin, **24**, by UV/Vis and CD spectroscopy at room temperature. This species was not soluble in water, so we used this solvent as "bad solvent" and an alcohol as "good solvent", namely ethanol, to be able to reach high temperatures. A solution of **24** in EtOH at room temperature, showed a sharp absorption spectrum, with the Soret band at 428 nm and the Q bands at 568 and 625 nm (Figure 1. 52. A). Furthermore, the absence of CD signal in Figure 1. 52. B confirmed the presence of the molecularly dissolved species. However, a solution of **24** in a water/ethanol mixture (95:5, v:v) showed a wider absorption Soret band ca. 5 nm blue-shifted. The Q bands were also slightly blue shifted (Figure 1. 52. A). Moreover, the CD spectrum showed a bisignate Cotton effect in the porphyrin Soret band region, with a positive Cotton at 442 nm and negative Cotton at 421 nm (Figure 1. 52. B). All the latter features pointed out to the presence of H-like aggregates with right handedness, from now on referred as **24_H**.

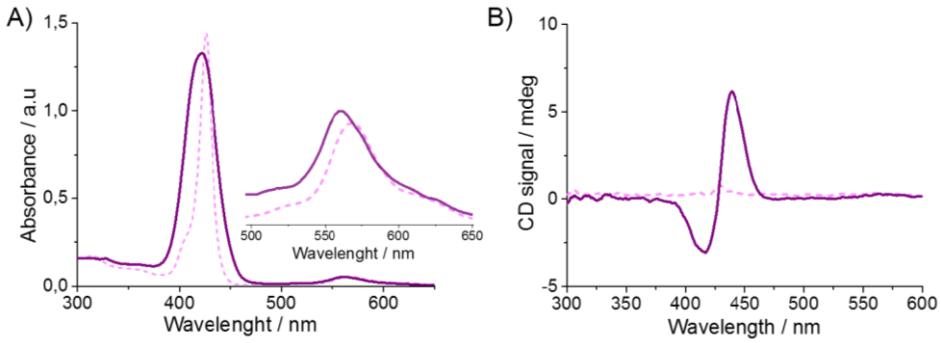

Figure 1. 52. UV/Vis (A) and CD (B) spectra of the molecularly dissolved species, **24**, in EtOH (pink dashed line) and freshly prepared **24_H** (purple solid line) in a H_2O/EtOH mixture (95:5, v:v). The inset in (A) is a magnification of the Q-bands absorption region. In all cases, c = 100 μM.

The latter solution of **24_H** was then quickly heated up to depolymerized the aggregate, but, on the contrary, we observed a different behavior. The spectrum showed a hypochromic and slightly red-shifted absorption maximum at 436 nm and a new band at 374 nm (Figure 1. 53. A). On the basis of Kasha's theory,[25] a red-shift in the main absorption band upon aggregation indicates the

formation of J-aggregates with a head-to-tail molecular stacking. However, observation of a shoulder Soret peak has been related in the literature to the formation of J-aggregates with a shorter slipping distance with an intimate intermolecular packing within porphyrin chromophores.[99] Moreover, the CD signal of this new assembly (Figure 1. 53. B), from now on referred as **24$_J$**, was much more intense when compared to **24$_H$**.

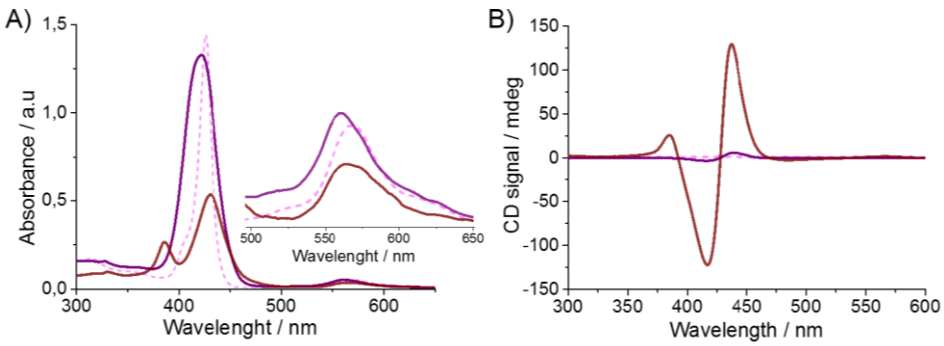

Figure 1. 53. UV/Vis (A) and CD (B) spectra of the molecularly dissolved species, **24**, in EtOH (pink dashed line) and H_2O/EtOH (95:5, v:v) freshly prepared, **24$_H$** (purple solid line) and upon very fast heating to 90 ºC, **24$_J$** (red solid line). The inset in (A) is a magnification of the Q-bands absorption region. In all cases, c = 100 μM.

To get insights about this atypical behavior, we performed the heating treatment in a more controlled manner by gradually heating a freshly prepared solution of **24$_H$**. Any spectroscopical changes were observed below 80 ºC, so we performed the experiment from 75 to 95 ºC with a heating rate of 1 ºC/min. A very pronounced change took place between 80 and 85 ºC, which can be clearly seen in Figure 1. 54. In the UV/Vis spectroscopy, the Soret band initially showed the characteristic absorption features of the **24$_H$** species, that is, a broad band with λ_{max} = 422 nm (T ≤ 80 ºC). However, a drastic change was observed at 85 ºC, with the appearance of new bands and shoulders between 370 and 400 nm and a new red-shifted band at 441 nm (Figure 1. 54. A). The multiple peaks that could be observed suggested the coexistence of different aggregates in the solution. Very complicated and intense CD signals were obtained as well, as depicted in Figure 1. 54. D. These spectroscopic features were stable once the

[99] S. Okada, H. Segawa, *J. Am. Chem. Soc.* **2003**, *125*, 2792-2796.

solution was cooled down to room temperature, with no recovery of the initial **24$_H$** assembly.

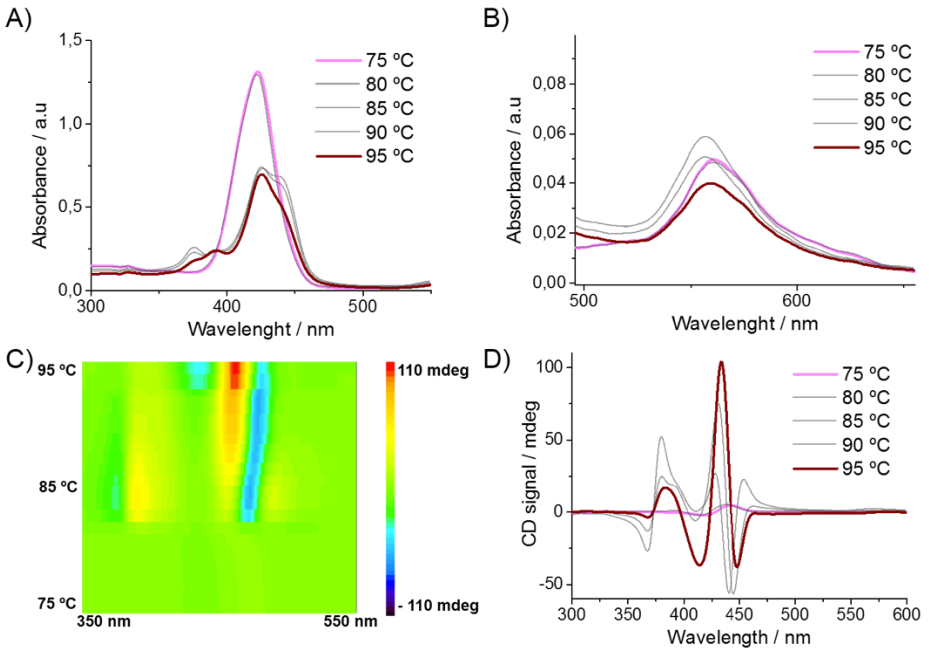

Figure 1. 54. Temperature-dependent UV/Vis studies in the Soret (A) and Q bands (B) regions and CD (C and D) from 75 to 95 ºC. H_2O/EtOH (95:5, v:v), *c* = 100 μM.

To try to avoid the formation of a mixture of aggregates, we monitored the evolution of the absorption and the CD signal at 80 ºC, which appeared to be the critical temperature for the formation of these new aggregates from our previous investigations. In this experiment, one spectrum was recorded every 5 minutes and the most representative ones are depicted in Figure 1. 55. After 15 minutes at 80 ºC, the spectroscopic features corresponding to **24$_H$** quickly and drastically changed, giving rise to the appearance of a new J aggregate with two sharp absorption bands at 375 and 440 nm. After 30 minutes, the process reached the equilibrium and the absorbance and CD signal remained stable, even upon cooling down the solution to room temperature.

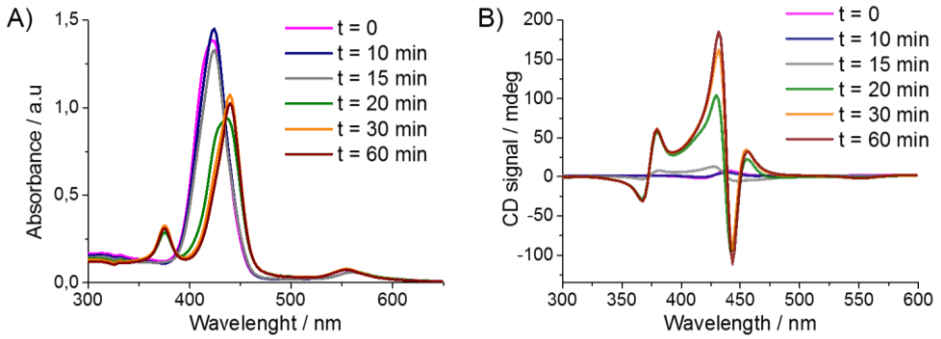

Figure 1. 55. UV/Vis (A) and CD (B) spectra showing the interconversion from $\mathbf{24_H}$ to $\mathbf{24_J}$. Monitorization was performed at 80 ºC starting from a freshly prepared solution of $\mathbf{24_H}$ (H_2O/EtOH (95:5, v:v), *c* = 100 μM).

Moreover, we analyzed the CD signal in the peptide region to evaluate its secondary structure. An equilibrated solution of $\mathbf{24_H}$ did not gave any sign of well-ordered conformation. However, the solution of $\mathbf{24_J}$, prepared by equilibration at 80 ºC over one hour, did showed the characteristic Cotton effect of a β-sheet conformation, with a negative Cotton with a minimum located at 230 nm as depicted in Figure 1. 56.

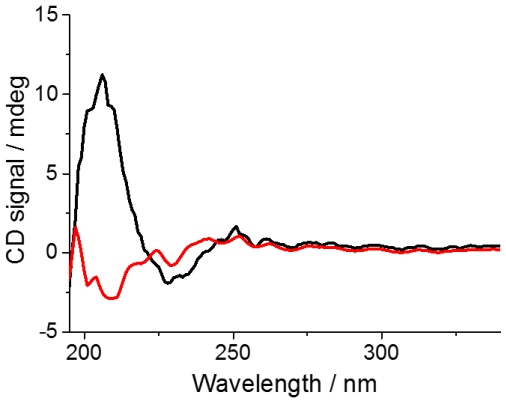

Figure 1. 56. CD spectra in the peptide region of $\mathbf{24_H}$ (red line) and $\mathbf{24_J}$ (black line). H_2O/EtOH (95:5, v:v), *c* = 100 μM

To confirm the secondary structure adopted by the peptide backbone, we decided to analyze the amide stretching vibration modes by FTIR spectroscopy. The molecularly dissolved sample of **24** in EtOH featured bands for the amide I

and amide II at 1658 and 1550 cm^{-1}, respectively. These bands can be assigned to a random coil conformation of the peptide. However, a sample in a D_2O/EtOH mixture equilibrated at 80 ºC, showed a much more complex IR spectrum. We could assign the bands at 1641 and 1565 cm^{-1} to the amide I and amide II stretching modes in a β-sheet conformation.[100] Moreover, it was also striking the appearance of new bands in this aggregate and we expect to properly assign them by comparison with the calculated vibrational spectra.

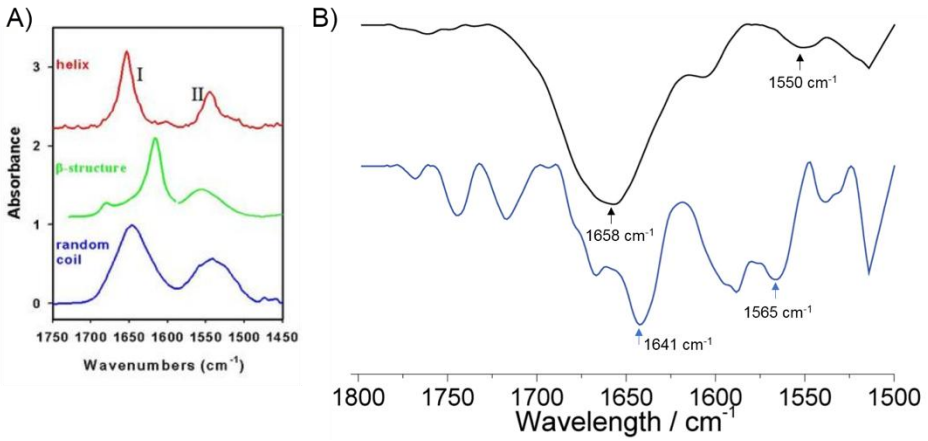

Figure 1. 57. A) Typical IR absorption bands corresponding to the amide I and amide II stretching vibrational modes of representative peptide secondary structures. B) FTIR spectra (transmittance) of **24** in EtOH (black line) and D_2O/EtOH after equilibration at 80 ºC (blue line), highlighting with arrows the the amide I and amide II bands.

These spectroscopic changes were investigated by AFM, which in fact, afforded very interesting morphological changes. A solution of $\mathbf{24_H}$ was deposited onto mica substrate and small aggregates of undefined shape were imaged (Figure 1. 58. A). The solution that was slowly heated up to 95 ºC (1 ºC/min) showed a mixture of nanostructures. On one hand, well defined fiber-like structures with heights of ca. 2 nm were observed, but on the other hand, also sheets and plaques of different sizes appeared (Figure 1. 58. B-C). A totally different morphology was then observed for the sample that was equilibrated at

[100] a) A. Barth, C. Zscherp, *Q. Rev. Biophys.* **2002**, *35*, 369-430; b) Y. Cordeiro, J. Kraineva, M. P. B. Gomes, M. H. Lopes, V. R. Martins, L. M. T. R. Lima, D. Foguel, R. Winter, J. L. Silva, *Biophys. J.* **2005**, *89*, 2667-2676; c) H. Shao, J. R. Parquette, *Chem. Commun.* **2010**, *46*, 4285-4287.

80 ºC for 1 hour. The latter showed closely-packed bundles of needle-like nanostructures (Figure 1. 58. D-F). This congested packing was much clearly seen in the AFM lithography, in Figure 1. 58. E. These results pointed out that after equilibration at 80 ºC a phase separation between the π-stacks and the water takes place in the system, leading to the collapse and bundling of the stacks, as described elswhere.[88]

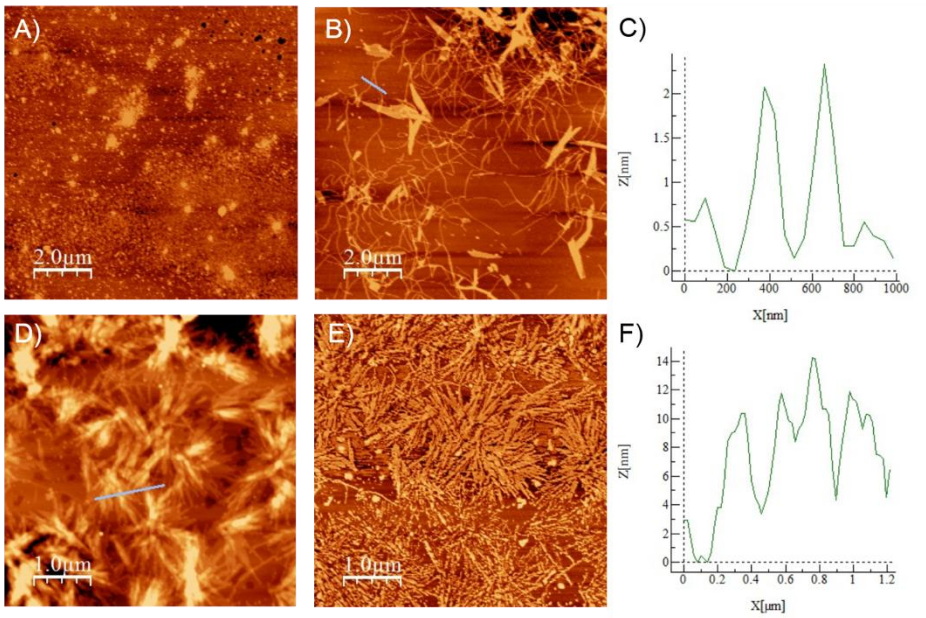

Figure 1. 58. AFM images of drop-casted solutions of **24** (H_2O/EtOH (95:5, v:v), c = 100 μM) under different heating treatments. A) $\mathbf{24_H}$, that is, any heating treatment applied. B) From 75 to 95 ºC at a heating rate of 1 ºC/min. C) Height profile corresponding to the blue line in image (B). D) Equilibrated at 80 ºC for 1 hour. E) Lithography of the same image in D, included for clarity. F) Height profile corresponding to the blue line in image (D).

Temperature-dependent spectroscopic studies were also carried out at different concentrations, namely between 50 and 5 μM (not investigated below that concentration). Even though a similar response to high temperature was observed, below c = 20 μM these experiments led to less complex spectra as observed in Figure 1. 59. It was not clear in this case the formation of the same J-aggregates, as the UV/Vis spectra did not showed a significant shift of the Soret band nor the appearance of the new band around 375 nm, although, a shoulder

peak did appear around 380 nm. The CD signature showed a trisignate profile with enhanced intensity over equilibration time.

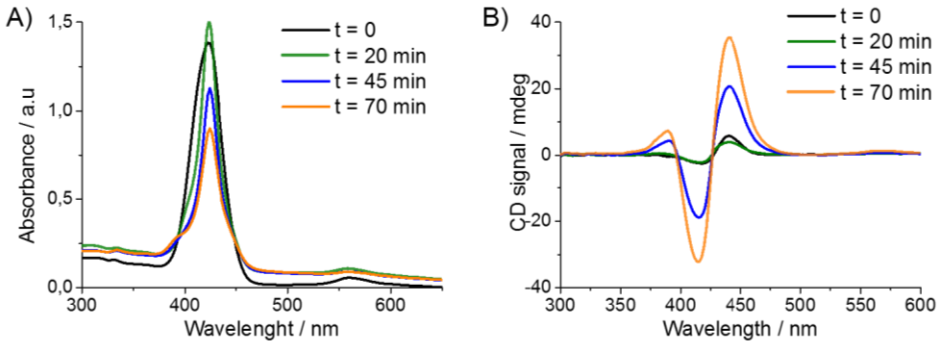

Figure 1. 59. UV/Vis (A) and CD (B) spectra showing the interconversion from $\mathbf{24_H}$ to $\mathbf{24_J}$ in diluted conditions (*c* = 10 μM). Monitorization was performed at 80 ºC starting from a freshly prepared solution of $\mathbf{24_H}$ (H_2O/EtOH, 95:5, v:v)

Surprisingly, the morphology of the aggregates was strongly affected by dilution. Between 100 and 20 μM the same needle-like bundles were found, but below that concentrations we found a new scenario. As a representative example, Figure 1. 60 shows the AFM images of a solution with a sample concentration of 10 μM. In this case, the same amorphous aggregates and molecular islands were found for the freshly prepared solution, while equilibrating at 80 ºC led to very homogeneous samples with the formation of vesicles or micelle-like structures with heights ranging from 10 to 20 nm.

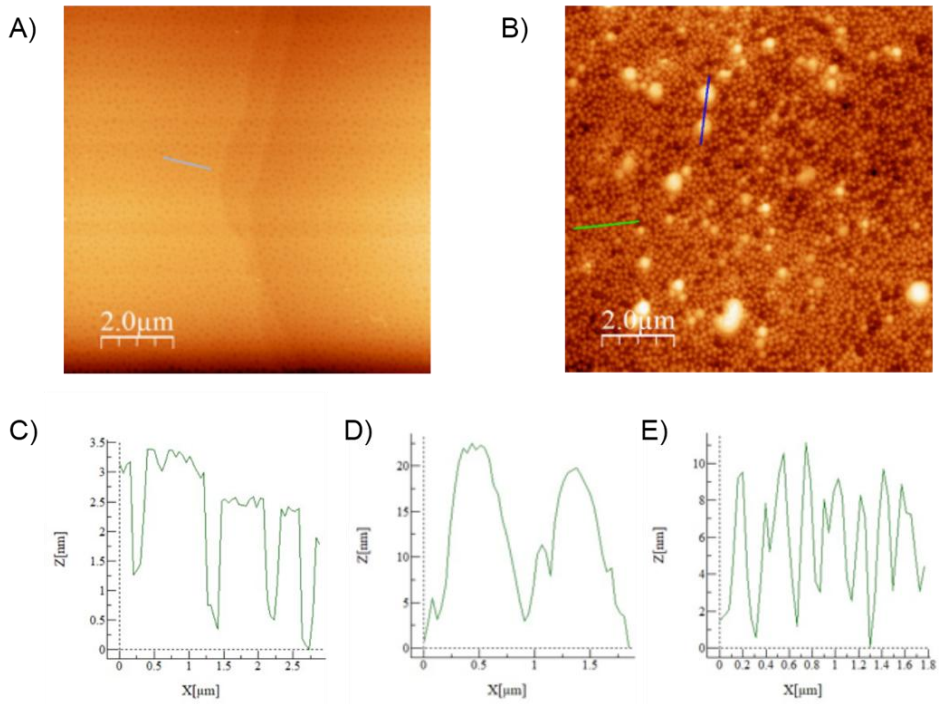

Figure 1. 60. AFM images of drop-casted solutions of **24** (c = 10 μM) under different heating treatments. A) $\mathbf{24_H}$, that is, any heating treatment applied. B) $\mathbf{24_J}$ above critical temperature. C) Height profile corresponding to the blue line in image (A). D) Height profile corresponding to the blue line in image (B). E) Height profile corresponding to the green line in image (B).

*1.3.3.4. Characterization of derivative **23***

After these results, we continued studying the free-base counterpart, porphyrin **23**, by UV/Vis and CD spectroscopies. This species had a similar solubility than derivative **24**, so we decided to use the same water/ethanol mixtures. A solution of **23** in EtOH at rt showed a sharp absorbance, with the Soret band at 416 nm and Q bands at 512, 525, 555 and 573 nm. The presence of the monomeric species was also confirmed with the absence of CD signal. However, a solution of **23** (c = 100 µM) in a water/ethanol mixture (95:5, v:v) showed a hypochromic and blue-shifted Soret band. The Q bands, on the other hand, were slightly red shifted (Figure 1. 61. A). The corresponding CD spectrum showed a negative Cotton effect in the porphyrin Soret band region, with a negative Cotton at 442 nm and positive Cotton at 421 nm (Figure 1. 61.

B). These features pointed out again to the presence of H-like structures, from now on referred as **23$_H$**. The latter solution was then heated up, and the spectrum showed a significant red-shifted absorption, with a maximum at 436 nm and a shoulder blue-shifted up to 350 nm (Figure 1. 61. A). Thus, a new J-aggregate appeared upon heating, namely **23$_J$**. The chiroptical properties of this new assembly were much enhanced if we compared to **23$_H$**, but preserving the same left-handed CD profile (Figure 1. 61. B). Curiously, this derivative did not show the characteristic Cotton effect related to a β-sheet secondary structure, that was previously seen for its **24$_J$** counterpart.

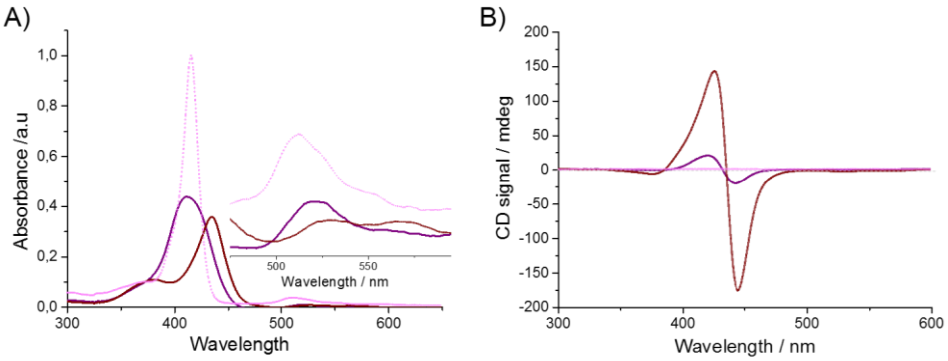

Figure 1. 61. UV/Vis (A) and CD (B) spectra of the molecularly dissolved species, **23**, in EtOH (pink dashed line) and the two different obtained aggregates (H_2O/EtOH, 95:5, v:v), freshly prepared **23$_H$** (purple solid line) and, upon heating, **23$_J$** (red solid line). The inset in (A) is a magnification of the Q-bands absorption region. In all cases, *c* = 100 μM.

After these results, we proceeded to heat a freshly prepared solution of **23$_H$** with a slow heating rate (1 ºC/min). We observed that the critical temperature for the H- to J-aggregate conversion stood around 40 ºC and was completed at 60 ºC (Figure 1. 62). Above this temperature, both the absorption and the CD signal, started to decrease as a result of the partial precipitation of the material, which was even more pronounced when cooling back to room temperature. Thus, the initially observed spectroscopic features were not recovered (Figure 1. 62. D).

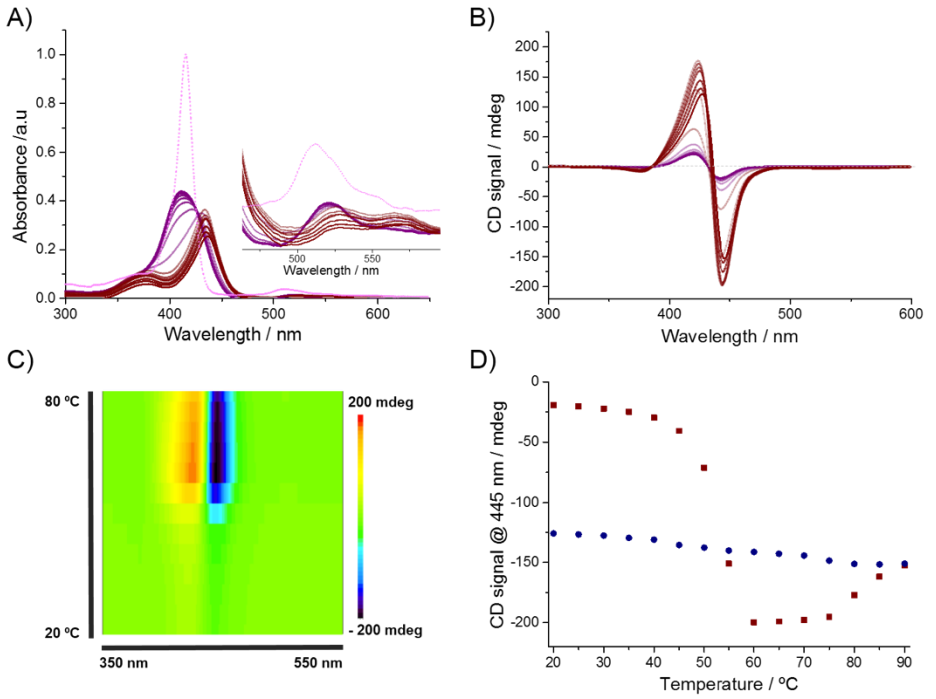

Figure 1. 62. Temperature-dependent UV/Vis (A) and CD (B) spectra showing the disappearance of $\mathbf{23_H}$ and appearance of $\mathbf{23_J}$. C) 2D CD experiment in (B). D) Evolution of the CD signal at 445 nm extracted from the heating (shown in B; red points) and cooling cycle (not shown; blue points). The inset in (A) is a magnification of the Q-bands absorption region. In all cases, *c* = 100 μM (H_2O/EtOH, 95:5, v:v).

Next, we study the morphology of the latter aggregates by AFM (Figure 1. 63). We assigned $\mathbf{23_H}$ to nanoparticles of different sizes and heights of ca. 2 nm, while $\mathbf{23_J}$ showed bigger and higher arrays, although showing an undefined shape.

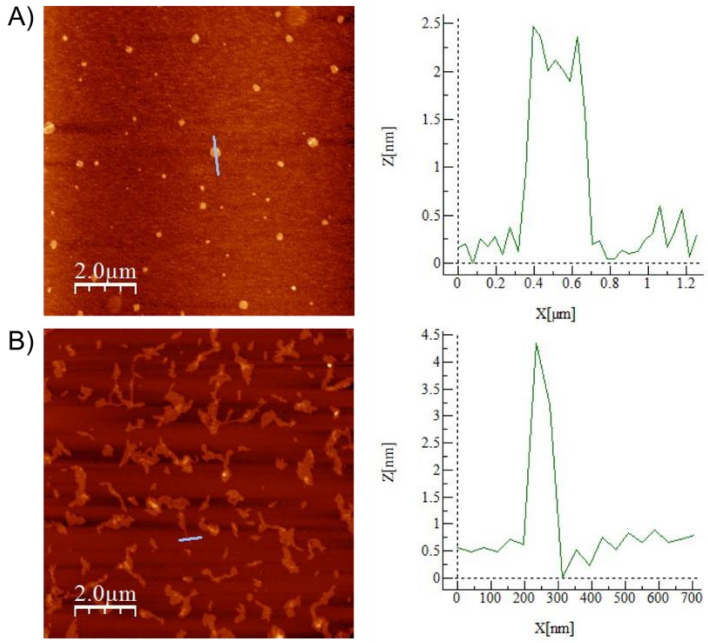

Figure 1. 63. A) AFM image of a drop-casted solution of $\mathbf{23_H}$ and its aqueous solution and height profile beneath the blue line. B) AFM image of a drop-casted solution of $\mathbf{23_J}$ and its aqueous solution and height profile beneath the blue line. c = 100 µM (H_2O/EtOH, 95:5, v:v).

1.3.3.5. Concluding remarks and outlook

Taking all the experimental findings together, we hypothesized that the H-like aggregates observed at room temperature are originated from loosely packed porphyrin species, similar to related water-soluble PBI derivatives described in the literature.[88] Accordingly, the observed temperature response is likely to be a transformation of a loosely packed aggregate into a well-structured J-aggregate, which over time, leads to a solvophobic collapse of the nanostructures and partial precipitation of the sample (Figure 1. 64). This process would involve the rearrangement of the chromophores, that is, with the consequence of rather big kinetic barriers. This hypothesis would be in good agreement with the high temperatures needed and the irreversibility of the process observed. Similar transitions between kinetically favored aggregates

with nanoparticle morphology and thermodynamically favored aggregates with fibrous morphology have been recently reported.[101, 102]

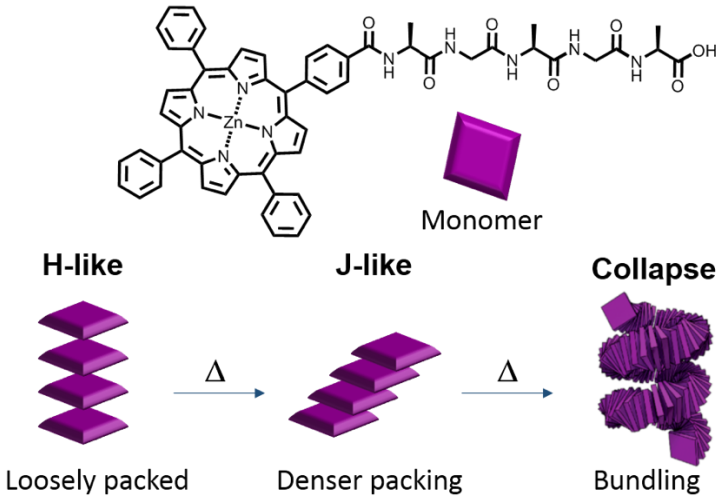

Figure 1. 64. Schematic representation of the possible aggregation patterns from experimental findings for derivative **24**.

However, more experiments would be necessary to shed light on the different behaviors that we have observed for derivative **24** and its free-base counterpart, **23**. Similarly, we will study the temperature-dependent spectroscopical features of derivatives **29** and **30** to get further insights. Understanding the self-assembly process and energy landscape of the latter porphyrin-based supramolecular species would be of paramount importance for these systems to be used as functional materials.

[101] S. Ogi, V. Stepanenko, J. Thein, F. Würthner, *J. Am. Chem. Soc.* **2016**, *138*, 670-678.
[102] S. Ogi, C. Grzeszkiewicz, F. Würthner, *Chem. Sci.* **2018**, *9*, 2768-2773.

1.4. Experimental section

1.4. Experimental section

1.4.1. Synthesis

Reagents were purchased from Sigma-Aldrich, Acros or Fluka and were used without further purification. Peptides were purchased from ChinaPeptides.Co.,Ltd as trifluoroacetate salts and used without further purification. All solvents were dried using a solvent purification system or by means of standard protocols. Column chromatography was carried out on silica gel 60 (Fluka, 40-63 μm). Reverse phase chromatography was carried out on an Agilent flash chromatography system with pre-packed flash chromatography columns (TELOS, Flash C18 12g). IR spectra were recorded on a Bruker Tensor 27 spectrometer equipped with ATR and reported as wavenumbers in cm^{-1} with band intensities indicated as s (strong), m (medium), w (weak), br (broad). ^{1}H and ^{13}C NMR spectra were recorded either on a Bruker Avance-300 or a Bruker Avance AMX-700 and reported as chemical shifts (δ) in ppm relative to tetramethylsilane (δ = 0 ppm) at room temperature unless other temperature was indicated. Spin multiplicities are reported as a singlet (s), broad singlet (br s), doublet (d), triplet (t) and quartet (q) with proton-proton coupling constants (*J*) given in Hz, or multiplet (m). Matrix-assisted laser desorption ionization (MALDI) mass spectrometry (MS) was performed on a Bruker Ultraflex spectrometer.

*1.4.1.1. Synthesis of exTTF precursor **6***

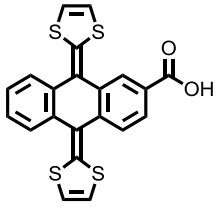

9,10-Di(1,3-dithiol-2-ylidene)-9,10-dihydroanthracene-2-carboxylic acid. This product was synthesized according to reported procedures[103] and its structure corroborated by ^{1}H NMR. To a solution of 1,3-dithiol-2-ylphosphonate (2 g, 9.43 mmol) in anhydrous THF (50 mL) at -78ºC, *n*-BuLi (1.6 M in n-

[103] J. L. López, C. Atienza, A. Insuasty, J. López-Andarias, C. Romero-Nieto, D. M. Guldi, N. Martín, *Angew. Chem. Int. Ed.* **2012**, *51*, 3857-3861

hexanes, 8 mL, 12.8 mmol) was added dropdwise. The mixture was stirred at this temperature over 30 min. Afterwards a suspension of anthraquinone-2-carboxylic acid (400 mg, 1.59 mmol) in anhydrous THF (20 mL) was added. The mixture was allowed to warm up and stirred 4 hours at room temperature. Solvent was removed under reduced pressure. The resultant oil crude was neutralized by addition of a solution of HCl 0.1 M and the mixture was extracted with CH_2Cl_2. The organic layer was dried over $MgSO_4$. The organic layers were combined and concentrated under low pressure. The dried crude was purified by silica gel column chromatography using CH_2Cl_2/CH_3OH (30:1, v:v) as eluent to give the pure product a an orange solid (351 mg , 53%). ^{1}H-NMR (300 MHz, DMSO-d_6): 8.24 (d, J = 1.71 Hz, 1 H), 7.90 (dd, J = 7.80, 1.71 Hz, 1 H), 7.76 (d, J = 7.80 Hz, 1 H), 7.72-7.65 (m, 2 H), 7.41-7.33 (m, 2 H), 6.80 (s, 2 H), 6.77 (d, J = 2.41 Hz, 2 H).

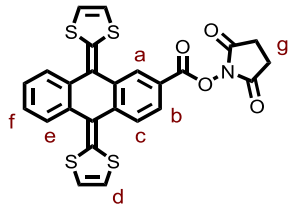

Compound 6. 9,10-Di(1,3-dithiol-2-ylidene)-9,10-dihydroanthracene-2-N-hydroxysuccinimidil ester. To a solution of 9,10-di(1,3-dithiol-2-ylidene)-9,10-dihydroanthracene-2-carboxylic acid (40 mg, 94.0 µmol) in anhydrous THF (5 mL), *N*-hydroxysuccinimide (28 mg, 236 µmol) and *N*,*N*′-dicyclohexylcarbodiimide (49 mg, 236 µmol) were added, and the reaction mixture was stirred under Argon atmosphere at room temperature for 5 hours. Then, the solvent was removed under reduced pressure and the product was purified by silica gel column chromatography (CH_2Cl_2/acetone, 20:1, v:v), obtaining a bright orange powder (43 mg, 88%). ^{1}H NMR (500 MHz, $CDCl_3$): 8.47 (d, J = 1.4 Hz, 1 H_a), 8.06 (dd, J = 8.2, 1,4 Hz, 1 H_b), 7.83 (d, J = 8.2 Hz, 1 H_c), 7.74-7.70 (m, 2 H_e), 7.34-7.30 (m, 2 H_f), 6.41-6.30 (m, 4 H_d), 2.92 (s, 4 H_g); ^{13}C NMR (125 MHz, $CDCl_3$): 169.4, 161.8, 141.6, 140.0, 138.2, 136.1, 135.0, 128.3, 127.2, 126.5, 125.3, 125.1, 122.0, 121.2, 120.6, 117.7, 117.5, 117.4, 25.9; HRMS (MALDI, $[M]^+$): calculated for $C_{25}H_{15}NO_4S_4$: 520.9884; found: 520.9867.

*General procedure for the synthesis of exTTF derivatives **1-5***

The desired peptide (1.1 eq) was dissolved in DMSO and $NaHCO_3$ (20 eq) was added. The mixture stirred at room temperature for 5 minutes and it was subsequently added to a solution of **6** in DMSO. The reaction stirred overnight at 60 ºC under inert atmosphere. Crude reaction was let to cool down to room temperature and the product was precipitated with ethyl acetate. The resulted solid was redissolved in distilled water to be purified by reverse phase chromatography using a water/methanol gradient (0 to 100 % in 20 minutes; 12 mL/min; TELOS Flash C18 12g). Pure products were lyophilized to remove any trace of water.

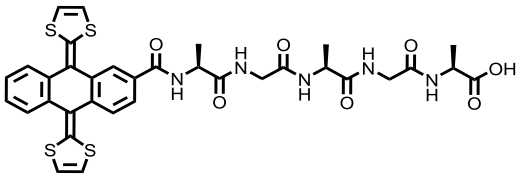

Compound 1. *N*-[9,10-Di(1,3-dithiol-2-ylidene)-9,10-dihydroanthracene-2-carbonyl]-L-alanyl-glycyl-L-alanyl-glycyl-L-alanine. Pure product was obtained as an orange solid (62 mg, 76%). This product was previously described in our research group.[55]

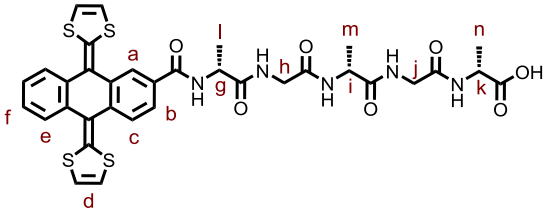

Compound 2. *N*-[9,10-Di(1,3-dithiol-2-ylidene)-9,10-dihydroanthracene-2-carbonyl]-D-alanyl-glycyl-D-alanyl-glycyl-D-alanine. Pure product was obtained as an orange solid (28 mg, 68%). IR (ATR): 3278 (br), 1639 (s), 1540 (s), 1507 (s), 1264 (m), 1090 (m), 1050 (m), 759 (m), 654 (m); ^{1}H NMR (700 MHz, DMSO-d_6): 9.41 (br s, 1 H, NH), 8.76 (br s, 1 H, NH), 8.42 (br s, 1 H, NH), 8.26-8.20 (m, 3 H_{a+b} + NH), 8.10-8.06 (m, 1 H_c), 7.71-7.63 (m, 2 H_e), 7.48 (br s, 1 H, NH), 7.39-7.33 (m, 2 H_f), 6.81-6.70 (m, 4 H_d), 4.50-4.44 (m, 1 H_g), 4.26-4.20 (m, 1 H_i), 3.82-3.65 (m, 4 H_{h+j}), 3.54-3.48 (m, 1 H_k), 1.37 (d, J = 7.2 Hz, 3 H_l), 1.23-1.26 (m, 3 H_m), 1.16-1.14 (m, 3 H_n); ^{13}C NMR (175 MHz, DMSO-d_6): 173.1, 172.2, 168.6, 167.2, 165.5, 138.3, 137.3, 136.0, 134.6, 131.4, 126.8, 126.4, 126.2, 125.5, 124.7, 124.3, 121.3, 120.1, 118.3, 118.0, 50.0, 49.8,

48.4, 42.6, 40.4, 19.2, 17.7, 17.6; HRMS (MALDI, $[M]^+$): calculated for $C_{34}H_{33}N_5O_7S_4$: 751.1257; found: 751.1255.

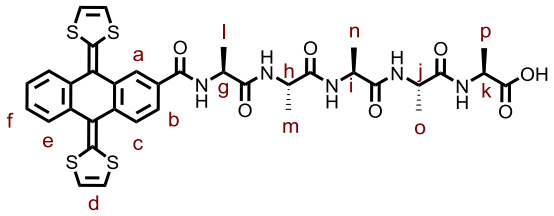

Compound 3. ***N*-[9,10-Di(1,3-dithiol-2-ylidene)-9,10-dihydroanthracene-2-carbonyl]-L-alanyl-L-alanyl-L-alanyl-L-alanyl-L-alanine.** Pure product was obtained as an orange solid (30 mg, 83%). IR (ATR): 3296 (br), 1638 (s), 1541 (s), 1515 (s), 1267 (m), 1091 (w), 1052 (m), 756 (m), 646 (m); ^{1}H NMR (700 MHz, DMSO-d_6): 8.69 (br s, 1 H, NH), 8.23-8.20 (m, 1 H_b), 8.17-8.12 (m, 1 H, NH), 7.97-7.91 (m, 1 H, NH), 7.90-7.86 (m, 1 H_a), 7.79 (br s, 1 H, NH), 7.73 (d, J = 8.2 Hz, 1 H_c), 7.62-7.70 (m, 2 H_e), 7.53 (br s, 1 H, NH), 7.39-7.33 (m, 2 H_f), 6.83-6.71 (m, 4 H_d), 4.54-4.44 (m, 1 H_g), 4.31-4.23 (m, 2 H_{h+n}), 4.17-4.12 (m, 1 H_j), 3.59-3.54 (m, 1 H_k), 1.37-1.33 (m, 3 H_l), 1.29-1.26 (m, 3 H_m), 1.25-1.23 (m, 3 H_n), 1.19 (dd, J = 6.9, 2.5 Hz, 3 H_o), 1.13 (d, J = 6.8 Hz, 3 H_p); ^{13}C NMR (175 MHz, DMSO-d_6): 173.6, 172.2, 171.8, 170.3, 138.4, 137.1, 135.9, 134.9, 134.5, 133.6, 126.8, 126.4, 125.4, 124.7, 124.1, 121.2, 120.1, 118.3, 117.8, 50.0, 49.2, 49.0, 48.1, 19.2, 18.4, 18.2, 18.0, 17.9; HRMS (MALDI, $[M]^+$): calculated for $C_{36}H_{37}N_5O_7S_4$: 779.1576; found: 779.1570.

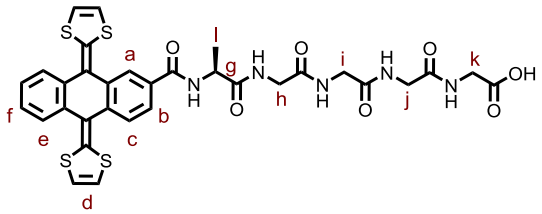

Compound 4. ***N*-[9,10-Di(1,3-dithiol-2-ylidene)-9,10-dihydroanthracene-2-carbonyl]-L-alanyl-glycyl-glycyl-glycyl-glycine.** Pure product was obtained as an orange solid (25 mg, 76%). IR (ATR): 3323 (br), 1651 (s), 1602 (s), 1547 (s), 1260 (m), 1085 (w), 1026 (w), 755 (m), 653 (m); ^{1}H NMR (700 MHz, DMSO-d_6): 9.54 (br s, 1H, NH), 8.64 (br s, 1H, NH), 8.43 (br s, 1H, NH), 8.36 (br s, 1H, NH), 8.23-8.20 (m, 2 H_{a+b}), 8.13 (br s, 1 H_c), 7.70-7.65 (m, 2 H_e), 7.40-7.32 (m, 2 H_f), 7.21 (br s, 1H, NH), 6.82-6.70 (m, 4 H_d), 4.55-4.46 (m, 1 H_g), 3.93-3.87

(m, 2 H_h), 3.74-3.65 (m, 4 H_{i+j}), 3.47-3.41 (m, 2 H_k), 1.37 (d, *J* = 7.2 Hz, 3 H_l); ^{13}C NMR (175 MHz, DMSO-d_6): 173.4, 169.8, 169.3, 167.6, 165.5, 138.2, 137.3, 137.2, 137.1, 134.6, 134.5, 131.3, 126.4, 124.7, 124.3, 120.1, 118.4, 118.3, 118.2, 118.1, 49.9, 43.8, 42.8, 42.3, 42.0, 17.7; HRMS (MALDI, $[M]^+$): calculated for $C_{32}H_{29}N_5O_7S_4$: 723,0950; found: 723.0944.

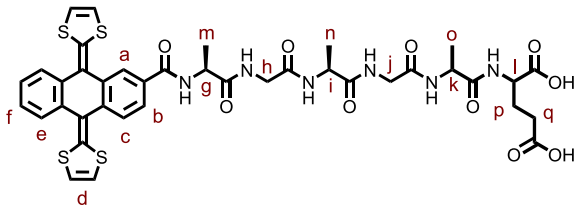

Compound 5. *N*-[9,10-Di(1,3-dithiol-2-ylidene)-9,10-dihydroanthracene-2-carbonyl]-L-alanyl-glycyl-L-alanyl-glycyl-L-alanyl-L-glutamine. Pure product was obtained as a reddish solid (38 mg, 84%). IR (ATR): 3301 (br), 1648 (s), 1598 (s), 1545 (s), 1260 (m), 1166 (w), 1020 (w), 757 (m), 654 (m); ^{1}H NMR (700 MHz, MeOD-d_4): 8.25 (d, *J* = 1.4 Hz, 1 H_a), 7.89-7.83 (dd, *J* = 8.2, 1.4 H_b), 7.77 (d, *J* = 8.2, 1 H_c), 7.73-7.66 (m, 2 H_e), 7.32-7.25 (m, 2 H_f), 6.55-6.48 (m, 4 H_d), 4.54-4.51 (m, 1 H_g), 4.44-4.38 (m, 2 H_{i+k}), 4.19-4.16 (m, 1 H_l), 4.14-4.05 (m, 2 H_h), 3.84-3.80 (m, 2 H_j), 2.32-2.27 (m, 1 H_q), 2.25-2.26 (m, 1 H_q), 2.17-2.11 (m, 1 H_p), 2.06-2.00 (m, 1 H_p), 1.52 (d, *J* = 7.1 Hz, 3 H_m), 1.47-1.40 (m, 3 H_n), 1.28 (d, *J* = 7.1 Hz, 3 H_o); ^{13}C NMR (175 MHz, MeOD-d_4): 182.2, 178.6, 176.5, 175.5, 173.8, 172.0, 169.7, 140.0, 139.1, 137.1, 136.7, 136.6, 131.9, 127.2, 127.1, 126.1, 126.0, 125.7,122.0, 121.7, 118.6, 118.6, 56.9, 52.2, 50.9, 50.6, 43.7, 40.4, 35.5, 30.0, 17.9, 17.7, 17.4; HRMS (MALDI, $[M]^+$): calculated for $C_{39}H_{40}N_6O_{10}S_4$: 880,1689; found: 880.1683

*1.4.1.2. Synthesis of derivative **8***

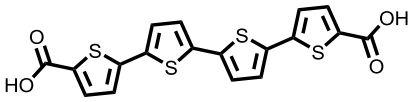

Compound 7. [2,2′;5′,2″;5″;2‴] quaterthiophene-5,5‴dicarboxylic acid. This product was synthesized according to reported procedures.[83] A three-necked round bottom flask was charged with freshly prepared 5,5′-bis(tributylstannyl)-2,2′-bithiophene[82] (1.93 g, 2.6 mmol) and 5-bromo-2-tert-butoxycarbonyl-thiophene (1.71 g, 6.5 mmol). The reagents were dissolved in anhydrous DMF (50 ml), and $Pd(PPh_3)_4$ (0.3 g, 0.78 mmol) was added. The reaction mixture was stirred for 12 h at 80 ºC. The crude reaction was quenched with methanol and the orange precipitate filtered and washed with diethyl ether to give an orange powder that was subsequently redissolved in a CH_2Cl_2/TFA (3:2) mixture and stirred 1h at room temperature. The solvent was removed and the crude product washed with diethyl ether and CH_2Cl_2. The product was isolated as an unsoluble deep red powder (762 mg, 70%).

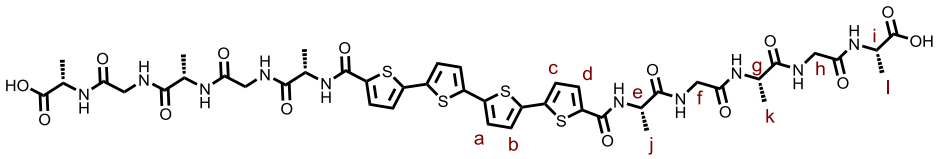

Compound 8. N-[[2,2’;5’,2’’;5’’,2’’’]-quaterthiophene-5,5’’’-biscarbonyl]-L-alanylglycyl-L-alanylglycyl-L-alanine. To a solution of **7** (50 mg, 0.119 mmol) in anhydrous DMF (6 mL), HATU (100 mg, 0.262 mmol) and TEA (50 µL, 0.357 mmol) were added. This mixture stirred at room temperature under inert atmosphere for 5 minutes. Meanwhile the pentapeptide, L-Alanyl-glycyl-L-alanyl-glycyl-L-alanine trifluoroacetate (131 mg, 0.286), was stirred at room temperature in 1,4-dioxane, THF and Na_2CO_3 2 M aqueous solution (1:1:1, 6 mL). The latter solution was added to the activated dicarboxylic acid precursor and the resultant mixture stirred 2 hours at room temperature. The solvent mixture was then removed after reduced pressure and the crude reaction redissolved in water. The solution was injected in a flash purification system to be purified by reverse phase chromatography in a water-methanol gradient (from 0 to 100 % in 20 minutes with a flow rate of 12 mL/min). Pure product was obtained as an orange powder (105 mg, 84%). IR (ATR): 3285 (w), 2985 (m), 1624 (s), 1517 (s), 1231 (m); ^{1}H NMR (DMSO-d_6, 700 MHz): 10.04 (br s, 2 H,

NH), 8.87 (br s, 2 H, NH), 8.44 (br s, 2 H, NH), 8.26 (br s, 2 H, NH), 8.15 (d, *J* = 3.8 Hz, 2 H_d), 7.49 (br s, 2 H, NH), 7.45 (d, *J* = 3.8 Hz, 2 H), 7.38-7.36 (m, 4 H_{a+b}), 4.41-4.37 (m, 2 H_e), 4.19-4.15 (m, 2 H_g), 4.83-3.85-3.75 (m, 4 H_f), 3.76-3.71 (m, 2 H_i), 3.65-3.60 (m, 2 H_h), 3.45-3.40 (m, 2 H_h), 1.35 (d, *J* = 7.1 Hz, 6 H_j), 1.22 (d, *J* = 7.1 Hz, 6 H_k), 1.18 (d, *J* = 7.1 Hz, 6 H_l); ^{13}C NMR (DMSO-*d*$_6$, 175 MHz): 173.6, 172.5, 169.0, 167.7, 161.1, 140.2, 139.2, 136.0, 135.7, 130.9, 126.8, 126.2, 125.4, 50.4, 50.1, 48.9, 43.2, 42.7, 19.5, 18.2, 17.7; MS (MALDI) calculated for $C_{44}H_{52}N_{10}NaO_{14}S_4$ ($[M+Na]^+$): 1095.24; found: 1095.20

*1.4.1.3. Synthesis of derivative **14***

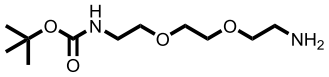

Compound 9. Tert-Butyl 2-[2-(2-aminoethoxy)ethoxy]ethylcarbamate. This product was synthesized according to stablished procedures[83] and the structure confirmed by ^{1}H NMR. 2,2'-(ethane-1,2-diylbis(oxy))diethaneamine (2 mL, 13.6 mol) was dissolved in anhydrous DCM (50 mL) and cool to 0 °C under nitrogen. Di-tert-butyl dicarbonate (1 g, 4.5 mmol) was dissolved in anhydrous CH_2Cl_2 (50 mL) and added dropwise over a period of 20 minutes. After that time, the reaction mixture was allowed to warm up to room temperature and stirred overnight under nitrogen. The solution was diluted with more CH_2Cl_2 and washed three times with water. The aqueous layer was extracted with CH_2Cl_2 and the organic layer dried over $MgSO_4$ and the solvent removed under reduced pressure. The product was used without further purification. ^{1}H NMR (300 MHz, $CDCl_3$): 3.58 (s, 4 H), 3.50 (dt, *J* = 10.5, 5.2 Hz, 4 H), 3.29 (q, *J* = 5.2 Hz, 2 H), 2.84 (t, *J* = 5.2 Hz, 2 H), 1.40 (s, 9 H).

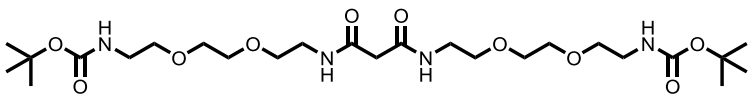

Compound 10. N(1),N(3)-bis-*tert*-Butyl-2-[2-(2-aminoethoxy)ethoxy] ethylcarbamate]malonamide. This product was synthesized according to stablished procedures[83] and the structure confirmed by ^{1}H NMR. Malonylchloride (247 μL, 2.46 mmol) was dissolved in anhydrous CH_2Cl_2 (50 mL) and cooled down to 0 ºC. A solution of **9** (1.22 g, 4.91 mmol) and TEA (1

mL, 7.37 mmol) was subsequently added to the first solution and the mixture was let to stirred at room temperature overnight. The crude reaction was washed with HCl (1M) and water, the organic phase was dried over $MgSO_4$ and the solvente was removed under reduced pressure. The product was used without further purification (600 mg, 43 %). ^{1}H MNR (300 MHz, $CDCl_3$): 7.34 (br s, 2 H), 5.26 (br s, 2 H), 3.62-3.51 (m, 8 H), 3.52 (t, *J* = 5.1 Hz, 8 H), 3.46-3.40 (m, 6 H), 3.28-3.23 (m, 4 H), 1.40 (s, 18 H).

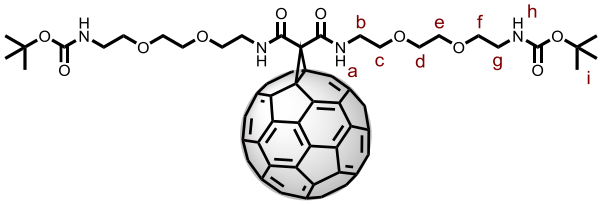

Compound 11. Di[N(1),N(3)-bis-*tert*-Butyl-2-[2-(2-aminoethoxy) ethoxy]ethylcarbamate]methano[60]fullerene. To a solution of C_{60} (500 mg, 0.694 mmol) in anhydrous toluene (250 mL), I_2 (180 mg, 0.694 mmol) and **10** (192 mg, 0.316 mmol) were added. A solution of DBU (150 µL, 0.948 mmol) in toluene (20 mL) was then added dropwise at 0 ºC. The mixture was stirred at room temperature under inert atmosphere overnight. The solvent was removed under reduced pressure and the residue purified in silica gel column chromatography (eluent: toluene to complete elution of free C_{60}, then CH_2Cl_2 to CH_2Cl_2/CH_3OH, 30:1, v:v). Pure product was obtained as a brown powder (226 mg, 25%). IR (ATR): 3270 (m), 2923 (m), 1709 (s), 1658 (s), 1274 (m), 1119 (m); ^{1}H NMR ($CDCl_3$, 500 MHz): 7.78 (br s, 2 H_a), 5.21 (br. s, 2 H_h) 3.78-3.68 (m, 8 H_{b+c}), 3.63-3.50 (m, 12 H_{d+e+f}), 3.33 (br s, 4 H_g), 1.45 (s, 18 H_i); ^{13}CNMR ($CDCl_3$, 125 MHz): 155.8, 145.1, 144.7, 144.6, 144.4, 144.3, 143.7, 143.0, 142.9, 142.9, 142.2, 142.1, 140.8, 137.8, 70.3, 70.2, 69.6, 40.4, 29.6, 28.4; HRMS (MALDI) calculated for $C_{85}H_{46}N_4NaO_{10}$ ($[M+Na]^+$): 1305.3112; found: 1305.3074

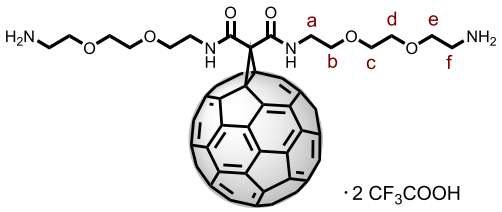

Compound 12. Di[2-[2-(2-aminoethoxy)ethoxy]ethylcarbamate]methano [60]fullerene. Compound **11** (110 mg, 0.086 mmol) was dissolved in $CHCl_3$ (5 mL) and TFA (1.5 mL) was added dropwisely. Reaction stirred overnight and the solvent was removed under reduced pressure. The crude product was washed with CH_2Cl_2 and pure product was obtained as a dark-brown solid (92 mg, quant.). IR (ATR): 2924 (m), 1679 (s), 1563 (m), 1203 (m), 1134 (m); ^{1}H NMR (MeOD-*d4*/$CDCl_3$, 1:4 (v:v), 500 MHz): 3.70-3.67 (m, 12H_{a+b+e}), 3.64 (br s, 8 H_{c+d}), 3.11-3.07 (m, 4 H_f); ^{13}CNMR (MeOD-*d4*/$CDCl_3$, 1:4 (v:v), 125 MHz): 163.4, 146.3, 145.3, 145.0, 144.6, 144.5, 144.4, 144.2, 143.6, 142.9, 142.8, 142.7, 141.9, 140.7, 137.4, 70.1, 69.8, 69.4, 66.2, 40.1, 39.2; HRMS (MALDI) calculated for $C_{75}H_{32}N_4O_6$ ([M+H]$^+$): 1083.2243; found: 1083.2223

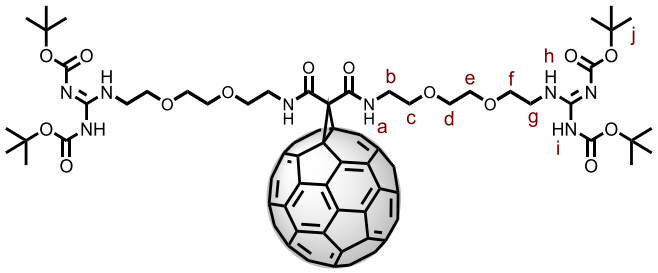

Compound 13. To a dispersion of **12** (65 mg, 0.06 mmol) in $CHCl_3$ (7 mL), TEA (40 µL, 0.3 mmol) was added. The mixture stirred 5 minutes at r.t and some drops of CH_3OH were added until complete solution of the starting material. Then, 1,3-Bis(*tert*-butoxycarbonyl)-2-methyl-2-thiopseudourea (32 mg, 0.109 mmol) was added. The reaction mixture was stirred at 40 ºC for three days. The crude reaction was purified in silica gel column chromatography with a CH_2Cl_2/CH_3OH, (30:1, v:v) mixture as eluent to yield pure product as a brown solid (49 mg, 52%). IR (ATR): 3275 (m), 2923 (m), 1722 (s), 1652 (s), 1565 (m); 1362 (m), 1139 (s); ^{1}H NMR ($CDCl_3$, 500 MHz): 11.48 (br s, 2 H_i), 8.58 (br s, 2 H_h), 7.62 (br s, 2 H_a), 3.78-3.69 (m, 8 H_{b+g}), 3.63-3.59 (m, 16 $H_{c+d+e+f}$), 1.49 (s, 36 H_j); ^{13}CNMR ($CDCl_3$, 125 MHz): 163.7, 162.9, 156.4, 153.2, 146.2, 145.5, 145.4, 145.4, 144.9, 144.9, 144.6, 144.0, 143.3, 142.4, 142.3, 141.1,

138.2, 83.2, 79.4, 70.6, 69.5, 40.8, 40.7, 28.5, 28.3; MS (MALDI) calculated for $C_{97}H_{66}N_8NaO_{14}$ ([M+Na]$^+$): 1589.46; found: 1589.5

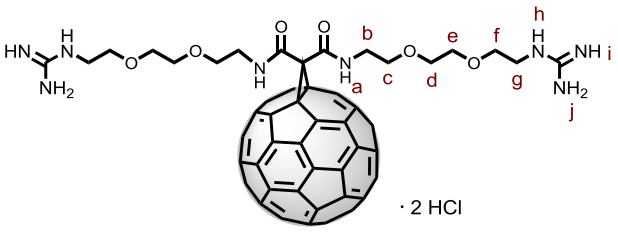

Compound 14. Chlorhydric acid (0.5 mL, 4.5 mmol) was added to a dispersion of **13** (70 mg, 0.045 mmol) in a $CHCl_3/CH_3OH$ mixture (1:4, v:v, 2.5 mL). This mixture was stirred at r.t. for two days. The solvents mixture was removed under reduced pressure and the crude product was washed with CH_2Cl_2. Pure product was obtained as a dark-brown solid (46 mg, 88%). IR (ATR): 3245 (m), 2920 (m), 1644 (s), 1603 (s), 1538 (m); 1083 (m); ^{1}H NMR (DMSO-*d*$_6$, 700 MHz): 9.76 (br s, 2 H$_i$), 7.61 (br s, 2 H$_a$), 7.24 (br s, 6 H$_{h+j}$), 3.59-3.48 (m, 24 H$_{b+c+d+e+f+g}$); ^{13}CNMR (DMSO-*d*$_6$, 175 MHz): 161.4, 157.0, 147.6, 145.6, 144.3, 144.2, 143.8, 143.3, 143.0, 142.2, 142.1, 142.1, 141.6, 141.5, 139.8, 136.6, 74.9, 69.6, 68.7, 68.4; HRMS (MALDI) calculated for $C_{77}H_{34}N_8NaO_6$ ([M+Na]$^+$): 1189.2499; found: 1189.2494

*1.4.1.4. Synthesis of derivative **18***

This compound and the corresponding precursors were synthesized following reported procedures described in our research group and their chemical structures have been confirmed by ^{1}H NMR.[55]

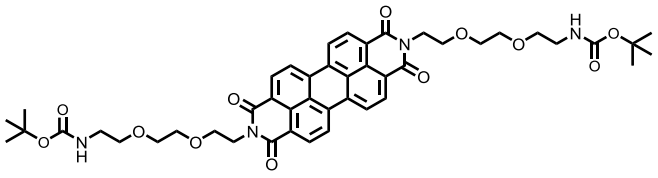

Compound 15. 2,9-Bis[2-(12, 12-dimethyl-10-oxo-3,6,11- trioxa-9-azatridec-1-yl)]-anthra[2,1,9-def:6,5,10-d'e'f']diisoquinoline-1,3,8,10(2H,9H)-tetrone. tert-Butyl 2-[2-(2-aminoethoxy)ethoxy]ethylcarbamate (2 g, 8.06 mmol),

perylene-3,4,9,10-tetracarboxylic acid bisimide (1.06 g, 2.7 mmol), zinc acetate (1.18 g, 5.37 mmol) and imidazole (1.54 g, 22.6 mmol) were stirred under argon atmosphere at 150 ºC for 3 hours. The reaction mixture was filtered through celite to remove the precipitate, and the filter was washed with CH_2Cl_2 (100 mL). After removing the solvent under reduced pressure, the crude product was purified by silica gel column chromatography using CH_2Cl_2/CH_3OH (30:1, v:v) as eluent, to give **15** as a red solid (1.8 g, 80%).^{1}H NMR (300 MHz, $CDCl_3$): 8.56 (d, *J* = 8.0 Hz, 4H), 8.40 (d, *J* = 8.0 Hz, 4H), 5.08 (br s, 2H), 4.51 (t, *J* = 5.8 Hz, 4H), 3.93 (t, *J* = 5.8 Hz, 4H), 3.81-3.74 (m, 4H), 3.69-3.62 (m, 4H), 3.55 (t, 4H, *J* = 5.2 Hz), 3.34-3.25 (m, 4H), 1.46 (s, 18H).

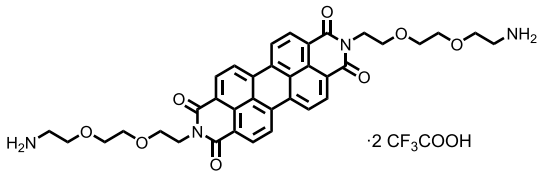

Compound 16. 2,9-Bis{2-[2-(2-aminoethoxy)ethoxy]ethyl]}-anthra[2,1,9-def:6,5,10-d'e'f']diisoquinoline-1,3,8,10(2H,9H)-tetroneditrifluoroacetate salt. A solution of **15** (1.0 g, 1.17 mmol) in $CHCl_3$ (6 mL) and TFA (4 mL) was stirred at room temperature for 1 h. The solvent was removed under reduced pressure. The solid residue was washed with $CHCl_3$ to remove any trace of starting material and then dried under vacuum. The pure compound was obtained as a red solid without further purification (801 mg, 92%). ^{1}H NMR (300 MHz, MeOD-*d4*): 8.02 (d, *J* = 8.0 Hz, 4H), 7.91 (d, *J* = 8.0 Hz, 4H), 4.33 (t, *J* = 6.0 Hz, 4H), 3.86 (t, *J* = 6.0 Hz, 4H), 3.83-3.78 (m, 4H), 3.78-3.70 (m, 8H), 3.16 (t, *J* = 5.2 Hz, 4H).

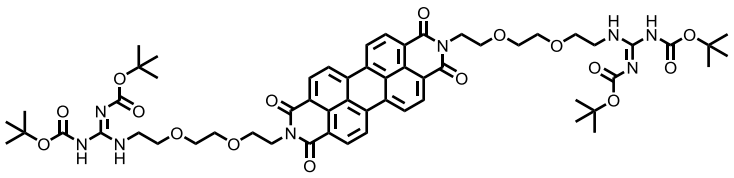

Compound 17. To a solution of **16** (800 mg, 0.91 mmol) in anhydrous DMF (10 mL) 1,3-Bis(*tert*-butoxycarbonyl)-2-methyl-2-thiopseudourea (528 mg, 1.82 mmol) and TEA (0.6 mL, 4.5 mmol) were added and the reaction was stirred at 40 ºC for two days. Most of the DMF was removed under reduced pressure and

the crude product redissolved in CH_2Cl_2 and washed with water (2 x 100 mL) and brine (100 mL). The organic layer was dried over $MgSO_4$ and the solvent was removed under reduced pressure. The crude product was purified by silica gel column chromatography (CH_2Cl_2/CH_3OH, 30:1, v:v) affording **17** as a red solid (456 mg, 46%). ^{1}H NMR (300 MHz, $CDCl_3$): 11.42 (s, 2H), 8.79 (br s, 2H), 8.32 (d, 4H, *J* = 8.0 Hz), 8.09 (d, *J* = 8.0 Hz, 4H), 4.49 (t, *J* = 5.2 Hz, 4H), 3.95 (t, *J* = 5.2 Hz, 4H), 3.86-3.64 (m, 16H), 1.57 (s, 18H), 1.49 (s, 18H).

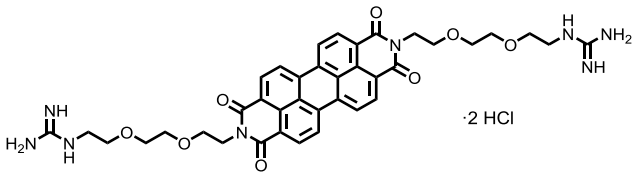

Compound 18. To a solution of **17** (400 mg, 0.135 mmol) in CH_3OH (15 mL), HCl (37%) (5 mL) was added and the mixture was stirred at room temperature. After 20 h, the solvent was removed under reduced pressure. The solid residue was precipitated and centrifuged in cold diethyl ether to remove any trace of impurities and then dried under vacuum. The pure compound was obtained as a purple solid without further purification (280 mg, 99%). ^{1}H NMR (700 MHz, DMSO-d_6): 8.54 (d, 4H, *J* = 6.5 Hz), 8.31 (d, *J* = 6.5 Hz, 4H), 7.53 (t, *J* = 4.7 Hz, 2H), 7.12 (br s, 8H), 4.26 (t, *J* = 5.8 Hz, 4H), 3.73 (t, *J* = 5.8 Hz, 4H), 3.65 (t, *J* = 4.5 Hz, 4H), 3.59 (t, *J* = 4.5 Hz, 4H), 3.51 (m, *J* = 4.8 Hz, 4H), 3.29-3.26 (m, 4H).

*1.4.1.5. Synthesis of derivatives **23** and **24***

The carboxylic suitable precursor was synthesized according to established procedures[98] and the structures were confirmed by ^{1}H NMR.

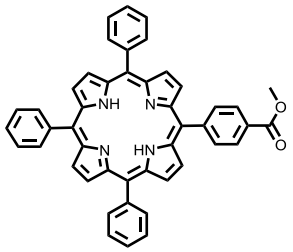

Compound 19. 5,10,15-tris-*meso*-(phenyl)-20-*meso*-(4-methylbenzoate) porphyrin. A mixture of benzaldehyde (1.5 g, 14.14 mmol), methyl 4-formylbenzoate (773 mg, 4.71 mmol) and freshly distilled pyrrole (967 μL, 18.8 mmol) was dissolved in chloroform under inert atmosphere. Boron trifluoride diethyl etherate (120 μL, 0.942 mmol) was added and the solution stirred overnight at room temperature. To this solution, tetrachloro-1,4-benzoquinone (4.64 g, 18.84 mmol) was added and the mixture was refluxed for 45 minutes. Solvent was then removed under reduced pressure and the crude product was purified by silica gel column chromatography (hexane/dichloromethane, from 1:1 to 1:2, v:v). Product was isolated as a deep purple solid (505 mg, 16 %). ^{1}H NMR (300 MHz, $CDCl_3$): 8.88 (d, *J* = 4.7 Hz, 2 H), 8.87 (s, 4 H), 8.80 (d, *J* = 4.7 Hz, 2 H), 8.46 (d, *J* = 8.1 Hz, 2 H), 8.33 (d, *J* = 8.1 Hz, 2 H), 8.26-8.20 (m, 6 H), 7.81-7.74 (m, 9 H), 4.13 (s, 3 H) -2.81 (s, 2 H).

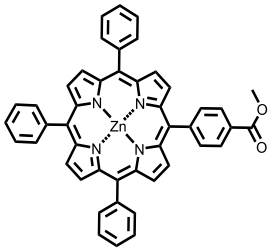

Compound 20. Zn(II) 5,10,15-tris-*meso*-(phenyl)-20-*meso*-(4-methyl-benzoate)porphyrin. Compound **19** (150 mg, 0,22 mmol) was dissolved in a chloroform/methanol mixture (5:1, v:v) and suspended with $Zn(OAc)_2$ (59 mg, 0,27 mmol) overnight under a nitrogen atmosphere in darkness. After filtration, the crude product was purified by silica gel column chromatography (hexane/dichloromethane, 1:2, v:v). The pure product was isolated as a purple solid (120mg, 74 %). ^{1}H NMR (300 MHz, $CDCl_3$): 8.98 (d, *J* = 4.7 Hz, 2 H), 8.97 (s, 4 H), 8.90 (d, *J* = 4.7 Hz, 2 H), 8.43 (d, *J* = 8.1 Hz, 2 H), 8.32 (d, *J* = 8.1 Hz, 2 H), 8.26-8.20 (m, 6 H), 7.81-7.73 (m, 9 H), 4.13 (s, 3 H).

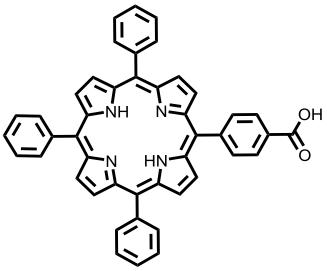

Compound 21. 5,10,15-tris-*meso*-(phenyl)-20-*meso*-(4-benzoic acid) porphyrin. Compound **19** (120 mg, 0,18 mmol) was dissolved in a THF/water mixture (8:2, v:v) and KOH (200 mg, 3.6 mmol) was added. The solution was stirred at 80 ºC for 6 hours until no sign of starting materials were found in the TLC. Solvents were removed under reduced pressure and the crude was redissolved in dicloromethane. The organic phase was washed with HCl (1M) (2 x 10 mL) and brine (1 x 10 mL) and used without further purification (116 mg, quant.). ^{1}H NMR (300 MHz, $CDCl_3$): 8.89 (d, *J* = 4.7 Hz, 2 H), 8.87 (s, 4 H), 8.82 (d, *J* = 4.7 Hz, 2 H), 8.46 (d, *J* = 8.1 Hz, 2 H), 8.33 (d, *J* = 8.1 Hz, 2 H), 8.26-8.20 (m, 6 H), 7.82-7.74 (m, 9 H), -2.81 (s, 2 H).

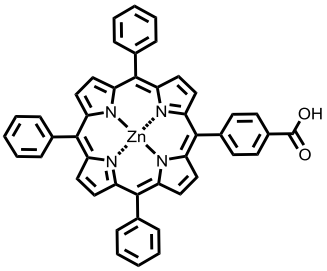

Compound 22. Zn(II) 5,10,15-tris-*meso*-(phenyl)-20-*meso*-(4-benzoic acid) porphyrin. Compound **20** (62 mg, 0,08 mmol) was dissolved in a THF/water mixture (8:2 v:v) and KOH was added (88 mg, 1.63 mmol). The solution stirred at 80 ºC for 6 hours until no sign of starting materials were found in the TLC. Solvents were removed under reduced pressure and the crude was redissolved in dicloromethane. The organic phase was washed with HCl (1M) (2 x 10 mL) and brine (1 x 10 mL) and used without further purification (60 mg, quant.). ^{1}H NMR (300 MHz, MeOD-d_4): 8.87-8.80 (m, 8 H), 8.43 (d, *J* = 8.2 Hz, 2 H), 8.32 (d, *J* = 8.1 Hz, 2 H), 8.24-8.20 (m, 6 H), 7.80-7.72 (m, 9 H).

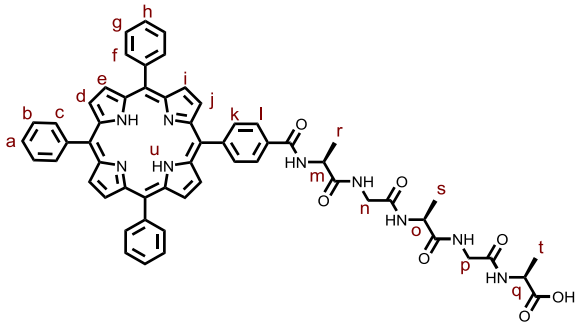

Compound 23. 5,10,15-tris-*meso*-(phenyl)-20-*meso*-[phenyl-4-carbonyl-(L-alanylglycyl-L-alanyl-glycyl-L-alanine)]porphyrin. To a solution of **21** (30 mg, 0.042 mmol) in anhydrous DMF (1.5 mL), HATU (17 mg, 0.046 mmol) and TEA (9 µL, 0.063 mmol) were added. This mixture was stirred at room temperature under inert atmosphere for 10 minutes. Meanwhile the pentapeptide, L-alanyl-glycyl-L-alanyl-glycyl-L-alanine trifluoroacetate (21 mg, 0.046 mmol), was stirred at room temperature 1,4-dioxane, THF and Na_2CO_3 2 M aqueous solution (1:1:1, 3 mL). The latter solution was added to the previously activated carboxylic acid precursor and the resultant mixture was stirred 2 hours at room temperature. The solvent mixture was removed under reduced pressure and the crude reaction redissolved in water. The solution was injected in a flash purification system to be purified by reverse phase chromatography in a water-methanol gradient (from 0 to 100 % in 20 minutes with a flow rate of 12 mL/min). Pure product was obtained as a purple solid (26 mg, 63 %). IR (ATR): 3295 (br), 1643 (s), 1599 (s), 1530 (s), 1247 (m), 962 (s), 795 (s); ^{1}H NMR (700 MHz, MeOD-*d*$_4$): 8.86 (br s, 8 $H_{d+e+i+j}$), 8.39-8.30 (m, 4 H_{k+l}), 8.25-8.18 (m, 6 H_{c+f}), 7.85-7.77 (m, 9 $H_{a+b+g+h}$), 4.73-4.66 (m, 1 H_m), 4.56-4.49 (m, 1 H_o), 4.35-4.28 (m, 1 H_q), 4.21-4.16 (m, 2 H_n), 3.95-3.86 (m, 1 H_p), 3.78-3.69 (m, 1 H_p), 1.64 (d, *J* = 7.1 Hz, 3 H_t), 1.49 (d, *J* = 7.1 Hz, 3 H_s), 1.34 (d, *J* = 7.1 Hz, 3 H_t); ^{13}C NMR (175 MHz, MeOD-*d*$_4$): 178.2, 175.2, 173.9, 170.4, 169.1, 150.1, 150.0, 150.0, 149.5, 147.4, 143.4, 134.3, 134.2, 132.2, 131.4, 131.2, 131.1, 130.7, 127.0, 126.0, 125.5, 120.7, 120.6, 118.9, 50.9, 50.3, 49.2, 42.5, 42.4, 17.8, 16.3, 16.0; HRMS (APCI) calculated for $C_{58}H_{52}N_9O_7$ ($[M+H]^+$): 986,3990; found: 986.4007.

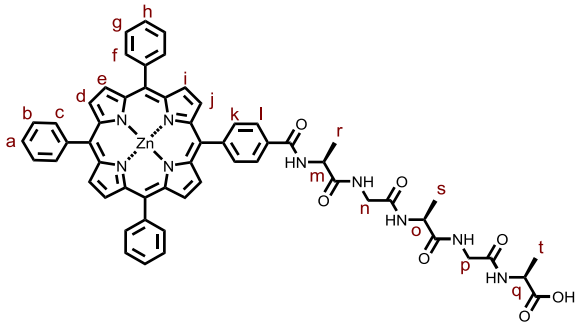

Compound 24. Zn(II) 5,10,15-tris-*meso*-(phenyl)-20-*meso*-[phenyl-4-carbonyl-(L-alanylglycyl-L-alanyl-glycyl-L-alanine)]porphyrin. To a solution of **22** (30 mg, 0.046 mmol) in anhydrous DMF (1.5 mL), HATU (20 mg, 0.05 mmol) and TEA (10 µL, 0.069 mmol) were added. This mixture was stirred at room temperature under inert atmosphere for 10 minutes. Meanwhile the pentapeptide, L-alanyl-glycyl-L-alanyl-glycyl-L-alanine trifluoroacetate (23 mg, 0.05 mmol), was stirred at room temperature in 1,4-dioxane, THF and Na_2CO_3 2 M aqueous solution (1:1:1, 3 mL). The latter solution was added to the previously activated carboxylic acid precursor and the resultant mixture stirred 2 hours at room temperature. The solvent mixture was removed under reduced pressure and the crude reaction was redissolved in water. The solution was injected in a flash purification system to be purified by reverse phase chromatography in a water-methanol gradient (from 0 to 100 % in 20 minutes with a flow rate of 12 mL/min). Pure product was obtained as a purple solid (41 mg, 86 %). IR (ATR): 3310 (br), 2934 (w), 1648 (s), 1599 (s), 1597 (s), 1542 (s), 1001 (s), 796 (s); ^{1}H NMR (700 MHz, MeOD-*d*$_4$): 8.83 (d, *J* = 4.5 Hz, 2 H_j), 8.81 (s, 4 H_{d+e}), 8.79 (d, *J* = 4.5 Hz, 2 H_i), 8.31 (br s, 4 H_{k+l}), 8.18-8.16 (m, 6 H_{c+f}), 7.74-7.69 (m, 9 $H_{a+b+g+h}$), 4.68-4.64 (m, 1 H_m), 4.51-4.48 (m, 1 H_o), 4.30-4.26 (m, 1 H_q), 4.17-4.10 (m, 2 H_n), 3.92-3.88 (m, 1 H_p), 3.78-3.74 (m, 1 H_p), 1.63 (d, *J* = 7.3 Hz, 3 H_t), 1.50 (d, *J* = 7.3 Hz, 3 H_s), 1.34 (d, *J* = 7.3 Hz, 3 H_t); ^{13}C NMR (176 MHz, MeOD-*d*$_4$): 178.2, 175.2, 173.9, 170.4, 169.1, 150.1, 150.0, 150.0, 149.5, 147.4, 143.4, 134.3, 134.2, 132.2, 131.4, 131.2, 131.1, 130.7, 127.0, 126.0, 125.5, 120.7, 120.6, 118.9, 50.9, 50.3, 49.2, 42.5, 42.4, 17.8, 16.3, 16.0; HRMS (APCI) calculated for $C_{58}H_{50}N_9O_7Zn$ ([M+H]$^+$): 1048.3125; found: 1048.3130.

*1.4.1.6. Synthesis of derivatives **29** and **30***

The suitable precursor was synthesized according to Rothemund-Lindsey conditions[98] and the structures were just confirmed by ^{1}H NMR.

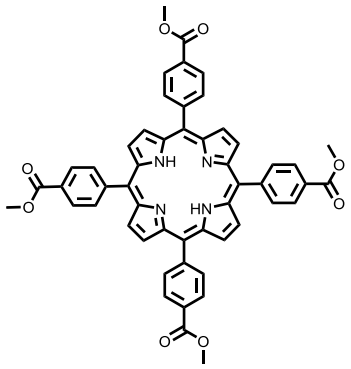

Compound 25. 5,10,15,20-tetrakis-*meso*-(4-methylbenzoato)porphyrin. A mixture of methyl 4-formylbenzoate (1 g, 6.1 mmol) and freshly distilled pyrrole (409 μL, 5.92 mmol) in propionic acid (15 mL) was refluxed (150 ºC) in dark overnight. Completion of the reaction was checked by TLC and crude product reaction was poured into cool water and filtered. The solid was washed thoroughly with methanol (100 mL) and dichloromethane (10 mL) respectively. The resulting deep purple solid was purified by column chromatography (silica gel, DCM/n-hexane, 1:5, v:v). The pure compound was obtained as a purple crystalline solid (1.19 g 23%). ^{1}H NMR (300 MHz, $CDCl_3$): 8.84 (s, 8 H), 8.47 (d, J = 8.2 Hz, 8 H), 8.32 (d, J = 8.2 Hz, 8 H), 4.13 (s, 12 H), -2.79 (s, 2 H).

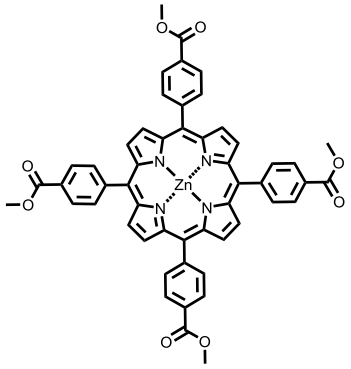

Compound 26. Zn(II) 5,10,15,20-tetrakis-*meso*-(4-methylbenzoato) porphyrin Compound **25** (100 mg, 0,15 mmol) was dissolved in a chloroform/methanol mixture (5:1, v:v, 5 mL) and suspended with $Zn(OAc)_2$ (33

mg, 0,15 mmol) overnight under a nitrogen atmosphere in darkness. After filtration, the crude product was purified by column chromatography on silica gel (5:1, v:v, CH_2Cl_2/ethyl acetate). The pure product was isolated as a purple solid (91 mg, 83%).^{1}H NMR (300 MHz, $CDCl_3$): 8.84 (s, 8 H), 7.72 (d, *J* = 8.2 Hz, 8 H), 7.54 (d, *J* = 8.2 Hz, 8 H), 4.13 (s, 12 H).

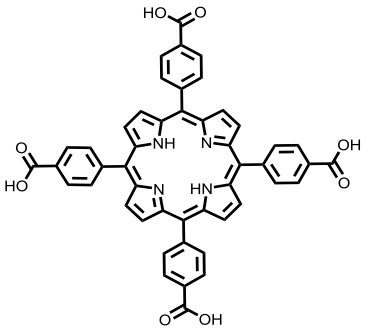

Compound 27. 5,10,15,20-tetrakis-*meso*-(4-benzoic acid) porphyrin. Compound **25** (100 mg, 0,12 mmol) was dissolved in a THF/water mixture (8:2 v:v, 8 mL) and KOH was added (660 mg, 1,2 mmol). The solution stirred at 80 ºC for 24 hours until no sign of starting materials were found in the TLC. Solvents were removed under reduced pressure and the crude was redissolved in water. Purification was carried out by reverse phase chromatography using a water/methanol gradient (0 to 100 % in 20 minutes; 12 mL/min; TELOS Flash C18 12g). The pure product was obtained as a purple solid (90 mg, 97 %). ^{1}H NMR (300 MHz, MeOD-d_4): 8.89 (br s, 8 H), 8.38 (d, *J* = 7.9 Hz, 8 H), 8.24 (d, *J* = 7.9 Hz, 8 H).

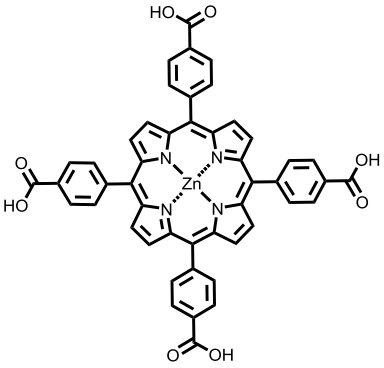

Compound 28. Zn(II) 5,10,15,20-tetrakis-*meso*-(4-benzoic acid)porphyrin. Compound **26** (110 mg, 0,12 mmol) was dissolved in a THF/water mixture (8:2

v:v, 10 mL) and KOH was added (678 mg, 1,2 mmol). The solution was stirred at 80 ºC for 24 hours until no sign of starting materials were found in the TLC. Solvents were removed under reduced pressure and the crude was redissolved in water. Purification was carried out by reverse phase chromatography using a water/methanol gradient (0 to 100 % in 20 minutes; 12 mL/min; TELOS Flash C18 12g). The pure product was obtained as a purple solid (98 mg, 96 %). ^{1}H NMR (300 MHz, MeOD-d_4): 8.86 (s, 8 H), 8.36 (d, J = 8.2 Hz, 8 H), 8.22 (d, J = 8.2 Hz, 8 H).

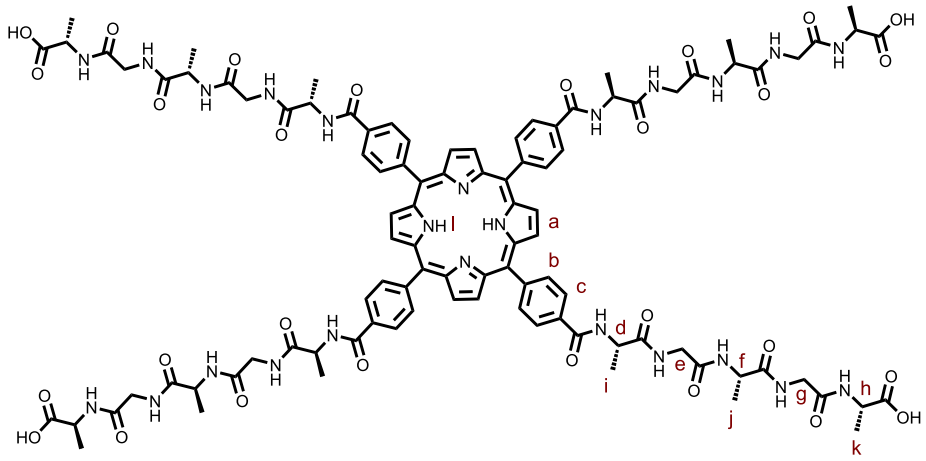

Compound 29. 5,10,15,20-tetrakis-*meso*-[phenyl-4-carbonyl-(L-alanyl-glycyl-L-alanyl-glycyl-L-alanine)]porphyrin. To a solution of **27** (30 mg, 0.038 mmol) in anhydrous DMF (3 mL), HATU (72 mg, 0.19 mmol) and TEA (32 µL, 0.228 mmol) were added. This mixture stirred at room temperature under inert atmosphere for 30 minutes. Meanwhile the pentapeptide, L-alanyl-glycyl-L-alanyl-glycyl-L-alanine trifluoroacetate (85 mg, 0.19 mmol), was stirred at room temperature in 1,4-dioxane, THF and Na_2CO_3 2 M aqueous solution (1:1:1, 6 mL). The latter solution was added to the previously activated carboxylic acid precursor and the resultant mixture stirred 2 hours at room temperature. The solvent mixture was removed under reduced pressure and the crude reaction redissolved in water. The solution was injected in a flash purification system to be purified by reverse phase chromatography in a water-methanol gradient (from 0 to 100 % in 20 minutes with a flow rate of 12 mL/min). Pure product was obtained as a purple solid (60 mg, 75 %). IR (ATR): 3305 (br), 1745 (m), 1743 (s), 1593 (s), 1529 (s), 1373 (m); ^{1}H NMR (700 MHz, MeOD-d_4): 8.78 (br s, 8

H_a), 8.35-8.14 (m, 16 H_{b+c}), 4.72-4.64 (m, 4 H_d), 4.52-4.45 (m, 4 H_f), 4.30-4.23 (m, 4 H_h), 4.17-4.06 (m, 8 H_e), 3.95-3.90 (m, 4 H_g), 3.81-3.76 (m, 4 H_g), 1.65 (d, J = 7.2 Hz, 12 H_i), 1.50 (d, J = 7.1 Hz, 12 H_j), 1.35 (d, J = 7.1 Hz, 12 H_k), -2.81 (s, 2 H_l); ^{13}C NMR (176 MHz, MeOD-*d*$_4$): 179.6, 176.7, 175.4, 171.9, 170.5, 148.4, 138.5, 135.7, 133.7, 132.6, 127.0, 121.0, 52.4, 51.8, 50.7, 43.9, 43.8, 19.2, 17.7, 17.4; MS (MALDI) calculated for $C_{100}H_{116}N_{24}O_{28}$ ($[M+H_2]^+$): 2100.84; found: 2100.8

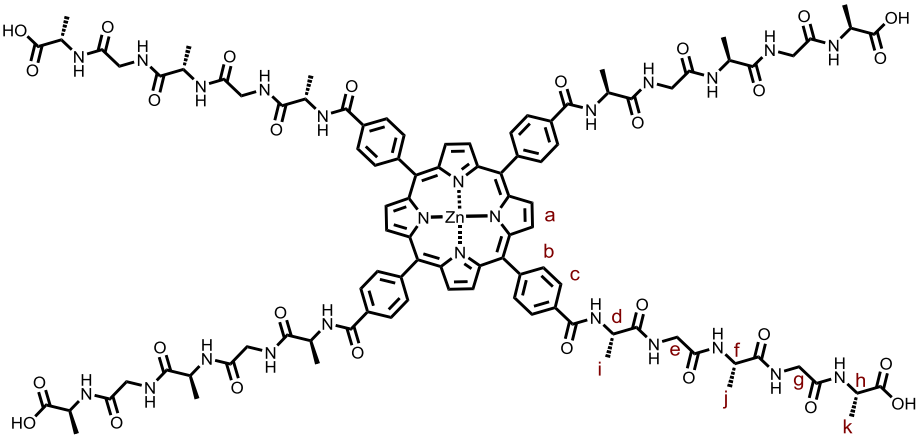

Compound 30. Zn(II) 5,10,15,20-tetrakis-*meso*-[phenyl-4-carbonyl-(L-alanyl-glycyl-L-alanyl-glycyl-L-alanine)]porphyrin. To a solution of **28** (20 mg, 0.023 mmol) in anhydrous DMF (2 mL), HATU (40 mg, 0.104 mmol) and TEA (20 µL, 0.138 mmol) were added. This mixture stirred at room temperature under inert atmosphere for 30 minutes. Meanwhile the pentapeptide, L-alanyl-glycyl-L-alanyl-glycyl-L-alanine trifluoroacetate (48 mg, 0.104 mmol), was stirred at room temperature in 1,4-dioxane, THF and Na_2CO_3 2 M aqueous solution (1:1:1, 6 mL). The latter solution was added to the previously activated carboxylic acid precursor and the resultant mixture stirred 2 hours at room temperature. The solvent mixture was removed under reduced pressure and the crude reaction redissolved in water. The solution was injected in a flash purification system to be purified by reverse phase chromatography in a water-methanol gradient (from 0 to 100 % in 20 minutes with a flow rate of 12 mL/min). Pure product was obtained as a purple solid (40 mg, 78 %). IR (ATR): 3310 (br), 2943 (m), 1648 (s), 1542 (s), 1002 (s), 796 (m); ^{1}H NMR (700 MHz, MeOD-*d*$_4$): 8.77 (br s, 8 H_a), 8.30-8.21 (m, 16 H_{b+c}), 4.67-4.61 (m, 4 H_d), 4.49-4.44 (m, 4 H_f), 4.26-4.22 (m, 4 H_h), 4.13-4.02 (m, 8 H_e), 3.95-3.90 (m, 4 H_g),

3.82-3.77 (m, 4 H_g), 1.62 (d, J = 7.2 Hz, 12 H_i), 1.49 (d, J = 7.2 Hz, 12 H_j), 1.34 (d, J = 7.0 Hz, 12 H_k); ^{13}C NMR (176 MHz, MeOD-d_4): 179.7, 176.6, 175.4, 171.8, 170.5, 151.0, 148.4, 135.7, 133.7, 132.6, 127.0, 121.0, 52.4, 51.8, 50.7, 43.9, 43.8, 19.2, 17.7, 17.4; MS (MALDI) calculated for $C_{100}H_{112}N_{24}NaO_{28}Zn$ ($[M+Na]^+$): 2183.72; found: 2183.7

1.4.2. Experimental details

Absorbance and circular dichroism measurements. Absorption and circular dichroism spectra were simultaneously recorded on a JASCO J-815 DC spectrometer. All spectra were acquired in a 1 cm or 1mm path length quartz cuvette using a 2 nm slit-width.

Voltammetry. Cyclic (CV) and differential pulse voltammograms (DPV) were recorded on a potentiostat/galvanostat AUTOLAB with PGSTAT30 equipped with a software GPES for windows version 4.8 in a conventional three compartment cell. All measurements were carried out at room temperature using a GCE (glassy carbon electrode) as working electrode, an Ag/AgCl reference electrode, and a platinum wire as counter electrode. H_2O or H_2O/DMSO mixtures were used as solvents using KCl (10 mM) as supporting electrolyte. Prior to any measurement, the appropriate temperature treatment was performed and the CD signal of the corresponding annealed solution evaluated to ensure the acquirement of the desired aggregate.

Transmission Electron Microscopy. TEM images were performed in a JEOL JEM 1011 electron microscope operated at 100 kV. Images were directly recorded using a GATAN Erlangshen ES 1000W camera attached to the microscope. In the case of HRTEM, images were acquired in a JEOL JEM 3000F electron microscope operated at 300 kV. The samples were prepared by drop-casting the samples on carbon film 200 mesh copper grids and blotted dry.

In the particular case of cryo-TEM, 3 μL of samples (derivatives **1**-**5** (c= 0.2 mM, I= 10 mM)) were applied to quantifoil 3.5/1 Cu/Rh grids at 20 ºC and 100% humidity inside vitrobot (FEI Company) chamber during 1 minute. Vitrification was done automatically using -15 force and 2 seconds blotting time parameters. Vitrified samples was introduced in a TALOS ARCTICA (FEI Company) operating at 200 KV and recorded automatically with a defocus of -3 μm using EPU software in a FALCON 2 Direct Detector Device at a nominal magnification of 73000X (1,37 Å/pix). Also manual registration and SerialEM automatic acquisition was used to record the images on a Tecnai F20 operating

at 200 KV. In this case the images were recorded in an Eagle 4k CCD camera at a nominal magnification of 50.000 (2.239 Å/pix). For time dependent studies, a solution of disaggregated **1** was prepared heating the samples at 90ºC, then the solution was cooled down from 90ºC to 50º in shortest period of time until no more amplification of the dichroic signal of **1-M** was observed. Then, the solution was cooled down to 10 ºC and kept in N_2 to preserve the metastable state. Then the evolution of the self-assembly was observed by cryo-TEM, pippetted onto a TEM grid to get samples at various time points.

Atomic Force Microscopy. AFM images were acquired under ambient conditions using SPM Nanoscope IIIa multimode working on tapping mode with a RTESPA tip (Veeco) at a working frequency of B235 Khz. Height and phase images were simultaneously obtained. The samples were prepared by drop-casting on freshly cleaved mica.

X-ray Photoelectron Spectroscopy. XPS analysis were obtained on a SPECS GmbH (PHOIBOS 150 9 MCD) spectrometer working in the constant analyzer energy mode and a non-monochromatic aluminium X-ray source (1486.61 eV) powered at 200 W and a voltage of 12 eV. For recording both survey and high resolution spectra pass energies of 75 and 25 eV were applied. Survey data were acquired from kinetic energies of 1487-400 eV with 0.1 eV of energy step and 100 ms dwell time per point. The high resolution scans were registered around the significant emission lines with 0.1 eV steps and 100 ms dwell time per point. The spectrometer control and data handling were monitorized using SpecsLab Version 2.48 software. Binding energies were calibrated relatively to the C 1s peak at 284.6 eV and the atomic ratios were computed from experimental intensity rations.

FP-TRMC and TAS measurements. Charge carrier mobility was evaluated by flash-photolysis time-resolved microwave conductivity (FP-TRMC) and transient absorption spectroscopy (TAS) techniques at room temperature under air. Solid films of **8**, **14**, **18**, **8:14** and **8:18** were prepared by drop-casting of their Milli-Q water solution. Charge carriers were photochemically generated using a third harmonic generation (λ = 355 nm) of a Spectra Physics model INDI-HG Nd:YAG laser with a pulse duration of 5-8 ns and frequency of 10 Hz. The TRMC signal, picked up by a diode (rise time < 1 ns), was monitored by a Tektronics model TDS3032B digital oscilloscope

Chapter 2

CTPR proteins as model scaffold for the arrangement of electroactive molecules.

2.1. Background

2.1. Background

2.1.1. Biomolecules and nanotechnology.

The convergence between biotechnology and nanotechnology is a highly important field of research and, despite being a young discipline, has already resulted in remarkable achievements. The term "bionanotechnology" is usually employed to describe the use of biological building blocks and/or biological specificity and activity for the development of modern technology at the nanoscale.[104] As our understanding on biological processes has improved, the interest in these biomimetic and bioinspired materials has grown. Biomaterials can be of natural origin, such as naturally derived sugars, be based on natural occurring monomers, as in the case of nucleic acid-based molecules, or fully synthetic. Due to their similarities with biological structures, either at the chemical, physical, or morphological level, biomimetic and bioinspired materials are expected to outperform many of the currently available materials. At the chemical level, it is possible to attain chemical specificity, reduce cytotoxicity, or tune biodegradability. At the supramolecular level, the self-assembly features of biomolecules have been widely explored.[105]

As mentioned in Chapter 1, enhanced electronic properties and potential applications in the field of electronics arise from the self-assembly of dyes and π-organic molecules. Biomolecules are seen as attractive scaffolds to guide this self-assembly process and to provide on-site control, monodispersity and chirality in the final material. The three main groups of biomolecules that have been used for nanotechnological purposes are proteins, DNA and carbohydrates. Due to their amphiphilicity and self-assembly properties, lipid-like structures are also very valuable in nanotechnology, although most of the research involves their combination with other families of biomolecules (glycolipids, aminolipids and lipopeptides, etc).[106]

---

[104] a) D. S. Goodsell, *Bionanotechnology: Lessons from Nature*, Wiley-VCH, Weinheim, 2004; b) G. M. Whitesides, *Interface Focus* **2015**, *5*, 20150031; d) Y. Lin, C. Mao, *Front. Mater. Sci.* **2011**, *5*, 247-265.

[105] Y. Tu, F. Peng, A. Adawy, Y. Men, Abdelmohsen, Loai K. E. A., D. A. Wilson, *Chem. Rev.* **2016**, *116*, 2023-2078.

[106] a) S. Mashaghi, T. Jadidi, G. Koenderink, A. Mashaghi, *Int. J. Mol. Sci.* **2013**, *14*, 4242-4282; b) M. U. Ahmad, *Lipids in Nanotechnology*, AOCS Press **2012**.

Below is given a brief overview of the main advances in the use of such biomolecules in the field of bionanotechnology. Proteins will be considered in a separate section as they comprise the central issue of this chapter.

DNA-based scaffolds

DNA has become a very attractive supramolecular scaffold due to its high chemical stability and predictable folding. Structural DNA nanotechnology was pioneered by Seeman and *col.*[107] and culminated over two decades later with the seminal contribution of Rothemund, who introduced the DNA origami method.[108] This technology allows the folding of a DNA strand into virtually any desired shape, as shown in Figure 2. 1. The unprecedented complexity and nanometer scale resolution achieved in DNA origami have found a variety of applications.[109] In the area of materials science, self-assembled DNA structures represent an attractive platform for the organization of molecules or nanomaterials, such as metal nanoparticles[110] and single-wall carbon nanotubes.[111]

[107] a) N. C. Seeman, *J. Theor. Biol.* **1982**, *99*, 237-247; b) N. C. Seeman, N. R. Kallenbach, *Biophys. J.* **1983**, *44*, 201-209; c) J. Chen, N. C. Seeman, *Nature* **1991**, *350*, 631-633.
[108] P. W. K. Rothemund, *Nature* **2006**, *440*, 297-302.
[109] F. Hong, F. Zhang, Y. Liu, H. Yan, *Chem. Rev.* **2017**, *117*, 12584-12640.
[110] a) A. Kumar, J. Hwang, S. Kumar, J. Nam, *Chem. Commun.* **2013**, *49*, 2597-2609; b) J. Sharma, Y. Ke, C. Lin, R. Chhabra, Q. Wang, J. Nangreave, Y. Liu, H. Yan, *Angew. Chem., Int. Ed.* **2008**, *47*, 5157-5159.
[111] a) H. T. Maune, S. Han, R. D. Barish, M. Bockrath, W. A. G. III, P. W. K. Rothemund, E. Winfree, *Nat. Nanotechnol.* **2009**, *5*, 61-66; b) Z. Zhao, Y. Liu, H. Yan, *Org. Biomol. Chem.* **2013**, *11*, 596-598.

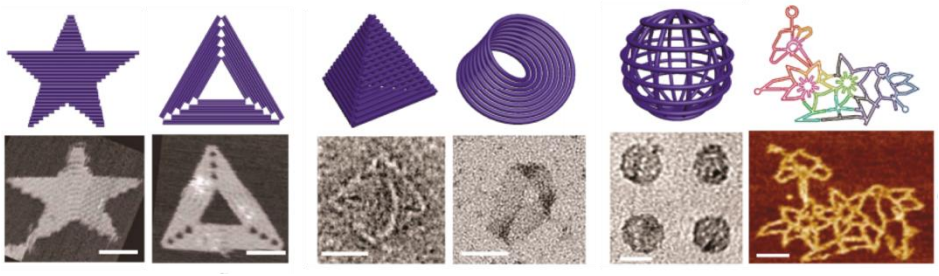

Figure 2. 1. DNA origami structures. From 2D planar patterns (left) to more complex 3D single-layered (middle) or multi-layered DNA units (right). All of the scale bars in images are 50 nm.

DNA has been used to arrange a great variety of π-conjugated molecules, yielding materials with enhanced optoelectronic properties.[112] In this regard, promising materials for applications as optical nanodevices as well as nucleic acid sensors for diagnostics have been developed. Stulz and coworkers reported the modification of DNA with porphyrin dyes (Figure 2. 2), giving insights about the electronic properties and stability of such hybrid systems.[113] The resulting zipper-like arrangement of stacked porphyrins led to the stabilization of the duplex and resonance energy transfer between chromophores. Moreover, the exciton coupling between the porphyrins could be tuned depending on the nature of the linker between the nucleobase and the porphyrin in the double strand.

[112] a) V. L. Malinovskii, D. Wenger, R. Häner, *Chem. Soc. Rev.* **2010**, *39*, 410-422; b) R. Varghese, H. Wagenknecht, *Chem. Commun.* **2009**, 2615-2624; c) S. Sezi, H. Wagenknecht, *Chem. Commun.* **2013**, *49*, 9257-9259; d) S. Kulala Vittala, J. Joseph, *Faraday Discuss.* **2018**, *207*, 459-469; e) J. Rubio-Magnieto, A. Thomas, S. Richeter, A. Mehdi, P. Dubois, R. Lazzaroni, S. Clément, M. Surin, *Chem. Commun.* **2013**, *49*, 5483-5485.

[113] D. G. Singleton, R. Hussain, G. Siligardi, P. Kumar, P. J. Hrdlicka, N. Berova, E. Stulz, *Org. Biomol. Chem.* **2016**, *14*, 149-157.

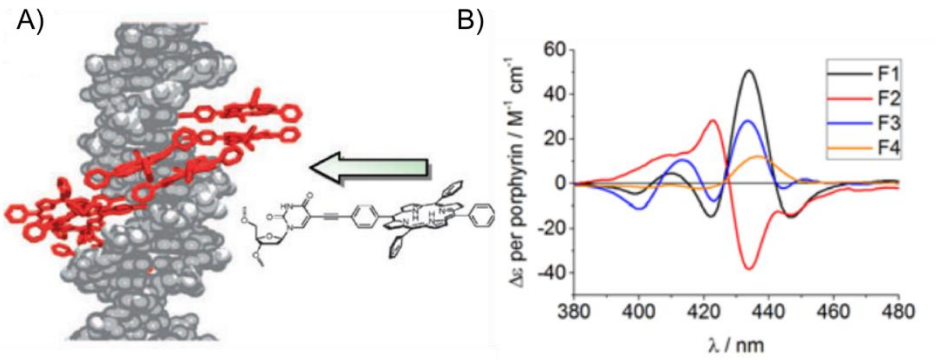

Figure 2. 2. A) Schematic reprentation of the porphyrin organization on the DNA scaffold. B) CD spectra in the porphyrin absorption region under different conditions (indicated as F1-4), demonstrating the chiral arrangement of the chomophore induced by the helical DNA scaffold.

Glycan-based materials

The field of glyconanotechnology has undergone a great advance along the past decades. Although carbohydrates were primarily considered mainly as storage and structural materials, it is nowadays clear that they exhibit a great variety of biological activities. They constitute an interesting motif to construct self-assembling building blocks due to their natural ability to self-associate through hydrogen-bonding. Glycan-based nanomaterials have been designed and applied for biosensing, interaction studies and biomedical applications.[35] Our research group has contributed to the field by incorporating manosse-based glycodendrons to [60]fullerene hexakis adducts for their interaction with lectins (Figure 2. 3). Ebola virus infections are mediated by the interaction between the DC-SIGN lectin and the mannose-containing glycans of the viral particles. Thus, the multivalent presentation of carbohydrates using a C_{60}-based scaffold has led to different inhibition efficiencies relying on the specific carbohydrate selection, the ligand density, or the chain length and flexibility.[114]

[114] a) J. Luczkowiak, A. Muñoz, M. Sánchez-Navarro, R. Ribeiro-Viana, A. Ginieis, B. M. Illescas, N. Martín, R. Delgado, J. Rojo, *Biomacromolecules* **2013**, *14*, 431-437; b) A. Muñoz, D. Sigwalt, B. M. Illescas, J. Luczkowiak, L. Rodríguez-Pérez, I. Nierengarten, M. Holler, J.-S. Remy, K. Buffet, S. P. Vincent, J. Rojo, R. Delgado, J.-F. Nierengarten, N. Martín, *Nat. Chem.* **2016**, *8*, 50-57; c) B. M. Illescas, J. Rojo, R. Delgado, N. Martín, *J. Am. Chem. Soc.* **2017**, *139*, 6018-6025; d) L. Rodríguez-Pérez, J. Ramos-

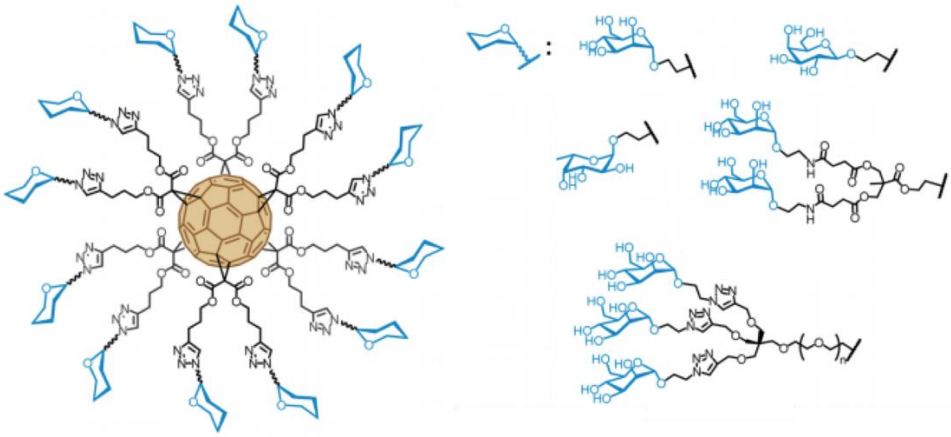

Figure 2. 3. Some examples of the [60]fullerene hexakis adducts decorated with carbohydrates designed in our research group.

However, while these protein-carbohydrates interactions can be very specific and quite strong due to multivalency effects, carbohydrate-carbohydrate interactions are weak and much poorly understood. The binding properties of multivalent nanostructures is highly dependent on their morphology. Hence, understanding how the self-assembly conditions (solvent, temperature, concentration) affect the aggregation is key to the development of this field. Self-assembling micelles, vesicles, nanofibers and gels have been reported by combining carbohydrate-carbohydrate interactions and hydrophobic interactions, such as π-π stacking.[35]

Amphiphilic perylene bisimides asymmetrically functionalized with a D-galactose unit and alkyl chains were reported by Huang *et al*.[115] Different assemblies were obtained by using binary solutions of poor (*n*-octane or water) and good solvents (chloroform or THF).[115a] Right-handed helixes where the hydrophilic sugar units are shielded, were observed in organic solvents. However, in the presence of water, the sugars were exposed to the aqueous media

Soriano, A. Pérez-Sánchez, B. M. Illescas, A. Muñoz, J. Luczkowiak, F. Lasala, J. Rojo, R. Delgado, N. Martín, *J. Am. Chem. Soc.***2018**, *140*, 9891-9898.

[115] a) Y. Huang, J. Hu, W. Kuang, Z. Wei, C. F. J. Faul, *Chem. Commun.* **2011**, *47*, 5554-5556; b) Y. Huang, J. Wang, Z. Wei, *Chem. Commun.* **2014**, *50*, 8343-8345.

stabilizing the structure via hydrogen bonding and forming left-handed superhelixes (Figure 2. 4). Moreover, the macroscopic properties were also affected as demonstrated by XRD studies, which showed a lamellar structure for the aqueous nanofibers. In a following work, the authors further adjusted the supramolecular helicity of the supramolecular asssemblies by changing the length of the alkyl chain (*n*-C_8H_{17}, *n*-$C_{12}H_{25}$ or *n*-$C_{16}H_{33}$).[115b] These small changes led to a larger π–π overlap of the vicinal perylene cores for the dodecyl-containing species, and consequently, an enhancement in the electron mobility and the conductivity of this material.

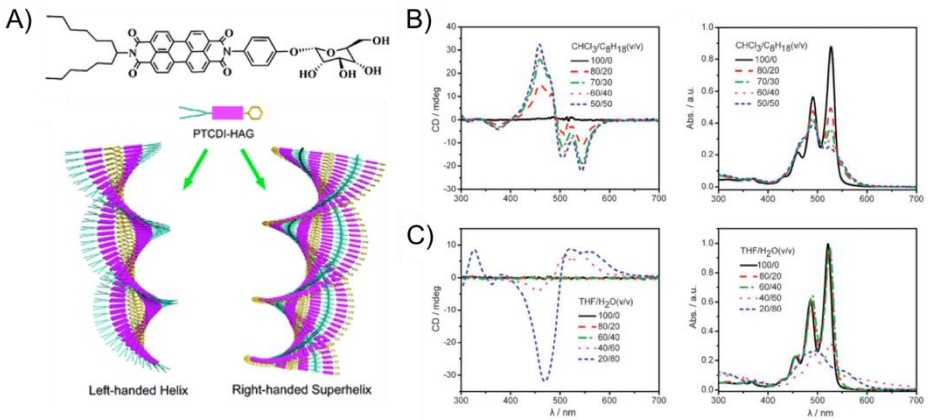

Figure 2. 4. A) Molecular structure of the PBI building block bearing a carbohydrate unit and schematic representation of the self-assembly helical nanofibers. CD and UV/Vis spectra in different volume ratios of $CHCl_3$/*n*-C_8H_{18} (B) or THF/H_2O (C).

2.1.2. Protein-based materials

Proteins are particularly attractive candidates for the construction of new biomaterials. Their versatility comes from their rich chemical alphabet, diversity of available assembly geometries, ability to bind other molecular species or nanomaterials, and the possibility of engineered function. Either computational[116] or rational approaches[117] have been developed in the area of engineering protein assemblies. Nonetheless, given the huge amount of possible structures or conformations available to proteins, engineering a sequence with predictable folding still remains as a major challenge.

The term structure in proteins, takes on a much more complex meaning than it does for small molecules. Proteins are macromolecules with four different levels of structure: primary, secondary, tertiary and quaternary (Figure 2. 5). The two most common secondary structural elements are β-sheets and α-helixes. The conformation is dictated by the amino acid sequence (primary structure) and the hydrogen-bonding pattern along the polypeptide chain (secondary structure). The α-helical arrangement is characterized by intra-peptide H-bonding along the peptide backbone, where the bonds are maintained by four amino acid pairs. This tightly-packed conformation gives rise to the formation of a twist, causing the formation of a rod. In contrast, β-strands cannot adopt the same type of hydrogen bonding and inter-peptide bonds are formed instead. The three dimensional arrangement of a single polypeptide chain containing one or more secondary structures is referred as tertiary structure. Finally, a quaternary structure is defined as the arrangement of different protein subunits, that is, multiple polypeptide chains, into a well-defined complex. Examples of natural proteins with quaternary structure include hemoglobin, DNA polymerase, and ion channels.

[116] a) S. Gonen, F. Di Maio, T. Gonen, D. Baker, *Science* **2015**, *348*, 1365-1368; b) G. Grigoryan, Y. H. Kim, R. Acharya, K. Axelrod, R. M. Jain, L. Willis, M. Drndic, J. M. Kikkawa, W. F. De Grado, *Science* **2011**, *332*, 1071-1076; c) N. P. King, J. B. Bale, W. Sheffler, D. E. McNamara, S. Gonen, T. Gonen, T. O. Yeates, D. Baker, *Nature* **2014**, *510*, 103-108.

[117] a) N. Koga, R. Tatsumi-Koga, G. Liu, R. Xiao, T. B. Acton, G. T. Montelione, D. Baker, *Nature* **2012**, *491*, 222-227; b) C. Xu, R. Liu, A. K. Mehta, R. Guerrero-Ferreira, E. R. Wright, S. Dunin-Horkawicz, K. Morris, L. C. Serpell, X. Zuo, J. S. Wall, V. P. Conticello, *J. Am. Chem. Soc.* **2013**, *135*, 15565-15578; c) J. D. Brodin, X. I. Ambroggio, C. Tang, K. N. Parent, T. S. Baker, F. A. Tezcan, *Nat. Chem.* **2012**, *4*, 375-382.

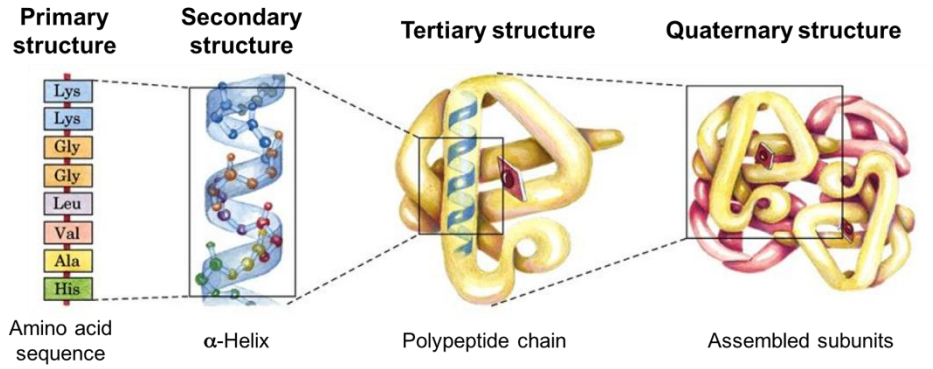

Figure 2. 5. Illustration of the different levels of structure in proteins.

Considering the structural properties of proteins, their conjugation with organic molecules would afford a precise control of the specific configuration of the chromophores relative to one another and relative to the protein itself. Many research efforts are addressed to that end, and both, natural and synthetic proteins have been reported as useful scaffold materials.[44] Really versatile protein platforms have been reported to date and are based on protein complexes naturally found in bacteria,[118] coat proteins of the filamentous plant virus Tobacco Mosaic Virus,[119] or amyloid-like protein fibrils[120], among others. Peptoid scaffolds based on α-helix arrangements have been also exploited in this field.[121] Inspired by nature, sophisticated pigment-helix conjugates that can mimic natural photosynthesis have been designed. Kang *et al.* reported a set of molecular dyads comprising Zn-porphyrins, as donors, and free-base porphyrins,

[118] a) Y. S. Nam, T. Shin, H. Park, A. P. Magyar, K. Choi, G. Fantner, K. A. Nelson, A. M. Belcher, *J. Am. Chem. Soc.* **2010**, *132*, 1462-1463; b) M. Tridgett, C. Moore-Kelly, J. H. A. Duprey, L. O. Iturbe, C. Tsang, H. A. Little, S. K. Sandhu, M. R. Hicks, T. R. Dafforn, A. Rodger, *RSC Adv.* **2018**, *8*, 29535-29543.
[119] a) R. A. Miller, A. D. Presley, M. B. Francis, *J. Am. Chem. Soc.* **2007**, *129*, 3104-3109; b) Y. S. Nam, T. Shin, H. Park, A. P. Magyar, K. Choi, G. Fantner, K. A. Nelson, A. M. Belcher, *J. Am. Chem. Soc.* **2010**, *132*, 1462-1463; c) M. Delor, J. Dai, T. D. Roberts, J. R. Rogers, S. M. Hamed, J. B. Neaton, P. L. Geissler, M. B. Francis, N. S. Ginsberg, *J. Am. Chem. Soc.* **2018**, *140*, 6278-6287.
[120] K. J. Channon , G. L. Devlin, C. E. MacPhee , *J. Am. Chem. Soc.* **2009**, *131*, 12520-12521.
[121] a) O. Y. Kas, M. B. Charati, L. J. Rothberg, M. E. Galvin, K. L. Kiick, *J. Mater. Chem.* **2008**, *18*, 3847-3854; b) R. J. Kumar, J. M. MacDonald, T. B. Singh, L. J. Waddington, A. B. Holmes, *J. Am. Chem. Soc.* **2011**, *133*, 8564-8573; c) B. Kang, W. Yang, S. Lee, S. Mukherjee, J. Forstater, H. Kim, B. Goh, T. Kim, V. A. Voelz, Y. Pang, J. Seo, *Sci. Rep.* **2017**, *7*, 4786-4796.

as acceptors, positioned with precise control along a α-helix (Figure 2. 6).[121c] Fluorescence emission and time-resolved transient absorption spectroscopy revealed efficient energy transfer processes in these structures. Interestingly, it was possible to modulate the energy transfer efficiency depending on the relative spatial arrangement of the donor-acceptor pairs in the helix.

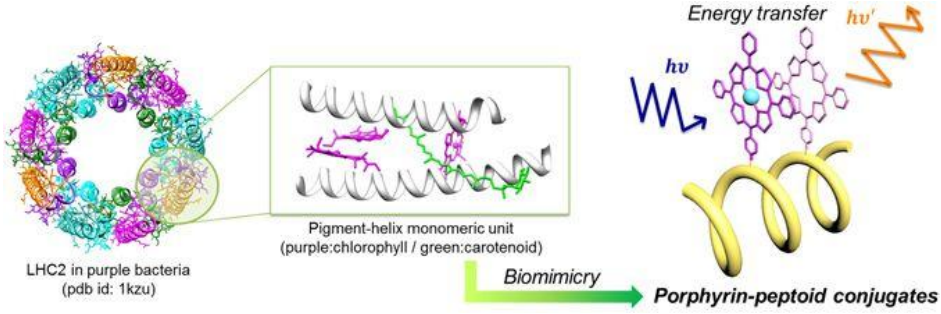

Figure 2. 6. Light-harvesting complex II in purple bacteria and a bioinspired peptoid-based conjugate containing porphyrin dyes exhibiting effective energy transfer.

A particularly abundant α-helix-based structural motif is the coiled-coil, which comprises two or more helices bundled together (Figure 2. 7. A). The sequence is frequently characterized by a seven residue repeating unit of alternating hydrophobic and hydrophilic residues. The analysis of naturally occurring coiled-coils, such as the leucine zipper,[122] has allowed scientist to predict the sequence requirements for the creation of these kind of structures. Thus, they have been exploited for a wide range of applications such as, drug delivery and the design of supramolecular materials. Coiled-coils display an inner hydrophobic core that results very attractive to carry hydrophobic drugs.[123] Moreover, the stability, selectivity and orientation of helices, make coiled-coils good candidates as template-motifs or scaffolds to create functional materials. Coiled-coils have been used to construct a variety of assemblies, including fibers, cages, and nanotubes (Figure 2. 7. B).[124]

[122] W. H. Landschulz, P. F. Johnson, S. L. McKnight, *Science* **1988**, *240*, 1759-1764.
[123] a) J. M. Mason, K. M. Arndt, *ChemBioChem* **2004**, *5*, 170-176; b) M. Pechar, R. Pola, *Biotechnol. Adv.* **2013**, *31*, 90-96.
[124] a) B. S. Der, B. Kuhlman, *Nat. Biotechnol.* **2013**, *31*, 809-810; b)J. M. Fletcher, R. L. Harniman, F. R. H. Barnes, A. L. Boyle, A. Collins, J. Mantell, T. H. Sharp, M.

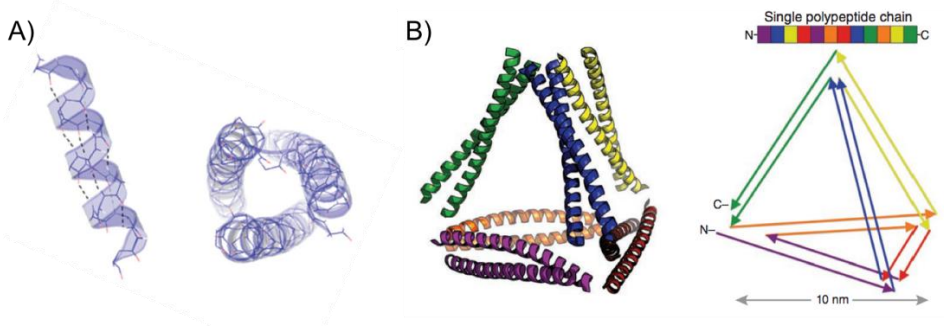

Figure 2. 7. A) α-Helix protein folding element and its oligomerisation state in coiled-coils. B) Protein nanocage engineered from 12 coiled-coil segments in a single polypeptide chain to build a regular tetrahedron.

The use of proteins for nanotechnological applications has exponentially grown in the last decades due to the great advances in experimental and theoretical methods. Another reason behind, is the possibility to produce proteins on a large scale through bacterial expression. The DNA sequence encoding the protein of interest is usually introduced in the bacteria through a plasmid, that is, circular DNA fragments naturally found in bacteria. Bacteria containing the plasmid are growth and will produce the recombinant protein using their own protein expression machinery. However, rational protein design is still far from straightforward due to the limited understanding of the sequence-structure-function relationship.[125] This problem is somewhat mitigated when working with small repeat proteins. Repeat proteins present a modular structure defined by local repeated interactions and are composed of tandem arrays of the same small structural motif.[126] Their simple architecture makes easier to understand the basic rules that relate sequence to structure for these repeated modules and make them

Antognozzi, P. J. Booth, N. Linden, M. J. Miles, R. B. Sessions, P. Verkade, D. N. Woolfson, *Science* **2013**, *340*, 595-599; c) N. C. Burgess, T. H. Sharp, F. Thomas, C. W. Wood, A. R. Thomson, N. R. Zaccai, R. L. Brady, L. C. Serpell, D. N. Woolfson, *J. Am. Chem. Soc.* **2015**, *137*, 10554-10562.

[125] J. Clarke, L. Regan, *Curr. Opin. Struct. Biol.* **2010,** *20* (4), 480-481.

[126] a) L. D. D'Andrea, L. Regan, *Trends Biochem. Sci.* **2003**, *28*, 655-662; E.R.G. Main, A.R. Lowe, S.G.J. Mochrie, S.E. Jackson, L. Regan, *Curr. Opin. Struct. Biol.* **2015**, *15*, 464-471.

ideal building blocks.[127] Among repeat protein motifs, the tricopeptide repeat module has a particular interest for the development of this chapter.

2.1.3. Tricopeptide repeat proteins.

The tricopeptide repeat, TPR, is a ubiquitous element, occurring in more than 300 natural proteins. This structural motif is normally involved in protein-protein interactions and serves as multi-protein complex mediator. In nature, TPRs are often found in tandem arrays, from 3 to 20 repeats.[128] The TPR consists of a degenerate sequence of 34 amino acids, structured into two antiparallel α-helices, designated A and B, which are separated by a short turn (Figure 2. 8. A).[128a] Helix A interacts with helix B with a packing angle of around 24º, and with helix A' of the adjacent unit, generating a right-handed super helical structure in which eight repeats comprise a full turn (Figure 2. 8. C).[129] As a consequence, the super-helix fold forms a pair of concave and convex curved surfaces which displays some extent of flexibility and permit the binding of diverse ligands.[130] The research group of Regan designed a consensus sequence (CTPR) from the statistical study of natural TPRs.[126a] They found that only a few residues are conserved, while the rest of the positions only displays a preference for small, hydrophobic or aromatic amino acids rather than for a specific residue (Figure 2. 8. B).

[127] T. Z. Grove, L. Regan, *Curr. Opin. Struct. Biol.* **2012**, *22*, 451-456; b) E. R. Main, J. J. Phillips, C. Millership, *Biochem. Soc. Trans.* **2013**, *41*, 1152-1158.
[128] a) J. R. Lamb, S. Tugendreich, P. Hieter, *Trends Biochem. Sci.* **1995**, *20*, 257-259; b) A. K. Das, P. W. Cohen, D. Barford, *EMBO J.* **1998**, *17*, 1192-1199.
[129] T. Kajander, A. L. Cortajarena, S. Mochrie, L. Regan, *Acta Crystallogr., Sect. D: Biol. Crystallogr.* **2007**, *63*, 800-811.
[130] A. L. Cortajarena, T. Kajander, W. Pan, M. J. Cocco, L. Regan, *Protein Eng., Des. Sel.* **2004**, *17*, 399-409; b) A. L. Cortajarena, L. Regan, *Protein Sci.* **2006**, *15*, 1193-1198.

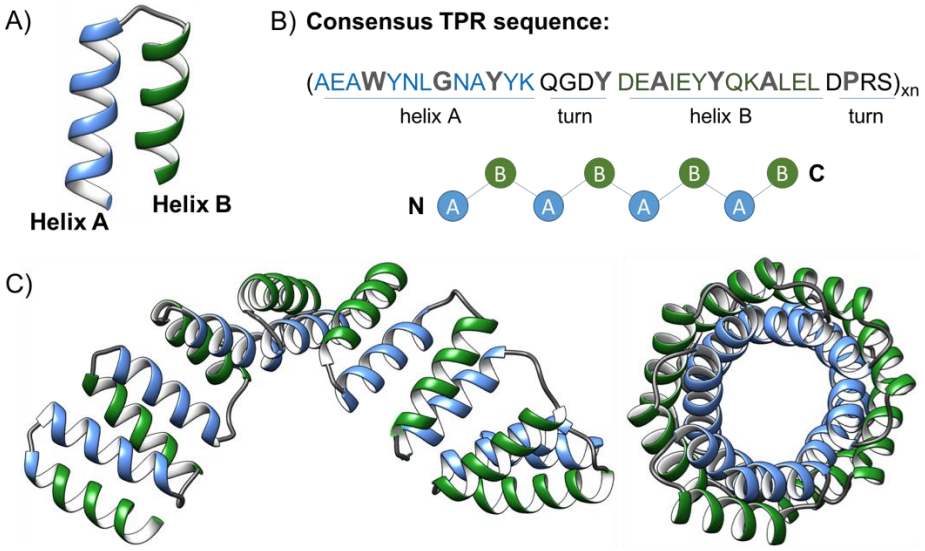

Figure 2. 8. A) CTPR unit structure is represented showing helix A in blue and helix B in green. B) Consensus TPR sequence highlighting in grey the conserved residues (positions 4, 7, 8, 11, 20, 24, 27 and 32). Below, schematic representation of the CTPR packing of A and B helixes from N-terminal to C-terminal. C) Crystal structure of a repeat protein composed of 8 CTPR repeats, showing the full turn of the super helix (PDB ID: 2AVP). On the left, perpendicular view to the super helical axis; on the right, parallel view.

The structure and stability of CTPR proteins are very well characterized. Consensus TPRs are more thermodynamically stable than their natural counterparts and are more tolerant to the destabilizing effects of mutations. Furthermore, the stability of CTPR proteins can be predicted and modulate using theoretical models by changing either the sequence of the repeats or the number of repeated units.[131]

The possibility to functionalize the CTPR protein in a controlled way opens the door to introduce functional groups at will to create hybrid materials. In this sense, Cortajarena and *col.* have successfully designed and built CTPR proteins with suitable functionalities to construct photoconductive and

[131] a) T. Kajander, A. L. Cortajarena, E. R. G. Main, S. G. J. Mochrie, L. Regan, *J. Am. Chem. Soc.* **2005**, *127*, 10188-10190; b) A. L. Cortajarena, S. G. J. Mochrie, L. Regan, *Protein Sci.* **2011**, *20*, 1042-1047.

electroactive systems, combining covalent and supramolecular modifications.[132] In collaboration with our research group, TPR scaffolds where engineered to organize porphyrin derivatives in a well-defined distance and orientation (Figure 2. 9).[132a] In this work, two cysteine residues were introduced in each repeat unit to provide reaction sites to immobilize the chromophores through thiol-maleimide click reaction. UV/Vis spectroscopy confirmed the formation of porphyrin J-type aggregates in the conjugates, certainly induced by the super helical structure of the protein scaffold. Moreover, anisotropic thin films where generated retaining the intrinsic capability of CTPR proteins to assemble into macroscopically ordered materials.

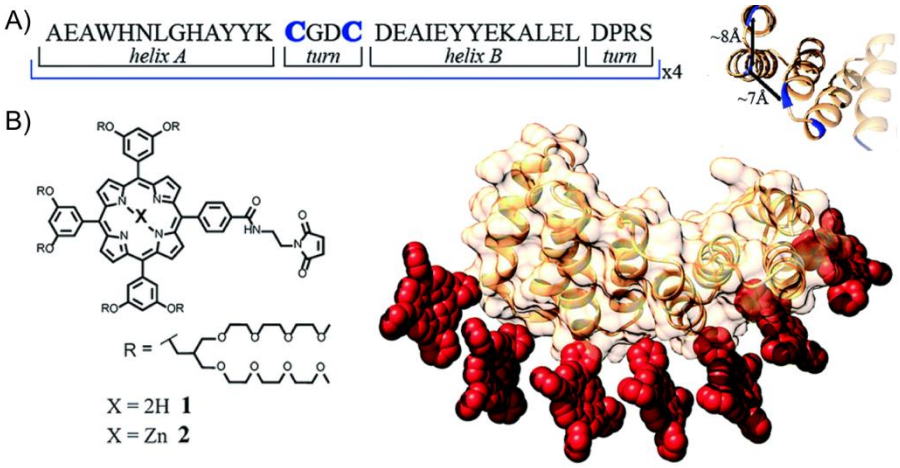

Figure 2. 9. A) Sequence of amino acids of the repeat module, highlighting the positions 14 and 17 that were mutated and its ribbon representation showing the distance between cysteine mutations. B) Molecular structure of porphyrin derivatives and 3D model structure of the **CTPR4-1** conjugate.

[132] a) S. H. Mejías, J. López-Andarias, T. Sakurai, S. Yoneda, K. P. Erazo, S. Seki, C. Atienza, N. Martín, A. L. Cortajarena, *Chem. Sci.* **2016**, *7*, 4842-4847; b) J. López-Andarias, S. H. Mejías, T. Sakurai, W. Matsuda, S. Seki, F. Feixas, S. Osuna, C. Atienza, N. Martín, A. L. Cortajarena, *Adv. Funct. Mater.* **2018**, *28*, 1704031; c) S. H. Mejias, P. Couleaud, S. Casado, D. Granados, M. A. Garcia, J. M. Abad, A. L. Cortajarena, *Colloids Surf. B Biointerfaces* **2016**, *141*, 93-101;

In a following study, the concave surface presented in CTPRs was envisioned as an attractive recognition site for the accommodation of carbon nanotubes (CNT).[132b] Positions 5 and 9, localized on the concave surface, were modified by histidine to increase the interaction with the CNT wall, together with the tyrosine residues already found in the consensus sequence. The previously reported cysteine-mutations were also included in the design to obtain donor-acceptor protein-porphyrin-CNT hybrids. Larger proteins showed an increased binding affinity for the CNT, which was even greater in the presence of the donor Zn-metalloporphyrin. Photoconductivity measurements suggested that porphyrins absorbed visible light and mobile charge carriers were generated on CNTs, with a value of electrical conductivity ($\Phi\Sigma\mu$) for the **CTPR16-porphyrin-CNT** drop-casted film of 1.8×10^{-4} cm^2 V^{-1} s^{-1}. This value was three times bigger than that obtained for the **CTPR16-CNT** film (lacking the donor species), which retained the conductivity of the pristine CNTs (Figure 2. 10. B).

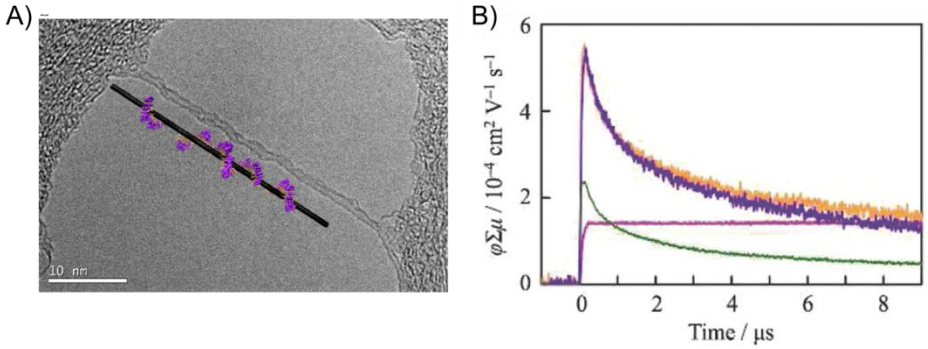

Figure 2. 10. A) TEM image of the **CTPR16-porphyrin-CNT** hybrid, showing an individualized CNT wrapped by organic material. B) Kinetic traces of conductivity transients of a film of **CTPR16-porphyrin** (magenta), **CTPR16-CNT** (yellow), and **CTPR16-porphyrin-CNT** photoexcited at 355 nm (purple), and photoexcited at 420 nm (green) at the time range of 10 μs.

2.1.4. Proteins and carbon nanoforms biohybrids

There is no doubt that the discovery of fullerenes,[77] carbon nanotubes[133] and graphene,[134] drastically changed and revolutionalised the world of nanotechnology. Recent advancement in nanoscience, biochemistry and materials chemistry has been driven by combining biological systems with carbon nanoforms. In this sense, considerable efforts have been devoted to understand the supramolecular interactions between carbon nanoforms and biological molecules.[135,136] Many works support the successful protein-conjugation with carbon nanoforms either by covalent functionalization, taking advantage of the exohedral reactivity or surface defects, or by non-covalent approaches, by weak interactions between the nanomaterial and the functional side chains. Naturally, both methodologies present drawbacks and advantages and choosing one over the other would depend on the potential application of the hybrid material. On one hand, the covalent functionalization provokes a disruption of the conjugated aromatic network, thereby modifying the structural and conductive properties of the nanomaterial. On the other hand, the non-covalent approach can be weaker and reversible, but it preserves the structural and electronic properties of the carbon nanomaterial.

Regarding the supramolecular interactions, the pockets and hydrophobic cavities of proteins are seen as ideal to host these largely hydrophobic materials. Moreover, many natural amino acids are able to interact with the π-surface of these materials through non-covalent interactions, although forming really strong conjugates. Among them, tryptophan and tyrosine, due to the presence of a bicyclic aromatic ring and an additional polar group (-OH), respectively, can give particularly stable aggregates by means of π-π stacking and XH···π (X = C, O, N) interactions. Charged and sulfur containing aa can also form strong conjugates through cation-π and S···π interactions, respectively. Hydrophobic aa are found in the binding pockets of proteins as well, entertaining CH···π interactions.[136]

[133] S. Iijima, *Nature* **1991**, *354*, 56-58.
[134] K. S. Novoselov, A. K. Geim, S. V. Morozov, D. Jiang, Y. Zhang, S. V. Dubonos, I. V. Grigorieva, A. A. Firsov, *Science* **2004**, *306*, 666-669.
[135] a) M. Calvaresi, F. Zerbetto, *Acc. Chem. Res.* **2013**, *46*, 2454-2463; b) C. Li, R. Mezzenga, *Nanoscale* **2013**, *5*, 6207-6218; c) K. Babooram, R. Narain, *Carbon Nanotubes and Fullerene C_{60} Bioconjugates* **2014**.
[136] F. De Leo, A. Magistrato, D. Bonifazi, *Chem. Soc. Rev.* **2015**, *44*, 6916-6953.

A brief introduction into the structural and electronic properties of fullerene C_{60} was already given in Section 1.3.2.3. In addition to its interesting physicochemical properties for organic electronics and materials science, fullerenes have a great potential for biomedical applications based on their unique free radical chemistry and antioxidant properties. Yet, fullerenes induce the formation of $O_2^{\cdot -}$ anions, lipid peroxidation, as well as cytotoxicity. These drawbacks may be circumvented by their bioconjugation with proteins.

The [60]fullerene surface has a relatively large affinity for binding to proteins, which is mainly driven by shape-complementarity.[136,137] The pioneer work of Friedman *et al.* revealed that the C_{60} structure presents an ideal size and shape for the formation of stable complexes with proteins.[138] They presented experimental binding essays between HIV protease (HIVP) and the water-soluble C_{60} derivative, bis(phenethylaminc-succinate) C_{60}. Through a theoretical model, they further showed the steric and chemical complementarity of the fullerene derivative with the active site. The main driving force encountered was extensive non-polar van der Waals interactions with the largely hydrophobic active site. In addition, the two amino groups in the C_{60} derivative effectively bridged the oxygens of the catalytic aspartate residues, thus inhibiting this protease. More recently, Calvaresi and Zerbetto reported a systematical screening of more than 1200 proteins from the drug target database (PDTD)[139] to shed light on the most probable sites where pristine C_{60} docks for each protein.[137] It was further verified that not only aromatic and charged aa are particularly disposed to interact with fullerene cages, but hydrophobic sites play a key role. Moreover, higher affinities may be achieved by incorporating functionalities in the pristine molecule. Primary strategies consist in adding functional groups able to form H-bonds with the residues of the protein, or water-solubilizing moieties.

Recently, fullerene-protein crystals were reported by Grigoryan and *col.*[140] They designed an artificial protein able to organize C_{60} fullerene into well-ordered lattices. The protein tetramer interacted with the fullerene molecules via

[137] M. Calvaresi, F. Zerbetto, *ACS Nano* **2010**, *4*, 2283-2299.
[138] S. H. Friedman, D. L. DeCamp, R. P. Sijbesma, G. Srdanov, F. Wudl, G. L. Kenyon, *J. Am. Chem. Soc.* **1993**, *115*, 6506-6509.
[139] Z. Gao, H. Li, H. Zhang, X. Liu, L. Kang, X. Luo, W. Zhu, K. Chen, X. Wang, H. Jiang, *BMC Bioinformatics* **2008**, *9*, 104-110.
[140] K. Kim, D. Ko, Y. Kim, N. H. Kim, J. Paul, S. Zhang, C. B. Murray, R. Acharya, W. F. DeGrado, Y. H. Kim, G. Grigoryan, *Nat. Commun.* **2016**, *7*, 11429-11438.

surface-binding sites and further self-assembled into an ordered crystalline superstructure (Figure 2. 11). Interestingly, the superstructure exhibits high charge conductance (1.40×10^{-7} S, corresponding to a resistance of 7.14×10^{6} Ω), whereas both, the protein itself and amorphous C_{60}, are electrically insulating (disordered C_{60} films showed a high electrical resistance of 2.24×10^{11} Ω). This work highlights the value of ordered fullerene-based assemblies as mentioned in the previous chapter.

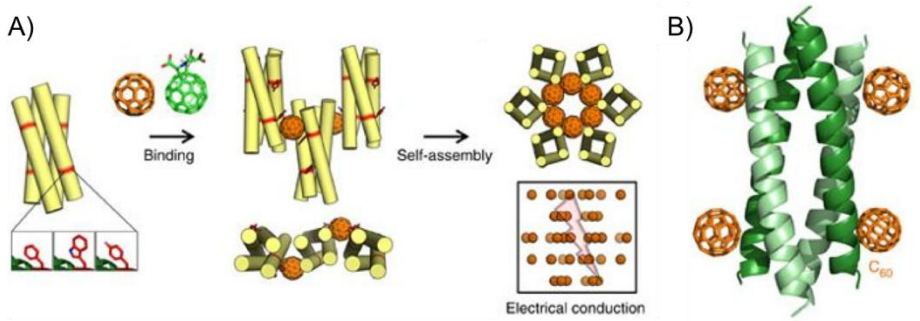

Figure 2. 11. A) Schematic representation of the tetramer in isolation, interaction with C_{60} moieties by means of a surface-binding site that includes Tyr residues (and other aromatic side chains), and further self-assembly into a conductive co-crystalline array with fullerene. B) C_{60}-peptide tetramer crystal showing the association of each tetramer with four fullerenes.

The bioconjugation of proteins with other carbon materials, such as CNTs and graphene, has been also addressed using, for instance, amyloid-like proteins to shed light on the effect of carbon nanomaterials on amyloid fibrillation.[135b] Amyloids, despite occupying a well-recognized role in degenerative diseases, can also offer a very attractive architecture to construct hybrid composites based on carbon nanomaterials. Regarding C_{60}, several derivatives have been synthesized and tested to inhibit amyloid formation with biomedical interest.[141] However, Hendler *et al.* reported the coassembly of tris-

[141] a) S. A. Andujar, F. Lugli, S. Hönger, R. D. Enriz, F. Zerbetto, *Phys. Chem. Chem. Phys.* **2012**, *14*, 8599-8607; b) A. G. Bobylev, A. B. Kornev, L. G. Bobylev, M. D. Shpagina, I. S. Fadeeva, R. S. Fadeev, D. G. Deryabin, J. Balzarini, P. A. Troshin, Z. A. Podlubnaya, *Org. Biomol. Chem.* **2011**, *9*, 5714-5719; c) A. G. Bobylev, M. D. Shpagina, L. G. Bobyleva, A. D. Okuneva, L. B. Piotrovsky, Z. A. Podlubnaya, *Biophysics*, **2012**, *57*, 300-304. d) E. G. Makarova, R. Y. a. Gordon and I. Y. a. Podolski, *J. Nanosci. Nanotechnol.* **2012**, *12*, 119-126; e) B. Ma, R. Nussinov, *Proc. Natl. Acad. Sci. U. S. A.* **2002**, *99*, 14126–14131.

malonic acid C_{60} and β-Lactoglobulin (β-Lg),[142] an amyloid-type protein with a calix-like conformation. They proved that their combination did not hinder the amyloid fibrillation process, but ensured the construction of a highly-fullerene doped fibril material (Figure 2. 12. A). Docking calculations, showed that the fullerene derivatives have preference for the entrance of the β-Lg calyxes. The shape of this ligand and the presence of carboxylic acids, promoted strong interactions with positively charged residues, besides van der Waals interactions with the hydrophobic aa in the calix entrance (Figure 2. 12. B).

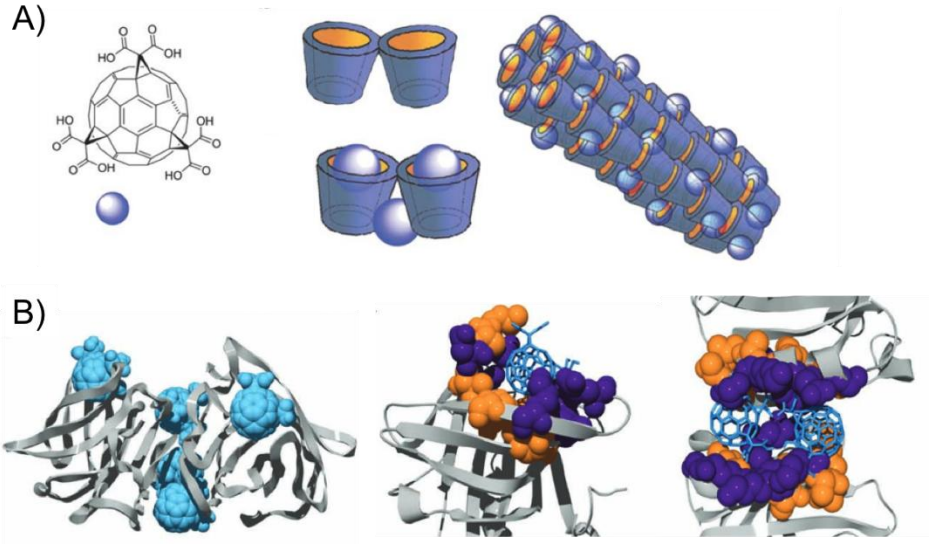

Figure 2. 12. A) Chemical structure of the C_{60} derivative and schematic representation of the ligand-protein coassembly of fibrils comprised of β-Lg complexes. B) Docking calculations of the complexes.

On the other hand, CNTs are constituted by rolled graphitic sheets.[133] They exhibit an extraordinary strength, unique electrical properties and are efficient heat conductors. The tubes can be formed out of a single layer of graphene sheet, single-walled CNT (SWCNT), or multiple graphene sheets simultaneously and concentrically rolled up, multi-walled CNTs (MWCNTs). The latter are characterized by a bigger diameter than the SWCNTs, which has

[142] N. Hendler, B. Belgorodsky, E. D. Mentovich, S. Richter, L. Fadeev, M. Gozin, *Adv. Funct. Mater.* **2012**, *22*, 3765-3776.

to be considered in reference to the size of the protein pocket. In any case, similarly to fullerenes, the driving forces for protein adsorption onto the CNT surface are van der Waals and hydrophobic interactions.[135,143] CNT-based biohybrids have demonstrated great potential for the development of novel chemical[144] and biological[145] sensing instruments, as well as for controlling binding and assembly onto templating surfaces.[146] As previously seen for fullerenes, the conjugation of CNTs with proteins ensures water-solubility and reduces their cytotoxicity.[135] More important, it has been demonstrated the great potential of proteins for the hierarchically controlled organization of nanotube-based materials (Figure 2. 13),[147] or their sorting, due to their preference for metallic CNTs.[148] In biology and medicine, promising results have been obtained in the area of implants and bioscaffolds,[149,150] cell growth and cell differentiation[151] or therapeutics.[149,152]

[143] G. Zuo, S. Kang, P. Xiu, Y. Zhao, R. Zhou, *Small* **2013**, *9*, 1546-1556.
[144] C. Staii, A. T. Johnson, M. Chen, A. Gelperin, *Nano Lett.* **2005**, *5*, 1774-1778.
[145] R. J. Chen, S. Bangsaruntip, K. A. Drouvalakis, S. K. Wong, M. Shim, Y. Li, W. Kim, P. J. Utz, H. Dai, *Proc. Natl. Acad. Sci. USA* **2003**, *100*, 4984-4989.
[146] a) P. Nednoor, M. Capaccio, V. G. Gavalas, M. S. Meier, J. E. Anthony, L. G. Bachas, *Bioconjugate Chem.* **2004**, *15*, 12-15; b) M. Sarikaya, C. Tamerler, A. K. -. Jen, K. Schulten, F. Baneyx, *Nat. Mater.* **2003**, *2*, 577-585.
[147] G. Grigoryan, Y. H. Kim, R. Acharya, K. Axelrod, R. M. Jain, L. Willis, M. Drndic, J. M. Kikkawa, W. F. DeGrado, *Science* **2011**, *332*, 1071-1076.
[148] a) K. Bradley, M. Briman, A. Star, G. Grüner, *Nano Lett.* **2004**, *4*, 253-256; b) D. Nepal, K. Geckeler, *Small* **2007**, *3*, 1259-1265.
[149] K. Kostarelos, A. Bianco, M. Prato, *Nat. Nanotechnol.* **2009**, *4*, 627-633.
[150] a) B. S. Harrison, D. Eberli, S. J. Lee, A. Atala, J. J. Yoo, Biomaterials **2007**, *28*, 4628-4634; b) C. Ménard-Moyon, K. Kostarelos, M. Prato, A. Bianco, Chem. Biol. **2010**, 17, 107-115.
[151] a) B. S. Harrison, D. Eberli, S. J. Lee, A. Atala, J. J. Yoo, *Biomaterials* **2007**, *28*, 4628-4634; b) E. Heister, E. W. Brunner, G. R. Dieckmann, I. Jurewicz, A. B. Dalton, *ACS Appl. Mater. Interfaces* **2013**, *5*, 1870-1891.
[152] Z. Liu, J. T. Robinson, S. M. Tabakman, K. Yang, H. Dai, *Materials Today* **2011**, *14*, 316-323.

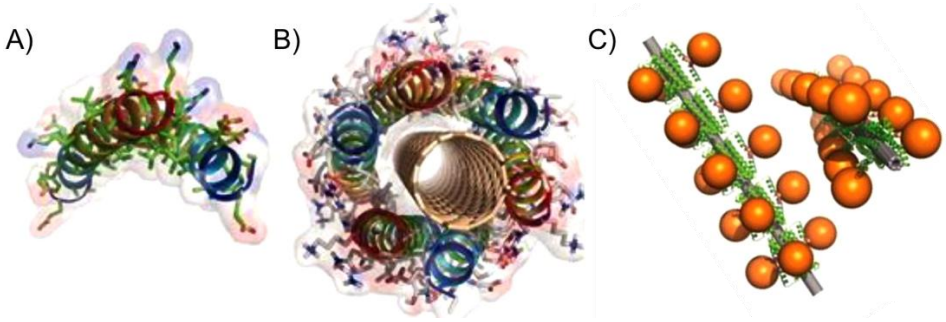

Figure 2. 13. A) *De novo* designed protein which is well poised to interact with SWCNTs. B) Model structure of the assembled-protein with a (3,8) SWCNT. C) Computational model of the hierarchical organization of CNTs with proteins and gold complexes.

Finally, graphene is a 2D material consisting of a single layer of sp^2-carbon atoms arranged in a hexagonal lattice.[134] Its fascinating electronic and physicochemical properties have generated a great interest for its combination with biomolecules. Several studies have been reported on the bioapplicability and biosafety of graphene,[153] and, as in the case of other carbon-nanomaterials, promising results arise from its bioconjugation with proteins. In this sense, nanotechnological applications, such as the development of organic electronics,[154] biosensors[155] or biomedical applications,[156] have been exploited to date. Graphene nanosheets have been stabilized by proteins to give stable dispersions in water and to feature good electron conductivity. This property was investigated by Mezzenga and co-workers to design efficient biosensors.[157] Well-organized layered structures of alternating graphene and amyloid

[153] a) S. Syama, P. V. Mohanan, *Int. J. Biol. Macromol.* **2016**, *86*, 546-555; b) A. M. Pinto, I. C. Gonçalves, F. D. Magalhães, *Colloids and Surfaces B: Biointerfaces* **2013**, *111*, 188-202; c) S. Gurunathan, J. Kim, *International journal of nanomedicine* **2016**, *11*, 1927-1945.
[154] I. M. Mosa, A. Pattammattel, K. Kadimisetty, P. Pande, M. El-Kady, G. W. Bishop, M. Novak, R. B. Kaner, A. K. Basu, C. V. Kumar, J. F. Rusling, *Adv. Energy Mater.* **2017**, *7*, 1700358.
[155] S. Viswanathan, T. N. Narayanan, K. Aran, K. D. Fink, J. Paredes, P. M. Ajayan, S. Filipek, P. Miszta, H. C. Tekin, F. Inci, U. Demirci, P. Li, K. I. Bolotin, D. Liepmann, V. Renugopalakrishanan, *Materials Today* **2015**, *18*, 513-522.
[156] S. F. Oliveira, G. Bisker, N. A. Bakh, S. L. Gibbs, M. P. Landry, M. S. Strano, *Carbon* **2015**, *95*, 767-779.
[157] C. Li, J. Adamcik, R. Mezzenga, *Nat. Nanotechnol.* **2012**, *7*, 421-427.

structures were obtained as observed by TEM and AFM in Figure 2. 14. B. The process involved the self-assembly of β-Lg amyloid fibrils at acid pH; the electrostatic aggregation of amyloid fibrils and graphene oxide; reduction of GO; and finally, layered organization of amyloid fibrils and graphene nanosheets into hybrid nanocomposites using vacuum filtration (Figure 2. 14. A). These materials showed very good physical properties in terms of Young's moduli, elongation to break and conductivity. Moreover, the nanocomposites could be degraded by simple enzymatic reactions, or used in biosensors to quantify enzymatic activities.

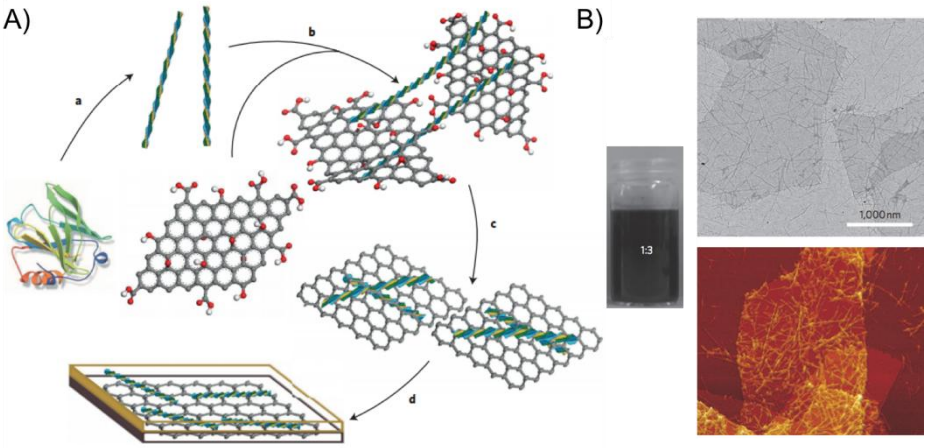

Figure 2. 14. A) Experimental methodology to obtain β-Lg-graphene composites. B) TEM and AFM images of of reduced graphene dispersions with a graphene/amyloid fibril ratio of 1:3.

The covalent modification of proteins has been widely explored as well, as shown in the examples in Section 2.1.2. Nonetheless, this is a less desirable approach to create novel bioelectronics based on CNTs and graphene. As aforementioned, a covalent transformation implies the modification of their π-surface and, as a consequence, their conductive properties.

Amide formation, reductive amination and thiol Michael addition are probably the most used chemical reactions for the conjugation with reactive

amino acids. However, no universal method to provide optimal attachment exists, and a myriad of methodologies have been developed (Figure 2. 15).[158,159]

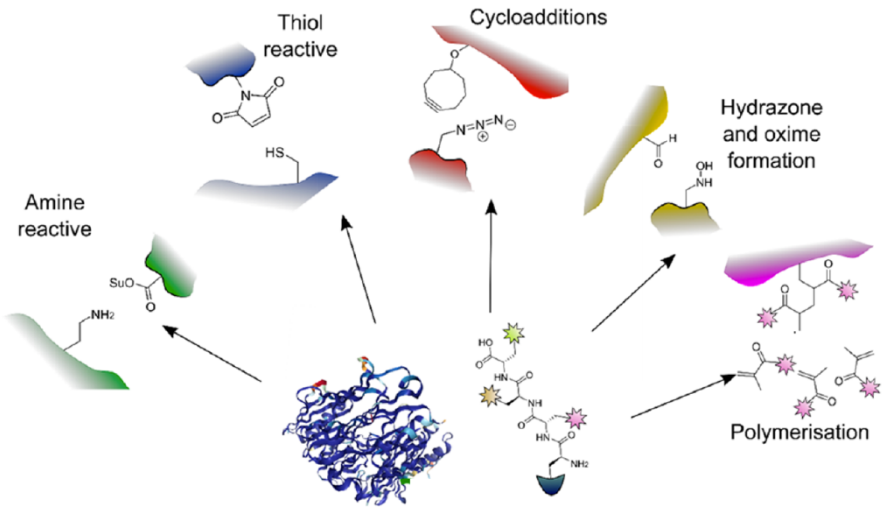

Figure 2. 15. Some of the most common covalent functionalization approaches in protein and peptide chemical modification.

[158] C. D. Spicer, E. T. Pashuck, M. M. Stevens, *Chem. Rev.* **2018**, *118*, 7702-7743.
[159] E. A. Hoyt, Cal, Pedro M. S. D., B. L. Oliveira, G. J. L. Bernardes, *Nat. Rev. Chem.* **2019**, *3*, 147-171.

2.2. Objectives

2.2. Objectives.

The aim of this chapter is the use of protein-based scaffolds for the arrangement of different organic molecules to create new biohybrids for nanotechnological applications. Based on recent advances and the knowledge and control over the stability and structure of the CTPR proteins, we will focus on this class of repeat protein as model system. We aim to introduce functionalities at defined positions of the protein for its latter conjugation with electroactive systems.

Two different approaches have been carried out using covalent or supramolecular chemistry in order to construct the new conjugates. Furthermore, we will characterize the functional properties of the generated structures. These studies will be the basis for future functional materials and structures with many potential applications in nanotechnology.

- *Exploring TPR scaffolds for the self-assembly of C_{60}.*

In the first section, CTPR proteins have been considered as good candidates for the self-assembly of C_{60}, due to the ability of fullerene derivatives to bind to proteins by means of shape-complementarity and van der Waals interactions. The CTPR sequence encompasses: i) the structural requirements to accommodate the fullerene cage through concave-convex interactions with the curved π-surface of this organic molecule; and ii) possesses a great number of aromatic amino acids, which can stabilize the C_{60} through π-π interactions.

Experimental studies will validate the composition of the protein to host fullerene and, if needed, we will consider modifying those non-conserved positions of the repeat sequence by more interacting amino acids, without affecting the structure of the protein framework.

- *Orthogonal functionalization of CTPRs for the construction of n-/p-bio-hybrids.*

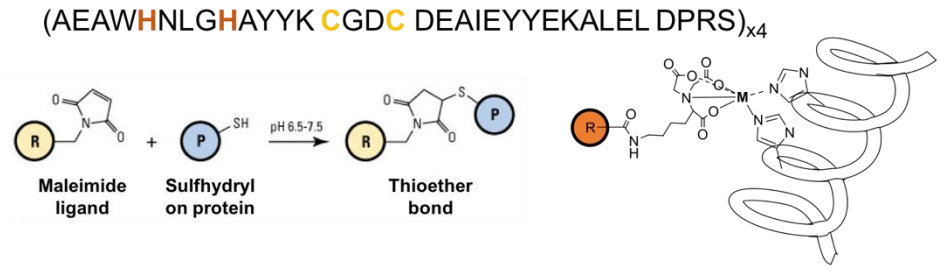

In this section we will take advantage of a previously engineered CTPR protein with two different kinds of mutations, namely, two cysteine residues pointing to the external face of the protein, and two histidines pointing to the concave cavity of the TPR. The thiol functionality would allow the covalent functionalization through thiol-ene Michael addition, while the histidines afford a coordination site by using an appropriate chelate ligand.

The latter arrangement will be tested for the construction of donor-acceptor biohybrids with enhanced electronic properties than the parent protein and the organic building blocks themselves.

2.3. Results and discussion

2.3. Results and discussion

2.3.1. Exploring TPR scaffolds for the self-assembly of C_{60}

As previously stated, proteins represent sophisticated structures capable of complex and specific reactions. A fundamental understanding of the properties of protein-based biomaterials at the nanoscale is essential for the development of new bio-nanohybrids and their application in nanotechnology.

In this work, we address the use of a designed repeat protein to organize pristine C_{60} fullerene and a more water-soluble C_{60} monoadduct, namely, C_{60} pyrrolidine tris-acid. In particular, we have selected the consensus tetraticopeptide repeat (CTPR) comprising eight repeat units as the protein scaffold (Figure 2. 16). Having in mind the structural and chemical properties of TPRs mentioned in Section 2.1.3, the existence of aromatic, hydrophobic and charged residues in the CTPR sequence could provide π-stacking and cation-π interaction sites. Moreover, working with this highly versatile repeat protein, we can introduce new residues to reinforce the interactions where needed as previously reported.[132]

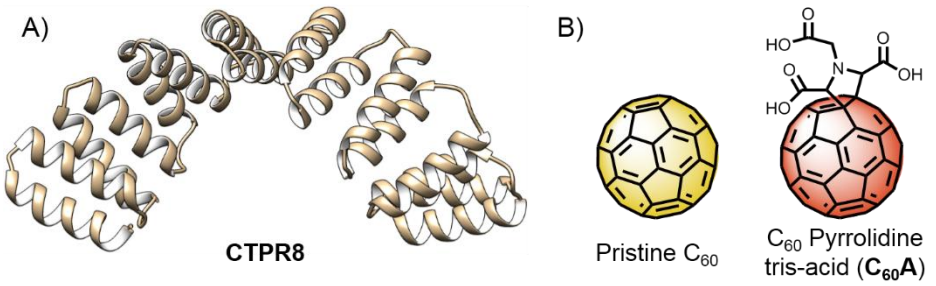

Figure 2. 16. Protein scaffold (A) and [60]fullerene derivatives (B) used in this section.

2.3.1.1. Design and synthesis of the proteins and bioconjugates.

CTPR proteins were identified as good candidates to bind to pristine C_{60} due to the high abundance of tyrosine residues (6 per repeat) to form π-π stacking interactions with the fullerenes, among other akin amino acids (Figure 2. 17. A

and C). Moreover, the existence of concave surfaces on the protein is very desirable to induce the self-assembly of the fullerene by shape-complementarity.[135,137] The protein composed of eight repeats, **CTPR8**, was chosen as the scaffold, given the stability and the well characterized properties of the eight-repeat protein. This macromolecule comprised one full superhelical turn, with a molecular dimension of approximately 80 x 36 Å (Figure 2. 17. B).

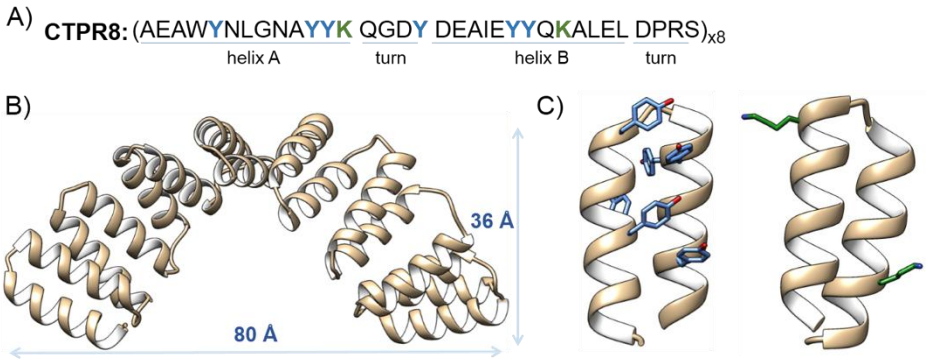

Figure 2. 17. A) Consensus TPR sequence highlighting in blue (tyrosine) and green (lysine) relevant aa for interacting with C_{60}. B) Ribbon diagram of the **CTPR8** protein indicating its size. C) CTPR unit highlighting the presence of 6 tyrosine (left) and 2 lysine (right) residues as interesting π-π or cation-π binding sites.

Excess of pristine C_{60} was added to a solution of **CTPR8** and the suspension was homogenized by tip-sonication (20 min, 0 ºC; more details in Section 2.4). The resultant suspension was centrifuged to analyze and purify the supernatant. Initial observations were promising, as the supernatant retained some dark color, revealing that some of the otherwise completely water-insoluble fullerene, was solubilized thanks to the protein. The crude was analyzed by fast protein liquid chromatography (FPLC). As we can observe in the chromatogram depicted in Figure 2. 18. A, while the former **CTPR8** appeared with a retention time of 9 min, a new material was observed at 7.5 min. This fact corroborated the successful formation of a new species with a higher hydrodynamic radius, although the major product corresponded to non-functionalized protein, **CTPR8**. This new material was isolated from the non-functionalized protein and the absorption spectra confirmed the presence of the fullerene (Figure 2. 18. B). The absorption spectra corresponding to the hybrid material, **CTPR8-C_{60}**, presented two bands at 265 and 343 nm and an additional

broad band around 450 nm (Figure 2. 18. B), while the protein itself (**CTPR8**) just posses one absorption band at 280 nm. Comparing the absorption spectra of the material with the one of pristine C_{60} (toluene solution), the first band at 265 nm should correspond to the absorption of both species, the fullerene and the protein. The other two contributions belong to the fullerene units inserted in the protein scaffold. The weak absorption at 410 nm, characteristic of the S_0-S_n transitions of C_{60}, is enhanced and very broad in the material, **CTPR8-C_{60}**. We attributed this fact to the inter-molecular interactions of the organic molecule with the residues in the protein.

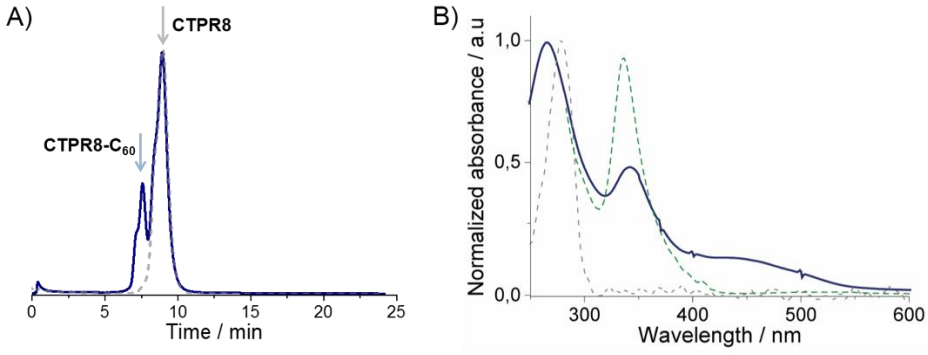

Figure 2. 18. A) FPLC chromatograms of **CTPR8** (dashed grey line) and the crude material after sonication of a solution containing pristine C_{60} and **CTPR8** (solid blue line). B) UV/Vis spectra of pristine C_{60} in toluene (dashed green line), **CTPR8** (dashed grey line) and the isolated new material, **CTPR8-C_{60}** (solid blue line).

The low extent of complex formation was attributed to the poor dispersion of the pristine fullerene in aqueous solutions even under sonication. Hence, conjugation was attempted with a more water soluble fullerene derivative, C_{60} pyrrolidine tris-acid, **C_{60}A**. In this case, a higher degree of functionalization was achieved, clearly observed in the chromatogram, which only showed a small amount of remaining free protein (Figure 2. 19. A). UV/Vis spectra of the isolated **CTPR8-C_{60}A** material showed very broad absorption features along the visible range (Figure 2. 19. B), again indicative of intermolecular interactions with the π-surface of the fullerene. This is in agreement with the spectroscopic features previously observed for the **CTPR8-C_{60}** counterpart.

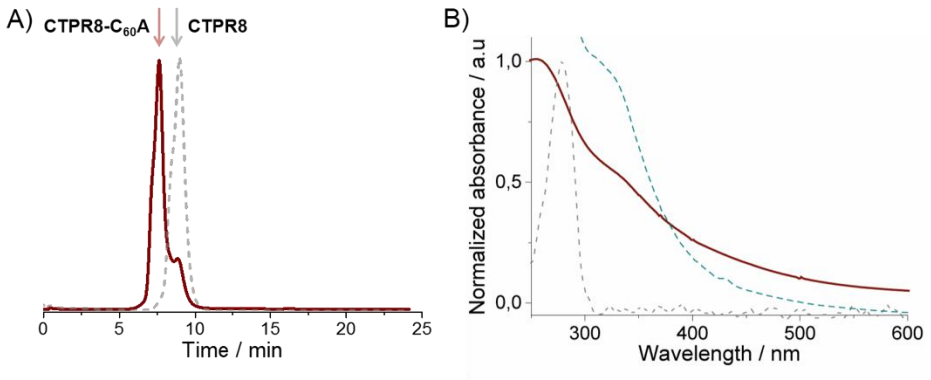

Figure 2. 19. A) FPLC chromatograms of **CTPR8** (dashed grey line) and the crude material after sonication of a solution containing **C_{60}A** and **CTPR8** (solid red line). B) UV/Vis spectra of pristine **C_{60}A** in DMSO (dashed green line), **CTPR8** (dashed grey line) and the isolated new material, **CTPR8-C_{60}** (solid red line).

The secondary structure of both materials, **CTPR8-C_{60}** and **CTPR8-C_{60}A**, was analyzed by circular dichroism spectroscopy. Virtually, no changes in the spectra were distinguished, verifying the preservation of the characteristic helical structure of the protein also in the presence of the fullerene units (Figure 2. 20).

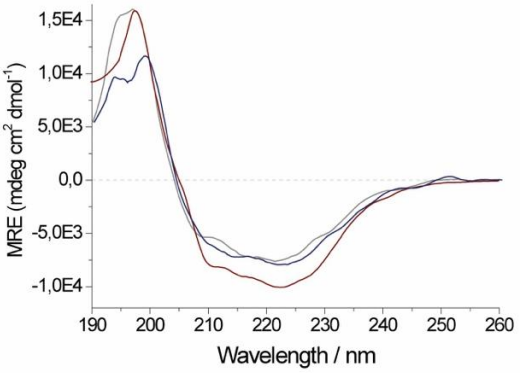

Figure 2. 20. CD spectra for the characterization of the secondary structure of **CTPR8** (grey line), **CTPR8-C_{60}** (blue line) and **CTPR8-C_{60}A** (red line).

As reported in the literature, a tight and ordered supramolecular packing in fullerenes is beneficial for intermolecular charge transport and energy transfer, which is very convenient for device development.[140,160] For that reason, we decided to reengineer the protein in order to exert more protein-fullerene interactions and, thus, take advantage of the potential conductive nature of fullerene-based assemblies. Two additional tyrosine residues were introduced in positions 2 and 9 of the A helix of every repeat, thus positioning two aromatic rings *ca*. 1 nm apart, optimal to clamp a fullerene molecule (Figure 2. 21).

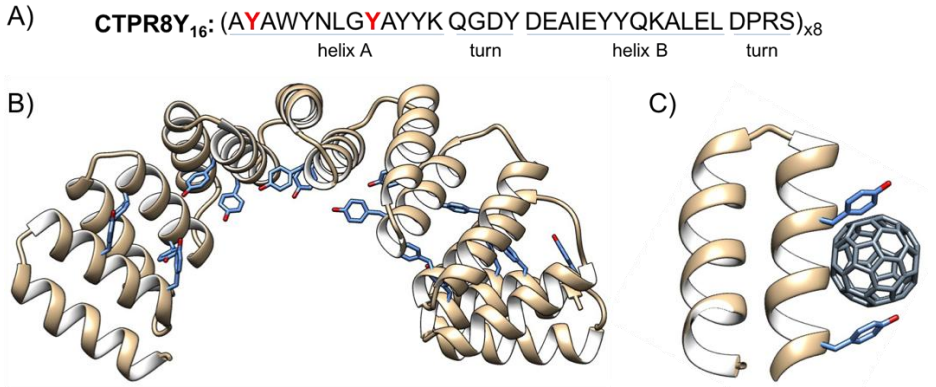

Figure 2. 21. A) Amino acid sequence of the mutated protein CTPR8Y$_{16}$ highlighting the new tyrosine residues (carbon chain in blue, O heteroatom in red). B) Modelization of the CTPR8Y$_{16}$ showing the new tyr residues. C) Modelization of one repeat unit showing the correct size of the tyrosine clamp to guest a C_{60} molecule.

The modified protein, **CTPR8Y$_{16}$**, expressed well and showed the same helical structure as the original protein. The mutant protein afforded improved fullerene binding, resulting in significantly greater amounts of hybrid materials and no free protein recovery during purification in the case of the more water-soluble **C$_{60}$A** (Figure 2. 22).

[160] a) O. Ito, F. D'Souza, *Molecules* **2012**, *17*, 5816-5835; b) J. Zhang, C. Li, S. T. Williams, S. Liu, T. Zhao, A. K. -. Jen, *J. Am. Chem. Soc.* **2015**, *137*, 2167-2170.

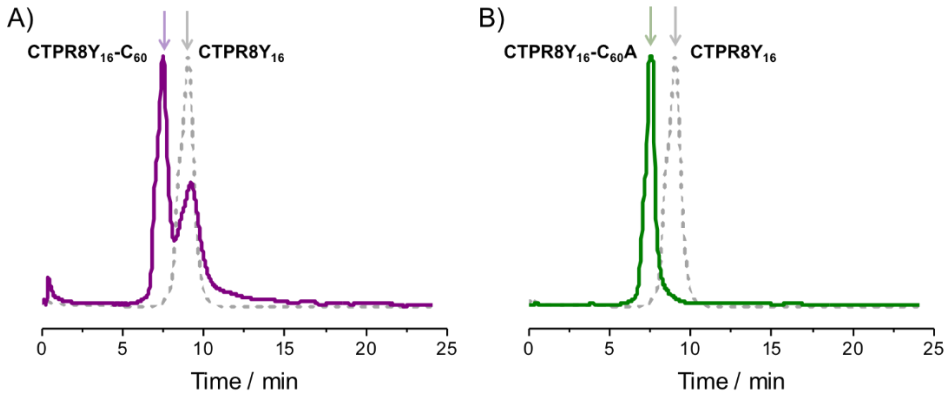

Figure 2. 22. A) FPLC chromatogram of the binding study between the mutated protein, **CTPR8Y$_{16}$** and pristine C_{60}. B) FPLC chromatogram of the binding study between the mutated protein, **CTPR8Y$_{16}$** and **C$_{60}$A**.

The **CTPR8Y$_{16}$-C$_{60}$** and **CTPR8Y$_{16}$-C$_{60}$A** hybrid materials also retained the characteristic α-helical structure of the protein. To determine the stability of these samples, the distinctive CD signal minimum at 222 nm was followed as a function of the temperature from 10 to 95°C (Figure 2. 23). Significantly, fullerene-bound proteins became more resistant to thermal denaturation than the former **CTPR8Y$_{16}$** protein. As the temperature increased, the free protein **CTPR8Y$_{16}$** reached its midpoint denaturation at T_m = 70.5 ºC. The pristine C_{60}-based conjugate, **CTPR8Y$_{16}$-C$_{60}$**, was marginally more stable (T_m = 73.0ºC), while the midpoint denaturation temperature of **CTPR8Y$_{16}$-C$_{60}$A** could not be directly determined as the protein was not completely unfolded even at 95 ºC.

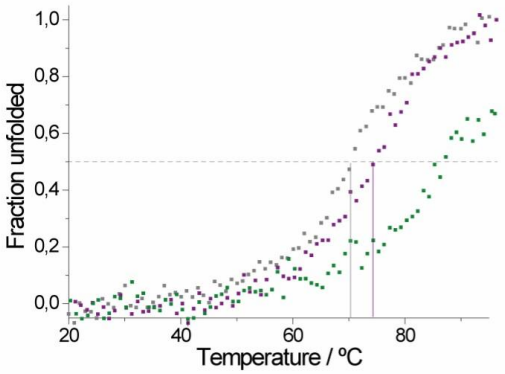

Figure 2. 23. Melting curves for **CTPR8Y$_{16}$** (grey dots), **CTPR8Y$_{16}$-C$_{60}$** (purple dots) and **CTPR8Y$_{16}$-C$_{60}$A** (green dots).

Thermal denaturation of this complex was then monitored in the presence of increasing concentrations of urea. This denature agent forms H-bonds to exposed amide groups on the protein backbone, thus destabilizing the amide-amide hydrogen bonds necessary to support the folded structure. This experiment afforded a calibration curve and the T_m for **CTPR8Y$_{16}$-C$_{60}$A** was extrapolated to 90.0ºC (Figure 2. 24). These facts confirmed the increased efficiency in the fullerene insertion not only as a matter of the water-solubility of the organic molecule, but additionally by the increased number of binding sites; and the efficient π-π interactions between the protein and the C_{60} derivatives which gave rise to a robust new material with enhanced thermal stability.

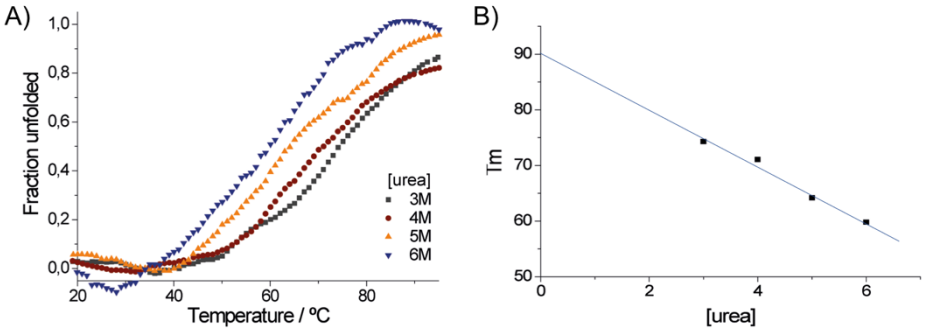

Figure 2. 24. A) Melting curves for **CTPR8Y$_{16}$-C$_{60}$A** in the presence of different concentrations of urea. B) Calibration curve obtained from the previous experiment.

2.3.1.2. Cryo-electron microscopy characterization

Cryo-electron microscopy was employed to provide structural insights into the protein-fullerene assemblies. Well-defined structures were visible in the micrographs of the **CTPR8Y$_{16}$-C$_{60}$A** assembly. 3D analysis of the samples revealed that the protein-fullerene hybrids assemble into thin 2D sheets of irregular shape, that are mostly flat, but may have a small twist. The sheets are ca. 2 nm thick, with dimensions of 20 nm x 20 nm on average, although reaching up to 50 nm (Figure 2. 25 A and C).

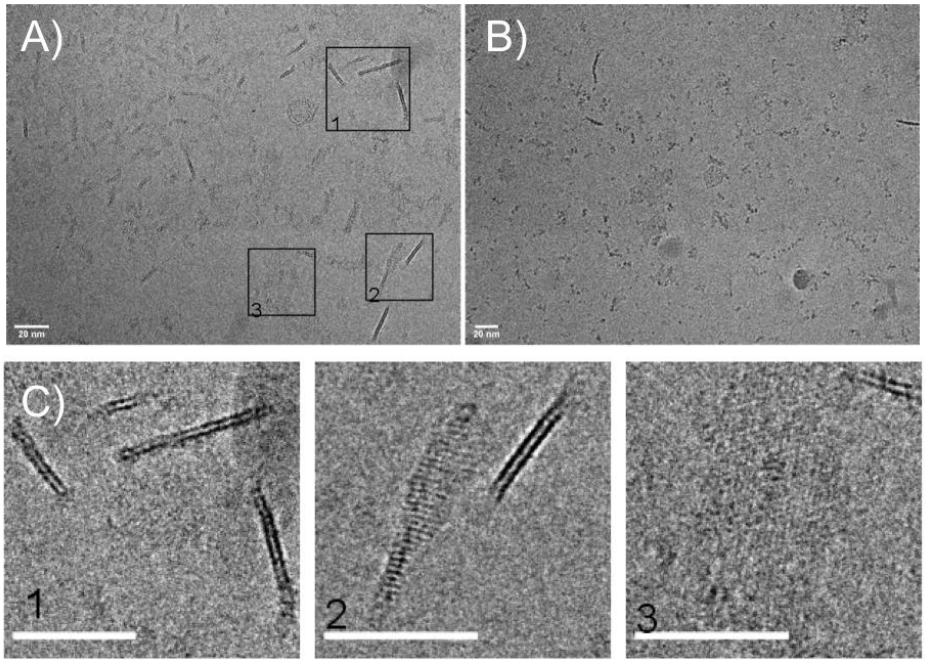

Figure 2. 25. Cryo-electron micrographs of **CTPR8Y$_{16}$-C$_{60}$A** (A) and **CTPR8-C$_{60}$A** (B) hybrid materials. C) Close-up images of the areas marked with black squares in A. Scale bars: 20 nm.

From a side view, the sheets appeared made up of two parallel high contrast bands of ca. 0.7 nm, with a low contrast band of similar thickness in between. The thickness of the film is consistent with a monolayer of CTPR protein, and the high contrast bands suggest the fullerenes are (predominantly) assembling on the surfaces of the protein monolayers. From face view, the plaques have very low contrast due to their thickness, but they are identifiable

due to a very strong diffraction pattern, which indicates that the assemblies are ordered on the molecular level. As the particles are dispersed in the vitrified fluid, diffraction patterns from individual aggregates can be studied. The observed interplanar spacing can be divided into two groups, localized in the 0.85-0.79 nm region and the region between 0.50 nm and 0.40 nm. The observed interplanar distances are consistent with the diffraction signal from ordered fullerenes, as the distances are far too big for salt crystals, but far too small to originate from protein crystals. The observed variability of diffraction distances could be a consequence of differing orientations of the ordered assemblies within the vitrified fluid, exposing diffraction patterns from different planes, or could signify that slightly different arrangements are possible for the fullerenes.

The **CTPR8-C_{60}A** assembly also formed similar 2D objects (Figure 2. 25. B), but more sparsely and of smaller size, and without the two distinct bands in the side view, but rather of uniform contrast along the 2 nm thickness. The sample also produced similar diffraction patterns, although generally of lower intensity. This result strongly suggests that although the CTPR fold alone is able to facilitate fullerene nucleation, the "tyrosine clamps" direct fullerene assembly with much higher specificity, resulting in more extensive arrangements.

In the cases of **CTPR8Y_{16}-C_{60}** and **CTPR8-C_{60}**, where pristine fullerene was used, the thin sheets were not free-floating, but instead clumped into large clusters, with various independent diffraction patterns in different parts of the clusters (Figure 2. 26).

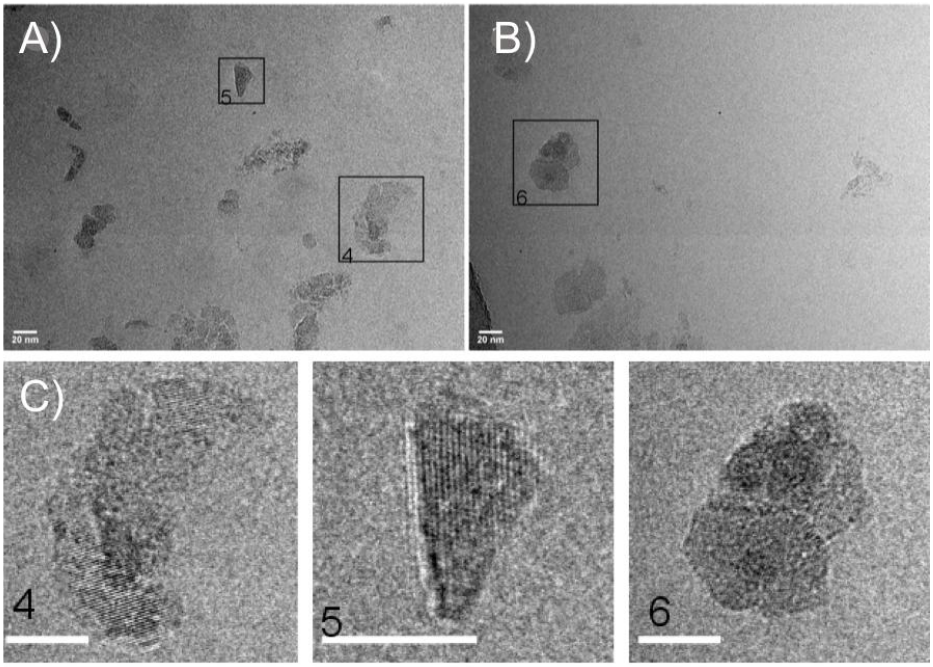

Figure 2. 26. Cryo-electron micrographs of **CTPR8Y$_{16}$-C$_{60}$** (A) and **CTPR8-C$_{60}$** (B) hybrid materials. C) Close-up images of the areas marked with black squares in A and B. Scale bars: 20 nm.

This behavior is also explained by the proposed fullerene binding mode: when bound on the surface of the protein sheets, **C$_{60}$A** orient themselves to expose the hydrophilic tris-acid appendages to the solvent, thus contributing to the solubility of the superstructures; whereas pristine C_{60} introduces hydrophobic patches of carbon, causing the sheets to coalesce (Figure 2. 27). The diffraction patterns of the C_{60} assemblies showed on average smaller spacing (0.82-0.77 nm) than those of **C$_{60}$A**, which could be an indication that greater spacing is required to accommodate the pyrrolidine-tris acid groups.

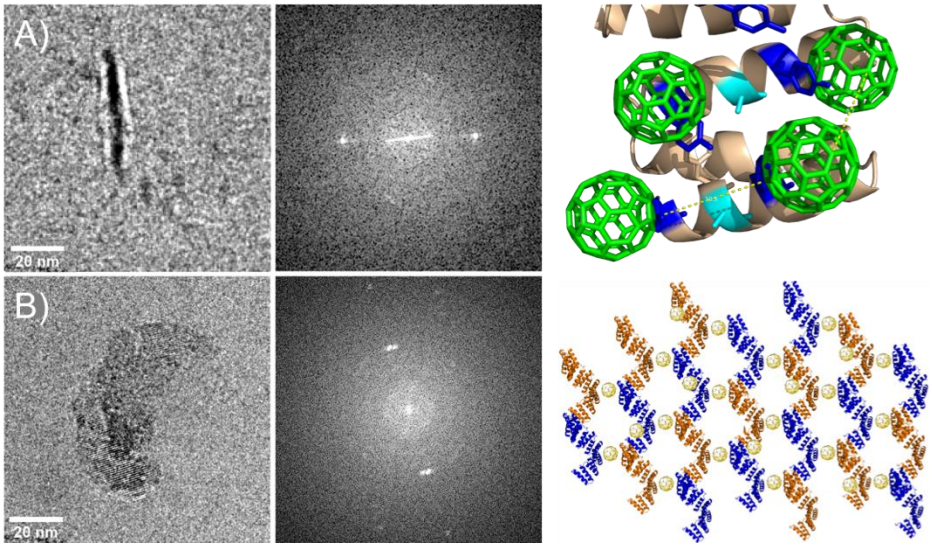

Figure 2. 27. A) From left to right, cryo-electron micrograph of **CTPR8Y$_{16}$-C$_{60}$A** and its corresponding FFT image, showing the diffraction patterns of crystalline assemblies and schematic representation of the possible assembling mode (**C$_{60}$A** is represented in green). B) From left to right, cryo-electron micrograph of **CTPR8Y$_{16}$-C$_{60}$** and its corresponding FFT image and schematic representation of the formation of the semi-crystalline plaques (C$_{60}$ is represented in yellow; every protein unit is represented with alternated colors for clarity).

2.3.1.3. Theoretical calculations.

For the better understanding of these experimental findings, theoretical calculations were performed in collaboration with the group of Prof. Silvia Osuna (Universidad de Girona).

To elucidate the molecular basis of the conjugation process, binding events were reconstructed with molecular dynamics (MD) simulations. Five replicas of 800 ns of MD were performed in the presence of eight [60]fullerene units (either pristine C$_{60}$ or **C$_{60}$A**) and one protein unit (either **CTPR8** or **CTPR8Y$_{16}$**) simulating the **CTPR8-C$_{60}$**, **CTPR8-C$_{60}$A**, **CTPR8Y$_{16}$-C$_{60}$**, and **CTPR8Y$_{16}$-C$_{60}$A** conjugates. To characterize the spontaneous binding process, all [60]fullerene species were initially placed in the solvent at least 10 Å far from the protein surface and were allowed to freely diffuse from the solvent to the

protein surface along the MD trajectory. From these spontaneous binding MD simulations, the interactions established between the fullerene species and protein units were monitored along time to identify the most visited binding sites (hot spots) on the protein surface. In all cases, we observed that [60]fullerene species rapidly collapse over the CTPR surface establishing transient interactions with the side chains of superficial protein residues. The initial recognition with CTPR8 took place in few nanoseconds of simulation time and, then, the fullerene units are displaced over the protein surface until they identify a binding site (Figure 2. 28) where commonly they remained for the rest of the simulation. Both, pristine C_{60} and **C_{60}A**, preferred to interact with the CTPR modules located at both extremes of the **CTPR8** unit while it was less frequent to observe permanent interactions with the inner hydrophobic cavity. To identify the most visited binding sites we extracted representative snapshots from the last 100 ns of each replica of the MD simulations and plotted the position of each fullerene with respect to the protein surface (see colored spheres in Figure 2. 28).

As shown in Figure 2. 28, **CTPR8-C_{60}**, **CTPR8-C_{60}A**, and **CTPR8Y_{16}-C_{60}** co-ensembles showed a wide dispersion of fullerene molecules all over the protein surface. These results indicate that, even though the fullerene species tend to be in contact with protein residues, these interactions are not stable along the MD simulation and among replicas. On the contrary, for the **CTPR8Y_{16}-C_{60}A** co-ensemble, fullerene molecules accumulate in selected hot spots independently of which MD simulation is analyzed. These results indicate that the new tyrosine residues introduced favor the association and stabilization of C_{60}A at specific binding sites of the protein surface. These observations are in line with the highest fullerene/protein ratio experimentally observed for **CTPR8Y_{16}-C_{60}A** co-ensemble.

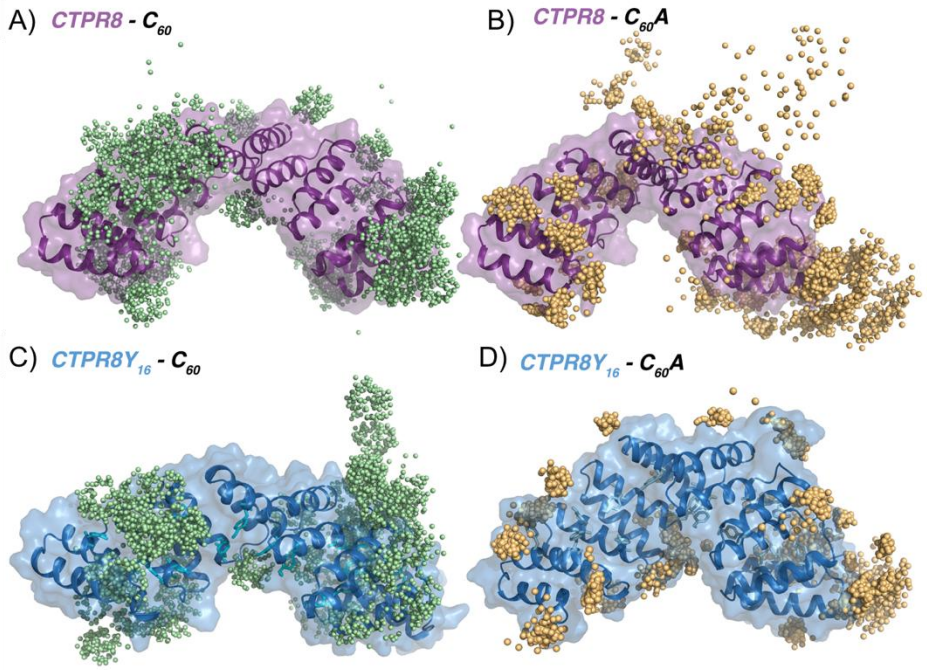

Figure 2. 28. Representative snapshots extracted from the MD simulations of: **CTPR8-C_{60}** (A), **CTPR8-C_{60}A** (B), **CTPR8Y_{16}-C_{60}** (C), and **CTPR8Y_{16}-C_{60}A** (D) co-ensembles, where colored spheres indicate the position of the pristine C_{60} (pale green) or **C_{60}A** (orange) fullerene species on the protein surface during the last 100 ns of five replicas of MD simulations.

To explore the binding mechanism of **CTPR8Y_{16}-C_{60}A** in more detail, we monitored the distance between the center of mass of **CTPR8Y_{16}** and the center of mass of each of the eight **C_{60}A** molecules along the MD trajectory (Figure 2. 29. A). As shown in Figure 2. 29. B, all **C_{60}A** units were recognized by the protein in less than 100 ns of MD simulation time. The molecules reached the final binding site after 300 ns, where they remained for the rest of the simulation. Six out of the eight fullerene molecules bound hot spots located more than 25 Å far away from the **CTPR8Y_{16}** center of mass indicating that **C_{60}A** prefer to interact with the CTPR modules located at the N- and C- terminal domains of **CTPR8Y_{16}**. Close examination of molecular interactions shows predominantly π–π interactions between **C_{60}A** and some of the introduced tyrosine residues (Figure 2. 29. C). Thus, introducing tyrosine mutations

enhanced supramolecular interactions with the aromatic surface of the fullerene, fixing the molecule in particular binding sites. In some hot spots, the fullerene is stabilized by π–stacking interactions from a total of six tyrosine residues, i.e. Tyr209, Tyr213, Tyr216, Tyr240, Tyr243, and Tyr247 (see 1 in Figure 2. 29. C) located at the extreme of the CTPR unit. These interactions retain the **C_{60}A** units in the hot spot for the rest of the simulation time. Additional binding sites were located at the inner hydrophobic cavity and displayed a broader range of interactions (see 2 in Figure 2. 29. C). The simulations revealed that Arg203 established cation···π interactions, the introduced Tyr138 on helix A displayed OH···π interactions, and Lys81 and Lys115 stabilized the carboxylate groups of the **C_{60}A** units by salt bridge interactions. Such strong interactions are not observed in the simulations where pristine C_{60} was used, being this fullerene more delocalized all over the protein surface.

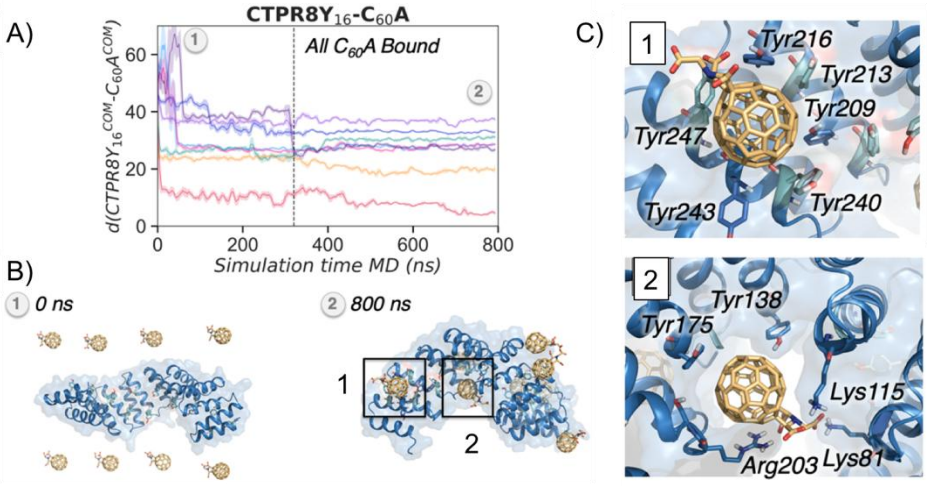

Figure 2. 29. A) Plot of the distance (Å) between the center of mass of **CTPR8Y$_{16}$** and the center of mass of the eight **C_{60}A** molecules. B) Representative snapshot extracted from the MD simulations of the **CTPR8Y$_{16}$-C_{60}A** co-ensemble at 0 ns and 800 ns simulation time. C) Relevant residues of two representative binding sites (1 and 2) of the **CTPR8Y$_{16}$-C_{60}A** co-ensemble.

To gain a deeper insight into the recognition and binding processes, five replicas of 500 ns of MD simulations with 24 **C_{60}A** molecules were performed for the mutated protein, **CTPR8Y$_{16}$**. Increasing the number of fullerenes led to their aggregation in groups of 6-8 molecules mediated by sodium cations.

Interestingly, these fullerene aggregates were accumulated at the same binding sites previously observed with a reduced number of **C_{60}A** units (Figure 2. 30. A). Finally, we explored the potential role of **C_{60}A** on **CTPR8Y$_{16}$** aggregation. To this end, five replicas of 200 ns of MD simulations were carried out with 24 **C_{60}A** molecules and three **CTPR8Y$_{16}$** protein units (Figure 2. 30. B). Our simulations show that, fullerene molecules first aggregate and, then, they contribute to the formation of **CTPR8Y$_{16}$** aggregates acting as bridge molecules between **CTPR8Y$_{16}$** units. Despite the short simulation time of these simulations and the model system used, MD simulations revealed a direct contribution of **C_{60}A** on the formation of **CTPR8Y$_{16}$** aggregates.

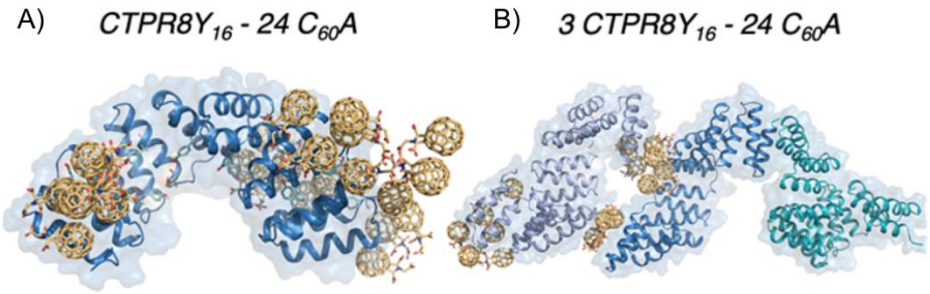

Figure 2. 30. A) Representative snapshot extracted from the MD simulations of the **CTPR8Y$_{16}$-24C_{60}A** co-ensemble at 500 ns of MD simulation. (e) Representative snapshot extracted from the MD simulations of the **3CTPR8Y$_{16}$-24C_{60}A** co-ensemble at 200 ns of MD simulation.

2.3.1.4. Photoconductivity measurements.

Finally, transient photoconductivity measurements, namely flash-photolysis time-resolved microwave conductivity (FP-TRMC),[161] were performed in the group of Prof. Shu Seki (Kyoto University) to shed light on the electron transporting nature of **CTPR8Y$_{16}$-C$_{60}$A**.

Photoexcitation of the drop-casted film of **CTPR8Y$_{16}$-C$_{60}$A** by 355 nm pulses recorded time-dependent conductivity transients whose maximum values were linear to the absorbed photon density (Figure 2. 31. A). The decay in the curve is indicative the extinction of charges due to charge trapping and/or recombination processes. The conductivity transients are plotted in Figure 2. 31. B, after normalizing the conductivity values by the absorbed photon density. The y-axis, $\phi\Sigma\mu$, represents the product of the photocarrier generation yield (ϕ) and the sum of hole and electron mobilities ($\Sigma\mu$). The maximum conductivity values $(\Sigma\mu)_{max}$ were almost constant as 2.1×10^{-5} cm^2 V^{-1} s^{-1}, independent of the photon density of the excitation pulses. Both, the films of **CTPR8** and **CTPR8Y$_{16}$** alone, did not show significant photoconductivity using the same methodology ($< 4 \times 10^{-6}$ cm^2 V^{-1} s^{-1}). Thus, the observed photoconductivity for the **CTPR8Y$_{16}$-C$_{60}$A** hybrid originates from the charge transport through fullerene contacts.

The decay curve, observed for **CTPR8Y$_{16}$-C$_{60}$A** at the excitation photon density of 9.1×10^{15} cm^{-2}, was deconvoluted by the fitting analysis and successfully fitted with a sum of exponential functions with two different time constants (Figure 2. 31. C):

$$y(t) - y_0 = y_1 \exp(-k_1 t) + y_2 \exp(-k_2 t) \qquad (1),$$

where the rate constants k_1 and k_2 are 8.12×10^4 s^{-1} and 1.26×10^6 s^{-1}, respectively. An exponential decay represents a first-order kinetics, where the generated charge carriers are trapped by some factors with a constant concentration. In the present case, two dominant charge-trapping factors would

[161] a) M. P. De Haas, J. M. Warman, *Chem. Phys.* **1982**, *73*, 35-53; b) F. C. Grozema, L. D. A. Siebbeles, *J. Phys. Chem. Lett.* **2011**, *2*, 2951-2958; c) S. Seki, A. Saeki, T. Sakurai, D. Sakamaki, *Phys. Chem. Chem. Phys.* **2014**, *16*, 11093-11113; d) O. G. Reid, D. T. Moore, Z. Li, D. Zhao, Y. Yan, K. Zhu, G. *J.* Rumbles, *Phys. D: Appl. Phys.* **2017**, *50*, 493002.

be present. We considered that carboxylic acid groups in **C_{60}A** and H_2O are the possible charge-trapping species in the material.

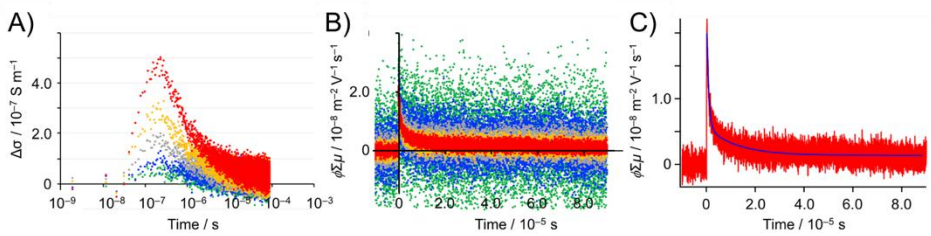

Figure 2. 31. A, B) Photoconductivity transients of **CTPR8Y$_{16}$-C$_{60}$** upon photoexcitation with 355 nm pulses with photon densities of 9.1×10^{14} (green), 1.8×10^{15} (blue), 3.7×10^{15} (gray), 6.4×10^{15} (yellow), and 9.1×10^{15} (red) cm^{-2}. A) is shown as raw conductivity changes, while B) is normalized as the product of charge carrier generation efficiency (ϕ) and sum of hole and electron mobility ($\Sigma\mu$). C) Conductivity transients (red) with fitted curve (blue) of **CTPR8Y$_{16}$-C$_{60}$** with photon densities of 9.1×10^{15} cm^{-2}.

The observed conductivity value of **CTPR8Y$_{16}$-C$_{60}$A** up to 2.1×10^{-5} cm^2 V^{-1} s^{-1} suggests a sufficient photocarrier generation yield by the self-assembled fullerene derivatives over the protein scaffold.

2.3.2. Orthogonal functionalization of CTPRs for the construction of *n*-/*p*-bio-hybrids.

For this section we proposed going one step further and use CTPR scaffolds to insert [60]fullerene derivatives in a more selective manner and subsequently construct *n*-/*p*-biomaterials by further functionalization of the protein with electron-donor moieties.

Cortajarena and co-workers previously designed and successfully expressed a set of mutated TPR proteins with different numbers of repeats (4, 8 or 16) bearing two kinds of mutations: i) two cysteine residues in the turn; and ii) two histidine residues in positions 5 and 9 of helix A (see also Section 2.1.3).[132b] To take advantage of this previous design, we have selected histidine-coordination as the most convenient method to introduce the C_{60} as *n*-type material. This arrangement will offer the possibility to further functionalize the protein through cysteine-maleimide coupling reaction to include an electron-donor as *p*-type material (Figure 2. 32).

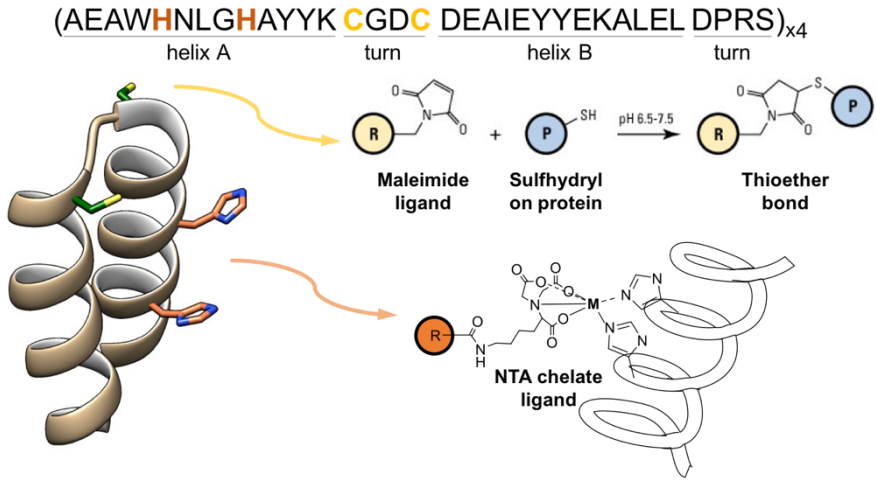

Figure 2. 32. Ribbon diagram of a single unit of mutated CTPR highlighting the cysteine and histidine residues and schematic representation of the functionalization strategy for each mutation.

In collaboration with the group of Cortajarena, an optimized approach to attach porphyrin derivatives in the turns of the helixes through a thioether by introducing two mutated cysteine residues was already developed as depicted in

Section 2.1.3.[132a] Thus, this same procedure will be followed to covalently connect porphyrins as electron donor materials. To introduce the acceptor, we have designed a C_{60} derivative suitably functionalized with a nitrilotriacetic acid chelate ligand, which has good affinity for the imidazole-based side chains of the histidine residues.

2.3.2.1. Design of mutated CTPR protein.

Considering the structural features of CTPRs, an appropriate disposition of the active sites for the orthogonal functionalization of the protein would be reached by performing a mutation in the convex surface and a different one in the concave cavity. For that reason, our previously designed protein was presented as ideal. Without going into details, since the protein used in this section was already reported in the literature,[132b] we will briefly comment on the protein features:

The mutations on the convex surface, that is, the cysteine residues on the turns between helix A and B (positions 14 and 17), were intended to immobilize water-soluble porphyrins through thiol Michael addition to a maleimide functional group on the organic dye. According to the crystal structure of CTPR, the side chains of the amino acids were located with distances of 7-8 Å, which allows stablishing π-π interactions between the porphyrin rings in a J-type arrangement. On the other hand, binding residues on the concave face in TPR proteins are mainly localized in helix A. Thus, positions 5 and 9 were mutated for histidine residues. The engineered protein, referred as **CTPR4(Cys_2His_2)** (Figure 2. 33), was successfully expressed and the mutations did not disrupt the α-helical structure characteristic of the parent protein.

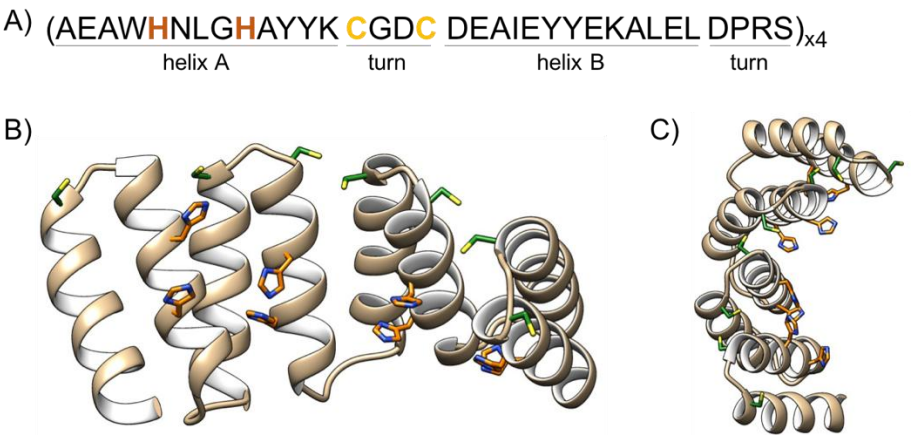

Figure 2. 33. A) Sequence of the repeat module highlighting the mutated residues: histidine, in orange, and cysteine, in yellow. B) Ribbon diagram of the mutated **CTPR4(Cys$_2$His$_2$)** showing the cysteine residues in the turns (carbon chain in green, S heteroatom in yellow) and the histidine residues in helix A (carbon chain in orange, N heteroatom in blue). C) View along the superhelical axis showing the histidine residues pointing to the concave surface and the cysteine residues pointing to the external site.

2.3.2.2. Design and synthesis of the porphyrin derivative, ***37****.*

As aforementioned, we considered reproducing the synthesis of the water-soluble Zn-porphyrin derivative previously reported in our research group.[132b] The molecular design included twelve triethylene glycol water-soluble tails and a maleimide reactive group for the conjugation with the protein.

To obtain this derivative, the first step was the synthesis of the suitably functionalized solubilizing chains (**31**). Following reported procedures,[162] we carried out the *o*-alkylation reaction of two units of triethyleneglycol monomethyl ether and 3-chloro-2-(chloromethyl)-1-propene, followed by hydroboration-oxidation of the alkene moiety and finally, tosylation of the primary alcohol (Scheme 2. 1). Product **31** was obtained with moderate yields in multigram scale.

[162] I.-S. Park, Y.-R. Yoon, M. Jung, K. Kim, S. Park, S. Shin, Y.-b. Lim, M. Lee, *Chem. Asian J.* **2011**, *6*, 452-458.

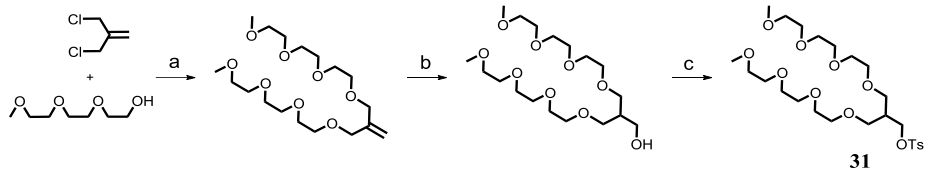

31

Scheme 2. 1. Synthesis of tosylate **31**. a) NaH, THF, rt-65 ºC, 85%; b) i) BH_3, THF, 0 ºC; ii) NaOH, 0 ºC; iii) H_2O_2, rt, 80%; c) 4-toluenesulfonyl chloride, TEA, CH_2Cl_2, rt, 55%.

On the other hand, the porphyrin precursor was synthesized under standard acid-catalyzed cross-condensation[98] of 3,5-dimethoxybenzaldehyde, methyl 4-formylbenzoate and pyrrole. Demethylation of **32** was carried out in the presence of BBr_3 to provide reactive alcohol functionalities for the etherification of **33** with the previously synthesized tosylate **31**, to yield porphyrin **34** in moderate yields. Then hydrolysis reaction of ester **34** was carried out in standard basic conditions to render the carboxylic acid **35**, suitable for amidation reaction with 2-maleimidoethylamine. Finally, the target compound **37** was obtained by metallation of the pyrrolic macrocycle in the presence of zinc acetate (Scheme 2. 2).

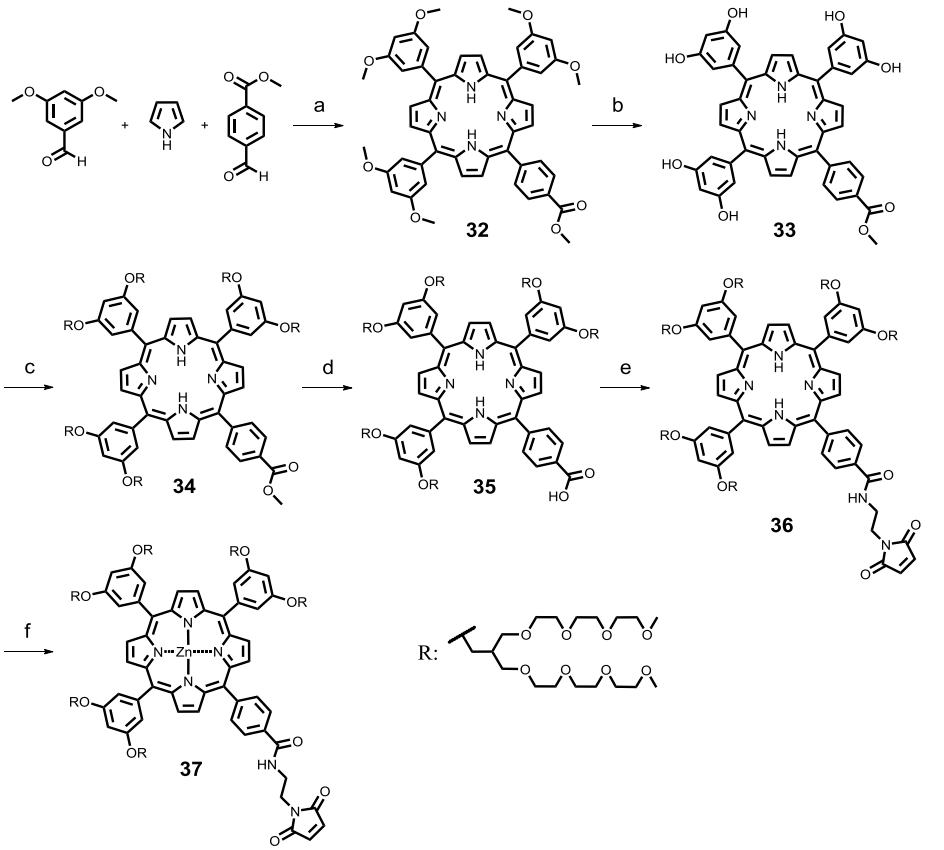

Scheme 2. 2. Synthesis of porphyrin **37**. a) i) $BF_3 \cdot Et_2O$, $CHCl_3$, rt; ii) tetrachloro-1,4-benzoquinone, 15%; b) BBr_3, CH_2Cl_2, 0 ºC-rt, 90%; c) **31**, K_2CO_3, 18-crown-6, DMF, 80 ºC, 64%; d) KOH, THF/H_2O, reflux, 51%; (e) 2-maleimidoethylamine trifluoroacetate salt, HBTU, TEA, CH_2Cl_2, rt, 73%; f) $Zn(OAc)_2 \cdot 2H_2O$, CH_2Cl_2/CH_3OH, rt, 83%.

*2.3.2.3. Design and synthesis of C_{60} monoadduct, **46**.*

In the design of the C_{60} derivative we needed to consider several requirements: i) the molecule should contain a chelate group as efficient coordination site to the histidine residues in the presence of a suitable metallic center; ii) include solubilizing groups which are not able to interact with metals, that is, anionic or highly coordinating groups should be avoided. Moreover, it is preferable that most of the hydrophobic fullerene surface is exposed to interact with the concave surface of the protein to improve protein-ligand interactions. Thus, we considered synthesizing a C_{60} monoadduct, particularly a

fulleropyrrolidine, endowed with ethyleneglycol solubilizing chains and a nitriloacetic acid-based ligand. Nitrilotriacetic acid (NTA) is a chelating agent with a strong affinity for coordinating to metal ions such as Ni^{2+}, Ca^{2+}, Co^{2+}, Cu^{2+} and Fe^{3+}. Moreover, Ni-NTA chelate-based resins are very well known for its laboratory-use for protein isolation and purification through the His-tag method.[163] The His-tag is an amino acid motif in proteins that consists of at least six histidine residues, often located at the N-terminus. Pairs of histidine residues in the His-tag bind to the vacant positions in the coordination sphere of the immobilized nickel ions with high specificity and affinity. This property has been widely exploited for the functionalization of proteins for nanotechnological and biomedical purposes.[164]

For the synthesis of the target compound, we sought to synthesize a suitable amino ester derivative for the 1,3-dipolar cycloaddition reaction with pristine C_{60}. Firstly, we started with the conversion of triethyleneglycol monomethyl ether in the corresponding tosylate **38** (Scheme 2. 3) following stablished procedures.[165]

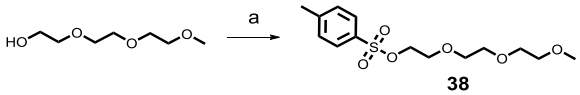

38

Scheme 2. 3. Synthesis of tosylate **38**. a) 4-toluenesulfonyl chloride, NaOH, THF/H_2O, 0 ºC-rt, 82%.

[163] a) J. Porath, J. Carlsson, I. Olsson, G. Belfrage, *Nature* **1975**, *258*, 598-599; b) J. Porath, *Protein Expr. Purif.* **1992**, *3*, 263-281.

[164] a) J. M. Abad, S. F. L. Mertens, M. Pita, V. M. Fernández, D. J. Schiffrin, *J. Am. Chem. Soc.* **2005**, *127*, 5689-5694; b) P. Jolly, A. Miodek, D. Yang, L. Chen, M. D. Lloyd, P. Estrela, *ACS Sens.* **2016**, *1*, 1308-1314; c) D. L. Johnson, L. L. Martin, *J. Am. Chem. Soc.* **2005**, *127*, 2018-2019; d) C. Xu, K. Xu, H. Gu, X. Zhong, Z. Guo, R. Zheng, X. Zhang, B. Xu, *J. Am. Chem. Soc.* **2004**, *126*, 3392-3393.

[165] a) Z. Liu, B. X. Dong, M. Misra, Y. Sun, J. Strzalka, S. N. Patel, F. A. Escobedo, P. F. Nealey, C. K. Ober, *Adv. Funct. Mater.* **2019**, *29*, 1805220; b) S. Erbas-Cakmak, F. P. Cakmak, S. D. Topel, T. B. Uyar, E. U. Akkaya, *Chem. Commun.* **2015**, *51*, 12258-12261.

Alkylation of methyl 3,4,5-trihydroxybenzoate with tosylate **38**, yielded benzoate **39**. Then, the reduction of the ester group with $LiAlH_4$ rendered alcohol **40**, which was oxidized in the presence of PCC to give rise to the aldehyde **41**.[165] Further treatment of **41** with glycine tert-butyl ester afforded imine **42**, which was reduced *in situ* with $NaBH_3CN$ to yield amine **43** (Scheme 2. 4).

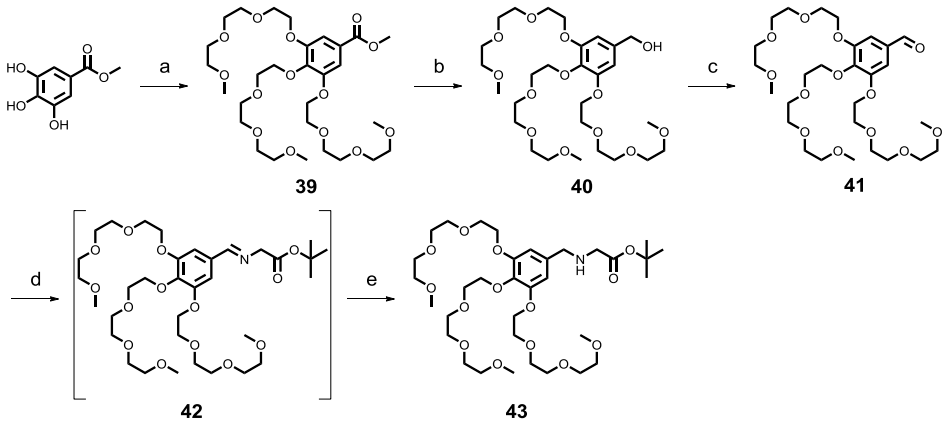

Scheme 2. 4. Synthesis of aminoester **43**. a) **38**, K_2CO_3, 18-crown-6, butanone, reflux, 86 %; b) $LiAlH_4$, THF, 0 ºC-rt, quant.; c) PCC, CH_2Cl_2, rt, 92 %; d) glycine tert-butyl ester hydrochloride, TEA, Na_2SO_4, CH_2Cl_2, rt; e) $NaBH_3CN$, acetic acid, CH_2Cl_2, 0 ºC-rt, 67 % (two steps).

1,3-Dipolar cycloaddition of the azomethine ylide precursor, which was *in situ* generated from the reaction between amino acid **43** and formaldehyde, rendered the N-substituted pyrrolidine, **44**. Finally, the tert-butyl ester group was hydrolyzed in the presence of TFA to yield pyrrolidine **45** and the NTA ligand was introduced by performing an amidation reaction with N-hydroxy succinimide as coupling agent to obtain the target product, **46** (Scheme 2. 5).

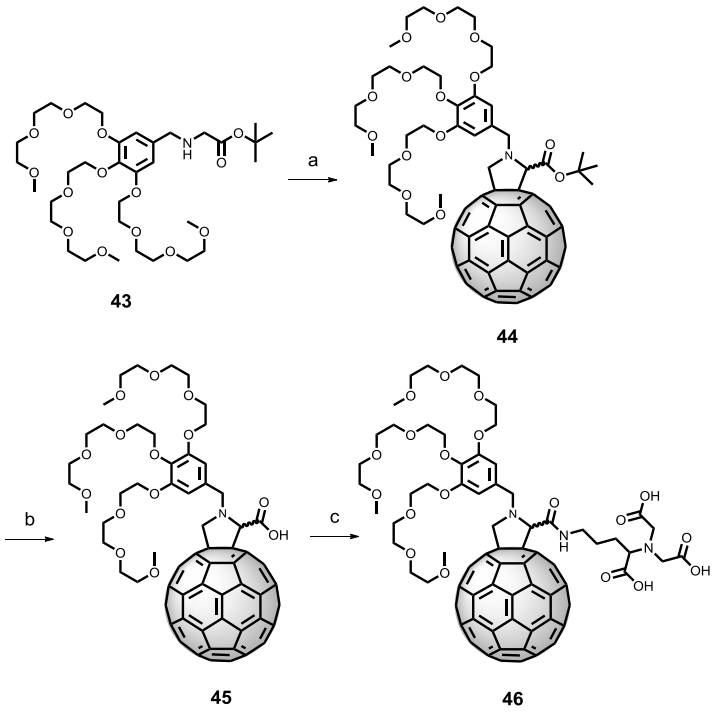

Scheme 2. 5. Synthesis of fulleropyrrolidine **46**. a) C_{60}, formaldehyde, toluene, reflux, 28 %; b) TFA, $CHCl_3$, rt, 81 %; c) i) NHS, DCC, THF, rt; ii) N_{α},N_{α}-Bis(carboxymethyl)-L-lysine hydrate, $NaHCO_3$, H_2O.

2.3.2.4. Synthesis of the CTPR conjugates.

Prior to conjugation with fulleropyrrolidine **46**, we reproduced the conjugation of porphyrin **37** with a CTPR containing four repeats with the cysteine and histidine mutations aforementioned, namely **CTPR4(Cys$_2$His$_2$)**. This protein was freshly reduced with dithio-DL-treitol (DTT) and after removal of the reducing agent, **37** was added in a ratio of 1:5 cysteine:maleimide. This mixture was mixed gently and incubated at 37 ºC for one hour. After that time, an extra excess of dye was added, giving a final ratio 1:7.5 cysteine:maleimide. The crude reaction was purified by FPLC to remove the exccess of porphyrin and isolate the new material. The success of the reaction was confirmed by gel electrophoresis that showed a new conjugate around 45 kDa, that is, a higher molecular weight than the parent **CTPR4(Cys$_2$His$_2$)** protein (19 kDa) and the porphyrin (3223 Da). This assesment could just be made with the naked eye and no need of staining, due to the characteristic color of the porphyrins. Latter on,

staining with Coomassie Blue confirmed the presence of both protein and porphyrin in the new isolated material, **CTPR4(Cys$_2$His$_2$)-37** (Figure 2. 34. A). Moreover, the UV/Vis spectrum of the latter conjugate confirmed the presence of the porphyrin, with its characteristic absorption bands as shown in Figure 2. 34. B.

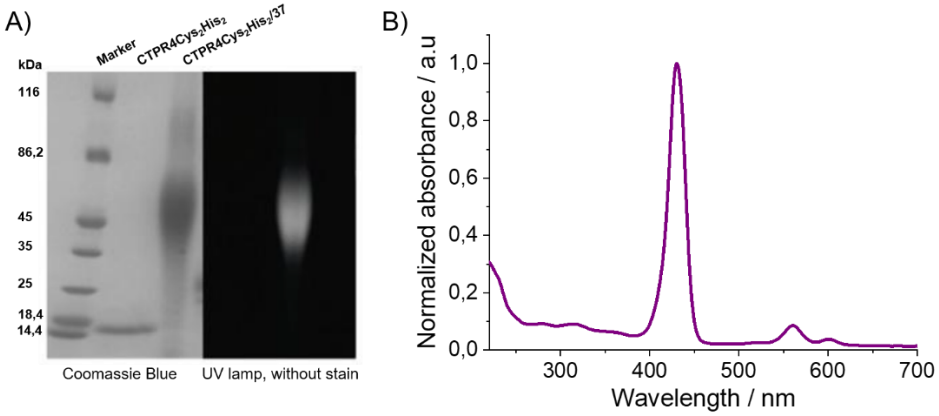

Figure 2. 34. A) SDS-Page electrophoresis gel. The gel was imaged prior staining under UV-light to monitor the fluorescence of the porphyrins (right panel); then, the gel was imaged using Coomassie Blue (left panel). Molecular weight marker (lane 1), **CTPR4(Cys$_2$His$_2$)** protein (lane 2) and **CTPR4(Cys$_2$His$_2$)-37** conjugate (lane 3). B) Absorption spectrum of **CTPR4(Cys$_2$His$_2$)-37** conjugate.

Due to the high synthetic efforts put into obtaining the C_{60} derivative **46**, we decided to test in the first place the ability of the NTA ligand to bind the mutated histidine residues in **CTPR4(Cys$_2$His$_2$)** and the corresponding conjugate containing the metalloporphyrin, **CTPR4(Cys$_2$His$_2$)-37**. For that purpose, we decided to use a rhodamine-based label, as it can be easily visualized by UV/Vis spectroscopy. In Figure 2. 35. A, the absorption and emission features of this dye are depicted. The absorption maximum of rhodamine (λ_{max} = 644 nm) does not overlap with the Soret band of porphyrin **37** (λ_{max} = 430 nm), thus allowing the monitorization of the conjugation reaction. Moreover, the commercially available isothiocyanate derivative allowed the straightforward functionalization of the dye to introduce the NTA ligand giving the corresponding thiourea derivative as depicted in Figure 2. 35. B.

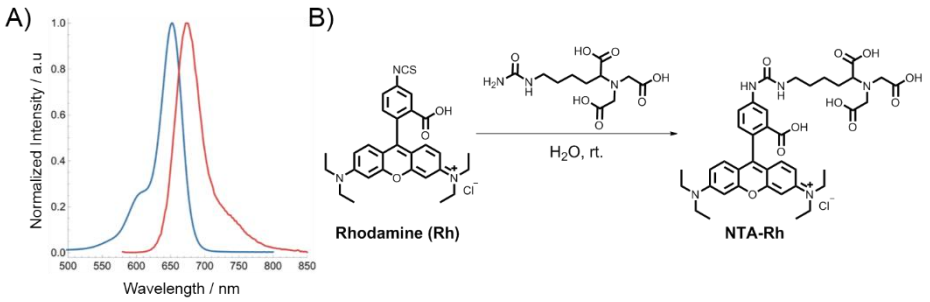

Figure 2. 35. A) Absorbance and emission spectra of rhodamine B dye. B) Functionalization of rhodamine B isothiocyanate with a NTA-containing group.

This rhodamine derivative suitably functionalized with NTA was added to an aqueous solution of **CTPR4(Cys$_2$His$_2$)** or the conjugate, **CTPR4(Cys$_2$His$_2$)-37**, in the presence and the absence of Ni^{2+}. After purification by size exclusion column chromatography, we monitored the binding assay by UV/Vis spectroscopy. We observed the absorption signature of the rhodamine only when nickel(II) chloride was added to the solution, confirming that the interaction was possible through the formation of the expected complex with the histidines in the A helix (Figure 2. 36). Moreover, in the case of the conjugate **CTPR4(Cys$_2$His$_2$)-37**, the Zn-center of the metalloporphyrin did not disrupt the coordination process.

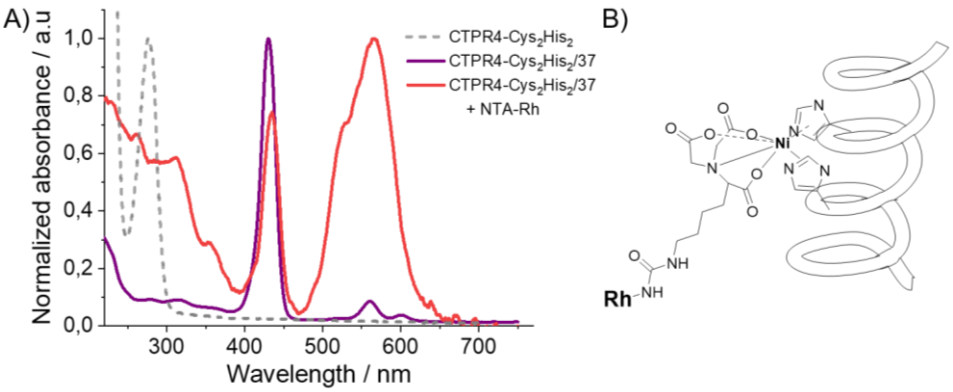

Figure 2. 36. A) UV/Vis spectra of **CTPR4(Cys$_2$His$_2$)** protein (dashed grey line) and **CTPR4(Cys$_2$His$_2$)-37** conjugate (solid purple line) and the latter conjugate after de addition of the rhodamine (**Rh**) label and a Ni^{2+} salt (solid red line). B) Schematic representation of the coordination fashion expected.

With this promising results, fullerene derivative **46**, which is under purification and characterization, will be test in due time for its conjugation with **CTPR4(Cys$_2$His$_2$)-37**.

2.4. Experimental section

2.4. Experimental section

2.4.1. Synthesis

Reagents were purchased from Sigma-Aldrich, Acros or Fluka and were used without further purification, including pristine C_{60} and C_{60} fulleropyrrolidine tris-acid used in the binding essays of Section 0. All solvents were dried using a solvent purification system or by means of standard protocols. Column chromatography was carried out on silica gel 60 (Fluka, 40-63 μm). Reverse phase chromatography was carried out on an Agilent flash chromatography system with pre-packed flash chromatography columns (TELOS, Flash C18 12g). IR spectra were recorded on a Bruker Tensor 27 spectrometer equipped with ATR and reported as wavenumbers in cm^{-1} with band intensities indicated as s (strong), m (medium), w (weak), br (broad). ^{1}H and ^{13}C NMR spectra were recorded either on a Bruker Avance-300 or a Bruker Avance AMX-700 and reported as chemical shifts (δ) in ppm relative to tetramethylsilane (δ = 0 ppm) at room temperature unless other temperature was indicated. Spin multiplicities are reported as a singlet (s), broad singlet (br s), doublet (d), triplet (t) and quartet (q) with proton-proton coupling constants (*J*) given in Hz, or multiplet (m). Matrix-assisted laser desorption ionization (MALDI) mass spectrometry (MS) was performed on a Bruker Ultraflex spectrometer.

*2.4.1.1. Synthesis of porphyrin **37***

This product was synthesized as previously reported by our research group[132] and the structures were confirmed by ^{1}H NMR.

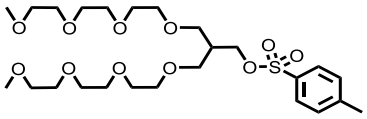

Compound 31. **13-(2,5,8,11-Tetraoxadodecyl)-2,5,8,11-tetraoxatetradecan-14-yl 4-methylbenzenesulfonate.** This product was synthesized in three steps accordingly to the established procedure. ^{1}H NMR (300 MHz, $CDCl_3$): 7.75 (d, *J* = 8.4 Hz, 2 H), 7.34 (d, *J* = 8.4 Hz, 2H), 4.08 (d, *J* = 5.6 Hz, 2H), 3.62-3.34 (m, 34H), 2.12-2.25 (m, 1H).

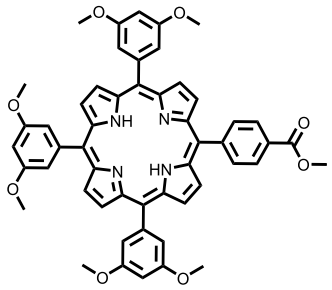

Compound 32. **Methyl 4-[10,15,20-tris(3,5-dimethoxyphenyl)-21H,23H-porphin-5-yl]-benzoate.** A mixture of 3,5-dimethoxybenzaldehyde (1.37 g, 8.22 mmol), methyl 4-formylbenzoate (450 mg, 2.74 mmol) and freshly distilled pyrrole (760 μL, 10.96 mmol) was dissolved in anhydrous chloroform (250 mL) under inert atmosphere. Boron trifluoride diethyl etherate (68 μL, 0.55 mmol) was added and the solution was stirred overnight at room temperature. Then, tetrachloro-1,4-benzoquinone (2.7 g, 11 mmol) was added to this solution, and the mixture was refluxed for 45 minutes. Solvent was then removed under reduced pressure and the crude product was purified by silica gel column chromatography (hexane/dichloromethane, from 1:1 to 1:2, v:v). Product was isolated as a deep purple solid (430 mg, 18 %). ^{1}H NMR (300 MHz, $CDCl_3$): 8.96 (d, *J* = 4.7 Hz, 2 H), 8.95 (s, 4 H), 8.77 (d, *J* = 4.7 Hz, 2 H), 8.44 (d, *J* = 8.2 Hz, 2 H), 8.30 (d, *J* = 8.2 Hz, 2 H), 8.41-8.38 (m, 6 H), 7.91-7.88 (m, 3 H), 4.11 (s, 3 H), 3.96 (s, 18 H), -2.83 (s, 2 H).

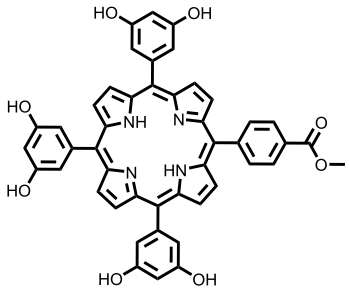

Compound 33. **Methyl 4-[10,15,20-tris(3,5-dihydroxyphenyl)-21H,23H-porphin-5-yl]-benzoate.** Compound **32** (430 mg, 0.50 mmol) was dissolved in anhydrous CH_2Cl_2 (10 mL) and the solution was cooled down to 0 ºC. Then, BBr_3 1M (5 mL, 5 mmol) was added dropwise and the solution was stirred at room temperature for two hours. Then CH_3OH (10 mL) was slowly added at 0 ºC and the mixture was stirred 20 minutes. Then, water (5 mL) were added and the irganic solvents were removed under reduced pressure. The aqueous dispersion was filtered and the solid was dried under vacuum. Pure product was obtained without further purification (385 mg, quant.). ^{1}H NMR (300 MHz, MeOD-d_4): 9.02-8.98 (m, 8 H), 8.41 (d, J = 8.2 Hz, 2 H), 8.29 (d, J = 8.2 Hz, 2 H), 7.16 (d, J = 2.2 Hz, 2 H), 7.15 (d, J = 2.2 Hz, 2 H), 6.72-6.73 (m, 3 H), 4.07 (s, 3 H).

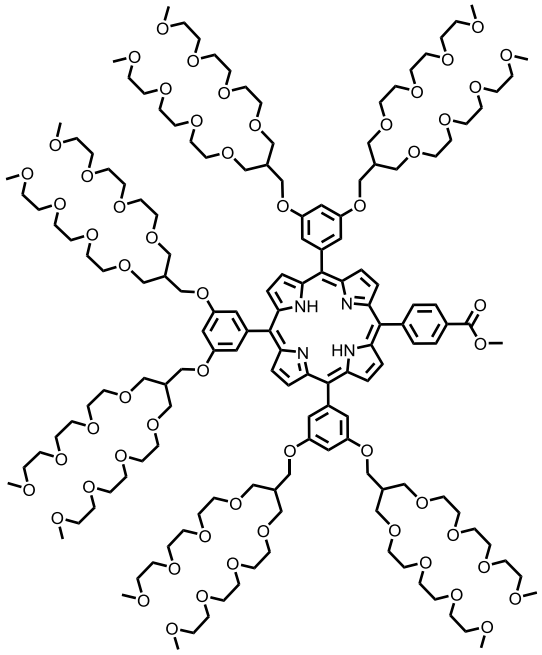

Compound 34. Methyl 4-{10,15,20-tris[3,5 -bis((13-(2,5,8,11-tetraoxadodecyl)-2,5,8,11-tetraoxatetradecan-14-yl)oxy) phenyl]-21H,23H-porphin-5-yl}-benzoate. To a solution of porphyrin **33** (350 mg, 0.45 mmol) in butanone (15 mL), 18-crown-6 (14 mg, 0.05 mmol) and K_2CO_3 (700 mg, 5.52 mmol) were added and the mixture was refluxed for one hour under inert atmosphere. To the resulting dispersion, **31** (2.05 g, 3.42 mmol) was added and the reaction mixture was refluxed for 24 hours. The solvent was then removed under reduced pressure and the crude product was dissolved in DCM and washed three times with water. The organic layer was dried over $MgSO_4$, evaporated and purified by silica gel column chromatography (CH_2Cl_2/CH_3OH 30:1), affording **30** as a purple sticky solid (879 mg, 64%). ^{1}H NMR (300 MHz, $CDCl_3$): 8.93 (br s, 6 H), 8.79 (d, *J* = 4.3 Hz, 2 H), 8.45 (d, *J* = 8.2 Hz, 2 H), 8.33 (d, *J* = 8.2 Hz, 2 H), 7.37 (d, *J* = 2.1 Hz, 6 H), 6.94 (d, *J* = 2.1 Hz, 3 H), 4.23-4.14 (m, 12 H), 4.14 (s, 3 H), 3.70-3.64 (m, 24 H), 3.60-3.54 (m, 72 H), 3.57-3.45 (m, 48 H), 3.42-3.39 (m, 24 H), 3.33-3.23 (m, 36 H), 2.55-2.47 (m, 6 H), -2.83 (br s, 2 H).

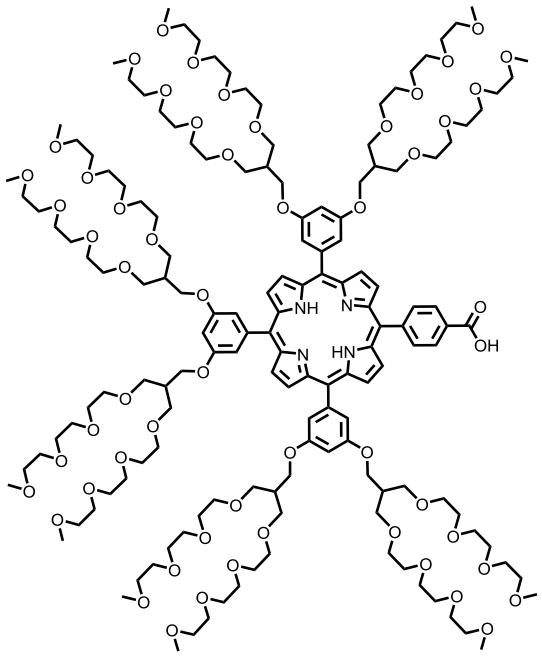

Compound 35. 4-{10,15,20- tris[3,5-bis((13-(2,5,8,11-tetraoxadodecyl)-2,5,8,11-tetraoxatetradecan-14-yl)oxy) phenyl]-21H,23H-porphin-5-yl}-benzoic acid. Compound **34** (570 mg, 0.19 mmol) was dissolved in THF/H_2O (9:1, v:v, 40 mL) and KOH (522 mg, mmol) was added. The reaction mixture was refluxed overnight. The next day, THF was removed under reduced pressure and around CH_2Cl_2 was added. The solution was transferred to an extraction funnel and HCl 0.1 M was added up to neutral pH. The product was extracted in CH_2Cl_2 (3 x 50 mL), dried over $MgSO_4$ and the solvent was removed under reduced pressure. Derivative **35** was obtained as a purple sticky oil without further purification (470 mg, 83%). ^{1}H NMR (300 MHz, $CDCl_3$): 8.93 (br s, 6 H), 8.78 (d, *J* = 4.8 Hz, 2 H), 8.54 (d, *J* = 8.2 Hz, 2 H), 8.37 (d, *J* = 8.2 Hz, 2 H), 7.42-7.35 (m, 6 H), 6.93-6.90 (d, *J* = 2.1 Hz, 3 H), 4.23-4.14 (m, 12 H), 3.72-3.64 (m, 24 H), 3.60-3.54 (m, 72 H), 3.57-3.45 (m, 48 H), 3.42-3.39 (m, 24 H), 3.33-3.23 (m, 36 H), 2.55-2.47 (m, 6 H), -2.83 (br s, 2 H).

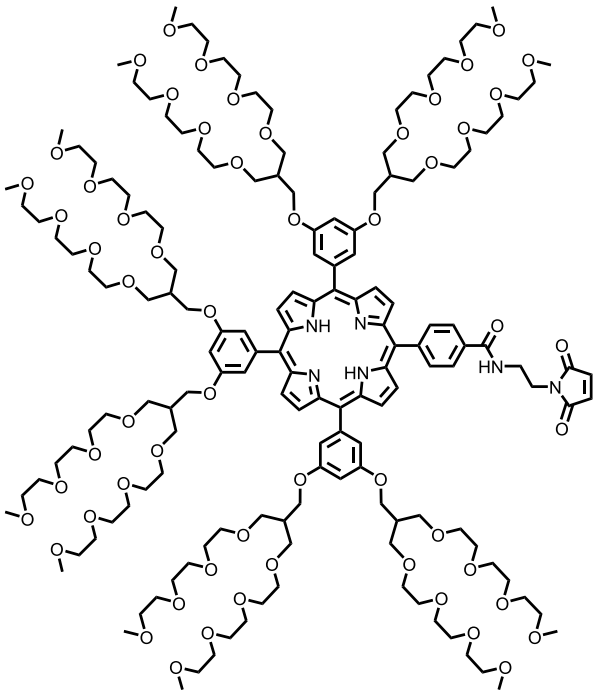

Compound 36. 4-{10,15,20-tris[3,5 -bis((13-(2,5,8,11-tetraoxadodecyl)-2,5,8,11-tetraoxatetradecan-14-yl)oxy) phenyl]-21H,23H-porphin-5-yl}- *N*-[2-(2,5-dioxo-2,5-dihydro-1H-pyrrol-1-yl) ethyl]benzamide. To a solution of **35** (120 mg, 0.039 mmol), 2-maleimidoethylamine trifluoroacetate salt (15 mg, 0.059 mmol) and HBTU (17 mg, 0.044 mmol) in anhydrous CH_2Cl_2 (3 mL), TEA (17 µL, 0.112 mmol) was added. The reaction mixture was stirred at room temperature. After 15 min, CH_2Cl_2 (25 mL) was added and the crude was washed with a saturated solution of $NaHCO_3$ (3 x 10 mL). The organic layer was dried over $MgSO_4$ and the solvent was removed under reduced pressure. The crude product was purified by PTLC (CH_2Cl_2/CH_3OH 25:1), affording **36** as a purple sticky oil (83 mg, 66%).^{1}H NMR (500 MHz, $CDCl_3$): 9.01-8.90 (m, 6 H), 8.78 (d, *J* = 4.6 Hz, 2 H), 8.29 (d, *J* = 8.0 Hz, 2 H), 8.18 (d, *J* = 8.0 Hz, 2 H), 7.37 (d, *J* = 1.8 Hz, 6 H), 7.24-7.17 (m, 1 H), 6.91 (d, *J* = 1.8 Hz, 3 H), 6.86 (s, 2 H), 4.27-4.12 (m, 12 H), 4.03-3.97 (m, 2 H), 3.89-3.85 (m, 2 H), 3.70-3.64 (m, 24 H), 3.63-3.55 (m, 72 H), 3.55-3.45 (m, 48 H), 3.44-3.37 (m, 24 H), 3.33-3.21 (m, 36 H), 2.49 (m, 6 H), -2.85 (br s, 2 H).

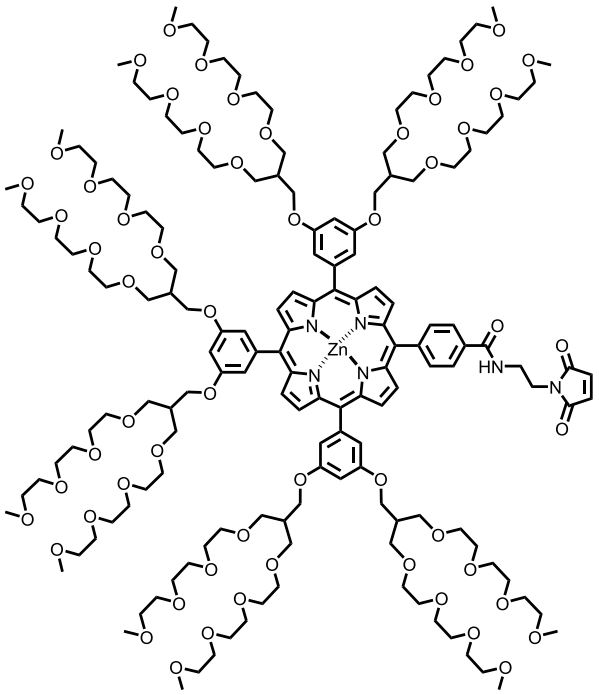

Compound 37. 4-{10,15,20-tris[3,5 -bis[((13-(2,5,8,11-tetraoxadodecyl)-2,5,8,11-tetraoxatetradecan-14-yl)oxy) phenyl]-porphin-5-yl(2-)-κ*N*^{21}, κ*N*^{22}, κ*N*^{23}, κ*N*^{24}]zinc(II)}- *N*-[2-(2,5-dioxo-2,5-dihydro-1H-pyrrol-1-yl) ethyl]benzamide. To a solution of **36** (30 mg, 9.4 µmol) in CH_2Cl_2 (3 mL), $Zn(OAc)_2 \cdot 2H_2O$ (4 mg, 18.8 µmol) in CH_3OH (3 mL) was added. The mixture was stirred 2 hours at room temperature and then, the solvent was evaporated under reduced pressure and purified by PTLC (CH_2Cl_2/CH_3OH, 25:1). The pure compound was obtained as a purple sticky solid (26 mg, 86%). ^{1}H NMR (500 MHz, $CDCl_3$): 9.04-8.94 (m, 6 H), 8.84 (m, 2 H), 8.28 (d, *J* = 8.0 Hz, 2 H), 8.16 (d, *J* = 8.0 Hz, 2 H), 7.38 (d, *J* = 1.8 Hz, 6 H), 7.18-7.09 (m, 1 H), 6.90 (d, *J* = 1.8 Hz, 3 H), 6.86 (s, 1 H), 4.26-4.15 (m, 12 H), 4.03-3.97 (m, 2 H), 3.91-3.85 (m, 2 H), 3.70-3.50 (m, 96 H), 3.47-3.38 (m, 24 H), 3.33-3.24 (m, 24 H), 3.21-3.11 (m, 24 H), 3.06-2.99 (m, 18 H), 2.54-2.46 (m, 6 H).

*2.4.1.2. Synthesis of fulleropyrrolidine **46***

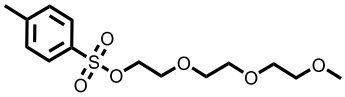

Compound 38. 2-[2-(2-ethoxyethoxy)ethoxy]-4-methylbenzenesulfonate. This product was synthesized according to reported procedures[165] and its structure corroborated by ^{1}H NMR. Triethylene glycol monomethyl ether (10 g, 61 mmol) was dissolved in water (30mL) and NaOH (4.9 g, 120 mmol) was added. Then, a solution of tosyl chloride (12.2 g, 64 mmol) in THF (30 mL) was added at 0 °C. The mixture was stirred overnight at room temperature. Afterwards, ethyl ether (60 mL) was added to the crude reaction and the organic phase was washed with water (3 x 20 mL). The combined organic layers were dried over $MgSO_4$ and evaporated under reduced pressure. The product was used without further purification (16.2 g, 84 ^{1}H NMR (300 MHz, $CDCl_3$): 7.74 (d, *J* = 8.3 Hz, 2 H), 7.30 (d, *J* = 8.3 Hz, 2 H), 4.17-4.15 (m, 2 H), 3.70-3.68 (m, 2 H), 3.61-3.59 (m, 6 H), 3.54-3.52 (m, 2 H), 3.32 (s, 3H), 2.40 (s, 3 H).

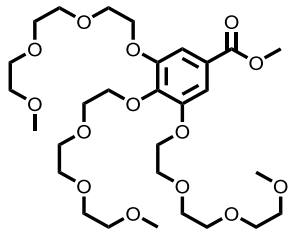

Compound 39. 3,4,5-Tris[2-[2-(2-methoxyethoxy)ethoxy]ethoxy] methylbenzoate. This product was synthesized according to reported procedures[165] and its structure corroborated by ^{1}H NMR. Methyl-3,4,5-trihydroxybenzoate (2.75 g, 15 mmol), compound **38** (15g, 47 mmol) and 18-crown-6 (1.98 g, 7.5 mmol) were dissolved in butanone (60 mL). K_2CO_3 (8.3 g, 60 mmol) was finally added and the reaction mixture was refluxed for 24 h. Then, solvent was removed under reduced pressure and the crude product was extracted with CH_2Cl_2 and brine. The organic layer was dried over $MgSO_4$ and evaporated under reduced pressure. The product was purified by silica gel column chromatography (CH_2Cl_2/CH_3OH, 50:1, v:v) and the pure product was obtained as a colorless oil (8 g, 86%). ^{1}H NMR (300 MHz, $CDCl_3$): 7.30 (s, 2

H), 4.25-4.18 (m, 6 H), 3.89 (s, 3 H), 3.88-3.79 (m, 6 H), 3.76-3.62 (m, 18 H), 3.57-3.53 (m, 6 H), 3.38 (s, 9 H).

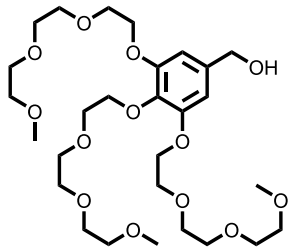

Compound 40. 3,4,5-Tris[2-[2-(2-methoxyethoxy)ethoxy]ethoxy] benzylalcohol. This product was synthesized according to reported procedures[165] and its structure corroborated by ^{1}H NMR. $LiAlH_4$ (0.28 g, 7.48 mmol) was dissolved in anhydrous THF (40 mL) at 0 ºC under inert atmosphere. Compound **39** (2.56 g, 4.12 mmol) in anhydrous THF (20 mL) was added dropwise into the solution, and the mixture was let to warm up to room temperature and was stirred 1 hour at this temperature. Quenching and workup of the crude reaction was carried out using Fieser workup to remove the unreacted $LiAlH_4$. The generated precipitate was removed by filtration through celite, and the filtrate was collected and evaporated under reduced pressure. The pure product was obtained as a yellowish oil and used without further purification (2.81 g, 95%) ^{1}H NMR (300 MHz, $CDCl_3$): 6.61 (br s, 2 H), 4.55 (s, 2 H), 4.17-4.10 (m, 6 H), 4.84-4.76 (m, 6 H), 4.73-4.61 (m, 18 H), 4.55-4.52 (m, 6 H), 3.46 (s, 1 H), 3.36 (s, 9H).

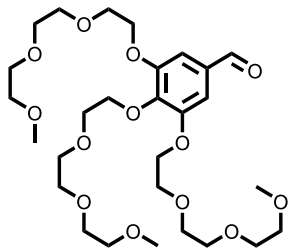

Compound 41. 3,4,5-Tris[2-[2-(2-methoxyethoxy)ethoxy]ethoxy] benzaldehyde. This product was synthesized according to reported procedures[165] and its structure corroborated by ^{1}H NMR. Compound **40** (2.4 g, 4 mmol) was dissolved in CH_2Cl_2 (25 mL). Pyridinium chlorochromate (2.15 g,

10 mmol) was added to the reaction mixture and it was stirred for two hours at room temperature. After that time, the crude reaction was directly filtered through silica gel using CH_2Cl_2/CH_3OH (40:1, v:v). The pure produt was obtained after solvent evaporation as a colorless oil (2.37 g, quant.). ^{1}H NMR (300 MHz, $CDCl_3$): 9.81 (s, 1 H), 7.13 (s, 2 H), 4.29-4.19 (m, 6 H), 3.89-3.77 (m, 6 H), 3.74-3.60 (m, 18 H), 3.56-3.51 (m, 6 H), 3.36 (s, 9 H).

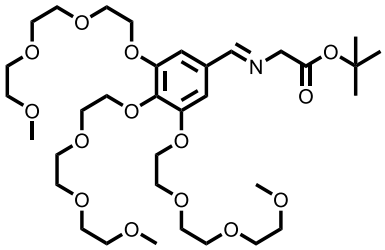

Compound 42. (E)-Tert-butyl-2-{3,4,5-Tris[2-[2-(2-methoxyethoxy)ethoxy] ethoxy]benzylidene}aminoacetate. Glycine *tert*-butyl ester hydrochloride (118 mg, 0.71 mmol) was dissolved in anhydrous CH_2Cl_2 (10 mL) over Na_2SO_4 and TEA (100 μL, 0.71 mmol). This mixture was stirred one hour at room temperature and a solution of compound **41** (420 mg, 0.71 mmol) in anhydrous CH_2Cl_2 (10 mL) was then added. The reaction was stirred two hours at room temperature and the completion of the reaction was confirmed by ^{1}H NMR. The obtained imine was directly used in the next reaction to avoid its hydrolysis. ^{1}H NMR (300 MHz, $CDCl_3$): 8.11 (s, 1 H), 7.03 (s, 2 H), 4.28 (s, 2 H), 4.19-4.12 (m, 6 H), 3.88-3.64 (m, 26 H), 3.55-3.51 (m, 6 H), 3.36 (s, 9 H), 1.48 (s, 9 H); MS (MALDI) calculated for $C_{34}H_{59}NNaO_{14}$ ($[M+Na]^+$): 728.3833; found: 728.283.

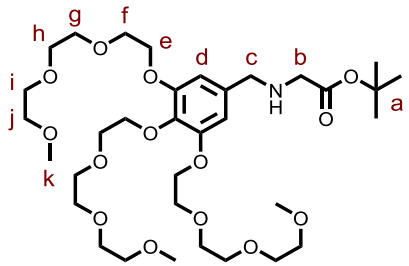

Compound 43. Tert-butyl-2-{3,4,5-Tris[2-[2-(2-methoxyethoxy)ethoxy] ethoxy]benzyl}aminoacetate. To the previously obtained imine **42**, acetic acid (100 μL, 1.78 mmol) was added at 0 ºC and the mixture was stirred for 15 min. Then, $NaBH_3CN$ (54 mg, 0.85 mmol) was added and the reaction stirred at 0 ºC one hour. The crude reaction was quenched with water and the organic phase was washed three times with water. The organic layer was dried over $MgSO_4$ and evaporated under reduced pressure. The crude product was purified by silica gel column chromatography using CH_2Cl_2/CH_3OH (50:1, v:v). The pure product was obtained as a yellowy oil (261 mg, 52%). IR (ATR): 2874 (m), 1731 (m), 1589 (s), 1200 (s), 1097 (s); 846 (s); ^{1}H NMR ($CDCl_3$, 300 MHz): 6.60 (s, 2 H_d), 4.85 (s, 1 H_{NH}), 4.20-4.12 (m, 6 H_e), 3.88-3.64 (m, 26 $H_{c+f+g+h+i}$), 3.58-3.55 (m, 8 H_{b+j}), 3.39 (s, 9 H_k), 1.44 (s, 9 H_a); ^{13}CNMR ($CDCl_3$, 125 MHz): 171.74, 153.21, 152.85, 152.61, 107.65, 81.40, 72.39, 72.05, 70.92, 70.81, 70.67, 69.87, 69.76, 69.15, 68.89, 59.17, 53.47, 50.96, 28.27; HRMS (MALDI) calculated for $C_{34}H_{61}NNaO_{14}$ ($[M+Na]^+$): 730.3990; found: 730.4014.

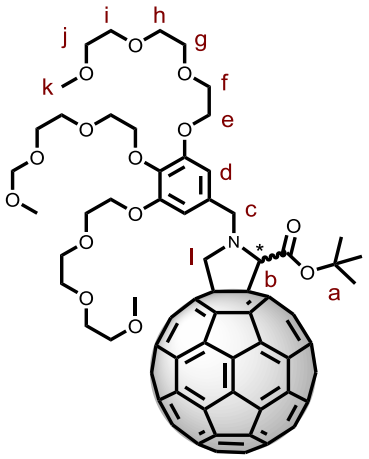

Compound 44. N-{3,4,5-Tris[2-[2-(2-methoxyethoxy)ethoxy] ethoxy]benzyl}-2-tert-butoxycarbonylpyrrolidino-[3,4:1,2][60]fullerene *(R,S)*. A solution of **43** (100 mg, 0.14 mmol), C_{60} (200 mg, 0.28 mmol) and formaldehyde (4.2 mg, 0.14 mmol) in anhydrous toluene (250 mL) was reacted at 100 ºC under inert atmosphere and monitored by TLC. After 2.5 hours the reaction was let to cooled down and most of the toluene was evaporated under reduced pressure. The crude product was purified by silica gel column chromatography (eluent: toluene to complete elution of free C_{60}, then CH_2Cl_2 to CH_2Cl_2/CH_3OH, 50:1, v:v). Pure product was obtained as a brown powder (86 mg, 43%). IR (ATR): 2917 (s), 2869 (s), 1731 (m), 1442 (m); 1106 (s), 849 (s); ^{1}H NMR ($CDCl_3$, 700 MHz): 6.95 (s, 2 H_d), 4.97 (s, 1 H_b), 4.92 (d, *J* = 9.3 Hz, 1 H_c), 4.56 (d, *J* = 13.1 Hz, 1 H_l), 4.28-4.21 (m, 1 H_c + 6 H_e), 4.06 (d, *J* = 13.1 Hz, 1 H_l), 3.92-3.83 (m, 6 H_f), 3.78-3.64 (m, 18 H_{g+h+i}), 3.57-3.53 (m, 6 H_j), 3.38 (s, 9 H_k), 1.53 (s, 9 H_a); ^{13}CNMR ($CDCl_3$, 125 MHz): 169.0, 154.9, 154.8, 153.9, 152.8, 151.3, 147.4, 147.3, 146.5, 146.4, 146.4, 146.3, 146.3, 146.1, 146.1, 145.9, 145.8, 145.7, 145.6, 145.5, 145.4, 145.4, 145.3, 145.3, 144.7, 144.6, 144.5, 144.5, 143.1, 143.1, 142.7, 142.7, 142.6, 142.3, 142.2, 142.2, 142.1, 142.1, 142.0, 142.0, 141.9, 141.8, 141.8, 140.3, 140.3, 139.8, 139.3, 137.8, 137.6, 136.4, 136.0, 135.5, 132.7, 132.1, 108.2, 83.1, 76.4, 72.9, 72.4, 72.0, 71.9, 70.8, 70.7, 70.7, 70.6, 70.5, 70.0, 69.5, 68.9, 64.6, 59.1, 55.8, 28.4; HRMS (MALDI) calculated for $C_{95}H_{61}NNaO_{14}$ ($[M+Na]^+$): 1462.3990; found: 1462.3936.

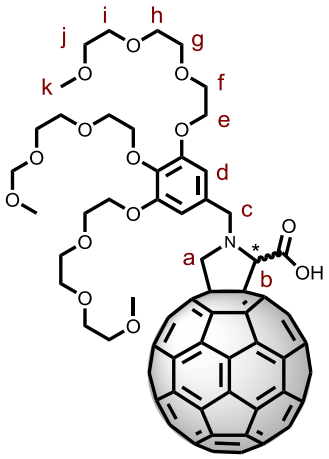

Compound 45. N-{3,4,5-Tris[2-[2-(2-methoxyethoxy)ethoxy] ethoxy]benzyl}-2-carboxypyrrolidino-[3,4:1,2][60]fullerene *(R,S)*. A solution of compound **44** (40 mg, 0.028 mmol) dissolved in a mixture of CH_2Cl_2/TFA (1:1, v:v, 2 mL) was stirred for 2 hours at room temperature. Afterwards, the solvent was removed under reduced pressure and the crude product was purified by silica gel column chromatography using a mixture of CH_2Cl_2:CH_3OH (50:1 to 25:1, v:v) as eluent. The product **45** was obtained as a brownish solid. (37 mg, 95%). IR (ATR): 3529 (br), 2924 (s), 2861 (s), 1732 (m), 1438 (m); 1107 (s), 839 (s); ^{1}H NMR ($CDCl_3$, 700 MHz): 7.01 (s, 2 H_d), 4.83 (d, *J* = 9.1 Hz, 1 H_c), 4.77 (s, 1 H_b), 4.61 (d, *J* = 13.5 Hz, 1 H_a), 4.36-4.24 (m, 6 H_e), 4.22-4.13 (m, 2 H_{a+c}), 3.89-3.51 (m, 30 $H_{f+g+h+i+j}$), 3.42 (s, 9 H_k); ^{13}CNMR ($CDCl_3$, 125 MHz): 169.1, 155.2, 154.2, 154.0, 152.6, 151.6, 147.2, 147.1, 146.9, 146.56, 146.1, 146.1, 146.0, 145.9, 145.9, 145.6, 145.4, 145.4, 145.3, 145.1, 145.0, 144.4, 144.3, 142.9, 142.9, 142.5, 142.5, 142.0, 141.8, 141.8, 141.7, 141.6, 141.5, 140.4, 140.0, 140.0, 139.5, 139.2, 137.2, 136.5, 135.4, 135.2, 133.5, 108.2, 72.7, 71.8, 71.3, 71.0, 69.9, 69.8, 69.7, 69.6, 69.5, 69.4, 69.1, 68.8, 67.6, 64.8, 58.7, 55.9; HRMS (MALDI) calculated for $C_{91}H_{53}NNaO_{14}$ ($[M+Na]^+$): 1406.3364; found: 1406.3339.

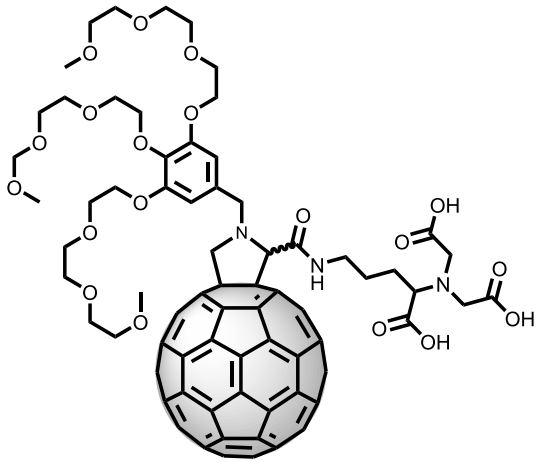

Compound 46. N-{3,4,5-Tris[2-[2-(2-methoxyethoxy)ethoxy] ethoxy]benzyl}-2-[N_{α},N_{α}-Bis(carboxymethyl)-L-lysine]carbonylpyrrolidino [3,4:1,2][60]fullerene (R,S). Carboxylic acid **45** (26 mg, 0.014 mmol) was dissolved in anhydrous THF (3 mL) and was activated by adding N-hydroxysuccinimide (2.5 mg, 0.015 mmol) and N,N′-Dicyclohexylcarbodiimide (5 mg, 0.017 mmol) under argon atmosphere. This mixtured was stirred at room temperature and monitored by TLC. After 5 hours of activation, a solution of N_{α},N_{α}-Bis(carboxymethyl)-L-lysine hydrate (4 mg, 0.015 mmol) in aqueous $NaHCO_3$ (2 M, 1.5 mL) was added. The mixture was stirred at room temperature overnight. Then, the solvents mixture was evaporated under reduced pressure and the crude product was washed with water, CH_3OH and finally CH_2Cl_2. The product was confirmed by MS (MALDI): calculated for $C_{99}H_{62}N_3O_{19}$ ($[M]^+$): 1597,4056; found: 1597,436. IR (ATR): 3529 (br, s), 2917 (s), 2845 (s), 1667 (s), 1450 (m); 1098 (m), 849 (s). Further purification and characterization of this derivative are under progress.

2.4.1.3. Conjugation and purification protocols

Protein design and production. Protein expression was carried out in the group of Prof. Aitziber Cortajarena. The process is briefly described below: molecular model of tyrosine mutations was built using Pymol. E2Y, N6A and N9Y point mutations constituting the mutated residues were introduced into C1 consensus repeat through QuickChange site-directed mutagenesis. CTPR8 proteins were constructed by sequential ligation of consensus and mutated C1 sequences into pPro-EX-HTa vector as described by Kajander *et al*. Proteins were expressed in *E.coli* C41 (DE3) cells with IPTG induction at 30°C or 37°C overnight. Histag-IMAC purification was carried out using HisTrap™ HP columns from GE Healthcare. The hexahistidine tags were then cleaved using TEV protease and proteins were purified by size exclusion chromatography. Size exclusion chromatography was conducted on ÄKTApure purifier with GE Fraction collector F9-R, using HiLoad™ 16/600 SuperdexTM 75 pg column and eluting with 50 mM Tris buffer, pH 8.

Conjugation with pristine C_{60} and C_{60} pyrrolidine tris-acid. *Ca*. 1 mg of pristine C_{60} or C_{60} pyrrolidine tris-acid was suspended in 1 ml of the test protein in 50 mM Tris, pH 8, and the suspension was subjected to probe-tip sonication for 20 min with 0.5 s on/off cycles at 0°C, using Sartorius stedim biotech Labsonic® P sonicator. Subsequently, the mixture was centrifuged in a bench top centrifuge at 21000 *g* for 10 min and the supernatant was analysed and purified by size exclusion chromatography. Chromatography was conducted on ÄKTApurifier with Frac-950 fraction collector, using Superdex™ 75 10/300 GL column, eluting with 50 mM Tris buffer, pH 8, and collecting fractions of 0.5 ml.

Conjugation reaction with porphyrin 37. Prior to any conjugation, purified **CTPR4** at a protein concentration of about 100µM was freshly reduced with 1 mM 1,4-dithio-DL-treitol (DTT) during 20 minutes to ensure full reduction of the cysteine residues. DTT was removed by buffer exchange over a NAP-5 column (GE Healthcare Life Science) in PBS buffer. Protein fractions without DTT are collected at 4 ºC and 1mM tris(2-carboxyethyl)phosphine (TCEP) was added to avoid the formation of disulfide bonds between cysteines during the conjugation reaction. The protein concentration was measured by UV-absorbance. 300 µL of 50 µM of freshly reduced protein was mixed with 40 equivalents of **25** or **26** (around 1.9 mg) giving a ratio of 1:5 cysteine:maleimide and mixed gently. After one hour, an extra of 20 equivalents of **25** or **26** was added to the mixture (around 1 mg) giving a final ratio 1:7.5 cysteine:maleimide. The reaction mixture was incubated during 3 hours shaking and protected from

light. 15% SDS-PAGE electrophoresis gels were used to monitor the conjugation process. Samples of the **CTPR4** protein control and marker were prepared using Amresco EZ-vision loading buffer and the conjugates were mixed with SDS loading buffer. The gel prior staining was imaged using UV-light to monitor the fluorescence of the porphyrins. Then, the gels were stained with Coomassie Blue.

Conjugation tests with Rhodamine B label. Commercially available Rhodamine B iosthiocyanate was reacted at room temperature in aqueous media with one equivalent of N_{α},N_{α}-Bis(carboxymethyl)-L-lysine hydrate. The resutlign NTA-Rhodamine moiety was added to a solution of **CTPR4(Cys$_2$His$_2$)** or **CTPR4(Cys$_2$His$_2$)-37** in the presence or absence of $NiCl_2$. After purification by size exclusion chromatography, samples were evaluated by UV/Vis using a NanoDrop (Thermo Fisher) microvolume spectrophotometer.

Gel filtration chromatography. To purify the conjugates from the excess of oranic molecule, gel filtration chromatography was performed using an AKTA prime plus Fast Protein Liquid Chromatography (FPLC) equipment (GE Healthcare). The conjugation reaction was injected into a Superdex 75 HR 10/30 size exclusion chromatography column (GE Healthcare) and run at 0.5 mL/min in PBS buffer with 2 mM β-mercaptoethanol. The purified samples were collected in 0.5 mL fractions and stored protected from light.

2.4.1.4. Characterization of the conjugates

Absorbance measurements. Absorbance spectra were recorded using a VARIAN-80 UV/Vis spectrophotometer or a NanoDrop (Thermo Fisher) microvolume spectrophotometer. The absorbance spectra of the protein, porphyrin, and protein-porphyrin conjugates from 230 nm to 1000 nm were acquired in a 1 cm path length quartz cuvette using a 4 nm slit-width.

Circular dichroism (CD) measurements. CD spectra were measured using a Jasco J-815 CD Spectrometer. CD spectra of proteins and conjugates in PBS buffer were acquired in a 0.1 cm path length quartz cuvette or a 1 cm path length quartz cuvette. All the CD spectra were recorded with a band-width of 1 nm at 1 nm increments and 10 second average time. The CD spectra were recorded at 1 nm increments and 10 second average time. 10 scans were accumulated.

Transmission electron microscopy (TEM). The samples for cryo-electron microscopy (cryo-TEM) experiments were vitrified on freshly glow-discharged (high vacuum coating system MED 020 BALTEC) holey carbon grids (Holey-carbon film on Copper 200 mesh; QUANTIFOIL R 2/2). The grids held with an ultra-thin tweezers inside the chamber of a Vitrobot Mark II (FEI Company, USA), maintained at 8 °C temperature and with a relative humidity close to saturation (90% rH) to prevent drying artefacts in the blotting process. Four microliters of the sample solution were adsorbed onto the grid for 30 seconds and most of the liquid in the grid was removed by automatically blotting the grid (blot time = 3 seconds, number of blots = 1, drain time = zero and blot offset = -3 mm) with absorbent standard Vitrobot filter paper (Ø55/20mm, Grade 595, Thermo Fisher Scientific FEI) to create an "ultra-thin liquid film" (i.e., typically bellow ~100 nm film thicknesses). After the blotting, the grid was abruptly plunged into a liquid ethane bath, previously cooled with liquid nitrogen to approximately -180°C. Vitrified grids were then removed from the plunger and stored under liquid nitrogen.

High resolution zero tilt two-dimensional (2D) images were collected on a JEM-2200FS/CR (JEOL, Ltd.) field emission gun (FEG) transmission electron microscope, operated at 200 kV at liquid nitrogen temperature, using a 626 DH cryo transfer holder (Gatan Inc.). An in-column energy filter was used to record images with improved signal to noise ratio by zero-loss filtering, with the energy slit width set at 15 eV. Digital images were recorded, under low-dose conditions (on the order of 20-30 electrons/Å^2 per exposure) with an under-focus range from 2.0 to 5.0 m using DigitalMicrograph™ (Gatan) software with a 4K 4K Ultrascan4000™ CCD camera (Gatan Inc.).

For electron tomography, a single-axis tilt series of ± 64° with 2° increments was recorded with under-focus values ranging from 5 to 8 m, using a 914 high tilt liquid nitrogen cryo transfer tomography holder (Gatan Inc.). Semiautomatic data acquisition software SerialEM was used for data collection. Vitrified grids contained 10 nm gold nanoparticles for image alignment. Other conditions as described above.

Computational Methods. Molecular Dynamics Simulations. Molecular Dynamics simulations (MD) have been used to study the spontaneous binding of **C_{60}** and **C_{60}A** in both **CTPR8** and **CTPR8Y$_{16}$** protein scaffolds. The parameters of the [60]fullerene species, **C_{60}** or **C_{60}A**, for the MD simulations

were generated within the ANTECHAMBER module of AMBER 16[166] using the general AMBER force field (GAFF)[167], with partial charges set to fit the electrostatic potential generated at the HF/6-31G(d) level by the RESP model.[168] The charges were calculated according to the Merz-Singh-Kollman scheme[169] using Gaussian 09.[170]

MD simulations of **CTPR8** were carried out using PDB 2HYZ as a reference, removing the crystallized samarium ion. The starting structure for the MD simulations of **CTPR8Y$_{16}$** was prepared by manually introducing the abovementioned tyrosine mutations with the mutagenesis tool from PyMOL software using the **CTPR8** crystal structure (PDB 2HYZ) as starting point. In all cases, i.e. **CTPR8-C$_{60}$**, **CTPR8-C$_{60}$A**, **CTPR8Y$_{16}$-C$_{60}$, and CTPR8Y$_{16}$-C$_{60}$A** simulations, we placed [60]fullerenes in arbitrary positions in the solvent region (more than 10 Å far from the protein surface and 20 Å far from other [60]fullerene molecules). In cases where more than one **CTPR8Y$_{16}$** unit was included in the simulation proteins were separated by at least 40 Å. From these coordinates, we started conventional MD simulations to allow the fullerene molecules to diffuse freely until it spontaneously associate with the surface of the protein, and finally interact with **CTPR8** binding sites.

Each system was immersed in a pre-equilibrated truncated octahedral box of water molecules with an internal offset distance of 10 Å, using the LEAP module.[171] All systems were neutralized with explicit counterions (Na^+ or Cl^-). A two-stage geometry optimization approach was performed. First, a short minimization of the water molecules positions, with positional restraints on solute by a harmonic potential with a force constant of 500 kcal mol^{-1} Å^{-2} was done. The second stage was an unrestrained minimization of all the atoms in the simulation cell. Then, the systems were gently heated using six 50 ps steps, incrementing the temperature 50 K each step (0-300 K) under constant-volume,

[166] D. A. Case, *et al.* AMBER 16, University of California, San Francisco, 2016.
[167] J. Wang, R. M. Wolf, J. W. Caldwell, P. A. Kollman, D. A. Case, *J. Comp. Chem.* **2004**, *25*, 1157-1174.
[168] C. I. Bayly, P. Cieplak, W. Cornell, P. A. Kollman, *J. Phys. Chem.* **1993**, *97*, 10269-10280
[169] a) B. H. Besler, K. M. Merz, P. A. Kollman, *J. Comp. Chem.* **1990**, *11*, 431-439; b) U. C. Singh, P. A. Kollman, *J. Comp. Chem.* **1984**, *5*, 129-145.
[170] Gaussian 09 v. Gaussian 09, Revision A.02 (Gaussian, Inc., Pittsburgh, PA, 2009).
[171] Schafmeister, C. E. A. F. R., W. F.; Romanovsky, V. University of California, San Francisco, **1995**.

periodic-boundary conditions and the particle-mesh Ewald approach[172] to introduce long-range electrostatic effects. For these steps, a 10 Å cutoff was applied to Lennard-Jones and electrostatic interactions. Bonds involving hydrogen were constrained with the SHAKE algorithm.[173] Harmonic restraints of 10 kcal mol^{-1} were applied to the solute, and the Langevin equilibration scheme is used to control and equalize the temperature.[174] The time step was kept at 2 fs during the heating stages, allowing potential inhomogeneities to self-adjust. Each system was then equilibrated for 2 ns with a 2 fs timestep at a constant pressure of 1 atm. Finally, conventional MD trajectories at constant volume and temperature (300 K) were collected. In total, we carried out five replicas of 800 ns MD simulations for **CTPR8** in the presence of eight $\mathbf{C_{60}}$, five replicas of 800 ns MD simulations for **CTPR8** in the presence of eight $\mathbf{C_{60}A}$, five replicas of 800 ns MD simulations for $\mathbf{CTPR8Y_{16}}$ in the presence of eight $\mathbf{C_{60}}$, five replicas of 800 ns MD simulations for $\mathbf{CTPR8Y_{16}}$ in the presence of eight $\mathbf{C_{60}A}$, five replicas of 500 ns MD simulations for $\mathbf{CTPR8Y_{16}}$ in the presence of twenty-four $\mathbf{C_{60}A}$, and five replicas of 1800 ns MD simulations for three $\mathbf{CTPR8Y_{16}}$ units in the presence of eight $\mathbf{C_{60}A}$. Gathering a total of 4 μs for each $\mathbf{CTPR8\text{-}C_{60}}$, $\mathbf{CTPR8\text{-}C_{60}A}$, $\mathbf{CTPR8Y_{16}\text{-}C_{60}}$, and $\mathbf{CTPR8Y_{16}\text{-}C_{60}A}$ co-ensembles, 2.5 μs for $\mathbf{CTPR8Y_{16}\text{-}24C_{60}A}$ co-ensemble, and 1 μs for $\mathbf{3CTPR8Y_{16}\text{-}24C_{60}A}$ co-ensemble.

FP-TRMC and TAS measurements. Nanosecond laser pulses from a Nd:YAG laser of Spectra-Physics INDI-HG (full width at half maximum ($\phi\Sigma\mu$) of 5-8 ns) was used as an excitation light source, and the third harmonic generation (THG) (355 nm) were exposed to the cast films. The laser power density was set at 1, 2, 4, 7, and 10 mW (0.91, 1.8, 3.7, 6.4, and 9.1×10^{15} photons cm^{-2}, respectively). The microwave frequency and power were set at approximately 9.1 GHz and 3 mW, respectively, and the TRMC signal was evolved in a diode (rise time < 1 ns), and output signal was led into a digital oscilloscope of Tektronix TDS 3032B. All experiments were conducted at room temperature. Reflected power change ratio ($\Delta P_r/P_r$) of microwave from the cavity in FP-TRMC apparatus is in relation with the total loss ($\Delta(1/Q)$) of microwave by the photo-induced transient species in the cavity as follows:

[172] C. Sagui, T. A. Darden, *Annu. Rev. Biophys. Biomolec. Struct.* **1999**, *28*, 155-179.
[173] J.-P. Ryckaert, G. Ciccotti, H. J. C. Berendsen, *J. Comp. Phys.* **1977**, *23*, 327-34.
[174] X. Wu, B. R. Brooks, *Chem. Phys. Lett.* **2003**, *381*, 512-518.

$$\frac{\Delta P_r}{P_r} = \frac{\left(\frac{1}{Q}\right)}{\left(\frac{\Delta\omega}{\omega_0}\right)^2 + \left(\frac{1}{2Q}\right)^2} \Delta\left(\frac{1}{Q}\right)$$

(2),[161]

where ω_0 and $\Delta\omega$ are the resonant frequency of 9.1 GHz and its shift by the photo-induced transient species. The loss and the frequency shift of the microwave are expressed as a function of complex conductivity ($\Delta\sigma_r + i\Delta\sigma_i$) of the transient species by:

$$\Delta\left(\frac{1}{Q}\right) - i\frac{2\Delta\omega}{\omega_0} = F\left(\Delta\sigma_r + i\Delta\sigma_i\right)$$

(3),

where F is a calibration factor derived from the measurements of total loss of microwave in the cavity loaded with materials with well-known conductivity values. The value of $\Delta P_r/P_r$ is proportional to the sum of the mobilities ($\Sigma\mu$) of charged species in case of negligibly small $\Delta\omega$:

$$\Delta\sigma_r = N\phi\sum\mu = \mathrm{A}\frac{\Delta P_R}{P_R}$$

(4),

where N, ϕ, and A are the number of absorbed photons, photo-carrier separation quantum yield, and the sensitivity factor (constant), respectively.

Concluding remarks

The results obtained in this Thesis have afforded the following general conclusions:

Guiding the supramolecular self-assembly of electroactive π-systems using peptides and proteins have demonstrated to be an adequate approach to obtain materials with enhanced photophysical properties. In general, simple and straightforward organic molecular building blocks have been synthesized and used for their self-assembly using peptides and proteins to guide or template the process. These biomolecules have exhibited great versatility and it has been possible to study very different electroactive organic molecules.

Chapter 1: Peptide-based electroactive assemblies with enhanced electronic properties.

The work developed in this chapter has provided valuable information on the key role of peptides in the construction of supramolecular polymers based on small and simple building blocks. Although we have studied different π-organic molecules in each section, a general strategy has been applied in all cases. That is, the combination of the electroactive π-core with a pentapeptide sequence based on alternated alanine and glycine residues. This amphiphilic design affords strong π-π interactions which are further enhanced in water by a pronounced hydrophobic effect. Additionally, well-ordered H-bonding patterns are promoted by the peptide, which was able to form β-sheet like structures in some experimental conditions.

The most relevant conclusions of each section are presented below:

In the first section, we have evaluated the self-assembly process of the exTTF derivative **1**, endowed with the pentapeptide AGAGA, and derivatives **2**-**5**, which contained small changes in the peptide sequence. Spectroscopic and microscopy techniques allowed detecting and characterizing two different supramolecular polymers. We have been able to obtain each aggregate under the same experimental conditions by simply changing the processing sequence. Moreover, time-lapse cryo-TEM has enabled following the morphological changes happening during the interconversion from the metastable aggregate (short tapes) to the thermodynamic one (twisted rods). Moreover, we could obtain the oxidation potential of the molecular species and the different aggregates. The best values were obtained for the long-aged thermodynamic assemblies, but in all cases we observed a great enhancement of the donor

character of the aggregates in comparison with the molecularly dissolved species.

In the second section, the self-assembly process of quaterthiophene derivative **8** has been investigated. Three different polymers can be obtained by changing the pH of the media. The ionic co-assembly of these donor-nature supramolecular polymers with the acceptor derivatives, **14** and **18**, afforded new *n*/*p*-materials where the order was imposed by the former ordered materials based on molecule **8**. The extent of excitonic coupling in the different aggregates was clearly observed by UV/Vis and emission spectroscopy, and these features could be related with the results obtained by photoconductivity measurements (FP-TRMC). In this sense, the *n*/*p*-materials showed charge carrier mobility values up to two orders of magnitude higher than the respective molecular building blocks. Moreover, the materials formed under acid and thermodynamic conditions showed remarkably high values, namely 1.5 $cm^2V^{-1}s^{-1}$ for **8:14-T** and 3.2 $cm^2V^{-1}s^{-1}$ for **8:18-T**. Additionally, the value of the yield of photogenerated charge carriers could be determined for **8:18-T**, with a value of 0.4 $cm^2V^{-1}s^{-1}$, which are in the regime of mobility values observed in lamellae stacking of oligothiophene, suggesting the high electric conductive nature of the present system.

In the third section, very interesting and scantly reported results were observed from the supramolecular polymerization of the Zn-porphyrin derivative **24**. While loosely packed H-aggregates were found at room temperature, J-aggregates could only be obtained by applying high temperatures to the solution. In the latter aggregates, it was noticeable the appearance of a β-sheet like secondary structure which eventually gave rise to a tertiary structure by means of solvophobic collapse. This approach seems to be promising to induce entropically driven self-assembly of this kind of amphiphilic π-conjugated molecules, giving rise to uncommon temperature dependencies.

Finally, we expect that the present studies will stimulate further exploration of aqueous self-assembly of amphiphilic electroactive systems in order to unravel this fascinating processes and bridge the gap towards the construction of new materials.

Chapter 2: CTPR proteins as model scaffold for the arrangement of electroactive molecules.

In this chapter, we have harnessed the molecular understanding of the CTPR proteins to generate different protein-based hybrid assemblies. The deep knowledge of the CTPR protein structure and stability makes possible to control the modification of the sequence and introduce mutations in a rational way. We have proved the great versatility of this protein platform as model system for the arrangement of electroactive organic molecules.

The most relevant conclusions of each section are presented below:

In the first part, we tested the ability of the CTPR to bind pristine C_{60} and the more water-soluble C_{60} pyrrolidine tris-acid. Although some extent of conjugation could be achieved, we decided to express a new CTPR with increased number of C_{60}-binding sites by introducing two extra tyrosine mutations per repeat. We demonstrated that both, the water-solubility of the C_{60} derivative and introducing this new mutations, were key to achieve a full conversion into the hybrid material. Theoretical calculations supported these experimental findings and photoconductivity measurements confirmed the enhancement of the charge mobility values by using the TPR scaffold to arrange the [60]fullerene species.

In the second part, we pursued achieving a higher degree of control in the arrangement of donor-acceptor molecular systems. We took advantage of a mutated CTPR previously described in the research group, which contains two cysteine mutations on the turns, where donor-like Zn-porphyrins can be introduced by thiol Michael addition. Moreover, this mutated protein also contains two histidine residues in the helix A, so we designed an acceptor counterpart based on fullerene C_{60} which contains a suitable NTA chelate ligand for the coordination to the imidazole side chain. Preliminary results have demonstrated this that strategy can successfully afford the expected *n*/*p*-biohybrid materials.

In conclusion, these repeat proteins have been demonstrated to be robust scaffolds for the fabrication of complex hybrid materials. More importantly, the approaches developed here can be expanded to other classes of active elements, thus opening the door to generate hybrid nanostructures with applications in different fields of nanotechnology.

Bibliography

Bibliography

1. a) C. J.Pedersen, *J. Am. Chem. Soc.* **1967**, *89*, 7017–7036; b) B. Dietrich, J.-M. Lehn, J. P. Sauvage, *Tetrahedron Lett.* **1969**, *34*, 2885-2888; c) G. W. Gokel, D. J. Cram, *J. Chem. Soc. Chem. Commun.* **1973**, *76*, 481-482.

2. a) J.-M. Lehn, *Supramolecular Chemistry. Concepts and Perspectives*, Wiley-VCH, Weinheim, **1995**; b) J.-M. Lehn, J. L. Atwood, J. E. D. Davies, D. D. Macnicol, F. Vögtle, *Comprehensive Supramolecular Chemistry*, Vol. 1-11, Pergamon/Elsevier, Oxford, **1996**; c) P. D. Beer, P. A. Gale, D. K. Smith, *Supramolecular Chemistry*, Oxford University Press, Oxford, **1999**; d) J. W. Steed, J. L. Atwood, Supramolecular Chemistry, 2nd ed., John Wiley & Sons, Wiltshire, **2009**; J. W. Steed, P. A. Gale, *Supramolecular Chemistry: From Molecules to Nanomaterials*, John Wiley & Sons, **2012**.

3. a) D. B. Amabilino, D. K. Smith, J. W. Steed, *Chem. Soc. Rev.* **2017**, *46*, 2404-2420; b) A. Jain, S. J. George, *Materials Today* **2015**, *18*, 206-214.

4. Y. Zubavicus, M. Grunze, *Science* **2004**, *304*, 974-976.

5. a) J. Kyte, *Biophys. Chem.* **2003**, *100*, 193-203; b) C. Tanford in *The Hydrophobic Effect: Formation of Micelles and Biological Membranes*, Wiley, New York, **1980**.

6. R. V. Ulijn, R. Jerala, *Chem. Soc. Rev.* **2018**, *47*, 3391-3394.

7. J. Clarke, L. Regan, *Curr. Opin. Struct. Biol.* **2010**, *20*, 480-481.

8. a) N. P. King, J. B. Bale, W. Sheffler, D. E. McNamara, S. Gonen, T. Gonen, T. O. Yeates, D. Baker, *Nature* **2014**, *510*, 103-108; (b) N. P. King, W. Sheffler, M. R. Sawaya, B. S. Vollmar, J. P. Sumida, I. André, T. Gonen, T. O. Yeates, D. Baker, *Science* **2012**, *336*, 1171-1174; (c) H. Garcia-Seisdedos, C. Empereur-Mot, N. Elad, E. D. Levy, *Nature* **2017**, *548*, 244-247.

9. B. B. Mandal, A. Grinberg, E. Seok Gil, B. Panilaitis, D. L. Kaplan, *Proc. Natl. Acad. Sci. U. S. A.* **2012**, *109*, 7699-7704.

10. R. Galland, P. Leduc, C. Guérin, D. Peyrade, L. Blanchoin, M. Théry, *Nat. Mater.* **2013**, *12*, 416-421.

11. L. A. Micol, M. Ananta, E.-M. Engelhardt, V. C. Mudera, R. A. Brown, J. A. Hubbell, P. Frey, *Biomaterials* **2011**, *32*, 1543-1548.

12. a) B. P. Lee, P. B. Messersmith, J. N. Israelachvili, J. H. Waite, *Annu. Rev. Mater. Res.* **2011**, *41*, 99-132; b) M. J. Webber, J. Tongers, C. J. Newcomb, K.-T. Marquardt, J. Bauersachs, D. W. Losordo, S. I. Stupp, *Proc. Natl. Acad. Sci. U. S. A.* **2011**, *108*, 13438.

13. H. Hosseinkhani, P. Hong, D. Yu, *Chem. Rev.* **2013**, *113*, 4837-4861.

14. J. D. Tovar, *Acc. Chem. Res.* **2013**, *46*, 1527-1537.

15. a) S. Zhang, T. Holmes, C. Lockshin, A. Rich, *Proc. Natl. Acad. Sci. U. S. A.* **1993**, *90*, 3334-3338; b) H. Xiong, B. L. Buckwalter, H.-M. Shieh, M. H. Hecht, *Proc. Natl. Acad. Sci. U. S. A.* **1995**, *92*, 6349-6353; c) J. P. Schneider, D. J. Pochan, B. Ozbas, K. Rajagopal, L. Pakstis, J. Kretsinger, *J. Am. Chem. Soc.* **2002**, *124*, 15030-15037; d) J. Gao, C. Tang, M. A. Elsawy, A. M. Smith, A. F. Miller, A. Saiani, *Biomacromolecules* **2017**, *18*, 826-834.

16. R. Stadler, L. de Lucca Freitas, *Colloid Polym. Sci.* **1986**, *264*, 773-779.

17. C. Fouquey, J.-M. Lehn, A.-M. Levelut, *Adv. Mater.* **1990**, *2*, 254-257.

18. a) R. P. Sijbesma, F. H. Beijer, L. Brunsveld, B. J. B. Folmer, Hirschberg, J. H. K. K., R. F. M. Lange, J. K. L. Lowe, E. W. Meijer, *Science* **1997**, *278*, 1601-1606; b) F. H. Beijer, R. P. Sijbesma, H. Kooijman, A. L. Spek, E. W. Meijer, *J. Am. Chem. Soc.* **1998**, *120*, 6761-6769.

19. De Greef, Tom F. A., M. M. J. Smulders, M. Wolffs, Schenning, Albert P. H. J., R. P. Sijbesma, E. W. Meijer, *Chem. Rev.* **2009**, *109*, 5687-5754.

20. F. Tantakitti, J. Boekhoven, X Wang, R. V. Kazantsev, T. Yu, J. Li, E. Zhuang, R. Zandi, J. H. Ortony, C. J. Newcomb, L. C. Palmer, G. S. Shekhawat, l. C. de, G. C. Schatz, S. I. Stupp, *Nat. Mater.* **2016**, *15*, 469-476.

21. A. Sorrenti, J. Leira-Iglesias, A. J. Markvoort, T. F. A de Greef, T. M. Hermans, *Chem. Soc. Rev.* **2017**, *46*, 5476-5490.

22. a) T. Aida, E. W. Meijer, S. I. Stupp, *Science* **2012**, *335*, 813-817; b) X. Yan, F. Wang, B. Zheng, F. Huang, *Chem. Soc. Rev.* **2012**, *41*, 6042-6065; c) E. A. Appel, J. Del Barrio, X. J. Loh, O. A. Scherman, *Chem. Soc. Rev.* **2012**, *41*, 6195-6214; d) G. R. Whittell, M. D. Hager, U. S. Schubert, I. Manners, *Nat. Mater.* **2011**, *10*, 176-188; e) L. Yang, X. Tan, Z. Wang, X. Zhang, *Chem. Rev.* **2015**, *115*, 7196-7239.

23. a) L. Voorhaar, R. Hoogenboom, *Chem. Soc. Rev.* **2016**, *45*, 4013-4031; b) M. Suzuki, K. Hanabusa, *Chem. Soc. Rev.* **2010**, *39*, 455-463; c) X. Du, J. Zhou, J. Shi, B. Xu, *Chem. Rev.* **2015**, *115*, 13165-13307; d) E. A. Appel, J. del Barrio, X. J. Loh, O. A. Scherman, *Chem. Soc. Rev.* **2012**, *41*, 6195-6214.

24. a) M. P. Hendricks, K. Sato, L. C. Palmer, S. I. Stupp, *Acc. Chem. Res.* **2017**, *50*, 2440-2448; b) J. D. Hartgerink, E. Beniash, S. I. Stupp, *Science* **2001**, *294*, 1684-1689; c) G. A. Silva, C. Czeisler, K. L. Niece, E. Beniash, D. A. Harrington, J. A. Kessler, S. I. Stupp, *Science* **2004**, *303*, 1352-1355; d) Jiang, H.; Guler, M. O.; Stupp, S. I. Soft Matter 2007, 3, 454; e) C. H. Chen, L. C. Palmer, S. I. Stupp, *Nano Lett.* **2018**, *18*, 6832-6841; f) R. Freeman, M. Han, Z. Álvarez, J. A. Lewis, J. R. Wester, N. Stephanopoulos, M. T. McClendon, C. Lynsky, J. M. Godbe, H. Sangji, E. Luijten, S. I. Stupp, *Science* **2018**, *362*, 808-813.

25. M. Kasha, H. R. Rawls, M. A. E. Bayoumi, *Pure Appl. Chem.* **1965**, *11*, 371-392.

26. A. H. Herz, *Adv. Colloid Interface Sci.* **1977**, *8*, 237-298.

27. F. Würthner, T. E. Kaiser, C. R. Saha-Möller, *Angew. Chem. Int. Ed.* **2011**, *50*, 3376-3410.

28. F. Würthner, C. R. Saha-Möller, B. Fimmel, S. Ogi, P. Leowanawat, D. Schmidt, *Chem. Rev.* **2016**, *116*, 962-1052.

29. T. E. Kaiser, H. Wang, V. Stepanenko, F. Würthner, *Angew. Chem., Int. Ed.* **2007**, *46*, 5541-5544; b) T. E. Kaiser, V. Stepanenko, F. Würthner, *J. Am. Chem. Soc.* **2009**, *131*, 6719-6732; c) S. Herbst, B. Soberats, P. Leowanawat, M. Lehmann, F. Würthner, *Angew. Chem., Int. Ed.* **2017**, *56*, 2162-2165.

30. L. Tropf, C. P. Dietrich, S. Herbst, A. L. Kanibolotsky, P. J. Skabara, F. Würthner, I. D. W. Samuel, M. C. Gather, S. Höing, *Appl. Phys. Lett.* **2017**, *110*, 153302.

31. P. Lova, V. Grande, G. Manfredi, M. Patrini, S. Herbst, F. Würthner, D. Comoretto, *Adv. Opt. Mater.*, **2017**, *5*, 1700523.

32. V. Grande, B. Soberats, S. Herbst, V. Stepanenko, F. Würthner, *Chem. Sci.* **2018**, *9*, 6904-6911.

33. K. Jalani, S. Dhiman, A. Jain, S. J. George, *Chem. Sci.* **2017**, *8*, 6030-6036.

34. a) L. M. Cassidy, B. T. Burcar, W. Stevens, E. M. Moriarty, L. B. McGown, *Astrobiology* **2014**, *14*, 876-886; b) P. Zhou, R. Shi, J. Yao, C. Sheng, H. Li, *Coord. Chem. Rev.* **2015**, *292*, 107-143; c) C. Aimé, R. Nishiyabu, R. Gondo, K. Kaneko, N. Kimizuka, *Chem. Commun.* **2008**, 6534-6536; d) G. M. Peters, J. T. Davis, *Chem. Soc. Rev*. **2016**, *45*, 3188-3206.

35. M. Delbianco, P. Bharate, S. Varela-Aramburu, P. H. Seeberger, *Chem. Rev.* **2016**, *116*, 1693-1752.

36. a) H. Klok, J. J. Hwang, J. D. Hartgerink, S. I. Stupp, *Macromolecules* **2002**, *35*, 6101-6111; b) S. Abraham, R. K. Vijayaraghavan, S. Das, *Langmuir* **2009**, *25*, 8507-8513.

37. a) S. Schmid, E. Mena-Osteritz, A. Kopyshev, P. Bäuerle, *Org. Lett.* **2009**, *11*, 5098-5101; b) S. Schmid, E. Marion Schneider, E. Brier, P. Bäuerle, *J. Mater. Chem. B* **2014**, *2*, 7861-7865.

38. D. González-Rodríguez, Schenning, Albertus P. H. J., *Chem. Mater.* **2011**, *23*, 310-325.

39. A. Jatsch, E. Schillinger, S. Schmid, P. Bäuerle, *J. Mater. Chem.* **2010**, *20*, 3563-3578.

40. S. S. Babu, V. K. Praveen, A. Ajayaghosh, *Chem. Rev.* **2014**, *114*, 1973-2129.

41. a) Y. Wu, J. H. Collier, *WIREs Nanomed Nanobiotechnol* **2017**, *9*, 1424-1430; b) B. Pepe-Mooney, R. Fairman, *Curr. Opin. Struct. Biol.* **2009**, *19*, 483-494; c) S. Kim, J. H. Kim, J. S. Lee, C. B. Park, *Small* **2015**, *11*, 3623-3640.

42. H. Ardoña Ann M., K. Besar, M. Togninalli, H. E. Katz, J. D. Tovar, *J. Mater. Chem. C* **2015**, *3*, 6505-6514.

43. a) P.-N. Cheng, J. D. Pham and J. S. Nowick, *J. Am. Chem. Soc.* **2013**, *135*, 5477-5492; b) J. D. Pham, R. K. Spencer, K. H. Chen and J. S. Nowick, *J. Am. Chem. Soc.* **2014**, *136*, 12682-12690.

44. S. S. Panda, H. E. Katz, J. D. Tovar, *Chem. Soc. Rev.* **2018**, *47*, 3640-3658.

45. I. Choi, I. Park, J. Ryu, M. Lee, *Chem. Commun.* **2012**, *48*, 8481-8483.

46. a) K. Sato, M. P. Hendricks, L. C. Palmer, S. I. Stupp, *Chem. Soc. Rev.* **2018**, *47*, 7539-7551; b) M. P. Hendricks, K. Sato, L. C. Palmer, S. I. Stupp, *Acc. Chem. Res.* **2017**, *50*, 2440-2448.

47. S. Khan, S. Sur, P. Y. W. Dankers, da Silva, Ricardo M. P., J. Boekhoven, T. A. Poor, S. I. Stupp, *Bioconjugate Chem.* **2014**, *25*, 707-717.

48. S. S. Lee, T. Fyrner, F. Chen, Z. Álvarez, E. Sleep, D. S. Chun, J. A. Weiner, R. W. Cook, R. D. Freshman, M. S. Schallmo, K. M. Katchko, A. D. Schneider, J. T. Smith, C. Yun, G. Singh, S. Z. Hashmi, M. T. McClendon, Z. Yu, S. R. Stock, W. K. Hsu, E. L. Hsu, S. I. Stupp, *Nat. Nanotech.* **2017**, *12*, 821.

49. a) Z. Yu, F. Tantakitti, T. Yu, L. C. Palmer, G. C. Schatz, S. I. Stupp, *Science* **2016**, *351*, 497; b) R. Helen Zha, Y. S. Velichko, R. Bitton, S. I. Stupp, *Soft Matter* **2016**, *12*, 1401-1410.

50. Y. Yamamoto, T. Fukushima, Y. Suna, N. Ishii, A. Saeki, S. Seki, S. Tagawa, M. Taniguchi, T. Kawai, T. Aida, *Science*, **2006**, *314*, 1761-1764.

51. Y. Yamamoto, G. Zhang, W. Jin, T. Fukushima, N. Ishii, A. Saeki, S. Seki, S. Tagawa, T. Minari, K. Tsukagoshi, T. Aida, *Proc. Natl. Acad. Sci. USA* **2009**, *106*, 21051-21056.

52. E. Busseron, J. Cid, A. Wolf, G. Du, E. Moulin, G. Fuks, M. Maaloum, P. Polavarapu, A. Ruff, A. Saur, S. Ludwigs, N. Giuseppone, *ACS Nano* **2015**, *9*, 2760-2772.

53. W. Zhang, W. Jin, T. Fukushima, A. Saeki, S. Seki, T. Aida, *Science* **2011**, *334*, 340-343.

54. Schenning, Albertus P. H. J., J. v. Herrikhuyzen, P. Jonkheijm, Z. Chen, F. Würthner, E. W. Meijer, *J. Am. Chem. Soc.* **2002**, *124*, 10252-10253.

55. J. López-Andarias, M. J. Rodriguez, C. Atienza, J. L. López, T. Mikie, S. Casado, S. Seki, J. L. Carrascosa, N. Martín, *J. Am. Chem. Soc.* **2015**, *137*, 893-897.

56. H. Ardoña Ann M., E. R. Draper, F. Citossi, M. Wallace, L. C. Serpell, D. J. Adams, J. D. Tovar, *J. Am. Chem. Soc.* **2017**, *139*, 8685-8692.

57. J. López-Andarias, J. L. López, C. Atienza, F. G. Brunetti, C. Romero-Nieto, D. M. Guldi, N. Martín, *Nat. Commun.* **2014**, *5*, 3763-3774.

58. a) A. Jatsch, E. K. Schillinger, S. Schmid and P. Bauerle, *J. Mater. Chem.* **2010**, *20*, 3563-3578; b) Q. Wang, Y. Chen, P. Ma, J. Lu, X. Zhang and J. Jiang, *J. Mater. Chem.* **2011**, *21*, 8057-8065; c) G. W. M. Vandermeulen, K. T. Kim, Z. Wang and I. Manners, *Biomacromolecules* **2006**, *7*, 1005-1010.

59. J. Yamada, T. Sugimoto, *TTF Chemistry: Fundamentals and Applications of Tetrathiafulvalene;* Kodansha, **2004**.

60. F. G. Brunetti, J. L. Lopez, C. Atienza, N. Martín, *J. Mater. Chem.* **2012**, *22*, 4188-4205.

61. N. Martín, L. Sánchez, C. Seoane, E. Ortí, P. M. Viruela, R. Viruela, *J. Org. Chem.* **1998**, *63*, 1268-1279.

62. J. L. Lopez, C. Atienza, W. Seitz, D. M. Guldi, N. Martin, *Angew. Chem. Int. Ed.* **2010**, *49*, 9876-9880.

63. H. C. Fry, J. M. Garcia, M. J. Medina, U. M. Ricoy, D. J. Gosztola, M. P. Nikiforov, L. C. Palmer, S. I. Stupp, *J. Am. Chem. Soc.* **2012**, *134*, 14646-14649.

64. J. P. Patterson, Y. Xu, M. Moradi, N. Sommerdijk, H. Friedrich, *Acc. Chem. Res.* **2017**, *50*, 1495-1501.

65. F. Huang, W. M. Nau, *Angew. Chem. Int. Ed*. **2003**, *42*, 2269-2272.

66. a) A. Mishra, C. Ma, P. Bäuerle, *Chem. Rev.* **2009**, *109*, 1141-1276; b) L. Zhang, N. S. Colella, B. P. Cherniawski, S. C. B. Mannsfeld, A. L. Briseno, *ACS Appl. Mater. Interfaces*, **2014**, *6*, 5327-5343.

67. F. Jäckel, M. D. Watson, K. Müllen, J. P. Rabe, *Phys. Rev. Lett.* **2004**, *92*, 188303; b) E. Mena-Osteritz, P. Bäuerle, *Adv. Mater.* **2006**, *18*, 447-451.

68. B. Liedberg, Z. Yang, I. Engquist, M. Wirde, U. Gelius, G. Götz, P. Bäuerle, R. M. Rummel, C. Ziegler, W. Gopel, *J. Phys. Chem. B*, **1997**, *101*, 5951–5962.

69. H. Ouchi, T. Kizaki, M. Yamato, X. Lin, N. Hoshi, F. Silly, T. Kajitani, T. Fukushima, K. Nakayama, S. Yagai, *Chem. Sci.* **2018**, *9*, 3638-3643.

70. a) E.-K. Schillinger, M. Kümin, A. Digennaro, E. Mena-Osteritz, S. Schmid, H. Wennemers, P. Bäuerle, *Chem. Mater.*, **2013**, *25*, 4511-4521; b) A. K. Shaytan; E.-K. Schillinger, P. G. Khalatur, E. Mena-Osteriz, J. Hentschel, H. G. Böner, P. Bäuerle, A. R. Khokhlov, *ACS Nano*, **2011**, *5*, 6894-6909.

71. a) D. A. Stone, L. Hsu, S. I. Stupp, *Soft Matter*, **2009**, *5*, 1990-1993; b) J. A. Lehrman, H. Cui, W. Tsai, T. J. Moyer, S. I. Stupp, *Chem. Commun.* **2012**, *48*, 9711-9713.

72. a) H. Zollinger, *Color Chemistry*, 3rd edn., VCH, Weinheim, **2003**; b) W. Herbst and K. Hunger, *Industrial Organic Pigments: Production, Properties, Applications*, 2nd edn., WILEY-VCH, Weinheim, **1997**.

73. a) A. Nowak-Król, K. Shoyama, M. Stolte, F. Würthner, *Chem. Commun.* **2018**, *54*, 13763-13772; b) F. Würthner, *Angew. Chem. Int. Ed*. **2001**, *40*, 1037-1039; c) L. Schmidt-Mende, A. Fechtenkötter, K. Müllen, E. Moons, R. H. Friend and J. D. MacKenzie, *Science*, **2001**, *293*, 1119–1122; d) K.-Y. Law, *Chem. Rev.* **1993**, *93*, 449-486.

74. H. Langhals, *Heterocycles*, **1995**, *40*, 477-500.

75. F. Würthner, *Chem. Commun.* **2004**, 1564-1579.

76. W. Wagner, M. Wehner, V. Stepanenko, S. Ogi, F. Würthner, *Angew. Chem. Int. Ed.* **2017**, *56*, 16008-16012.

77. H. W. Kroto, J. R. Heath, S. C. O'Brien, R. F. Curl, R. E. Smalley, *Nature*, **1985**, *318*, 162-163.

78. Q. Xie, E. Pérez-Cordero, L. Echegoyen, *J. Am. Chem. Soc.* **1992**, **114**, 3978-3980.

79. H. Ajie, M. M. Alvarez, S. J. Anz, R. D. Beck, F. Diederich, K. Fostiropoulos, D. R. Huffman, W. Kraetschmer, Y. Rubin, K. E. Schriver, D. Sensharma, R. L. Whetten, *J. Phys. Chem.* **1990**, *94*, 8630-8633.

80. G. Yu, J. Gao, J. C. Hummelen, F. Wudl, A. J. Heeger, *Science*, **1996**, *270*, 1789-1791.

81. A. Kira, T. Umeyama, Y. Matano, K. Yoshida, S. Isoda, J. K. Park, D. Kim, H. Imahori, *J. Am. Chem. Soc.* **2009**, *131*, 3198-3200.

82. a) S. Kawano, N. Fujita, S. Shinkai, *Chem. Eur. J.*, **2005**, *11*, 4735-4742; b) J. Areephong, E. Orentas, N. Sakai, S. Matile, *Chem. Commun.* **2012**, *48*, 10618-10620.

83. M. Braun, U. Hartnagel, E. Ravanelli, B. Schade, C. Böttcher, O. Vostrowsky, A. Hirsch, *Eur. J. Org. Chem.* **2004**, *2004*, 1983-2001.

84. a) E. E. Maroto, S. Filippone, A. Martín-Domenech, M. Suarez, N. Martín, *J. Am. Chem. Soc.*, **2012**, *134*, 12936-12938; b) K. Sawai, Y. Takano, M. Izquierdo, S. Filippone, N. Martín, Z. Slanina, N. Mizorogi, M. Waelchli, T. Tsuchiya, T. Akasaka, S. Nagase, *J. Am. Chem. Soc.*, **2011**, *133*, 17746-17752.

85. J. H. Olivier, P. Deria, J. Park, A. Kumbhar, M. Andrian-Albescu, M. J. Therien, *Angew. Chem. Int. Ed.* **2013**, *52*, 13080-13085.

86. A. Kamino, H. Koyano, K. Ariga, T. Kunitake, *Bull. Chem. Soc. Jpn.* **1998**, *69*, 3619−3631.

87. D. Gosztola, M. P. Niemczyk, W. Svec, A. S. Lukas, M. R. Wasielewski, *J. Phys. Chem. A*, **2000**, *104*, 6545-6551.

88. a) V. Grande, B. Soberats, S. Herbst, V. Stepanenko, F. Würthner, *Chem. Sci.* **2018**, *9*, 6904-6911; b) D. Görl, F. Würthner, *Angew. Chem. Int. Ed.* **2016**, *55*, 12094-12098; c) D. Görl, B. Soberats, S. Herbst, V. Stepanenko, F. Würthner, *Chem. Sci.* **2016**, *7*, 6786-6790; d) D. Görl, X. Zhang, V. Stepanenko, F. Würthner, *Nat. Commun.* **2015**, *6*, 7009-7017; e) X. Zhang, D. Görl, V. Stepanenko, F. Würthner, *Angew. Chem. Int. Ed.* **2014**, *53*, 1270-1274.

89. J. Deisenhofer, H. Michel, *Angew. Chem. Int. Ed.* **1989,** *28*, 829-847.

90. a) J. C. Kendrew, G. Bodo, H. M. Dintzis, R. G. Parrish, H. W. Wychoff, D. C. Phillips, *Nature* **1958**, *181*, 662-666 ; b) M. F. Perut, M. G. Rossmann, A. F. Cullis, H. Muirhead, A. C. T. North, *Nature* **1960**, 185, 416-420.

91. T. L. Poulos, B. C. Finzel, A. J. Howard, *Biochemistry* **1986**, *25*, 5314-5322.

92. a) T. S. Balaban, *Acc. Chem. Res.* **2005**, *38*, 612-623; b) M. R. Wasielewski, *Acc. Chem. Res.* **2009**, *42*, 1910-1921; c) M. J. Mayoral Muñoz, G. Fernández, *Chem. Sci.* **2012**, *3*, 1395-1398.

93. a) J. A. A. W. Elemans, R. van Hameren, R. J. M. Nolte, A. E. Rowan, *Adv. Mater.* **2006**, *18*, 1251-1266; b) C. M. Drain, A. Varotto, I. Radivojevic, *Chem. Rev.* **2009**, *109*, 1630-1658; c) C. J. Medforth, Z. Wang, K. E. Martin, Y. Song, J. L. Jacobsen, J. A. Shelnutt, *Chem. Commun.* **2009**, 7261-7277; d) A. Yella, H.-W. Lee, H. N. Tsao, C. Yi, A. K. Chandiran, M. Nazeeruddin, E. W.-G. Diau, C.-Y. Yeh, S. M. Zakeeruddin, M. Grätzel, *Science* **2011**, *334*, 629-634.

94. a) K. M. Smith, *Strategies for the synthesis of octaalkylporphyrin systems*. In: K. M. Smith, *The Porphyrin Handbook*. Vol. 1. Academic Press; Boston: **1999**. p. 1-43; b) N. Aratani, D. Kim, A. Osuka, *Acc. Chem. Res.* **2009**, *42*, 1922-1934; c) I. Beletskaya, V. S. Tyurin, A. Y. Tsivadze, R. Guilard, C. Stern, *Chem. Rev.* **2009**, *109*, 1659-1713; d) W.-S. Li, T. Aida, *Chem. Rev.* **2009**, *109*, 6047-6076; e) J. P. Lewtaka, D. T. Gryko, *Chem. Commun.* **2012**, *48*, 10069-10086; f) C. M. B. Carvalho, T. J. Brocksom, K. T. de Oliveira, *Chem. Soc. Rev.* **2013**, *42*, 3302-3317.

95. a) T. Hasobe, *J. Phys. Chem. Lett.* **2013**, *4*, 1771-1780; b) M. R. Wasielewski, *Acc. Chem. Res.* **2009**, *42*, 1910-1921.

96. a) S. S. Babu, D. Bonifazi, *ChemPlusChem* **2014**, *79*, 895-906; b) L. Li, E. W. Diau, *Chem. Soc. Rev.* **2013**, *42*, 291-304.

97. T. Fukui, S. Kawai, S. Fujinuma, Y. Matsushita, T. Yasuda, T. Sakurai, S. Seki, M. Takeuchi, K. Sugiyasu, *Nat. Chem.* **2016**, *9*, 493-500.

98. a) P. Rothemund, *J. Am. Chem. Soc.* **1935**, *57*, 2010-2011; b) J. S. Lindsey, I. C. Hsu, I. C. Schreiman, *Tetrahedron Lett.* **1986**, *27*, 4969-4970.

99. S. Okada, H. Segawa, *J. Am. Chem. Soc.* **2003**, *125*, 2792-2796.

100. a) A. Barth, C. Zscherp, *Q. Rev. Biophys.* **2002**, *35*, 369-430; b) Y. Cordeiro, J. Kraineva, M. P. B. Gomes, M. H. Lopes, V. R. Martins, L. M. T. R. Lima, D. Foguel, R. Winter, J. L. Silva, *Biophys. J.* **2005**, *89*, 2667-2676; c) H. Shao, J. R. Parquette, *Chem. Commun.* **2010**, *46*, 4285-4287.

101. S. Ogi, V. Stepanenko, J. Thein, F. Würthner, *J. Am. Chem. Soc.* **2016**, *138*, 670-678.

102. S. Ogi, C. Grzeszkiewicz, F. Würthner, *Chem. Sci.* **2018**, *9*, 2768-2773.

103. J. L. López, C. Atienza, A. Insuasty, J. López-Andarias, C. Romero-Nieto, D. M. Guldi, N. Martín, *Angew. Chem. Int. Ed.* **2012**, *51*, 3857-3861.

104. a) D. S. Goodsell, *Bionanotechnology: Lessons from Nature*, Wiley-VCH, Weinheim, 2004; b) G. M. Whitesides, *Interface Focus* **2015**, *5*, 20150031; d) Y. Lin, C. Mao, *Front. Mater. Sci.* **2011**, *5*, 247-265.

105. Y. Tu, F. Peng, A. Adawy, Y. Men, Abdelmohsen, Loai K. E. A., D. A. Wilson, *Chem. Rev.* **2016**, *116*, 2023-2078.

106. a) S. Mashaghi, T. Jadidi, G. Koenderink, A. Mashaghi, *Int. J. Mol. Sci.* **2013**, *14*, 4242-4282; b) M. U. Ahmad, *Lipids in Nanotechnology*, AOCS Press **2012**.

107. a) N. C. Seeman, *J. Theor. Biol.* **1982**, *99*, 237-247; b) N. C. Seeman, N. R. Kallenbach, *Biophys. J.* **1983**, *44*, 201-209; c) J. Chen, N. C. Seeman, *Nature* **1991**, *350*, 631-633.

108. P. W. K. Rothemund, *Nature* **2006**, *440*, 297-302.

109. F. Hong, F. Zhang, Y. Liu, H. Yan, *Chem. Rev.* **2017**, *117*, 12584-12640.

110. a) A. Kumar, J. Hwang, S. Kumar, J. Nam, *Chem. Commun.* **2013**, *49*, 2597-2609; b) J. Sharma, Y. Ke, C. Lin, R. Chhabra, Q. Wang, J. Nangreave, Y. Liu, H. Yan, *Angew. Chem., Int. Ed.* **2008**, *47*, 5157-5159.

111. a) H. T. Maune, S. Han, R. D. Barish, M. Bockrath, W. A. G. III, P. W. K. Rothemund, E. Winfree, *Nat. Nanotechnol.* **2009**, *5*, 61-66; b) Z. Zhao, Y. Liu, H. Yan, *Org. Biomol. Chem.* **2013**, *11*, 596-598.

112. a) V. L. Malinovskii, D. Wenger, R. Häner, *Chem. Soc. Rev.* **2010**, *39*, 410-422; b) R. Varghese, H. Wagenknecht, *Chem. Commun.* **2009**, 2615-2624; c) S. Sezi, H. Wagenknecht, *Chem. Commun.* **2013**, *49*, 9257-9259; d) S. Kulala Vittala, J. Joseph, *Faraday Discuss.* **2018**, *207*, 459-469; e) J. Rubio-Magnieto, A. Thomas, S. Richeter, A. Mehdi, P. Dubois, R. Lazzaroni, S. Clément, M. Surin, *Chem. Commun.* **2013**, *49*, 5483-5485.

113. D. G. Singleton, R. Hussain, G. Siligardi, P. Kumar, P. J. Hrdlicka, N. Berova, E. Stulz, *Org. Biomol. Chem.* **2016**, *14*, 149-157.

114. a) J. Luczkowiak, A. Muñoz, M. Sánchez-Navarro, R. Ribeiro-Viana, A. Ginieis, B. M. Illescas, N. Martín, R. Delgado, J. Rojo, *Biomacromolecules* **2013**, *14*, 431-437; b) A. Muñoz, D. Sigwalt, B. M. Illescas, J. Luczkowiak, L. Rodríguez-Pérez, I. Nierengarten, M. Holler, J.-S. Remy, K. Buffet, S. P. Vincent, J. Rojo, R. Delgado, J.-F. Nierengarten, N. Martín, *Nat. Chem.* **2016**, *8*, 50-57; c) B. M. Illescas, J. Rojo, R. Delgado, N. Martín, *J. Am. Chem. Soc.* **2017**, *139*, 6018-6025; d) L. Rodríguez-Pérez, J. Ramos-Soriano, A. Pérez-Sánchez, B. M. Illescas, A. Muñoz, J. Luczkowiak, F. Lasala, J. Rojo, R. Delgado, N. Martín, *J. Am. Chem. Soc.***2018**, *140*, 9891-9898.

115. a) Y. Huang, J. Hu, W. Kuang, Z. Wei, C. F. J. Faul, *Chem. Commun.* **2011**, *47*, 5554-5556; b) Y. Huang, J. Wang, Z. Wei, *Chem. Commun.* **2014**, *50*, 8343-8345.

116. a) S. Gonen, F. Di Maio, T. Gonen, D. Baker, *Science* **2015**, *348*, 1365-1368; b) G. Grigoryan, Y. H. Kim, R. Acharya, K. Axelrod, R. M. Jain, L. Willis, M. Drndic, J. M. Kikkawa, W. F. De Grado, *Science* **2011**, *332*, 1071-1076; c) N. P. King, J. B. Bale, W. Sheffler, D. E. McNamara, S. Gonen, T. Gonen, T. O. Yeates, D. Baker, *Nature* **2014**, *510*, 103-108.

117. a) N. Koga, R. Tatsumi-Koga, G. Liu, R. Xiao, T. B. Acton, G. T. Montelione, D. Baker, *Nature* **2012**, *491*, 222-227; b) C. Xu, R. Liu, A. K. Mehta, R. Guerrero-Ferreira, E. R. Wright, S. Dunin-Horkawicz, K. Morris, L. C. Serpell, X. Zuo, J. S. Wall, V. P. Conticello, *J. Am. Chem. Soc.* **2013**, *135*, 15565-15578; c) J. D. Brodin, X. I. Ambroggio, C. Tang, K. N. Parent, T. S. Baker, F. A. Tezcan, *Nat. Chem.* **2012**, *4*, 375-382.

118. a) Y. S. Nam, T. Shin, H. Park, A. P. Magyar, K. Choi, G. Fantner, K. A. Nelson, A. M. Belcher, *J. Am. Chem. Soc.* **2010**, *132*, 1462-1463; b) M. Tridgett, C. Moore-Kelly, J. H. A. Duprey, L. O. Iturbe, C. Tsang, H. A. Little, S. K. Sandhu, M. R. Hicks, T. R. Dafforn, A. Rodger, *RSC Adv.* **2018**, *8*, 29535-29543.

119. a) R. A. Miller, A. D. Presley, M. B. Francis, *J. Am. Chem. Soc.* **2007**, *129*, 3104-3109; b) Y. S. Nam, T. Shin, H. Park, A. P. Magyar, K. Choi, G. Fantner, K. A. Nelson, A. M. Belcher, *J. Am. Chem. Soc.* **2010**, *132*, 1462-1463; c) M. Delor, J. Dai, T. D. Roberts, J. R. Rogers, S. M. Hamed, J. B. Neaton, P. L. Geissler, M. B. Francis, N. S. Ginsberg, *J. Am. Chem. Soc.* **2018**, *140*, 6278-6287.

120. K. J. Channon , G. L. Devlin, C. E. MacPhee , *J. Am. Chem. Soc.* **2009**, *131*, 12520-12521.

121. a) O. Y. Kas, M. B. Charati, L. J. Rothberg, M. E. Galvin, K. L. Kiick, *J. Mater. Chem.* **2008**, *18*, 3847-3854; b) R. J. Kumar, J. M. MacDonald, T. B. Singh, L. J. Waddington, A. B. Holmes, *J. Am. Chem. Soc.* **2011**, *133*, 8564-8573; c) B. Kang, W. Yang, S. Lee, S. Mukherjee, J. Forstater, H. Kim, B. Goh, T. Kim, V. A. Voelz, Y. Pang, J. Seo, *Sci. Rep.* **2017**, *7*, 4786-4796.

122. W. H. Landschulz, P. F. Johnson, S. L. McKnight, *Science* **1988**, *240*, 1759-1764.

123. a) J. M. Mason, K. M. Arndt, *ChemBioChem* **2004**, *5*, 170-176; b) M. Pechar, R. Pola, *Biotechnol. Adv.* **2013**, *31*, 90-96.

124. a) B. S. Der, B. Kuhlman, *Nat. Biotechnol.* **2013**, *31*, 809-810; b)J. M. Fletcher, R. L. Harniman, F. R. H. Barnes, A. L. Boyle, A. Collins, J. Mantell, T. H. Sharp, M. Antognozzi, P. J. Booth, N. Linden, M. J. Miles, R. B. Sessions, P. Verkade, D. N. Woolfson, *Science* **2013**, *340*, 595-599; c) N. C. Burgess, T. H. Sharp, F. Thomas, C. W. Wood, A. R. Thomson, N. R. Zaccai, R. L. Brady, L. C. Serpell, D. N. Woolfson, *J. Am. Chem. Soc.* **2015**, *137*, 10554-10562.

125. J. Clarke, L. Regan, *Curr. Opin. Struct. Biol.* **2010,** *20* (4), 480-481.

126. a) L. D. D'Andrea, L. Regan, *Trends Biochem. Sci.* **2003**, *28*, 655-662; E.R.G. Main, A.R. Lowe, S.G.J. Mochrie, S.E. Jackson, L. Regan, *Curr. Opin. Struct. Biol.* **2015**, *15*, 464-471.

127. T. Z. Grove, L. Regan, *Curr. Opin. Struct. Biol.* **2012**, *22*, 451-456; b) E. R. Main, J. J. Phillips, C. Millership, *Biochem. Soc. Trans.* **2013**, *41*, 1152-1158.

128. a) J. R. Lamb, S. Tugendreich, P. Hieter, *Trends Biochem. Sci.* **1995**, *20*, 257-259; b) A. K. Das, P. W. Cohen, D. Barford, *EMBO J.* **1998**, *17*, 1192-1199.

129. T. Kajander, A. L. Cortajarena, S. Mochrie, L. Regan, *Acta Crystallogr., Sect. D: Biol. Crystallogr.* **2007**, *63*, 800-811.

130. A. L. Cortajarena, T. Kajander, W. Pan, M. J. Cocco, L. Regan, *Protein Eng., Des. Sel.* **2004**, *17*, 399-409; b) A. L. Cortajarena, L. Regan, *Protein Sci.* **2006**, *15*, 1193-1198.

131. a) T. Kajander, A. L. Cortajarena, E. R. G. Main, S. G. J. Mochrie, L. Regan, *J. Am. Chem. Soc.* **2005**, *127*, 10188-10190; b) A. L. Cortajarena, S. G. J. Mochrie, L. Regan, *Protein Sci.* **2011**, *20*, 1042-1047.

132. a) S. H. Mejías, J. López-Andarias, T. Sakurai, S. Yoneda, K. P. Erazo, S. Seki, C. Atienza, N. Martín, A. L. Cortajarena, *Chem. Sci.* **2016**, *7*, 4842-4847; b) J. López-Andarias, S. H. Mejías, T. Sakurai, W. Matsuda, S. Seki, F. Feixas, S. Osuna, C. Atienza, N. Martín, A. L. Cortajarena, *Adv. Funct. Mater.* **2018**, *28*, 1704031; c) S. H. Mejias, P. Couleaud, S. Casado, D. Granados, M. A. Garcia, J. M. Abad, A. L. Cortajarena, *Colloids Surf. B Biointerfaces* **2016**, *141*, 93-101.

133. S. Iijima, *Nature* **1991**, *354*, 56-58.

134. K. S. Novoselov, A. K. Geim, S. V. Morozov, D. Jiang, Y. Zhang, S. V. Dubonos, I. V. Grigorieva, A. A. Firsov, *Science* **2004**, *306*, 666-669.

135. a) M. Calvaresi, F. Zerbetto, *Acc. Chem. Res.* **2013**, *46*, 2454-2463; b) C. Li, R. Mezzenga, *Nanoscale* **2013**, *5*, 6207-6218; c) K. Babooram, R. Narain, *Carbon Nanotubes and Fullerene C_{60} Bioconjugates* **2014**.

136. F. De Leo, A. Magistrato, D. Bonifazi, *Chem. Soc. Rev.* **2015**, *44*, 6916-6953.

137. M. Calvaresi, F. Zerbetto, *ACS Nano* **2010**, *4*, 2283-2299.

138. S. H. Friedman, D. L. DeCamp, R. P. Sijbesma, G. Srdanov, F. Wudl, G. L. Kenyon, *J. Am. Chem. Soc.* **1993**, *115*, 6506-6509.

139. Z. Gao, H. Li, H. Zhang, X. Liu, L. Kang, X. Luo, W. Zhu, K. Chen, X. Wang, H. Jiang, *BMC Bioinformatics* **2008**, *9*, 104-110.

140. K. Kim, D. Ko, Y. Kim, N. H. Kim, J. Paul, S. Zhang, C. B. Murray, R. Acharya, W. F. DeGrado, Y. H. Kim, G. Grigoryan, *Nat. Commun.* **2016**, *7*, 11429-11438.

141. a) S. A. Andujar, F. Lugli, S. Hönger, R. D. Enriz, F. Zerbetto, *Phys. Chem. Chem. Phys.* **2012**, *14*, 8599-8607; b) A. G. Bobylev, A. B. Kornev, L. G. Bobylev, M. D. Shpagina, I. S. Fadeeva, R. S. Fadeev, D. G. Deryabin, J. Balzarini, P. A. Troshin, Z. A. Podlubnaya, *Org. Biomol. Chem.* **2011**, *9*, 5714-5719; c) A. G. Bobylev, M. D. Shpagina, L. G. Bobyleva, A. D. Okuneva, L. B. Piotrovsky, Z. A. Podlubnaya, *Biophysics*, **2012**, *57*, 300-304. d) E. G. Makarova, R. Y. a. Gordon and I. Y. a. Podolski, *J. Nanosci. Nanotechnol.* **2012**, *12*, 119-126; e) B. Ma, R. Nussinov, *Proc. Natl. Acad. Sci. U. S. A.* **2002**, *99*, 14126–14131.

142. N. Hendler, B. Belgorodsky, E. D. Mentovich, S. Richter, L. Fadeev, M. Gozin, *Adv. Funct. Mater.* **2012**, *22*, 3765-3776.

143. G. Zuo, S. Kang, P. Xiu, Y. Zhao, R. Zhou, *Small* **2013**, *9*, 1546-1556.

144. C. Staii, A. T. Johnson, M. Chen, A. Gelperin, *Nano Lett.* **2005**, *5*, 1774-1778.

145. R. J. Chen, S. Bangsaruntip, K. A. Drouvalakis, S. K. Wong, M. Shim, Y. Li, W. Kim, P. J. Utz, H. Dai, *Proc. Natl. Acad. Sci. USA* **2003**, *100*, 4984-4989.

146. a) P. Nednoor, M. Capaccio, V. G. Gavalas, M. S. Meier, J. E. Anthony, L. G. Bachas, *Bioconjugate Chem.* **2004**, *15*, 12-15; b) M. Sarikaya, C. Tamerler, A. K. -. Jen, K. Schulten, F. Baneyx, *Nat. Mater.* **2003**, *2*, 577-585.

147. G. Grigoryan, Y. H. Kim, R. Acharya, K. Axelrod, R. M. Jain, L. Willis, M. Drndic, J. M. Kikkawa, W. F. DeGrado, *Science* **2011**, *332*, 1071-1076.

148. a) K. Bradley, M. Briman, A. Star, G. Grüner, *Nano Lett.* **2004**, *4*, 253-256; b) D. Nepal, K. Geckeler, *Small* **2007**, *3*, 1259-1265.

149. K. Kostarelos, A. Bianco, M. Prato, *Nat. Nanotechnol.* **2009**, *4*, 627-633.

150. a) B. S. Harrison, D. Eberli, S. J. Lee, A. Atala, J. J. Yoo, Biomaterials **2007**, *28*, 4628-4634; b) C. Ménard-Moyon, K. Kostarelos, M. Prato, A. Bianco, Chem. Biol. **2010**, 17, 107-115.

151. a) B. S. Harrison, D. Eberli, S. J. Lee, A. Atala, J. J. Yoo, *Biomaterials* **2007**, *28*, 4628-4634; b) E. Heister, E. W. Brunner, G. R. Dieckmann, I. Jurewicz, A. B. Dalton, *ACS Appl. Mater. Interfaces* **2013**, *5*, 1870-1891.

152. Z. Liu, J. T. Robinson, S. M. Tabakman, K. Yang, H. Dai, *Materials Today* **2011**, *14*, 316-323.

153. a) S. Syama, P. V. Mohanan, *Int. J. Biol. Macromol.* **2016**, *86*, 546-555; b) A. M. Pinto, I. C. Gonçalves, F. D. Magalhães, *Colloids and Surfaces B: Biointerfaces* **2013**, *111*, 188-202; c) S. Gurunathan, J. Kim, *International journal of nanomedicine* **2016**, *11*, 1927-1945.

154. I. M. Mosa, A. Pattammattel, K. Kadimisetty, P. Pande, M. El-Kady, G. W. Bishop, M. Novak, R. B. Kaner, A. K. Basu, C. V. Kumar, J. F. Rusling, *Adv. Energy Mater.* **2017**, *7*, 1700358.

155. S. Viswanathan, T. N. Narayanan, K. Aran, K. D. Fink, J. Paredes, P. M. Ajayan, S. Filipek, P. Miszta, H. C. Tekin, F. Inci, U. Demirci, P. Li, K. I. Bolotin, D. Liepmann, V. Renugopalakrishanan, *Materials Today* **2015**, *18*, 513-522.

156. S. F. Oliveira, G. Bisker, N. A. Bakh, S. L. Gibbs, M. P. Landry, M. S. Strano, *Carbon* **2015**, *95*, 767-779.

157. C. Li, J. Adamcik, R. Mezzenga, *Nat. Nanotechnol.* **2012**, *7*, 421-427.

158. C. D. Spicer, E. T. Pashuck, M. M. Stevens, *Chem. Rev.* **2018**, *118*, 7702-7743.

159. E. A. Hoyt, Cal, Pedro M. S. D., B. L. Oliveira, G. J. L. Bernardes, *Nat. Rev. Chem.* **2019**, *3*, 147-171.

160. a) O. Ito, F. D'Souza, *Molecules* **2012**, *17*, 5816-5835; b) J. Zhang, C. Li, S. T. Williams, S. Liu, T. Zhao, A. K. -. Jen, *J. Am. Chem. Soc.* **2015**, *137*, 2167-2170.

161. a) M. P. De Haas, J. M. Warman, *Chem. Phys.* **1982**, *73*, 35-53; b) F. C. Grozema, L. D. A. Siebbeles, *J. Phys. Chem. Lett.* **2011**, *2*, 2951-2958; c) S. Seki, A. Saeki, T. Sakurai, D. Sakamaki, *Phys. Chem. Chem. Phys.* **2014**, *16*, 11093-11113; d) O. G. Reid, D. T. Moore, Z. Li, D. Zhao, Y. Yan, K. Zhu, G. J. Rumbles, *Phys. D: Appl. Phys.* **2017**, *50*, 493002.

162. I.-S. Park, Y.-R. Yoon, M. Jung, K. Kim, S. Park, S. Shin, Y.-b. Lim, M. Lee, *Chem. Asian J.* **2011**, *6*, 452-458.

163. a) J. Porath, J. Carlsson, I. Olsson, G. Belfrage, *Nature* **1975**, *258*, 598-599; b) J. Porath, *Protein Expr. Purif.* **1992**, *3*, 263-281.

164. a) J. M. Abad, S. F. L. Mertens, M. Pita, V. M. Fernández, D. J. Schiffrin, *J. Am. Chem. Soc.* **2005**, *127*, 5689-5694; b) P. Jolly, A. Miodek, D. Yang, L. Chen, M. D. Lloyd, P. Estrela, *ACS Sens.* **2016**, *1*, 1308-1314; c) D. L. Johnson, L. L. Martin, *J. Am. Chem. Soc.* **2005**, *127*, 2018-2019; d) C. Xu, K. Xu, H. Gu, X. Zhong, Z. Guo, R. Zheng, X. Zhang, B. Xu, *J. Am. Chem. Soc.* **2004**, *126*, 3392-3393.

165. a) Z. Liu, B. X. Dong, M. Misra, Y. Sun, J. Strzalka, S. N. Patel, F. A. Escobedo, P. F. Nealey, C. K. Ober, *Adv. Funct. Mater.* **2019**, *29*, 1805220; b) S. Erbas-Cakmak, F. P. Cakmak, S. D. Topel, T. B. Uyar, E. U. Akkaya, *Chem. Commun.* **2015**, *51*, 12258-12261.

166. D. A. Case, *et al.* AMBER 16, University of California, San Francisco, 2016.

167. J. Wang, R. M. Wolf, J. W. Caldwell, P. A. Kollman, D. A. Case, *J. Comp. Chem.* **2004**, *25*, 1157-1174.

168. C. I. Bayly, P. Cieplak, W. Cornell, P. A. Kollman, *J. Phys. Chem.* **1993**, *97*, 10269-10280

169. a) B. H. Besler, K. M. Merz, P. A. Kollman, *J. Comp. Chem.* **1990**, *11*, 431-439; b) U. C. Singh, P. A. Kollman, *J. Comp. Chem.* **1984**, *5*, 129-145.

170. Gaussian 09 v. Gaussian 09, Revision A.02 (Gaussian, Inc., Pittsburgh, PA, **2009**).

171. Schafmeister, C. E. A. F. R., W. F.; Romanovsky, V. University of California, San Francisco, **1995**.

172. C. Sagui, T. A. Darden, *Annu. Rev. Biophys. Biomolec. Struct.* **1999**, *28*, 155-179.

173. J.-P. Ryckaert, G. Ciccotti, H. J. C. Berendsen, *J. Comp. Phys.* **1977**, *23*, 327-34.

174. X. Wu, B. R. Brooks, *Chem. Phys. Lett.* **2003**, *381*, 512-518.